Analysis of the role of discontinuities on landslide instability at various scales utilising remote sensing data and numerical modelling

Submitted by Lingfeng He

to the University of Exeter as a thesis for the degree of

Doctor of Philosophy

in Mining and Minerals Engineering

August 2022

I certify that all material in this thesis which is not my own work has been identified and that any material that has previously been submitted and approved for the award of a degree by this or any other University has been acknowledged.

Author's declaration

I declare that the work in this dissertation titled 'Analysis of the role of discontinuities on landslide instability at various scales utilising remote sensing data and numerical modelling' has been carried out by me at Camborne School of Mines. The information derived from the literature has been duly acknowledged in the text and a list of references provided. No part of this dissertation was previously presented for another degree or diploma at this or any other institute.

The results obtained during this research have been presented in the following publications, corresponding to different chapters of the thesis:

Chapter 3

He, L., Coggan, J, Francioni, M, Eyre, M. (2021) Maximizing impacts of remote sensing surveys in slope stability—a novel method to incorporate discontinuities into machine learning landslide prediction, ISPRS International Journal of Geo-Information, volume 10, no. 4, pages 232-232, DOI:10.3390/ijgi10040232

Chapter 4

He, L., Coggan, J., Stead, D., Francioni, M., Eyre, M. (2021) Modelling discontinuity control on the development of Hell's Mouth landslide, Landslides, volume 19, no. 2, pages 277-295, DOI:10.1007/s10346-021-01813-3

Chapter 5

He, L., Francioni, M., Coggan, J., Calamita, F., Eyre, M. (2022) Modelling the influence of geological structures in paleo rock avalanche failures using field and remote sensing data, Remote Sensing, Volume 14, no.16, page 4090, DOI: 10.3390/rs14164090

Lingfeng He

30/08/2022

Abstract: This research focuses on the influence of discontinuities on the origin and development of landslide instability mechanisms at different scales. Various remote sensing techniques have been used for data acquisition to characterize discontinuity and landslide-related features. The remotely captured data was subsequently interrogated using a variety of analytical methods and numerical modelling to investigate the role of discontinuities at different scales in the origin and development of rock slides through analysis of selected case studies. The investigation has been carried out through landslide susceptibility mapping (LSM) with the inclusion of discontinuities, the use and application of 3D distinct element method (DEM) modelling of the Hell's Mouth landslide in the UK, 2D DEM modelling of a catastrophic rock avalanche in Italy, and the analysis of slope instability in an open pit mine (more than 200m height) in South America using both a 2D finite/discrete element method (FDEM) approach and a 3D DEM approach.

The result of LSM demonstrates that integration of discontinuity orientation through GIS based kinematic analysis can effectively improve landslide prediction using machine learning (ML) modelling. In Hell's Mouth case study, numerical modelling and field observations both suggest that the cliff instability was characterised by a combination of planar sliding, wedge sliding, and toppling modes of failure controlled by the discrete fracture network geometry. For the Italian pale landslide, it was controlled by translational sliding along a folded bedding plane, with toe removal induced by river erosion resulting in daylighting of the bedding, creating kinematic freedom for the landslide. In addition, due to the presence of an anticline, the landslide region was constrained in the middle-lower section of the slope where the relatively high inclination of the bedding plane was detected. With respect to the inter-ramp deformation in South America, modelling results indicate the potential control and influence of a rock bridge, constrained by two faults at the toe of the slope. It was also demonstrated that blasting-induced weak zones and sequential excavations were potential key triggers of the observed slope deformation.

Acknowledgement

First and foremost, I would like to express my sincere gratitude to my supervisors, Dr Matthew Eyre and Prof John Coggan, for their guidance and support throughout my entire PhD study and for their incredible patience in working with me over the past three years. During the coronavirus pandemic, their support has been extremely helpful for me to work from home and allow my PhD research to properly proceed. In addition, I am deeply grateful for their help in improving my research skills and polishing my academic writing skills. Their endless guidance is hard to forget throughout my life.

Apart from my supervisors, I would like to express my gratitude to Dr Mirko Francioni at the University of Urbino for sharing valuable research data and insightful suggestions to improve my research. I would also like to thank Mr Herman Aguirre for helping me obtain critical datasets to assist my research.

My gratitude also goes to thesis examiners Professor Lisa Borgratti from University of Bologna and Dr Andrew Wetherelt from University of Exeter. Their responsible review and critical comments are effective to improve my thesis quality.

I would also like to thank my friends who have always been a major source of support when things would get a bit discouraging: Mr Chia-Ho, Dr Chenyu Zhao and Dr Hailun Xie. The pressure from PhD research has been greatly relieved with your support. I would never forget the time with them in Cornwall.

Last, but not least, my family has been constantly giving me nothing but support, both emotionally and financially. However, I feel sorry that there is no chance to go back to China to visit and look after them due to the coronavirus. My love and gratitude for them can hardly be expressed in words.

Table of Contents

List of figures

List of tables

Abbreviation

Artificial neural network	ANN
Constant loading velocity	CLV
Discrete fracture network	DFN
Distinct element method	DEM
Discontinuous deformation analysis	DDA
Deep learning neural network	DLNN
finite/discrete element method	FDEM
Finite element method	FEM
Factor of Safety	FoS
Frequency ratio	FR
Ground control point	GCP
Geographic information system	GIS
Geological strength index	GSI
Joint wall compressive strength	JCS
Joint roughness coefficient	JRC
Light detection and ranging	LiDAR
Land cover and land use	LCLU
Line of intersection	LOI
Landslide susceptibility mapping	LSM
Machine learning	ML
Multilayer perceptron	MLP
Rectified linear unit	ReLU
Representative elementary volume	REV
Random forest	RF
Receiver operating characteristic	ROC
Remote sensing	RS
Standard deviation	SD
Structure from motion	SfM
Synthesize rock mass	SRM
Support vector machine	SVM
Unmanned aerial vehicle	UAV
Uniaxial compressive strength	UCS

Chapter 1. Introduction

1.1. Overview

Landslides are a significant geohazard that can have devastating impacts on human safety and infrastructure. It has been reported that the total land area over the world subjected to landslides is about 3.7 million square kilometres, affecting a population of nearly 300 million (Dilley et al., 2005). The relatively high-risk areas (top three deciles) cover about 820,000 square kilometres with an estimated population of 66 million. Worldwide attention has been drawn into this domain, which is focused on landslide analysis for purposes of investigating landslide mechanisms, analysing landslide development and following hazardous assessment, and proposing remedial measures.

The term ‘landslide’ describes the downward and outward movement of slope-forming materials including rock, soil, artificial fill, or a combination of these (USGS, 2004). Landslides can be classified in different ways, with their primary objectives of highlighting associated essential features (Varnes, 1978). One of the principal landslide classification methods, introduced by Varnes (1978), is based on the type of movement primarily and slope-forming material secondarily. With the type of movement, landslides are categorized into 6 groups: falls, topples, slides, lateral spreads, flows, and complex movements that include combinations of two or more of the above-mentioned five types. In addition, considering that landslides may occur in various types of lithological environments (e.g., bedrock or engineering soils), landslides can also be classified into rock slides, debris landslides and earth landslides, respectively. The classification of landslides, based on the types of movement and material, is presented in Table 1-1.

In multiple landslide cases, geological discontinuities (e.g., joints, joints, cleavages, bedding, foliation, faults, and folds) have shown their controls on rock or rock-involved landslide development/occurrence, which is more notable in some typical types of movement, such as slides, topples and falls.

Table 1-1. *Landslide classification based on types of movement and material (Varnes, 1978)*

Type of movement		Type of material		
		Bedrock	Engineering soils	
			Predominantly course	Predominantly fine
Falls		Rockfall	Debris fall	Earth fall
Topples		Rock topple	Debris topple	Earth topple
Slides	Rotational	Rock slide	Debris slide	Earth slide
	Translational			
Lateral spread		Rock spread	Debris spread	Earth spread
Flows		Rock flow (deep creep)	Debris flow (soil creep)	Earth flow
Complex		Combination of two or more principal types of movement		

A slide-type landslide is a downslope movement of material that occurs along a distinctive rupture or slip surface. Geological structures can act as slip surfaces for failure material sliding downward. When the slip surface is planar, the slide is said to be translational (Fig. 1-1a); if the slip surface is listric/curved, the slide is rotational (Fig. 1-1b). An example of discontinuity-controlled instability is the Downie Slide (British Columbia, Canada) where the failed rock mass was displaced along translational structure-related shear zones (Donati et al., 2021b). In addition, the earthquake-triggered Maoxian landslide (Sichuan, China) is another case to demonstrate the dominant role of discontinuities (i.e., bedding) that provide the basal surface for planar sliding (Shao et al., 2019). Additional examples of translational landslides include the Utiku landslide (Massey et al., 2013), the Wolong landslide(Sun et al., 2021), and the Qiyangou landslide (Fan et al., 2019), which were all influenced by discontinuities. Apart from translational slides, discontinuities can also influence large-scale rotational failures. A listric fault with a curved fault plane, characterized by a decreasing angle of dip with depth, was observed to provide a kinematic condition for the Hell's Mouth landslide (Cornwall, UK) to move downward, with the evidence/presence of an arc-shaped scarp (Francioni et al., 2018a). Seno and Thüring (2006) noted that five catastrophic landslides at Campo Vallemaggia, Cerentino, Peccia, Val Canaria, and Val Colla were predominantly rotational and structurally related, being controlled by the superimposition of local faults and major joints.

Topple or toppling is a common mode of instability where rock blocks rotate about their toes and overturn (Fig. 1-1c). This type of instability is more frequently observed in layered or blocky slopes where geological structures with relatively low strength

split rock columns into rock blocks. In accordance with different failure mechanisms (brittle or ductile), toppling can be classified as direct/blocky toppling (with the presence of basal cutting planes) and flexural toppling (with bending of layered rock strata) (Hoek and Bray, 1981). The evidence from some toppling failures has shown the control of geological structures and their role in landslide development. The analysis of Melbur Pit slope instability from Vanneschi et al. (2019) highlighted that the geometry and strength parameters of discontinuities have controlling effects on defining the geometry of the observed direct toppling and its subsequent development. The studies of the Mystery Creek landslide and Mount Breakenridge landslide both demonstate the distribution of discontinuities (local joints and schistosity, respectively) in influencing the toppling behaviour of large rock slopes (Nichol et al., 2002). More examples of toppling instability that demonstrate relationships with geological structures include (without limitation to) the Heather Hill landslide (Pritchard and Savigny, 1991), Moosfluh Landslide (Glueer et al., 2019), a deep-seated large-scale toppling failure in a section of Lancang Slope in Southwest China (Tu et al., 2020), flexural toppling of slate with high-angle faults in the Abe River catchment (Yokoyama, 2020).

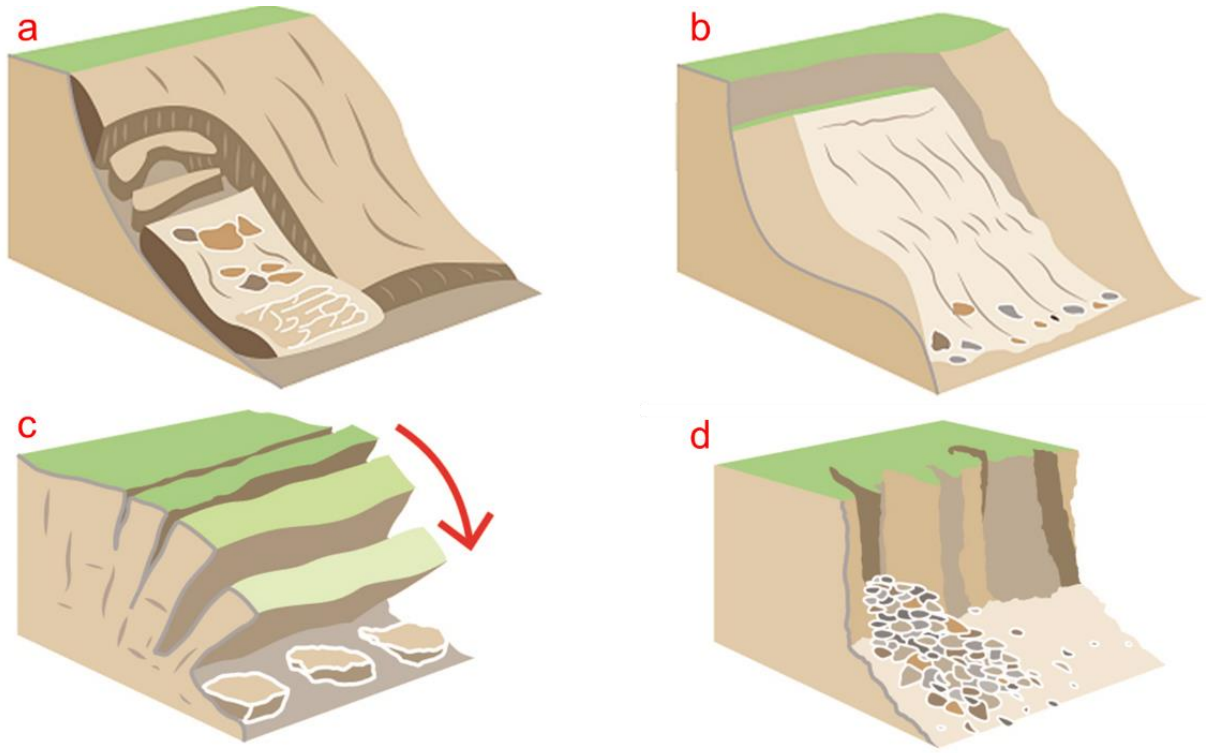

Fig. 1-1. *Sketch of different modes of landslides, including a) translational slide, b) rotational slide, c) topple, and d) rockfall (images from (British Geological Survey, 2018)).*

Rockfall is the downslope movement of rocks that are detached from steep slopes, which occurs by free-fall, bouncing, and rolling (Fig. 1-1d). The detachment of rock usually occurs along discontinuities, such as fractures, joints, and bedding, which potentially reflects the close relationship between rockfall and geological structures. Evaluation of the rockfall at Hongshiyan slope, using field survey and subsequent analysis, indicated that scale and structural features of discontinuities can have a significant influence on rockfall distribution and associated failure mechanism (Li et al., 2019). Other rockfall related case studies have also highlighted the controlling effect of structures (Palma et al., 2012; Teza et al., 2015; Robiati et al., 2019).

1.2. Thesis structure

This thesis is composed of eight chapters. A summary of the structure is provided below.

1) Chapter 1 presents an overview of the research topic, problem statement, and research objectives. Following these, research methods are provided to address the research gap and fulfil the objectives.
2) Chapter 2 presents a literature review associated with the types and properties of discontinuities. In addition, different methods of landslide prediction and analysis are summarised and reviewed, concentrating on LSM and numerical analysis.
3) Chapter 3 provides novel research on the incorporation of discontinuity information into ML modelling for LSM. The research involves: 1) an application of GIS-based kinematic analysis to assess a section of coastline kinematically prone to landslides. Results from the kinematic analysis, coupled with several landslide influencing factors, were then adopted as input variables in ML models to predict landslides. Various ML models, such as random forest (RF), support vector machine (SVM), multilayer perceptron (MLP) and deep learning neural network (DLNN) models were evaluated. Results highlight that inclusion of discontinuities into ML models can improve landslide prediction accuracy.
4) In Chapter 4, the controlling effects of discontinuities on a landslide that occurred in blocky rock mass are examined. Several integrated remote sensing (RS) techniques have been utilized for data acquisition to characterize the slope geometry, landslide features and tension crack extent and development. In view of the structurally controlled mechanism of the rock slope failures, a 3D DEM code 3DEC incorporating a discrete fracture network and rigid blocks, was adopted for the stability analysis. In addition, a sensitivity analysis was undertaken to provide further insight into the influence of key discontinuity parameters (i.e., dip, dip direction, persistence and friction angle) on the stability of the coastline within the chosen case study.
5) Chapter 5 presents a case study to examine the effect of an anticline on an ancient translational landslide in layered rocks. Combined use of RS

techniques (i.e., UAV-RS and satellite RS) have been utilized to interpret post-landslide features at various scales. In addition, a 2D discrete element method was used to simulate the development of the landslide under the influence of river erosion at the slope toe. The influence of folding of the bedding plane on the landslide failure mechanism is also investigated.

6) Chapter 6 provides analysis and modelling of a landslide or slope instability that involves rock fracturing and rock mass deformation. In this section, a DFN model has been constructed based on field mapping data to characterize the on-site or in-situ discontinuity fracture network within the slope geometry. 2D FDEM numerical analysis was used to investigate brittle rock fracturing and rock mass deformation of the failure within the case study slope. The analysis also provides an improved understanding of the impact of blasting activities and toe removal induced by excavation on the slope instability. In addition, a 3D DEM approach has also been used to model the deformation of rock bridges under the influence of sequential excavation and blasting. Importantly, the modelling results are verified by field observations from the case study site.
7) Chapter 7 provides a discussion on discontinuity control on landslides at different scales based on the findings of the investigations undertaken. In addition, precautions for ML-based LSM and numerical modelling for jointed rock mass are also provided for readers to avoid pitfalls when executing similar research.
8) Chapter 8 summarizes the main achievements and conclusions from the research and presents future research work that can be undertaken in this area.

1.3. Rationale of the research

In the above-mentioned case studies, discontinuities have been highlighted as one of the critical pre-conditioning factors for landslides, providing kinematic freedom for rock blocks. Rock slides preferentially occur in the slope under an unfavourable condition associated with the geometric arrangement of on-site discontinuities (Stead and Wolter, 2015). Therefore, efficient use of the information on geological structures, particularly the use and analysis of remotely captured data, can improve the understanding of the nature of rock slides, and the interpretation of landslides.

Landslide susceptibility mapping (LSM) has been used to predict landslide probability of a large-scale region (over hundreds of square kilometres in size). LSM is usually carried out by using statistical methods to construct mathematic/statistical relationships between landslides and selected influencing factors. Its effectiveness has been demonstrated in various cases with different statistical models which involve support vector machine (SVM) (Yilmaz, 2010; Xu et al., 2012; Kavzoglu et al., 2014), decision tree analysis (Dou et al., 2019), random forest (RF) (Behnia and Blais-Stevens, 2018; Dou et al., 2019), and logistic regression (Chen et al., 2018; Huang et al., 2020a), and more complicated deep learning neural networks (DLNN) (Bui et al., 2020; Lucchese et al., 2020; Samien et al., 2020a). To date discontinuities have rarely been used for LSM. Given the potentially significant role played by discontinuities on rock slide susceptibility, the incorporation of discontinuity properties (e.g., orientation, distribution, size, strength) may contribute to building more robust statistical models and improving landslide prediction accuracy. A method to incorporate discontinuities into statistical modelling is developed within the research undertaken described within this thesis.

The role of discontinuities on landslide development still requires further understanding, particularly for landslides in blocky rock masses. For example, discontinuities have been found to be related to the preferential propagation of tension cracks (Bovis and Evans, 1996; Brideau et al., 2007; Zhang, M. et al., 2018).

Further analysis of the development of tension cracks may be beneficial to the interpretation of the role of discontinuities as well as further understanding of the development of a landslide. However, the onset and opening of tension cracks, has to date had limited consideration in the numerical analysis of a landslide.

In addition, rock deformation and/or internal fracturing or damage may occur in cases where high stresses concentrations exceed rock strength, such as instabilities in large open pit mine slopes or underground excavations. In jointed rock masses, rock deformation and associated rock bridge failure increase complexity of stability analysis, which are highly influenced by discontinuities and the discrete fracture network. Practically, discontinuities (i.e., joints) exhibit a stochastic characteristic of their distribution, such as variations in the geometry of joints (e.g., dip, dip direction and size) belonging to the same set (Stead and Wolter, 2015; Elmo et al., 2018; Miyoshi et al., 2018; Bastola et al., 2020). In this context, joints identified in the field are commonly represented by using a discrete fracture network (DFN) to characterize their intrinsic relations and stochastic nature (Miyoshi et al., 2018; Pan et al., 2019; Zhang et al., 2021). Mechanical behaviours of the rock mass have been frequently investigated through the integration of DFN and numerical modelling. However, as the integration of a stochastic DFN into numerical analysis may result in excessive modelling computation intensity and memory requirements (Elmo et al., 2018), further understanding of rock block deformation and mechanically anisotropic behaviour of jointed rock mass is still required in large-scale slopes.

The previous overview suggests that control of discontinuities on landslide development needs further in-depth understanding, both for large-scale LSM or for a relatively small-scale and slope-specific landslide investigation in a blocky rock mass. In this context, this PhD research was conducted to provide comprehensive understanding of the importance of discontinuities, at different scales, on rock slides. This was undertaken to analyse how discontinuities (e.g., faults, bedding, and joints) can influence rock slides, providing a reference and analogue for scientists to investigate the mechanism of other rock slides effectively and rapidly.

1.4. Research methods

The primary goal of this research is to effectively use and incorporate geological structures for landslide prediction and analysis, establishing a multi-scale investigation from a specific slope stability assessment (relatively small-scale) to an extensive landslide survey (relatively large-scale investigation). In addition, the research will also demonstrate utilisation and use of remote sensing (RS) techniques to capture important geospatial information concerning geological structures and post-landslide features (e.g., slope topography, landslide scarp, tension cracks) that provides critical input data for both LSM analysis and numerical landslide analysis.

The LSM study explores a novel way to incorporate discontinuities into machine learning modelling for landslide prediction. Discontinuities, detected from remote sensing mapping, were incorporated into a GIS-based kinematic analysis. Results from the kinematic analysis were then taken as additional input variables to improve the accuracy of ML landslide prediction algorithms.

Numerical analysis of a specific blocky rock slope was undertaken during the investigation to evaluate the role of discontinuities in the origin and development of landslides and slope instability. This part of the study contains 3 main sections (3 case studies) to highlight different controlling influences of discontinuities at different scales.

The first case study adopts a 3D DEM method to simulate the Hell's Mouth landslide where rigid behaviour of rock mass is assumed. The modelling of the Hell's Mouth landslide is used to evaluate discontinuity control on the formation of a 'zawn' or inlet, the occurrence of two successive landslides and evidence of ongoing instability through the opening of tension cracks behind the cliff top.

The second case study employs a 2D DEM method to investigate the role of folded bedding and river erosion in the development of a historic translational landslide in Italy. The effect of discontinuities (i.e., a bedding plane and local joints) is analysed to define the extent and geometry of the landslide.

The third case study is related to the numerical analysis of an identified slope instability in a jointed rock mass with consideration of rock block deformation and rock bridge failures. In this case study, a slope instability occurred in an open pit mine in South America and was modelled by using a finite/discrete element method (FDEM) coupled with a DFN to assess role and impact of discontinuities on the modelled slope instability failure mechanism. The modelling provides opportunities to analyse the mechanical behaviour of rock bridges in the slope that is more than 200-metre high. The case study is also analysed using 3D DEM modelling to understand the influence of sequential excavation and blasting on the instability mechanism.

9)

Chapter 2. Background and literature review

2.1. Types of geological discontinuity

Discontinuity is a collective term for most types of faults, joints, weak bedding planes, weak schistosity planes, weakness zones (ISRM, 1978), to describe any mechanical weakness in rock masses with zero or low tensile strength.

Faults

Faults are a typical type of discontinuities with an observable amount of displacement. They are formed in the Earth's crust where the movement of the tectonic plates provides excessive stress and brittle fracturing occurs in response to the stress. Faults are rarely single planar units; normally they occur as parallel or sub-parallel sets of discontinuities. In accordance with different mechanisms and types of driving stress, faults can be categorized into 3 classes: dip-slip faults, strike-slip faults and oblique faults as summarized in Table 2-1 (Haakon Fossen, 2016).

Table 2-1. *Brief description of faults, including their types, causes and motions (Haakon Fossen, 2016).*

Type		Cause	Motion
Dip-slip faults	Normal faults	tension	Hanging wall slides down relative to the footwall
	Thrust faults	compression	The hanging wall moves up relative to the footwall (less than 45° inclination)
	Reverse faults		The hanging wall moves up relative to the footwall (more than 45° inclination)
Strike-slip faults	Left lateral	shearing	The opposite block moves to left
	Right lateral		The opposite block moves to right
	Left-lateral/normal	Shearing and tension	Combination of dip-slip and strike-slip motions
	Right-lateral/normal		
	Left-lateral/reverse	Shearing and compression	
	Right-lateral/ reverse		

Dip-slip faults are fractures where the blocks have moved in the dip direction of fault planes. When hanging-wall blocks move down (Fig. 2-3a), faults are termed normal faults. Normal faulting occurs when tensional stresses cause the crust to be stretched, pulling blocks apart away from each other which is the case of divergent plate boundaries. Thrust faults (Fig. 2-3b) and reverse faults (Fig. 2-3c) are characterized by convergent plate boundaries where the hanging-wall block moves up relative to the footwall block induced by compressional stresses. The difference between them is related to the inclination of fault planes where thrust faults are of an inclination less than 45° and reverse faults are more than 45°.

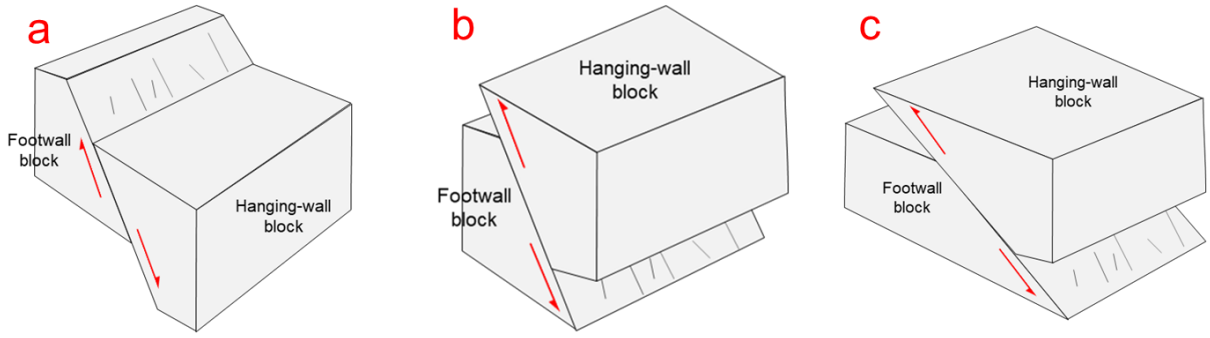

Fig. 2-1. *a) normal fault, b) reverse fault, c) thrust fault (modified after Haakon Fossen, 2016).*

Strike-slip faults (also called transcurrent faults, wrench faults, or lateral faults) are vertical or near-vertical fractures where the blocks have moved in the strike direction of the fault plane. Strike-slip faults are left-lateral (Fig. 2-2a) or right-lateral (Fig. 2-2b), depending on whether the block on the opposite side of the fault from an observer has moved to the right or left. A typical example is the transform plate boundary of two plates sliding past each other, horizontally, and induced by shear stresses dominantly.

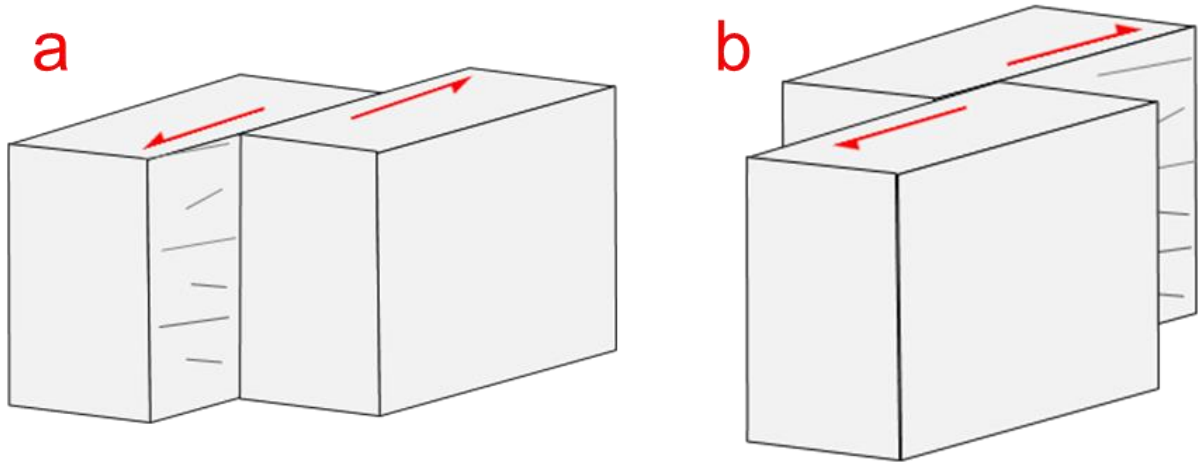

Fig. 2-2. *a) left-lateral strike-slip fault, b) right-lateral strike-slip fault (modified after Haakon Fossen, 2016).*

Oblique faults are controlled by both dip-slip and strike-slip displacements and are caused by a combination of shearing and tension/compressional stresses. In accordance with their motions, oblique faults can be classified as left-lateral/normal faults (Fig. 2-3a), right-lateral/normal faults (Fig. 2-3b), left-lateral/reverse faults (Fig. 2-3c), right-lateral/reverse faults (Fig. 2-3d).

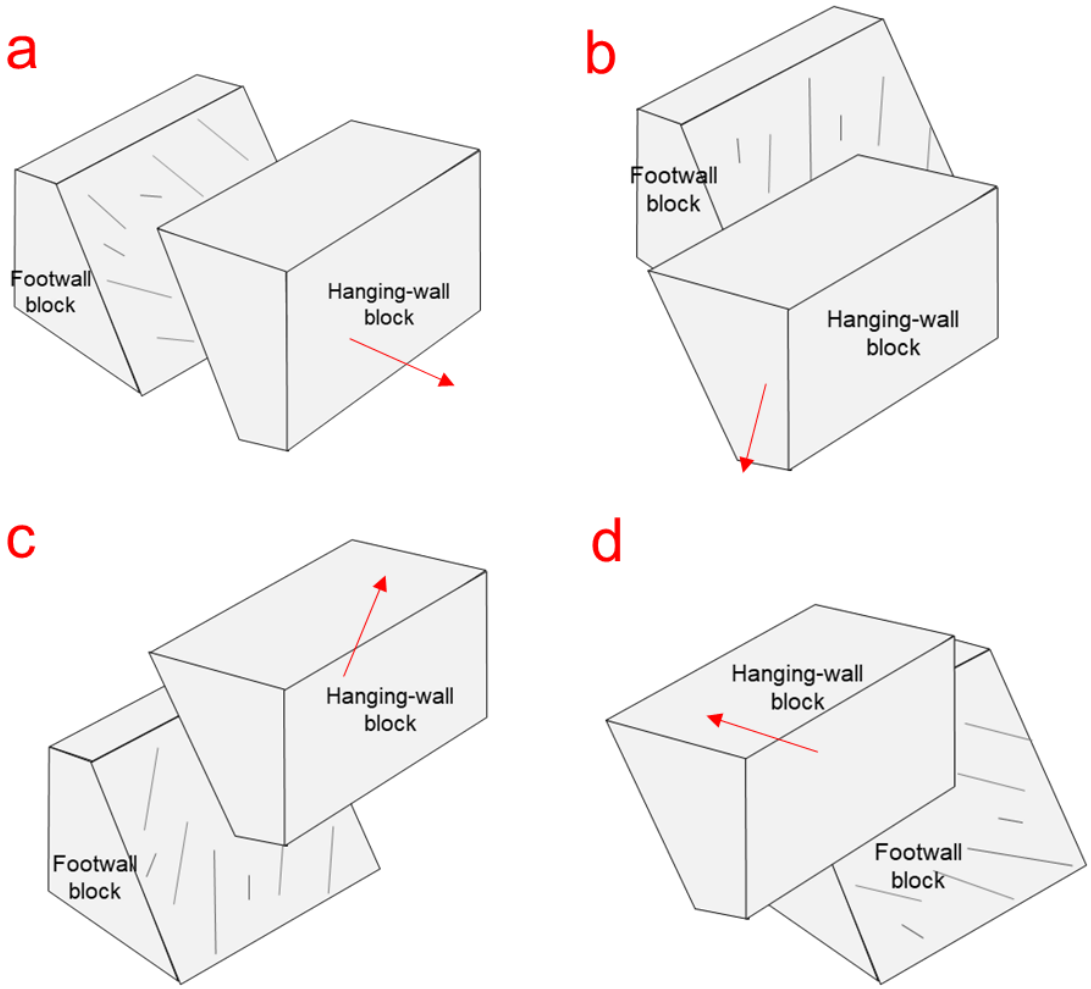

***Fig. 2-3.**, a) left-lateral/normal fault, b) right-lateral/normal fault, c) left-lateral/reverse fault, d) right-lateral/reverse fault (modified after Haakon Fossen, 2016).*

Joints

Joints are fractures with no visible displacement. They are formed by brittle rock fracturing as a consequence of the contraction of rocks induced by cooling and consolidation of rocks, or compression and tension during earth movements. For instance, sedimentary rocks observed in outcrops or excavations have undergone deposition at the surface and gradual burial to depths of several kilometres with the imposition of heat and pressure which can cause brittle fracturing when induced stresses in rocks exceed their strength (Hoek and Bray, 1981). In general, rock joints appear in a group of a parallel or sub-parallel distribution, called a set, and joint sets intersect to form a joint network/system as displayed in Fig. 2-4.

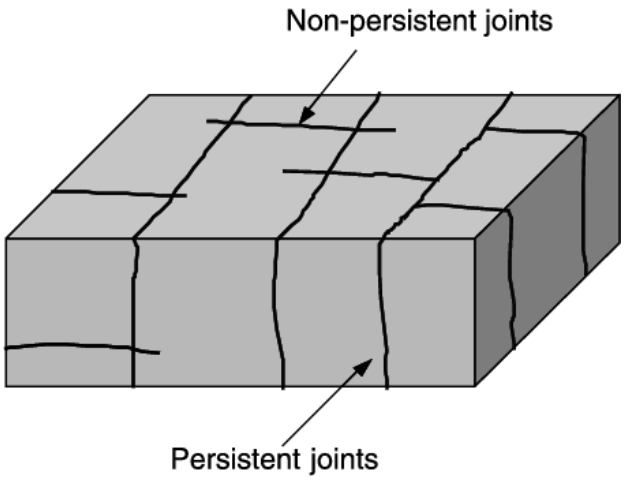

Fig. 2-4. *The pattern of joints in the rock mass.*

Others

Other types of geological structures include bedding, foliations, cleavage etc.

- Bedding is one of the principal features for sedimentary rocks. It is made up of strata sediments deposited overlying another. Bedding planes are the interface between adjacent layers of stratified sedimentary rock.
- Foliations are formed from the parallel orientation of platy minerals, or mineral banding in metamorphic rocks.
- Cleavage is a type of planar rock feature that developed as a consequence of deformation and metamorphism.

2.2. Discontinuity characterization

Discontinuity geometry is a key factor in rock slope stability analysis. In general, rock slopes are prone to instabilities with the presence of unfavourably oriented

discontinuities. These unfavourable conditions of discontinuities may be associated with relative orientation with the slope, a highly persistent weak plane crossing the slope, or a very disadvantageous location. The characterization of discontinuity geometry allows investigation of slope stability conditions and provides insight into the assessment of mechanical properties of the involved rock mass.

As aforementioned in section 2.1, discontinuities belonging to an identical set normally appear in the form of parallel or sub-parallel lineaments. Depending on whether variability is considered or not, two principal methods have been widely adopted for the characterization of discontinuity geometry: one represents a uniform distribution of discontinuities in the rock mass, and another considers the variation of discontinuity geometry.

2.2.1. Methods used to characterize uniform distribution

A commonly adopted approach to characterize the geometry of a discontinuity set follows a uniform distribution and discontinuities belonging to an identical set are represented by a series of parallel lineaments. Major parameters to characterize a discontinuity set may include orientations (dip and dip direction), persistence, spacing, aperture, and roughness.

Discontinuity orientation

The orientation of discontinuities is defined by the dip and dip direction (or strike) of the plane surface. The dip of the plane is the maximum angle of the plane to the horizontal (angle ψ), while the dip direction is the direction of the horizontal trace of the line of dip, measured clockwise from north, angle α (see Fig. 2-5) (Hoek and Bray, 1981). Discontinuity orientation is one of the basic parameters in geotechnical engineering, providing the basis for initial estimation of slope stability (Hoek and Bray, 1981), and assessing mechanical characteristics of discontinuous rock masses (e.g., anisotropy of layered sedimentary rocks) (Wittke, 1990).

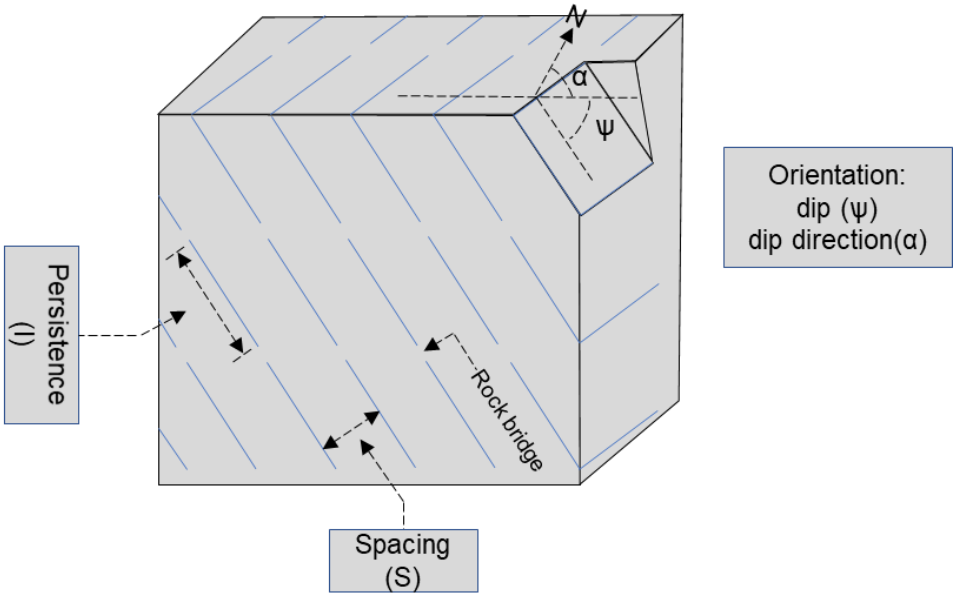

Fig. 2-5. *A discontinuity set in the rock mass, showing its geometry parameters that include dip (ψ), dip direction (α), persistence (I), and spacing (S).*

Persistence

Discontinuity persistence (I) is an index to characterize continuous length of a discontinuity (Fig. 2-5). It is measured as trace length in the dip direction through scanline sampling and window sampling. This parameter explicitly defines the size of a discontinuity, for example, assigning a diameter value to a disc-shaped joint plane.

Alternatively, persistence can be expressed as the ratio of the discontinuity size to a reference size as the representative of discontinuity persistence as either 1D (linear) or 2D (planar) features (Einstein et al., 1983; Elmo et al., 2018). Specifically, as presented in Fig. 2-6, it is calculated either as the ratio of the sum of the trace length l_i (diameter) to the length of a collinear scanline L, in which $\sum l_i/L$ is called linear discontinuity persistence in 1D (Itasca Consulting Group, Inc., 2017); or as the ratio of the sum of the individual discontinuity areas a_i to the area of a coplanar reference discontinuity plane A where $\sum a_i/A$ is referred to as areal discontinuity persistence in 2D (Shang et al., 2017, 2018a). The latter definition defines the percentage of discontinuity or the content of rock bridges instead (0% persistence infers intact rock; 100% persistence indicates a persistent discontinuity cutting across rock mass), and it has been widely adopted in probabilistic analysis (Einstein et al., 1983; Park, 2005) and numerical modelling analysis (Kim et al., 2007; Vanneschi et al., 2019; Sun,

2021).

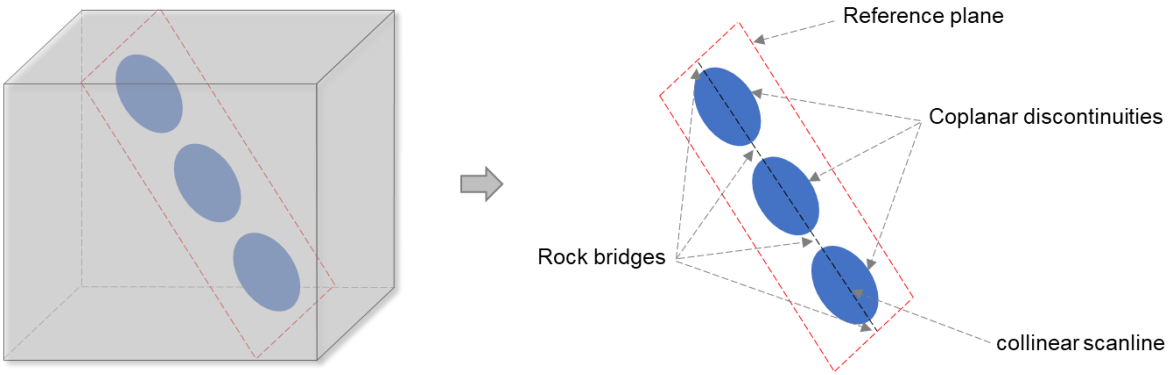

Fig. 2-6. *The 3D sketch of discontinuities, showing a statistical concept of persistence.*

Spacing

Discontinuity spacing (S) is the distance between two adjacent discontinuity planes (Fig. 2-5). It represents the reciprocal of discontinuity frequency and indicates the number of discontinuities in a unit volume of the rock mass. Therefore, it has been widely used as a measure of the quality of a rock mass for classification schemes (Priest, 1993), such as the associated Rock Mass Rating (RMR) system (Bieniawski, 1989) and Q classification (Barton et al., 1974). In addition, discontinuity spacing is also one of the critical parameters to define the size and shape of the rock block, which provides basis for rock stability analysis, such as the determination of toppling and sliding failure by the aspect ratio of the rock block (Goodman and Bray, 1976).

Aperture

Discontinuity aperture is the mean thickness of the opening separating the two walls of a discontinuity. In the field, it is very seldom that the two surfaces are in complete contact. They usually exist in a gap or opening between the two sides. A description of discontinuity aperture, suggested by ISRM, has been presented in Table 2-2. The aperture usually governs friction of two rock surfaces of a discontinuity. Open apertures usually have low friction and low shear strength. In addition, they are more likely associated with water flow and permeability enhancement in a rock mass. In the field, discontinuities with the opening can be filled with infill materials that are termed infilling (such as sands, clays, crushed rocks, or mixture). Infillings can have

impacts on the discontinuity strength, particularly regarding shear strength and deformability (Papaliangas et al., 1993; Indraratna et al., 2008, 2010, 2014; Pellet et al., 2013; Mokhtarian et al., 2020), depending on their mineralogy, condition of consolidation, water content, infilling thickness etc.

Table 2-2. *A description of discontinuity aperture suggested by ISRM (1978).*

Magnitude of aperture	Description	
＜ 0.1 mm	Very tight	Closed feature
0.1 – 0.25 mm	Tight	
0.25 – 0.5 mm	Partly tight	
0.5 - 2.5 mm	Open	Gapped feature
2.5 – 10 mm	Widely open	
1 -10 cm	Very widely open	Open feature
10 -100 cm	Extremely widely open	
＞ 1m	Cavernous	

Roughness

The roughness of discontinuity surfaces is one of the critical parameters to estimate discontinuity shear strength where the discontinuity is nondisplaced and interlocked. Roughness is less important in shear strength estimation where significant apertures are observed because of the absence of an interlocking effect between the two surfaces of a discontinuity. Joint Roughness Coefficient (JRC) is a widely used index for roughness characterization (Barton, 1973). JRC quantifies roughness with various values from 0 to 20, to characterize surfaces from a smooth, planar and particularly slickenside condition to a rough and undulating condition (Appendix A). The index plays an important role in the estimation of discontinuity shear strength (e.g., Barton's empirical criterion (Barton, 1973)) and rock mass classification (such as the RMR system and Q classification) etc.

2.2.1. Methods used to characterize stochastic distribution

Another method for discontinuity characterization, called DFN, takes into account the stochastic nature of the geometry (Miyoshi et al., 2018; Pan et al., 2019; Zhang et al., 2021). DFN refers to a computational model that explicitly represents the geometrical properties of each fracture (e.g., orientation, size, position) and the topological relationships between individual fractures (Lei et al., 2017a). Fractures are commonly characterized by disc-shaped geometry and configured by specific

probability distributions of orientation, size, aperture, and intensity/density.

In the field, it is rare to identify two discontinuities with an identical geometry, even when they belong to the same set. DFN models can fully account for the spatial variation of the fractures through different probability distributions. These probability distributions include uniform distribution (no geometry variability), power-law distribution, lognormal distribution, fisher distribution, normal, gamma distribution etc. Table 2-3 summarises previous research and associated publications, showing the preferential use of probability distributions for DFN realisation.

Table 2-3. *Different probability distributions for DFN realization and associated case studies.*

	Orientation	Size	Aperture
Uniform	(Lei et al., 2017b) (Vanneschi et al., 2019)	(Zhang, Y. et al., 2018)	(R. Liu et al., 2019)
Normal	(Zanbak, 1977) (Marcotte and Henry, 2002) (Zhang et al., 2021)		(N. Huang et al., 2019)
Fisher	(Darcel et al., 2018) (Wang, J. et al., 2020) (Yin and Chen, 2020) (Kong et al., 2021b) (Karimzade et al., 2017) (L. Li et al., 2019) (Zheng et al., 2014) (Han et al., 2016)		
Exponential		(Call et al., 1978) (Cruden, 1977) (Priest and Hudson, 1981) (Sturzenegger et al., 2011)	
Lognormal		(Baecher et al., 1977) (Guo et al., 2015) (Zhan et al., 2016) (Zhang et al., 2021)	(Snow, 1970) (Bonnet et al., 2001) (Baghbanan and Jing, 2007) (Zou et al., 2019) (Yin and Chen, 2020)
Power law		(Painter et al., 1998) (Odling, 1997) (Davy et al., 2013) (Liu et al., 2016) (Lei et al., 2017b) (Feng et al., 2021)	(de Dreuzy et al., 2002) (Lei et al., 2017a)
Gamma		(Zhang and Einstein, 2000) (Han et al., 2016) (Zhan et al., 2016)	

For DFN realisation, the concept of orientation is consistent with the aforementioned

definition or representation using dip and dip direction or strike. To the author's knowledge, uniform distribution, normal distribution (including bivariate normal distribution) and fisher distribution are preferentially used for orientation characterization (Table 2-3). Normally, the uniform distribution is used to reduce model complexity, creating a simplified DFN model that consists of a series of parallel discontinuity planes.

The size refers to the diameter of a disc-shaped fracture plane which is measured by the maximum trace length of a fracture plane in outcrops or excavation walls. However, deviations, between true trace length and measured trace length sampled on a finite window, may exist because of orientation bias, size bias, truncation bias, and censoring bias (Pahl, 1981; Kulatilake and Wu, 1984; Zhang and Einstein, 1998). The biases potentially diminish and neglect when the sampling window is large enough (Yin and Chen, 2020), whereas they are inevitable on a finite window. To address these biases, some mathematical methods have been proposed to determine mean trace length from a finite sampling window (Pahl, 1981; Mauldon, 1998; Zhang and Einstein, 1998; Song and Lee, 2001; Zhu et al., 2014). The size might follow the different probability distributions, and one would be chosen based on the best fit with geotechnical mapping data. Previous studies indicate that exponential distribution, lognormal distribution, power-law distribution, and gamma distribution are preferred options over other distributions (e.g., uniform, normal and fisher distributions).

Aperture is another critical parameter for DFN realization. It refers to the mean width of a discontinuity opening, which is vital in assessing the hydraulic properties of rock mass (Baghbanan and Jing, 2007; Yao et al., 2019). Whereas it has been considered less for estimating rock mass strength or stability analysis. This is due to its low magnitude, particularly for discontinuity of closed-feature aperture with several millimetres in size (see table 2-1 for aperture description), which may bring huge challenges for the precise identification and measurement. Alternatively, linear and non-linear aperture-length scaling relationships (Cowie and Scholz, 1992; Clark and Cox, 1996; Renshaw and Park, 1997; Olson, 2003; Schultz et al., 2008), corresponding to shear strength and elasticity of the rock, potentially provide the likelihood to estimate discontinuity aperture.

Intensity is a nondirectional intrinsic index which incorporates both a frequency measure and a fracture size component (Rogers et al., 2015). Discontinuity intensity can be measured in 1, 2, or 3 dimensions as linear, areal and volumetric fracture intensity, respectively (Dershowitz and Herda, 1992). Representative intensity indexes include,

1) P_{10}: the linear fracture intensity, expressed as the number of fractures per unit length.
2) P_{21}: Areal fracture intensity is expressed as the length of fracture traces per unit area.
3) P_{32}: Volumetric fracture density, expressed as the area of fracture planes per unit volume.

Fracture intensity can be measured in 1D from a borehole survey or in 2D from window sampling, whist 3D measurement is less possible in practice. However, in 3D DFN analysis a volumetric intensity may be required, such as P32 required by the embedded DFN generator in 3DEC (Itasca Consulting Group, Inc., 2017). In this case, a conversion from a 1D/2D index to a 3D index is a potential and feasible option to derive the volumetric intensity practically, which has been applied in many studies (Manda and Mabee, 2010; Elmo et al., 2014; Rogers et al., 2015; Hekmatnejad et al., 2020).

To date, tools are readily available for automatic or semi-automatic identification of DFN information. These tools include Fracman (Golder Associates Ltd., 2018), the Compass plugin in Cloudcompare software (Thiele et al., 2017), the ADFNE software (Fadakar Alghalandis, 2017), the FraNEP software (Zeeb et al., 2013), the FracPaQ Matlab toolbox (Healy et al., 2017). The variety of DFN tools ensures that data acquired from various sources, such as LIDAR data, aerial photographs, and borehole televiewers, can be used to identify the characteristics of discontinuities in the field.

2.3. Discontinuity shear strength

In stability analysis of a rock slope, a critical aspect is to determine the shear strength of a potential failure surface that may be associated with a single discontinuity plane or a complex path constrained by multiple discontinuities (Hoek and Bray, 1981). This section will give a brief introduction about estimation of discontinuity strength with different surface conditions. In addition, the explanation of basic parameters associated with discontinuity strength and deformability will be provided.

2.3.1. Shear strength of a planar discontinuity

For individual planar discontinuities, a stress-strain curve (Fig. 2-7b) can conceptually outline the shear stress level at various shear strains, which can be obtained from direct shear tests that are carried out under a constant normal stress condition (presented in Fig. 2-7a). The stress-strain curve depicted in Fig. 2-7b outlines 4 stages involved in the displacement process of the rock mass specimen. Stage 1 is characterized by linear elasticity, where the rock mass behaves elastically, and shear stress increases linearly with strain. After that, at stage 2, the curve becomes non-linear and then reaches a peak at which the shear stress achieves its maximum value called the peak shear strength at the specific normal stress level. Following this, a rapid drop in the shear stress occurs with during stage 3, consequently remaining a constant value (residual shear strength) at stage 4. The drop in the shear stress at stage 3 corresponds to the gradual loss of cementation (called cohesion, c) with incremental shear displacement.

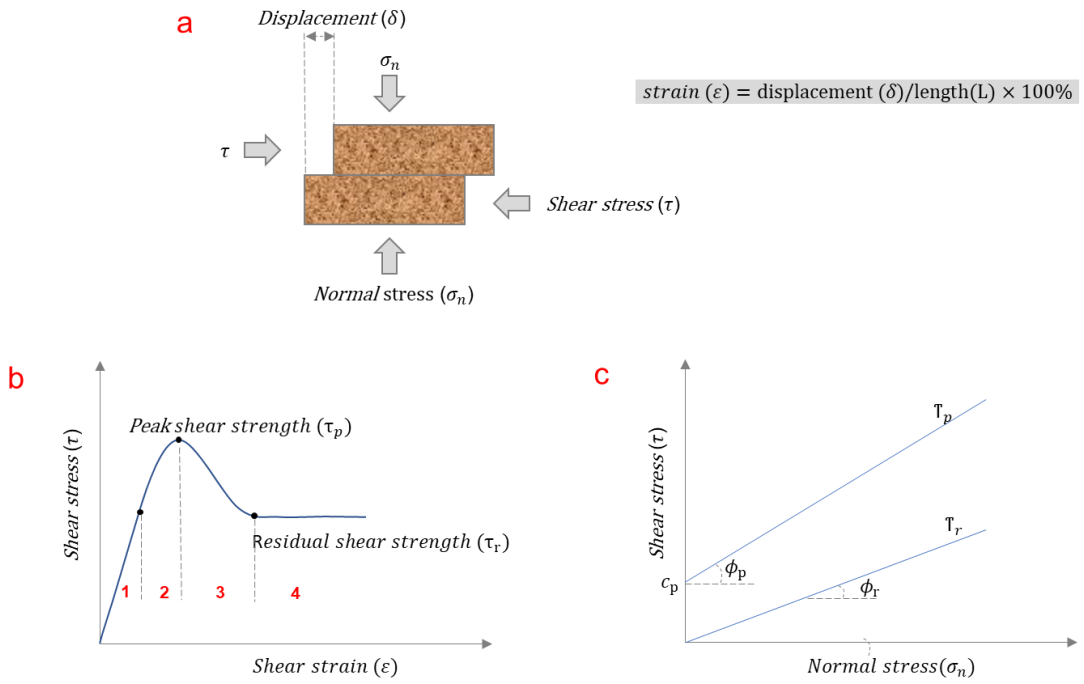

Fig. 2-7. *a) the sketch of a shear test under a constant normal loading condition, b) a conceptual stress-strain curve from the shear test, c) a graph plotting peak and residual shear strength obtained from tests carried out at different normal stress levels.*

The relationship between the peak shear strength τ_p and the normal stress σ_n (Fig. 2-7c) can be expressed by the Mohr-Coulomb equation,

$$\tau_p = \sigma_n tan\phi_p + c_p \qquad (Eq. 2-1)$$

Where, c_p is the cohesive strength of the cemented surface and

ϕ_p is the friction angle at the moment of peak shear strength.

In the case of residual shear strength, the cementation of a discontinuity vanishes and cohesion drops to zero. The relationship between the residual shear strength (τ_r) and σ_n can be expressed as

$$\tau_r = \sigma_n tan\phi_r \qquad (Eq. 2-2)$$

Where, ϕ_r is friction angle during the residual shear strength.

2.3.2. Shear strength of an undulated discontinuity

It is very rare in the field that a natural discontinuity surface is planar and smooth. In general, it exhibits variously rough surface conditions. Joint roughness can improve its shear strength, and shear resisting effect is usually counted as an addition of friction angle.

As suggested by Patton (1966), the inclination of a sawtooth face was taken as an addition to friction angle, and the associated shear strength is expressed as

$$\tau = \sigma_n \tan(\phi_b + i) \qquad (Eq. 2-3)$$

Where, ϕ_b is the basic friction angle of the sawtooth face and

i is the angle of the sawtooth face.

Patton's equation may be applicable to the case of low normal stress loading, in which the sawtooth would be not broken. In the case of high or extremely high normal stress loading conditions, the sawtooth of the surface will be gradually sheared off with ongoing shear displacement, and the friction angle will progressively diminish to a minimum value of basic or residual rock friction angle. With the consideration of the effect of high normal stress loading, Barton (1973) then developed a non-linear strength criterion for rock joints, which is expressed as

$$\tau = \sigma_n \tan(\phi_b + JRC \log_{10}\left(\frac{JCS}{\sigma_n}\right)) \qquad (Eq. 2-4)$$

Where, JRC is joint roughness coefficient and

JCS is joint wall compressive strength.

In addition, according to the results derived from the direct shear tests of 130 samples with variably weathered rock joints, Barton and Choubey (1977) revised Eq. 2-4 to

$$\tau = \sigma_n \tan(\phi_r + JRC \log_{10}\left(\frac{JCS}{\sigma_n}\right)) \qquad (Eq. 2-5)$$

Where, ϕ_r is the residual friction angle of the rock that can be estimated by

$$\phi_r = (\phi_b - 20) + 20\,(r / R) \qquad (Eq. 2-6)$$

Where, r is the Schmidt rebound number wet and weathered fracture surfaces and

R is the Schmidt rebound number on dry unweathered sawn surfaces.

Barton's empirical equations (Eq. 2-4 and Eq. 2-5) highlight a dynamic influence of normal stresses on the reduction of friction angle. However, these two equations haven't considered a scale effect that JRC and JCS values will reduce with the increase in the discontinuity size, which facilitates the proposal of the scale corrections for JRC and JCS (Barton and Bandis, 1982).

2.3.3. Discontinuity deformability parameters

Apart from strength parameters (e.g., cohesion, friction angle), deformability parameters are also vital to characterize the mechanical behaviour of a discontinuity. Normal stiffness (K_n) and Shear stiffness (K_s) are two parameters to describe the overall stress-deformation characteristic of a discontinuity (Goodman et al., 1968; Barton, 1972). It is common that these two parameters are used in the numerical modelling of rock mass analysis, and are two important parameters for numerical analysis in this thesis.

K_n is defined as the normal stress per unit closure of the joint, and the K_s is the mean gradient of the shear stress-shear displacement curve, taken up to the point of peak strength (Barton, 1972). Some attempts have been endeavoured to estimate stiffness, such as analytical analysis (Indraratna et al., 2015), and experimental studies (Kulatilake et al., 2016; Abolfazli and Fahimifar, 2020; Packulak et al., 2021).

Alternatively, in a simple way, knowing discontinuity spacing it is possible to estimate the K_n of individual bedding joints from the following empirical equation (Barton, 1972)

$$K_n = \left(\frac{E_i \cdot E_m}{L\,(E_i - E_m)}\right) \qquad (Eq. 2-7)$$

Where, E_m is the deformation modulus of the rock mass

E_i is the deformation modulus of the intact rock

L is the mean joint spacing.

By analogy, K_s can be derived from the expression

$$K_s = \left(\frac{G_i \cdot G_m}{L\,(G_i - G_m)}\right) \qquad (Eq. 2-8)$$

Where, G_m is rock mass shear modulus

G_i is intact rock shear modulus

From the definitions, it is known that K_n is dependent on normal stress level, and the K_s is both normal stress and size-dependent which has been also demonstrated by previous studies (Jing et al., 1994). This characteristic potentially imposes unpredictable impacts to a dynamic mechanical analysis in which Kn and Ks may be varied with the normal stress level.

2.4. Strength of jointed rock mass

It is common that discontinuities are not persistent in rock masses. The presence of rock bridges (intact rocks between adjacent discontinuities) can highly increase rock mass strength (Stead and Wolter, 2015), as such the content and strength of rock bridges are extra key factors for estimating the rock mass strength. Laboratory tests are frequently carried out to estimate strength of jointed rock mass (Shang et al., 2016, 2018b). Apart from laboratory tests, some alternative methods to date have been developed for the estimation of jointed rock mass strength.

2.4.1. Analytical method

Jennings (1970) developed an analytical approach, based on the concept of continuity (K) along the potential failure plane (Fig. 2-8), to estimate equivalent cohesion (c_{eq}) and friction (ϕ_{eq}) of the equivalent discontinuity as follow

$$c_{eq} = (1-K)\,c + Kc_j \qquad (Eq.2-9)$$

$$tan\phi_{eq} = (1-K)\,tan\phi + Ktan\phi_j \qquad (Eq.2-10)$$

Where, c is cohesion of the intact rock

ϕ is friction of the intact rock

c_j is cohesion of the joint plane

ϕ_j is the friction of the joint plane.

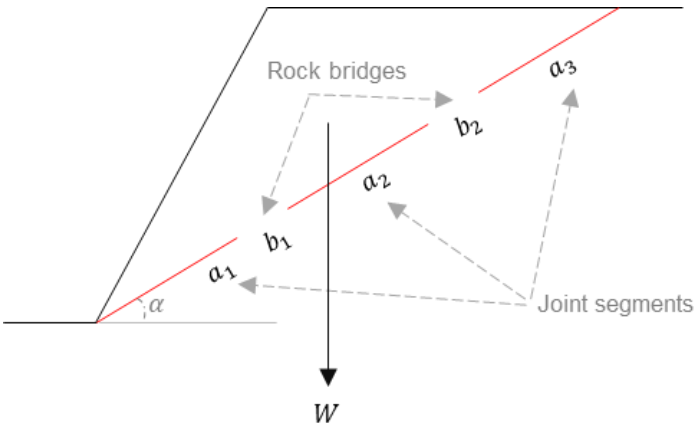

$$K = \frac{\sum b_i}{\sum a_i + \sum b_i}$$

Fig. 2-8. *The measurement of continuity (K) along a potential failure plane.*

An important hypothesis of Eq. 2-9 and Eq. 2-10 is that intermittent joints are co-planar, which means the method may not be applicable to other cases of more complicated discontinuity geometry, such as step-path failures and failures characterized by irregular geometry. Another limitation of this method is that tensile strength is not considered, as stated by Stead et al. (2006).

2.4.2. Empirical method

The generalized Hoek-Brown failure criterion (Hoek, 1994), developed on the original version (Hoek and Brown, 1980a), has been widely used to determine rock mass strength. The criterion takes into consideration of GSI for estimating the reduction in rock mass strength for different geological conditions, and is expressed as

$$\sigma_1{}' = \sigma_3{}' + \sigma_{ci}\left(m_b \frac{\sigma_3{}'}{\sigma_{ci}} + s\right)^a \qquad (Eq. 2-11)$$

Where, $\sigma_1{}'$ and $\sigma_3{}'$ are major and minor effective stress at failure, respectively; σ_{ci} is uniaxial compressive strength of intact rock material; m_b is a reduced value of material constant m_i, which is given by

$$m_b = m_i \, exp\left[\frac{GSI - 100}{28 - 14D}\right] \qquad (Eq. 2-12)$$

The parameter D, a "disturbance factor", denotes the degree of disturbance to which the rock mass has been subjected by blast damage and/or stress relaxation. Appendix B provides reference values of m_i for a wide variety of rock types. s and a are constants for rock mass, which are associated with GSI and given by

$$s = exp\left[\frac{GSI - 100}{9 - 3D}\right] \qquad (Eq. 2-13)$$

$$a = \frac{1}{2} + \frac{1}{6}\left[e^{\frac{-GSI}{15}} - e^{\frac{-20}{3}}\right] \qquad (Eq. 2-14)$$

The uniaxial compressive strength of the rock mass (σ_c) is derived by setting $\sigma_3{}'$ = 0 in Eq. 2-11, giving

$$\sigma_c = \sigma_{ci} \cdot s^a \qquad (Eq. 2-15)$$

The equivalent friction angle and cohesive strength are determined by fitting a tangent to Mohr's circles, as presented in Fig. 2-9.

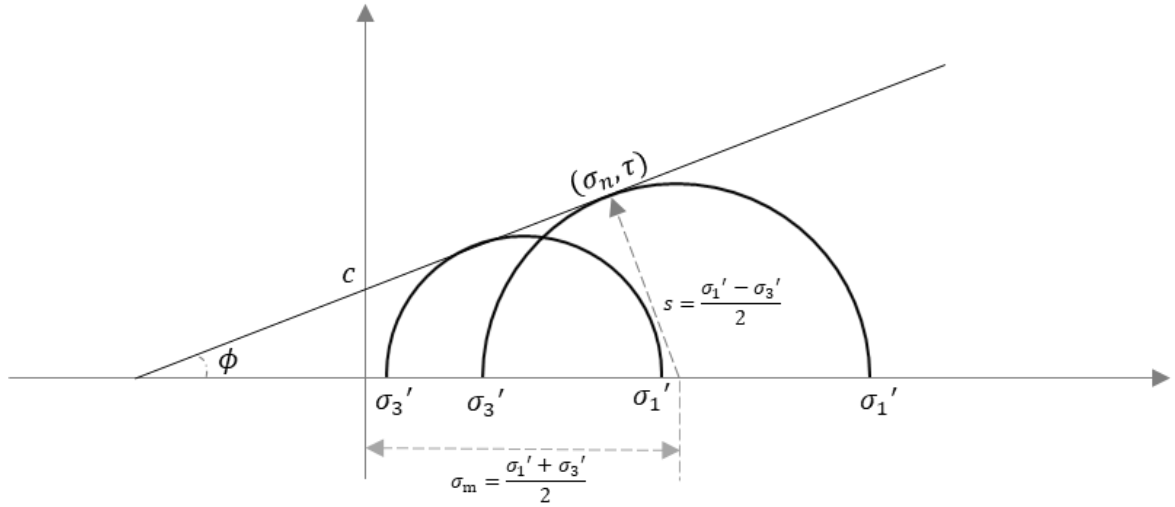

Fig. 2-9. *The measurement of rock mass strength from Mohr's circle.*

From Mohr's circle,

$$\tau = s\,cos\varphi \qquad (Eq. 2-16)$$

$$\sigma_n = \sigma_m - s\,sin\varphi \qquad (Eq. 2-17)$$

Substituting for τ and σ_n, the Mohr-Coulomb criterion can be rewritten as,

$$s + \sigma_m \cdot sin\varphi - c \cdot cos\varphi = 0 \qquad (Eq. 2-18)$$

Where,

$$s = \frac{1}{2}(\sigma_1 - \sigma_3) \qquad (Eq. 2-19)$$

$$\sigma_m = \frac{1}{2}(\sigma_1 + \sigma_3) \qquad (Eq. 2-20)$$

2.4.3. Numerical method

Due to the advantage of modelling discontinuous rocks, numerical methods, especially DEM and FDEM approaches, are an alternative for laboratory tests to estimate rock mass strength in a deterministic way. In numerical modelling, joint properties are well known and compressive loadings are imposed on surfaces of

rock mass. A stress-strain curve can be obtained from the modelling based on the modelled stress and displacement.

Various types of compression tests can be simulated through numerical modelling. For example, uniaxial compression tests were carried out with a symmetric constant loading velocity (CLV) in the vertical direction, being free of boundary conditions (confining stresses) on sidewalls (see Fig. 2-10) (Cao et al., 2016, 2018; Laghaei et al., 2018; Mehranpour et al., 2018; Wang and Cai, 2020). With respect to triaxial compression test, a SRM is exposed to a symmetric CLV in the vertical direction and confined by lateral stresses (Turichshev and Hadjigeorgiou, 2015; Laghaei et al., 2018). The tests provide the estimation of the rock mass properties, including UCS and deformability modulus (e.g., Young's modulus and Poisson's ratio). The reliability of numerical tests has been validated by experimental tests that are carried out under an identical condition (Turichshev and Hadjigeorgiou, 2015; Cao et al., 2016, 2018).

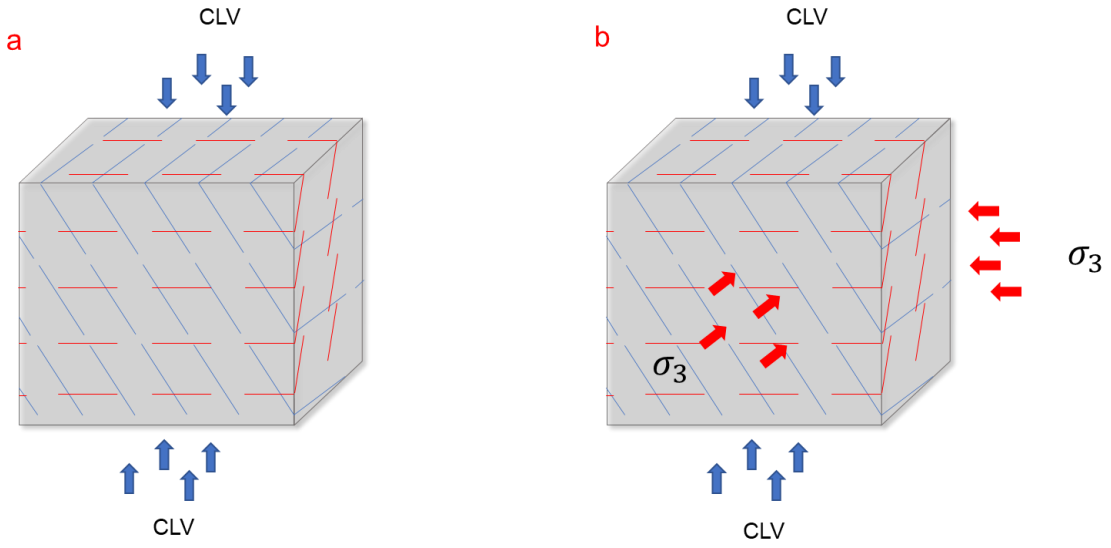

Fig. 2-10. *Numerical modelling of a) a uniaxial compression test of a SRM that is exposed to a symmetric CLV in vertical direction and free of confining stresses, b) a triaxial compression test of a SRM that is exposed to a symmetric CLV in and confined by latera.*

2.5. Review on landslide susceptibility mapping

Landslide susceptibility mapping (LSM) aims to divide a land surface into zones of varying degrees of stability (Anbalagan, 1992). Unlike conventional kinematic or mechanical analysis, this approach is statistically based and constructs a mathematical relation between landslides (dependent variables) and selected pre-conditioning factors (independent variables) which is built on GIS data. The mathematical relation may be quantitative and explicit, or unclear like a black box, depending on the selected method.

2.5.1. Methods used for LSM

Aleotti and Chowdhury (1999) classified the LSM methods into two subdivisions: qualitative and quantitative approaches. LSM analysis based on qualitative approaches is determined directly in the field or by the synthesis of different index maps. The result highly depends on the site-specific experience of experts which may not be rigorous, and time-consuming, particularly for large-scale investigations.

Compared with qualitative methods, quantitative methods are preferentially used for LSM at present. The classification of quantitative methods, modified after Aleotti and Chowdhury (1999), has been presented in Fig. 2-11. They can be divided into 3 groups: statistical analysis, ML analysis, and DL analysis. Note that although ML and DL models are built upon statistical frameworks, they are considered two individual groups in this classification system.

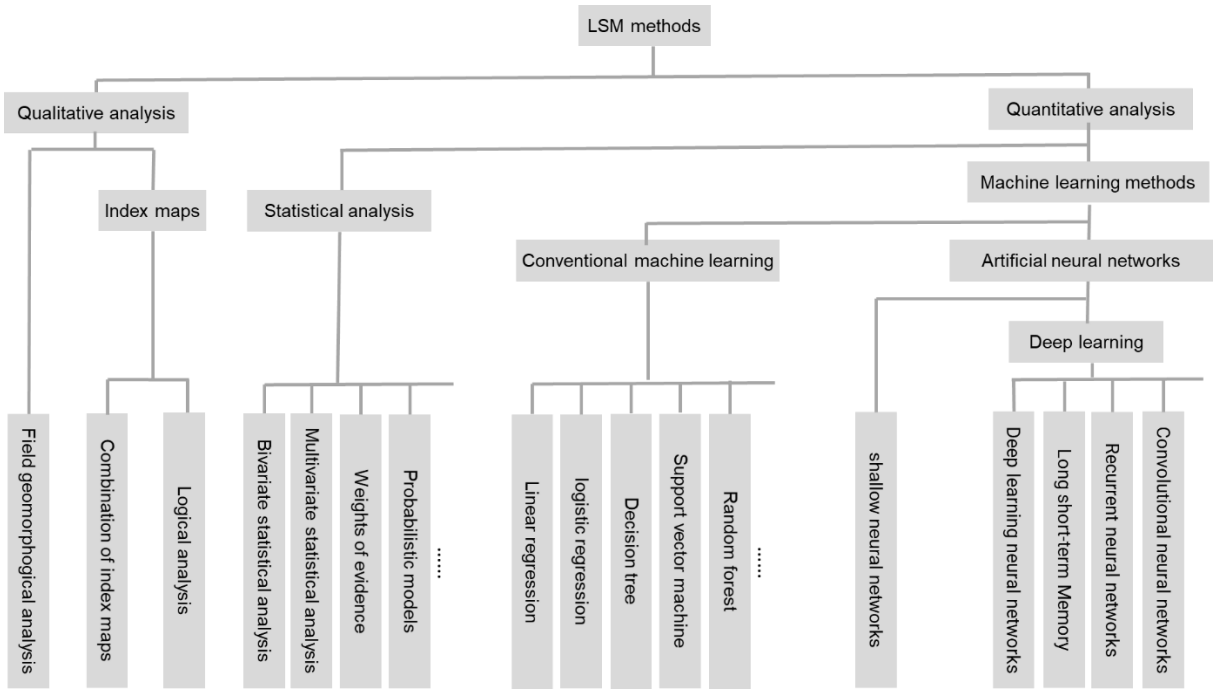

Fig. 2-11. *Summary of the methods used for LSM which can be categorized into two groups: qualitative analysis and quantitative analysis (modified after Aleotti and Chowdhury, 1999).*

Statistical analysis is undertaken to evaluate the relationships between variables (specifically, independent and dependent variables). Bivariate analysis is one of the fundamental statistical methods for LSM. It involves the analysis of two variables (an independent variable – a landslide causative factor, and a dependent variable – landslide occurrence), to determine the empirical relationship between them. FR analysis is one of the bivariate analysis methods and has been widely used to determine the ratio of the landslide area in reference to the total study area, considering the probabilistic ratio of the landslide occurrence probability to a non-occurrence probability for a given factor's attribute (Lee and Pradhan, 2006; Ozdemir and Altural, 2013). Multivariate analysis is another statistical analysis approach which can analyse multiple landslide causative factors simultaneously. Multiple multivariate methods are readily available and have been successfully applied for LSM, including logistic regression (Ayalew and Yamagishi, 2005; Lee, 2005), discriminant analysis (Eiras et al., 2021) etc. Other statistical landslide susceptibility analysis may involve the use of weights of evidence (Poli and Sterlacchini, 2007; Wang et al., 2013; Sujatha et al., 2014) and probabilistic models (Oh and Lee, 2011; Sujatha et al., 2013; Dahal et al., 2014).

Unlike the aforementioned statistical analysis, ML analysis is designed to make the most accurate prediction possible using general-purpose learning algorithms to find patterns in often rich and unwieldy data (Bzdok et al., 2017, 2018), without the identification of an explicit relationship between variables. In general, ML performs better than statistical analysis when dealing with cases of high-dimensional prediction problems or big data (Goetz et al., 2015; Merghadi et al., 2020). Conventional ML algorithms for LSM involve linear regression (Kayastha et al., 2013), logistic regression (Colkesen et al., 2016), support vector machine (SVM) (Yao et al., 2008; Ballabio and Sterlacchini, 2012; Tehrany et al., 2015; Wang et al., 2015; Huang and Zhao, 2018), decision trees (Thai Pham et al., 2018; Arabameri et al., 2021; Kutlug Sahin and Colkesen, 2021), and random forest (RF) (Catani et al., 2013; Micheletti et al., 2014; Xie et al., 2015), with high prediction accuracy examined. Previous studies analysed landslide predictive performance of these algorithms, indicating that in terms of the overall performance, RF shows great generalization performance and outperforms the other models (Goetz et al., 2015; Pham et al., 2021; Youssef and Pourghasemi, 2021)

As an important part of ML, artificial neural networks (ANN) were developed to mimic the biological neural networks. It normally consists of three or more layers: an input layer, one or more than one hidden layers, and an output layer. Each node in the hidden layers and the output layer produces output through a nonlinear activation function considering weights of all preceding connections. The weights are updated through back-propagation that calculates the gradient of the cost function associated with a given state with respect to the weights. Shallow neural networks (less than 3 hidden layers) were initially used for LSM (Lee et al., 2004, 2020; Chauhan et al., 2010; Choi et al., 2010; Tsangaratos and Benardos, 2014).

DL is developed upon ANN with multiple hidden layers (more than three). To date, DL has been proved to be effective in discovering intricate structures in high-dimensional data and has been applied into many domains (LeCun et al., 2015). It also achieves great success in the field of LSM, which includes the use of deep learning neural networks (DLNN) (Bui et al., 2020; Dao et al., 2020; Zhu et al., 2020; Hua et al., 2021; Saha et al., 2021), convolutional neural network (CNN) (Wang et al., 2019; Fang et al., 2020; Yi et al., 2020; Wei et al., 2021), recurrent neural network

(RNN) (Mutlu et al., 2019; Zhu et al., 2020; Li et al., 2021).

2.5.2. Rock slide factors

Accurate prediction of LSM not only depends on the selection of an appropriate model but also on the scientific selection of landslide factors that inherently correspond to the occurrence of landslides. This kind of inherent dependency should be related to spatial continuity, as well as temporal consistency between landslides and selected factors to make sure that LSM is logically plausible. Landsliding is a complicated process, and it may be triggered by the superimposition of various factors. These factors can be categorized into two groups, predisposing factors and triggering factors (Clague and Stead, 2012).

Predisposing factors can bring a slope from a stable state to a marginally stable state. Slope topography is considered one of the most influential factors that provide preconditions for a landslide. In general, the topography is characterised by features associated with slope gradient, orientation, and curvature. Slope angle and orientation/aspect are two key topographic indexes that can indicate the potential of a slope for instability through kinematic analysis (Hoek and Bray, 1981). In addition, slope orientation can also provide the basis for stability analysis in other respects. For example, a coastal slope of an unfavourable orientation preferentially suffers from wave attacks and sea erosion, which may result in subsequent slope collapse and coastal retreat (Edil and Vallejo, 1980; Lantuit and Pollard, 2008). Further examples include slopes susceptible to higher landslide risks caused by synergistic effects of wind-driven rainfall and wind toppled trees, inferring an inherent interrelationship between landslides, slope aspect and wind direction (Gorokhovich and Vustianiuk, 2021). Curvature is another topographic index to characterize the degree of concave or convex terrain. Statistics data from previous studies (Dai and Lee, 2002; Ohlmacher, 2007) shows that slopes of concave curvature are more susceptible to landslides. It is likely caused by the concentration/convergence of ground and surface water within a concave slope, resulting in higher pore-water pressure in the rock mass (Sharma, 2013). Through slope topography, it is also possible to characterise surface drainage and associated indexes, such as drainage density, proximity to drainage, and topographic wetness index (TWI), which have

been used for LSM (Lee and Pradhan, 2006; Yilmaz, 2009; Kayastha et al., 2013).

In addition, unfavourable geological conditions can also behave as a preconditioning factor for landslides. Geological structures are a common type of weakness in rocks, and their roles in undermining rock strength and controlling landslides have been illustrated above. Their controlling effects on landslides have been widely investigated, which can be highlighted by unfavourably orientated joint/fracture networks (Bozzano et al., 2011; Cui et al., 2018; Francioni et al., 2018a), fault-related shear zones (Alberti et al., 2019; Donati et al., 2021b; Furuki and Chigira, 2019; Seguí et al., 2021), bedding (Bromhead and Ibsen, 2004; Duman, 2009; Santangelo et al., 2015), foliations (Dunning et al., 2006; Regmi et al., 2013; Zhu et al., 2021), providing the kinematic possibility or freedom for the displacement of overlying rocks. An interlayer of relatively weak rock may also act as a release surface when a driving force exceeds the shear strength of the interlayer (Sun et al., 2019; Liu et al., 2020; Xu et al., 2020; Ying et al., 2021). Lithology, a description of geological engineering characteristics of outcrops, is another geological aspect to be considered for landslide prediction. In general, weaker materials are more prone to instability under the same external conditions. As such, lithology has been widely adopted in LSM as an independent variable (Kamp et al., 2008; Xu et al., 2013; Wang et al., 2015; Chen et al., 2017; Youssef and Pourghasemi, 2021; Yu et al., 2021).

Causative factors can directly trigger the occurrence of a landslide from a marginally stable state to an unstable state. USGS published a landslide handbook, indicating 4 major triggering mechanisms: water, seismic activities, volcanic activities, and disturbance by human activities (Highland and Bobrowsky, 2008). Water condition, associated with pore water pressure in rocks, has profound influences on normal stresses acting on discontinuity planes. Therefore, it becomes an essential aspect for landslide analysis. The water condition in rock masses can be affected by many factors and the most significant one is rainfall. It has been reported in many cases heavy or prolonged rainfall led to a significant increase in pore-water pressure, consequently triggering landslides (Collins and Znidarcic, 2004; Montrasio et al., 2009; Li et al., 2016, 2017; Rosi et al., 2016). In addition, surface drainage may

affect groundwater by controlling surface runoff, causing high water in the proximity of the drainage lines, particularly during heavy rainfall (Neuhäuser et al., 2012). Surface drainage networks are usually delineated by using a digital elevation model (Liu and Zhang, 2010; Reddy et al., 2018), and as introduced above, represented by topographic indexes.

Seismic activities (otherwise called earthquakes) are another major landslide trigger. Seismic wave propagation, including compression waves and shea waves, can lead to strains (compression and tensile strains caused by compression waves, and shear strain from shear waves) in the ground within a certain distance from the epicentre of an earthquake (Huang et al., 2018). In the case of repeated earthquakes or a strong earthquake of an excessive magnitude, rocks suffer from significant deformation, and slope stability can be largely undermined, consequently forming a landslide (Dunning et al., 2007; Changwei et al., 2014; D. Huang et al., 2019). As such, landslides are commonly considered a kind of secondary earthquake hazard.

Although not as common as earthquakes, vibration from volcanic activities (i.e., the rise and eruption of molten rock) also imposes risks on slope stability (Ponomareva et al., 2006; Tommasi et al., 2005). Compared with seismic activities, volcanic activities may only have detrimental impacts on local slopes in the vicinity of the volcano.

From the perspective of human causes, landslides may be triggered by excavation and construction through human engineering. Blasting, a source of anthropogenic vibration in excavation operations, imposes shocks on local rocks. Under a long-term blasting operation, an accumulative effect of high-frequency shocks can result in crack propagation in rock masses (Wang, M. et al., 2021). Therefore, in some cases, blasting is reported as a trigger of instabilities in mine slopes (Song and Cui, 2016).

Land cover and land use (LCLU) change mostly caused by deforestation and urbanization has detrimental effects on groundwater balance (runoff), subsequently influencing the occurrence of rainfall-triggered landslides (Glade 2003). In addition, a change in vegetation cover, through deforestation or cultivation, could have impacts on slope stability conditions in three potential ways: 1) modifying the soil moisture regime via evapotranspiration (Mugagga et al., 2012; Gonzalez-Ollauri and

Mickovski, 2017); 2) providing root reinforcement within the soil mantle (Stokes et al., 2009); and 3) from a negative perspective, the growth of vegetation roots may cause the additional opening of rock cracks and thus destabilizing slopes (Tang et al., 2015). Accordingly, vegetation cover, integrated with other environmental conditions, potentially provides an indicator of slope stability. The vegetation cover is usually assessed by using the normalized difference vegetation index (NDVI) that is widely used in LSM case studies (Bui et al., 2020; Youssef and Pourghasemi, 2021).

Other triggering factors involve weathering. Weathering is a prolonged process that causes the gradual weakness of geological units. Multiple landslide cases have evidenced the weathering of rock materials or discontinuities (Pánek et al., 2010; Regmi et al., 2017; Abe et al., 2018; Thiery et al., 2019). Rock weathering can progress in physical and chemical ways, termed physical weathering and chemical weathering. Physical weathering, sometimes called mechanical weathering, is caused by the effects of changing temperature on rocks, resulting in rock fatigue and a major decrease in rock strength. For example, freeze-thaw cycles are a representative form of physical weathering and have been considered a major factor that deteriorates rock strength in some landslide cases (Mateos et al., 2012; Zhou et al., 2016). Chemical weathering describes the process of chemicals in water making changes to the minerals in a rock. Rainfall is a typical source to provide a condition of chemical weathering for rocks, causing rock strength decay (Yalcin, 2007; Joshi et al., 2018).

Toe erosions are frequently observed in slopes in proximity of gullies, seepages, rivers, reservoirs, lakes, and sea, as a result of interaction with water or glacier in physical or chemical ways (Lee et al., 2002; Schulz, 2007; Hsieh et al., 2016; Qi et al., 2017; Singh et al., 2012). Although more critical in soil slopes toe erosion can also trigger failure of rock slopes through:

1) Loss of support from the toe to the overlying slope, resulting in the decrease in instability resisting force. An excessive driving force from overburden leads to the yielding of a rock layer, which is the case of the landslide presented in (Gu and Huang, 2016). The associated detrimental effect would be more notable in weak rocks.
2) An increase in the possibility of an unfavourably oriented structure daylighting

in the eroded section.

Table 2-4 summarizes the landslide factors adopted in LSM by using quantitative methods. It is found that discontinuities (e.g., fractures, bedding, foliations) are simply considered in the manner of ‘the proximity to faults’ in previous studies, while the influence of their orientation on slope stability was not included. In this context, a novel method incorporating discontinuity orientation into ML models for LSM is proposed in order to improve landslide prediction. This research is presented in Chapter 3 and has been published by the *International Journal of Geo-Information* (He et al., 2021a).

Table 2-4. *Summary of landslide factors and potential use of quantitative index to characterize the corresponding factor.*

	Category	Factor
Predisposing factors	Topographic factors	Slope gradient
		Slope orientation (aspect)
		Curvature
		Height
		drainage
	Geological factors	Fault
		lithology
Triggering factors	Earth vibration	Earthquake
		blasting
		Volcanic activity
	Water	Rainfall
	Erosion	River incision
		Wave attack (sea erosion)
	Anthropogenic factors	Blasting
		LCLU change
	Others	Erosion
		Physical and chemical weathering

2.6. Review on slope-specific instability analysis

To perform landslide analysis for a specific slope the general aims are to investigate the landslide mechanism, the deformation and/or displacement (i.e., compression, tension, shearing) of rock masses, stress redistribution in the slope, and the change in the stability condition of the slope alongside the instability. To achieve this, analysis is undertaken utilising different methods, including kinematic analysis, limit equilibrium analysis, and numerical modelling analysis.

Kinematic analysis

Kinematic analysis evaluates the kinematic possibility of a rock slope being susceptible to discontinuity-related instabilities (i.e., planar sliding, wedge sliding, direct toppling and flexural toppling). The analysis takes discontinuity properties (i.e., orientation and friction angle) into consideration for determining the potential failure mechanism (Brideau et al., 2012). In general, this is carried out by using a stereonet plot in which the orientations of discontinuities identified by field mapping are plotted to compare with the analysed slope orientation (Brideau et al., 2012; Budetta and De Luca, 2015; Cerri et al., 2018; Francioni et al., 2018a; Kumar et al., 2019).

In practice, in the absence of the consideration of slope geometry, spatial locations of discontinuities, mechanical properties of discontinuities, in-situ stresses of rock mass, water conditions in the slope etc, this method can only be considered a preliminary investigation of potential landslide or slope instability mechanisms.

limit equilibrium analysis

Limit equilibrium (LE) analysis investigates the force and/or moment equilibrium of a soil or rock mass tending to slide down a slope. Compared with kinematic analysis, LE can also take into consideration potential external forces (e.g., from pore-water pressure, blasting, earthquake, the weight of extra overburden) in the slope, and calculates the FoS of the slope with the prior assumption of a failure mode (planar sliding, wedge sliding, circular sidling and toppling) (Chen et al., 2016; Friedli et al., 2017; Hess et al., 2017). In addition, the effect of reinforcements or remediation on slope stability can also be estimated by this method (Kul Yahşi and Ersoy, 2018).

To date, various codes and software are readily available for LE analysis. These involve commercial codes developed by Rocscience inc. (e.g., Slide2 for the 2D analysis of a sliding, Slide3 for 3D analysis of a sliding, Swedge for wedge analysis, and RocTopple for toppling analysis) (Rocscience, 2021), SLOPE/W developed by Geoslope inc. (Geoslope, 2021), and open-source codes such as Scoops3D (Reid et al., 2015).

Numerical analysis

In comparison with kinematic analysis and limit equilibrium, 2D/3D numerical analysis can provide an improved and comprehensive understanding of slope stability conditions and associated failure mechanisms. It can also simulate mechanical behaviour of a slope in response to static or dynamic stress conditions, allowing for the simulation of progressive displacement and/or deformation in slopes (Jing, 2003; Stead et al., 2006). In addition, another advantage of numerical analysis is the improved integration of slope geometry for a more accurate estimation of in-situ stresses that are dependent on slope topography (Vanneschi et al., 2019).

Numerical methods can be divided into three categories: continuum methods, discontinuum methods and hybrid methods (Stead et al., 2006). Continuum methods are appropriate for the analysis of soil slope, intact rock mass and highly jointed rock, therefore, they are not explained in detail here. In terms of the rock slope controlled by discontinuities, discontinuum methods are more suitable than continuum methods for modelling the mechanical behaviour of blocky rock mass and rock masses controlled by discontinuities.

In discontinuum modelling, the rock mass is considered as an ensemble of distinct blocks with mutual interactions. Two principal methods are being widely used, the distinct element method (DEM) (Cundall, 1971, 1988; Hart et al., 1988) and discontinuous deformation analysis (DDA) (Shi, 1992). Between them, the former has found broader applications in slope stability analysis and landslide analysis (Stead et al., 2006). The applicability of DEM methods has been demonstrated in the analyses of structurally controlled landslides. For example, UDEC from Itasca Inc. is capable of dealing with discontinuity-related problems for 2D landslide analysis (Itasca Consulting Group, Inc., 2019), and 3DEC is designed for 3D problems. More DEM codes involve the PFC (Particle Flow Code) suite (Itasca Consulting Group, Inc., 2021), including PFC2D and PFC3D, which are specialised in the analysis of rock fracturing and associated slope instability. Although DDA is a type of DEM method, particularly accounting for the interaction of independent particles (blocks) along discontinuities in fractured and jointed rock masses (Shi, 1992; Cheng, 1998), the major theoretical difference is that DDA is a displacement-based method whilst DEM is a force-based method.

However, continuum and discontinuum methods are limited when dealing with the cases involving the combination of brittle fracturing and block deformation, which facilitates the development of a hybrid finite/discrete element approach, proposed by Munjiza et al. (1995). This solution method is particularly suitable for problems in which progressive fracturing takes place (Munjiza et al., 1995a). Based on the original approach, the open-source Y-2D and Y-3D were developed (Munjiza, 2004a). More codes developed upon the concept include Y-Geo (Mahabadi et al., 2012), and Irazu 2D and 3D (Lisjak et al., 2018).

Therefore, discontinuum or hybrid methods are preferred options for modelling slope-specific landslides in the jointed rock mass. In this research, three case studies have been selected, including a coastal landslide that occurred on a cliff slope of approximately 70-metre height, a catastrophic translational landslide sliding along a folded bedding plane, and a landslide involving rock fracturing in the large open pit mine slope. The selection of an appropriate numerical modelling method is dependent on the mechanical behaviour of discontinuities and rock mass on site. In the first case study where rock block fracturing is rare or absent, a 3D DEM code,

3DEC, has been selected to investigate the displacement of failed rock blocks that were constrained by discontinuities. In the second case, that could be represented by simple geometry, a 2D DEM code, UDEC, has been used for landslide analysis. In the third case, where brittle rock fracturing and associated rock deformation may be prevalent, the slope was analysed by using a combination of 3DEC and a finite/discrete element code, Irazu 2D.

Chapter 3. A novel method to incorporate discontinuities into ML-based LSM (adapted from the paper (He et al., 2021a))

3.1. Introduction

As introduced in Chapter 2.5.1, numerous studies have confirmed the suitability and application of ML models for LSM. Encouraging results from these studies confirm that ML methods can provide accurate landslide predictions, and have highlighted specific influencing factors of landslides developed in natural slopes. However, discontinuities (such as joints, fractures, and bedding planes), especially their orientations, have been only considered in LSM studies through the metric 'the proximity to faults', even though many publications have highlighted that unfavourable orientations of discontinuities may cause rock slope failures (Stead and Wolter, 2015; Ferrero et al., 2016; Francioni et al., 2018a).

In this context, a novel application of unfavourably orientated discontinuities into ML landslide prediction is proposed by using GIS-derived kinematic analysis. Discontinuities, detected from remote sensing surveys obtained in areas prone to rock slope instability, were incorporated into GIS-based kinematic analysis. Results from the kinematic analysis were taken as additional input variables to improve the accuracy of ML landslide prediction algorithms. In addition, FR analysis was implemented to quantitatively investigate the potential relationship between the discontinuity-related variables and landslide occurrence.

This study highlights the benefit of point clouds in the extraction of geological discontinuities, through which GIS-based kinematic analysis is performed to assess

the potential of rock slope failures, while also providing a novel application of the discontinuities to improve the accuracy of ML-based landslide prediction.

3.2. Study area description

This research study is focused on the North Coast of Cornwall, UK. The study area is a section of a coastal rock cliff with a minimum height of 40 m between the Godrevy Point and Portreath (Fig. 3-1), experiencing a warm temperate climate with an average yearly temperature of 10 °C and an average annual rainfall of 1062 mm. Almost half the annual rainfall occurs between October and January (approximately 500 mm), with a marked minimum from April to July. This section of the steep coast is known to be prone to landslides of various sizes (Shail et al., 1998), with geological structures (such as faults and joints) playing a vital role in their occurrence (Francioni et al., 2018a).

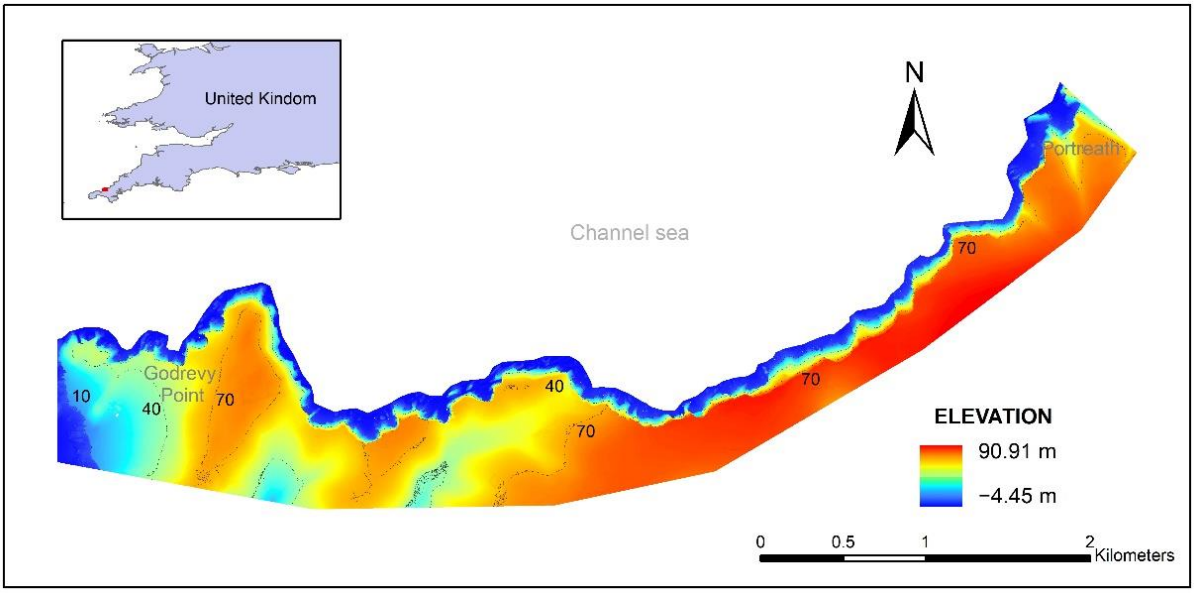

Fig. 3-1. *The study area, a section of coastal rock cliff located on the north coast of Cornwall, UK, highlight the elevation of the analysed cliff.*

3.3. Data and methods

3.3.1. Landslide detection and sampling strategy

Landslides were detected through a widely used method based on elevation change during a given time period (Maurer and Rupper, 2015; Turner et al., 2015; Kim et al., 2020). It was implemented through a comparison of multitemporal LiDAR elevation data with 1 m pixel resolution and ± 40 cm positional accuracy (years 2008 and 2014) collected from an open-source database (Digimap) (Digimap, 2020). Pixels with more than 5 m decreases in elevation from the years 2008 to 2014 were recognized as potential landslides, with which the detection accuracy of landslides developed in the coastal cliff and the disturbance of noise points from LiDAR data, to some extent, could be balanced. Since ground truthing of the detected landslides is difficult to conduct in coastal environments, an alternative method using visual interpretation of landslide scarps and fresh exposures in Google Earth was adopted to verify the detections. In total, 17 landslide sites comprising approximately 10,000 pixels with 1 m resolution were detected as landslides in the study area (Fig. 3-2). As landslide pixels at the same site possessed properties, such as bedrock conditions and geometric conditions, in order to reduce sampling bias, 30 pixels were selected from each landslide site for further analysis.

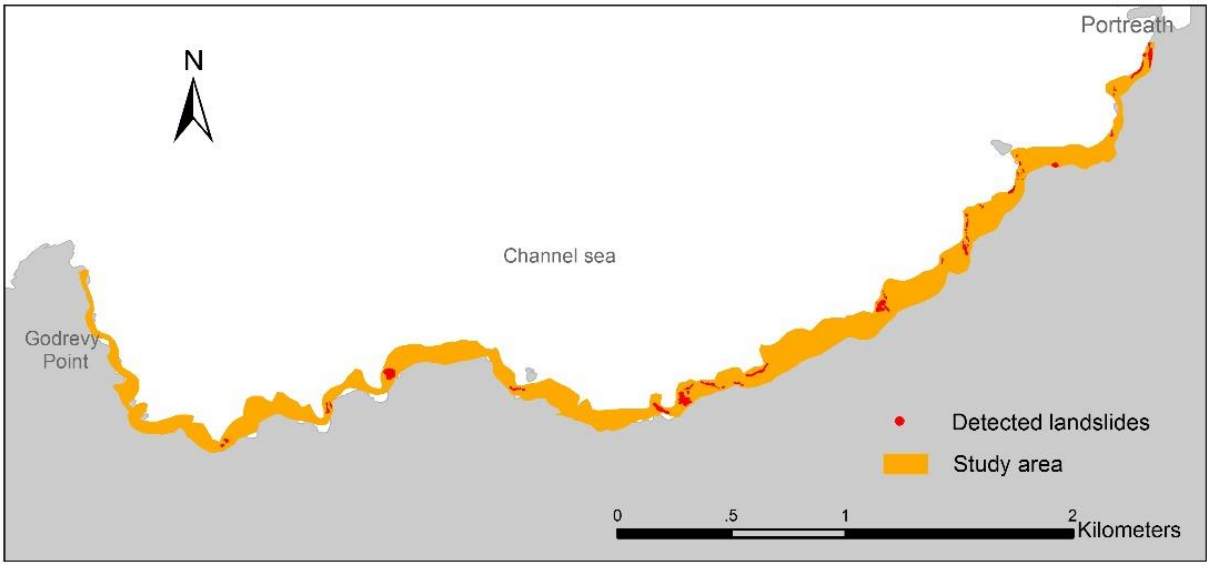

Fig. 3-2. *The boundary of the study area in which landslides occurred in 2008–2014 is identified.*

The same amount of landslide absence data (510 pixels) was collected through random sampling from stable (non-landslide) ground in the study area (the yellow zone in Fig. 3-2) to build robust ML models. From the landslide presence and landslide absence data collected, a 70%:30% training and validation split was applied to the datasets for training and validation of the ML models.

3.3.2. Geological structure extraction from RS surveys

The high risk involved in accessing steep coastal slopes dramatically increases the difficulty of undertaking field surveys by means of conventional methods. Therefore, it was determined that remote sensing techniques were a more appropriate solution to detect geological structures of a representative slope within the study area (at Hell's Mouth). In this study, UAV photogrammetric and aerial LiDAR surveys were combined to provide a data basis for geological structure extraction. The photogrammetric survey was implemented in an oblique manner to obtain images of the steep and high coastal cliff. Due to its high performance in terms of accuracy, vegetation penetration and robustness against geometric distortions, aerial LiDAR provides appropriate detection of geological structures daylighted on the slope surface.

A Panasonic DMC-GH4 camera on a UAV was used to capture overlapped stereo

images (resolution: 4608 x 3456). From the UAV photogrammetric survey, a point cloud was constructed using the structure from motion algorithm by using Metashape software (Agisoft, 2016), and georeferenced by eight GCPs that were derived from 180 corrected observations using Trimble R10 RTK GNSS. In addition, another LiDAR point cloud with a 1 m grid resolution was collected from the CCO (Channel Coastal Observatory, 2020) for complementary use. The software Split FX was adopted to load the point cloud, through which fracture 'patches' were manually identified by fitting collections of triangles that conform to a flatness criterion (Fig. 3-3). Orientations of the fracture traces derived from patches were then extracted (Split Engineering LLC, 2016). The method used has been explained in many case studies (Lato et al., 2009; Poluga et al., 2018). A greater number of discontinuities could be obtained by defining the discontinuity sets with the combination of features identified from the two point clouds.

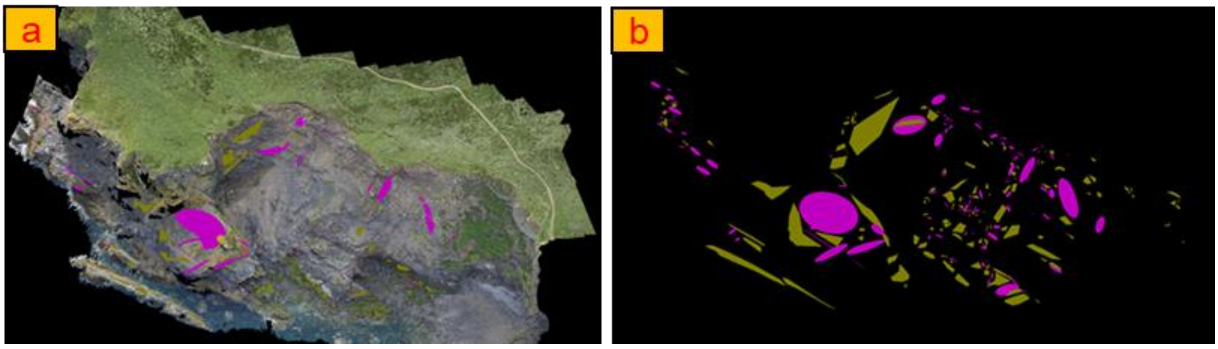

Fig. 3-3*. An example of structure extraction using Split FX based on an UAV photogrammetry-derived point cloud. a) the point cloud collected from UAV photogrammetry, b) Structures extracted from the point cloud.*

Six discontinuity sets were recognized over the study, as presented in Fig. 3-4 and Table 3-1. They mainly followed two trends (NW–SE and NE–SW) and have a potential contribution to the geological evolution of the area, as the trends of the discontinuity sets coincide with the predominant trends of the evolution. Bedding (S0) was slightly tilted, with the highest persistence among the identified discontinuity sets. The joints in S3 have a dip direction parallel to the bedding, but were highly tilted. Joint sets J2 and J5 were sub-vertical and have a dip direction sub-orthogonal to each other. Joint set S1, with the lowest persistence, was sub-parallel to J2. It is

likely that J4 and J5 are subsets of the same features, but were included separately for analysis purposes.

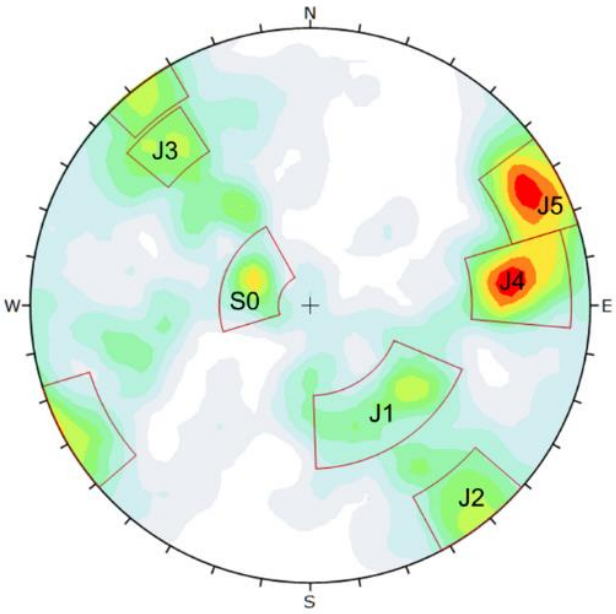

Fig. 3-4. *Stereonet representing 589 discontinuities collected during remote sensing surveys of a representative section of coast within the study area.*

Table 3-1. *Properties of six discontinuity sets identified through remote sensing surveys, including dip angle, dip direction, and some descriptions associated with the surface conditions obtained from (Francioni et al., 2018a).*

Joint set	Dip (°) / Dip direction (°)	Description
S0	26/114	Bedding. Smooth, undulating, planar.
J1	51/309	Rough, undulating, stepped.
J2	90/322	Smooth, undulating, planar.
J3	74/141	Rough, undulating, planar.
J4	70/264	Smooth, undulating, planar.
J5	84/242	Smooth, undulating, planar.

3.3.3. Variables associated with geometric conditions, sea erosion and geological conditions

Given that the case study area was a section of coast, the major influencing factors leading to spatial variation of the landslides shown in Table 3-2 were mainly concerned with geological conditions, geometric conditions of slopes, and sea erosion conditions.

Aspect, profile and plan curvature, slope, and cliff height, as prominent factors, have

frequently been adopted to assess geometric conditions of slopes (Kavzoglu et al., 2014; Dou et al., 2019; Pham et al., 2019; Shao et al., 2019; Wang et al., 2019); in the context of coastal landslides, distance from sea was adopted to assess sea erosion conditions (Levin et al., 2006; Abanades et al., 2015); the material of the bedrocks has been applied as a representative feature of geological conditions (Bui et al., 2020; Chen and Li, 2020; Pourghasemi et al., 2020), since it influences rock mass strength with different compressive strength and material constant according to the Hoek-Brown criterion (Hoek and Brown, 1980b). Their relationship with landslides is illustrated in Table 3-2. These commonly used factors were brought into ML models as input variables for landslide prediction.

Table 3-2. *Selected input variables associated with geometric conditions, sea erosion conditions and geological conditions, and the description of their relationship with landslides.*

Category	Variable	Description
Geometric conditions	Aspect	Aspect is the dip direction of slopes, and used to analyse effects of weather/sea conditions (such as wind directions) or unfavourable orientations of discontinuities
	Profile curvature	Two types of curvatures indicate the amount of overburden on a failure plane (convex terrain of slope surface could result in more overburden than concave terrain
	Plan curvature	
	Slope angle	Slope angle indicates the potential for kinematic failures of slopes together with unfavourable orientated discontinuities
	Cliff height	As the slope height increases, the shear stress within the toe of the slope increases due to added weight
Sea erosion conditions	Distance from sea	Distance from sea partially characterizes the conditions of sea erosion, which may cause physical and chemical change of coastal slopes, such as the removal of mass on the lower part, providing increases in the shear stress of the slopes and thus decreases in the factor of safety
Geological condition	Material of bedrock	This component influences the shear strength of a rock mass

The input variables associated with geometric conditions were derived from the 1 m LiDAR elevation data; distance from sea was measured through the distance between a coastline and slope in a satellite image, which can characterize the sizes of the beaches between the sea and the slope. The material of the bedrock was obtained from a 1:50,000 scale geological map from the open-source Digimap database (Digimap, 2020). The GIS maps shown in Fig. 3-5 present these input variables in the study area. Specifically, they are the map of slope aspect, profile curvature, plan curvature, slope angle, cliff height, distance from sea, and material of bedrock, from Fig. 3-5a to Fig. 3-5g, respectively. Note that the bedrock of the study area is dominated by Porthtowan Formation and Mylor Slate Formation over where Porthtowan Formation is consisted of mudstone/sandstone, mudstone and metamudstone/mudstone, and Mylor Slate Formation is composed of sandstone and slate/siltstone, as presented in Fig. 3-5g.

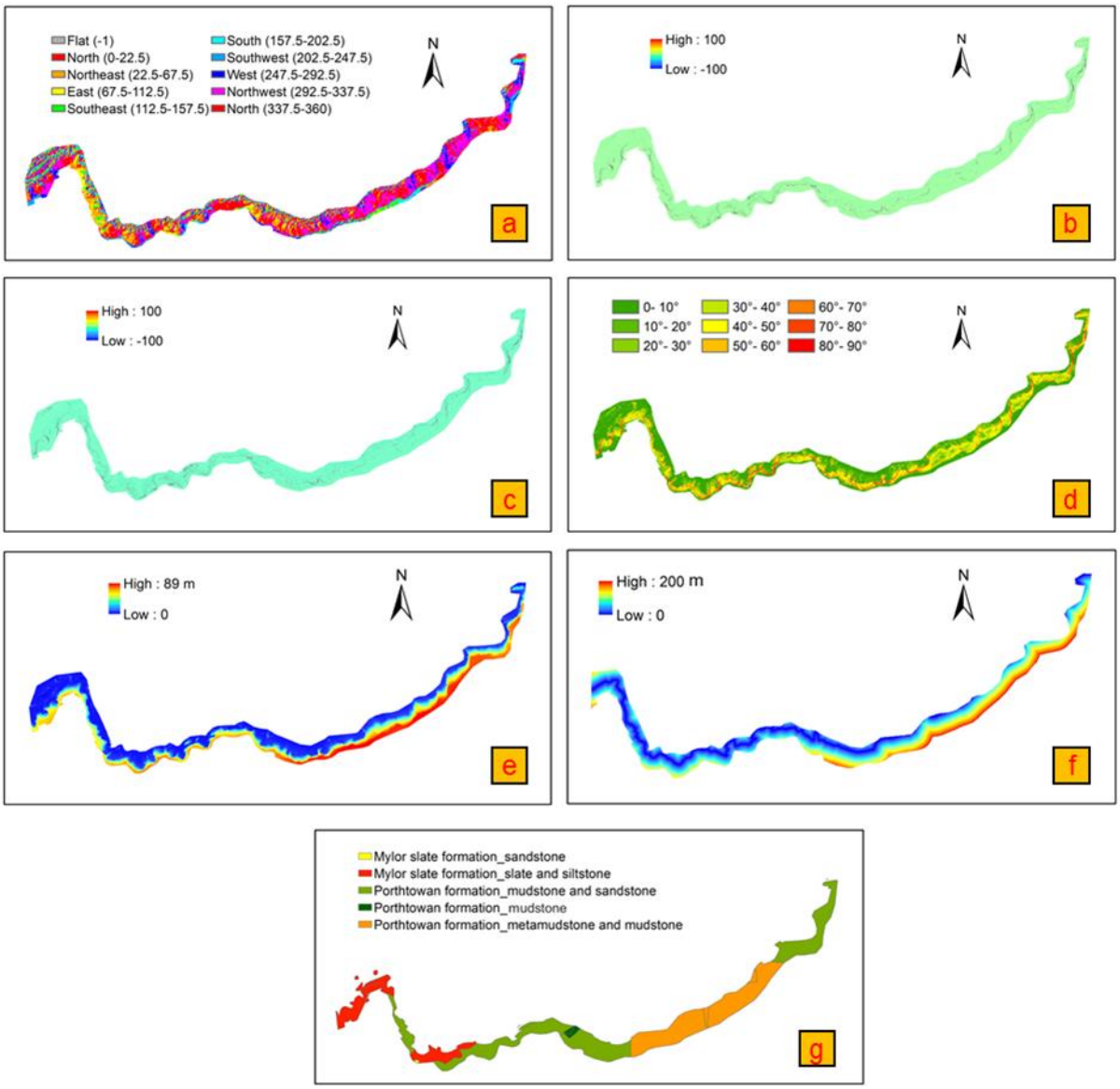

Fig. 3-5. *GIS maps showing the input variables associated with a) aspect, b) plan curvature, c) profile curvature, d) slope angle, e) cliff height, f) distance to sea and g) material of bedrock.*

3.3.4. Variables associated with discontinuities

To incorporate discontinuities into ML landslide analysis, kinematic analysis was applied to estimate places prone to rock slope failures caused by unfavourably orientated discontinuities. In conventional kinematic analysis, a specific slope with a uniform direction is considered. However, this causes it to be inapplicable for characterizing large areas in which the orientations of the slope faces vary considerably (Francioni et al., 2018).

To solve this limitation, GIS-based kinematic analysis similar to that used by Yilmaz et al. (2012) and Francioni et al. (2018) was adopted within a GIS framework. In the

context of GIS-based kinematic analysis, structures were determined to assess the potential of slopes with variable orientations to landslides. Therefore, mathematical representations of the criteria of kinematic failures are required to substitute the conventional stereonet analysis. The GIS-based kinematic analysis was executed within ESRI's ArcGIS platform and followed rock failure conditions proposed by Hoek and Bray (Hoek and Bray, 1981).

Planar sliding kinematic analysis

Planar rock slope failure occurs when a mass of rock in a slope slides down and along a relatively planar failure surface. In conventional kinematic analysis, the criteria for planar instability are: 1) Dip of failure plane must be greater than angle of friction, so as to exceed the shear strength of the discontinuity; 2) Dip of failure plane must be less than dip of slope face, so as to 'daylight' in the slope face; 3) Strike of failure plane must strike parallel to slope crest.

In GIS-based kinematic analysis, a slope prone to planar failure has to meet the requirements associated with the strength, daylighting and orientation conditions as follows (presented in Fig. 3-6a):

1) The dip of the major discontinuity is greater than the friction angle (30° was assumed for the mixture of sandstone and mudstone (Barton, 1973)).
2) The apparent dip of a slope as seen from the dip direction of the critical discontinuity plane is greater than the dip of the discontinuity plane to allow the discontinuity to daylight on the slope face.
3) The slope must be dipped in the same direction as the critical discontinuity plane (a lateral limit of 20° was assumed).

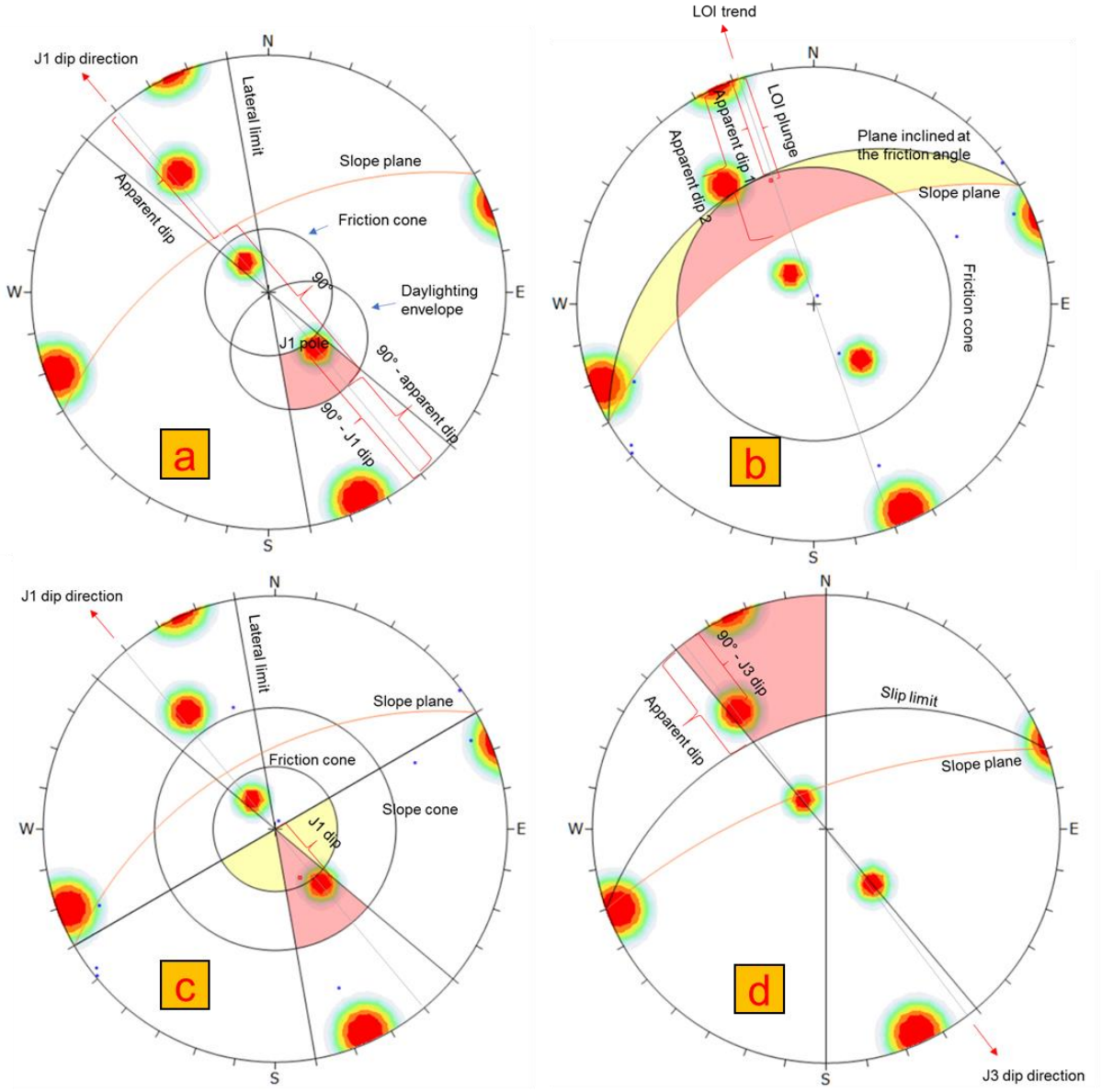

Fig. 3-6. *Graphic representation of GIS-based kinematic stereonet analysis to evaluate the potential of a slope for different modes of instability, including a) planar, b) wedge, c) direct toppling and d) flexural toppling failures.*

Wedge Sliding Kinematic Analysis

Wedge sliding kinematic analysis is a test for the sliding of the wedge formed by the intersection of two planes. The wedge block can either slide along the line of intersection (LOI) or a single plane, depending on their orientations. This can be established by stereonet analysis in which the primary and secondary critical zones represent different sliding modes (Fig. 3-6b). The primary critical zone for wedge sliding is the crescent-shaped area (red zone), in which a wedge slides along the

LOI or a single plane. The secondary critical zone for wedge sliding is the area between the slope plane and a plane (great circle) inclined at the friction angle (yellow zone), in which LOIs are inclined less than the friction angle, but sliding takes place on a single joint plane that has a dip vector greater than the friction angle.

In GIS-based kinematic analysis, a slope prone to wedge instability in the primary critical zone is required to meet the condition that the apparent dip of a slope as seen from the dip direction of the critical discontinuity is greater than the LOI plunge, which is higher than the friction angle (apparent dip > LOI plunge > friction angle). A slope prone to wedge instability in the secondary critical zone should meet the requirement that the LOI plunge is located between the apparent dip of a slope plane and the apparent dip of the friction angle plane (apparent dip of a slope > LOI plunge > apparent dip of friction angle plane).

Direct Toppling Kinematic Analysis

Direct toppling is a normal rock instability mechanism in which near vertical intersections dip into the slope and near horizontal base planes undercut the blocks and form release planes. The key elements of direct toppling analysis are:

1) Two joint sets intersect such that the intersection lines dip into the slope and can form discrete toppling blocks.
2) A third joint set exists that acts as a release plane or a sliding plane, allowing the blocks to topple.

As graphically illustrated in the stereonet direct toppling analysis presented in Fig. 3-6c, the pole of the third joint set falls in the red cone whose angle is equal to the slope angle, but also the LOI of two joints falls in the red (direct toppling) or yellow zone (oblique direct toppling).

In GIS-based kinematic analysis, a slope prone to direct toppling instability must meet the requirements associated with the LOI of two intersecting sets as well as the sliding joint set. With respect to the joint set as a sliding plane, the slope should satisfy the following conditions:

1) The dip of the slope is greater than the dip of the discontinuity plane.

2) The slope dips in the same direction as the discontinuity plane (a lateral limit of 20° was assumed).

As to the LOI, the conditions for the slope are: The slope dips in the same direction as the LOI trend (a lateral limit of 20° was assumed) (primary critical zone for direct toppling), or the slope fails to dip in the same direction as the LOI trend, but falls within a 90° deviation (secondary critical zone for oblique direct toppling). For oblique direct toppling, the LOI must fall within the friction cone, which requires that the LOI plunge needs to be greater than the '90° — friction angle'.

Flexural Toppling Kinematic Analysis

Flexural toppling failure is one of the specific modes of toppling failure that occurs due to bending stresses. For flexural toppling, the critical zone for toppling is defined by the region (see Fig. 3-6d) that falls outside the slip limit plane and inside the lateral limits. The slip limit plane is not an actual physical plane, although it is derived from the slope angle and friction angle. The dip angle of the slip limit plane is derived from the 'slope dip - friction angle'. The dip direction of the slip limit plane is equal to that of the slope face.

In the context of GIS-based kinematic analysis, a slope prone to flexural toppling instability must meet the following requirements:

1) The dip of the slope is greater than the friction angle (30° was assumed).
2) The apparent dip of the slip limit plane as seen from the dip direction of a critical discontinuity plane is greater than '90°- dip of the critical discontinuity plane'.
3) The slope dips in the opposite direction to the critical discontinuity plane (a 20° lateral limit was assumed).

In GIS-based kinematic analysis, the apparent dip is used to calculate the distance of the great circle of the slope plane from the stereonet perimeter in the apparent dip direction in the stereonet analysis (see Fig. 3-6). Apparent dip is calculated as follows:

$$\alpha = arctan(\sin\beta \cdot \tan\delta) \qquad (Eq. 3-1)$$

Where, α is apparent dip; δ is the real dip of the slope plane; β is the angle between the strike direction of the slope plane and the apparent dip direction.

Mechanisms potentially involved in previous landslides within the study area are listed in Table 3-3. It is suggested that failure mechanisms W1/W2/W5, P1/DT1, and P2/DT2, respectively, were similar failure criteria, causing close results in the kinematic analysis for each group. To reduce complexity, representative mechanisms (W1, P1 and P2) were selected from each group, meaning that W2, W5, DT1 and DT2 were not included in the kinematic analysis. This means that mechanisms P1 (planar failure associated with J1), P2 (planar failure associated with J4), W1 (wedge failure associated with J1/J4), W3 (wedge failure associated with J2/J4), W4 (wedge failure associated with J3/J4), and F1 (flexural toppling failure associated with J3) were considered in the GIS-based kinematic analysis for further landslide prediction.

Table 3-3. *Slope failure criteria associated with different rock instability mechanisms, in which a is slope apparent dip, d is slope dip direction, δ is slope real dip, and a_s is the apparent dip of the slip limit plane for flexural toppling analysis.*

Mechanism		Joint Set	Dip/DD (Plunge/Trend)	Failure Criteria
Planar	P1	J1	51°/309°	$a \geq 51°, d \in (309° \pm 20°)$
	P2	J4	70°/264°	$a \geq 70°, d \in (264° \pm 20°)$
Wedge	W1	J1/J4	49°/329°	$a \geq 49°, d \in (329° \pm 90°)$
	W2	J1/J5	50°/325°	$a \geq 50°, d \in (325° \pm 90°)$
	W3	J2/J4	67°/232°	$a \geq 67°, d \in (232° \pm 90°)$
	W4	J3/J4	56°/206°	$a \geq 56°, d \in (206° \pm 90°)$
	W5	J4/J5	54°/324°	$a \geq 54°, d \in (324° \pm 90°)$
Direct toppling	DT1 (oblique)	Sliding: J1	51°/309°	$\delta \geq 51°, d \in (309° \pm 20°), d \in (351° \pm 90°)$
		LOI: J3/J5	72°/171°	
	DT2 (oblique)	Sliding: J4	70°/264°	$\delta \geq 70°, d \in (264° \pm 20°), d \in (351° \pm 90°)$
		LOI: J3/J5	72°/171°	
Flexural toppling	F1	J3	74°/141°	$a_s \geq 16°, d \in (321° \pm 20°), \delta \geq 50°$

Kinematic analysis estimated the possibility of each pixel being prone to landslides through a binary classification (yes/no), without consideration of their subsequent

effects on local slope stability. To consider local effects, the binary results of the kinematic analysis were converted into density maps (Fig. 3-7). The density was calculated in ArcMap software by counting the number of points (pixels) that were prone to instability in a circle with a 50 m radius. The unit was the number of points/square meter. The input variables provided by GIS-based kinematic analysis were labelled with Planar_J1, Planar_J4, Wedge_J1/J4, Wedge_J2/J4, Wedge_J3/J4, and Flexural_J3 to represent associated failure modes.

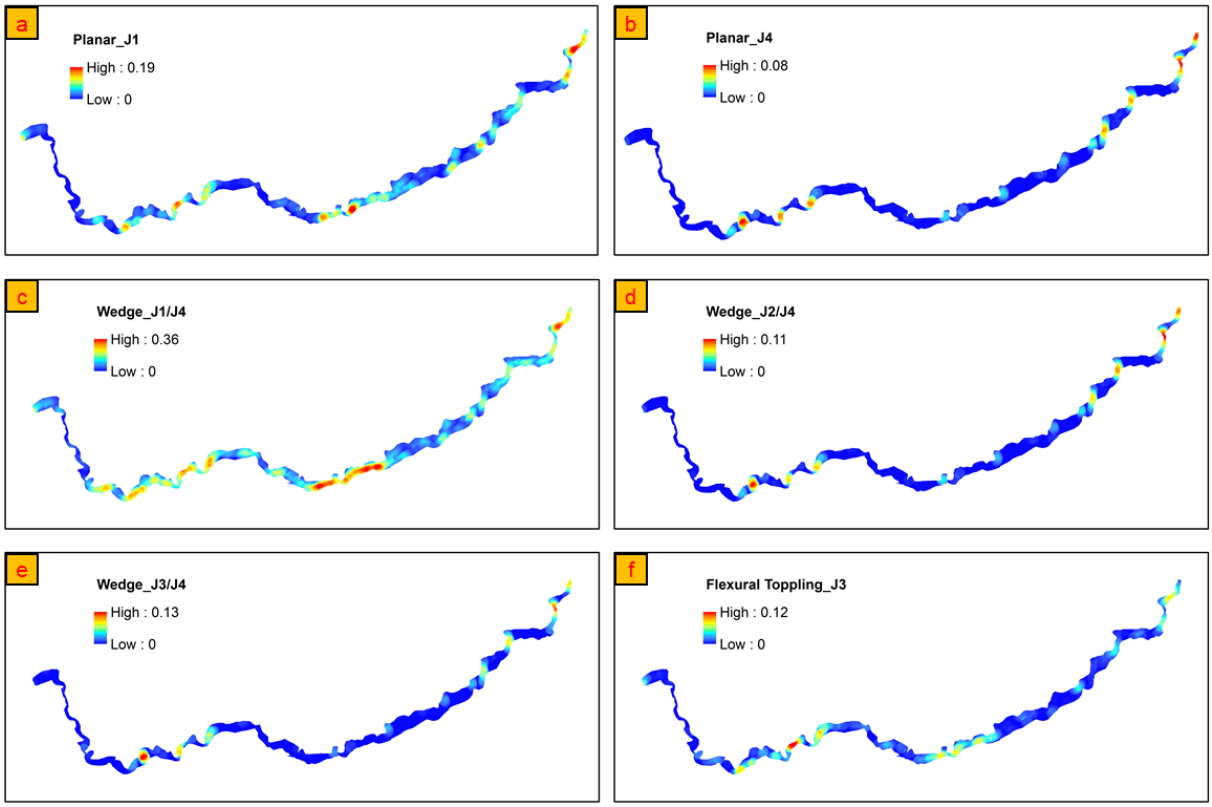

Fig. 3-7. *Discontinuity-related factors, a) planar sliding caused by J1, b) planar sliding caused J4, c) wedge sliding caused by J1/J4, d) wedge sliding caused by J2/J4, e) wedge sliding caused by J3/J4 and f) flexural toppling caused by J3.*

3.3.5. ML analysis

ML models were used to statistically simulate the relationship of landslides and the input variables. Models were constructed and trained using the training set. Modelling of each ML algorithm returned results of variable importance. Variable importance revealed the significance of each input variable with respect to the dependent variables (0/1 for landslide presence/absence). After the models were constructed, their learning and predictive ability was assessed through the Confusion

Matrix and Receiver Operating Characteristic (ROC) curves. These assessments were implemented using the validation set. Two series of ML modelling were carried out. The initial series of modelling was based on the seven commonly used input variables. In addition, a second series of modelling with the inclusion of the discontinuity-related variables was undertaken to make a comparative study.

The predictive capabilities of the two models were assessed on the basis of the confusion matrix and the ROC curve. The confusion matrix was used to assess model performance with respect to their binary classification capability (prediction of landslide absence/presence, 0/1), and the ROC curve was used to evaluate their capability with respect to landslide susceptibility mapping (probability of landslide occurrence).

In this paper, two conventional ML algorithms (RF and SVM) and two neural network algorithms (MLP and DLNN) were adopted, and modelling was performed in a Python environment.

Random forest

RF, an ensemble algorithm, is comprised of decision trees using bootstrap aggregating methods. The metric, Gini impurity, was used in decision tree algorithms to decide the optimal split from a root node, and subsequent splits. The results from the constitutive decision trees in a random forest are aggregated to produce a prediction (binary classification). In addition, the class probability was given based on the proportion of votes of the trees in the ensemble. The predictive ability of an RF model is sensitive to two parameters: the number of tress (ntree) in the RF and the number of variables for the selection in each node (mtry) of a decision tree (Genuer et al., 2010). Thus, in this research RF modelling was carried out after tuning these two parameters.

Support vector machine

SVM has been widely used for classification objectives. The algorithm attempts to fit a hyperplane in an N-dimensional space (N—the number of variables) that distinctly classifies the data points. In this case study, landslide prediction parameter tuning

was conducted on the regularization parameter (C) and kernel type used in the algorithm.

Multilayer perceptron

MLP is a class of feedforward ANN. Basically, its architecture consists of at least three layers: an input layer, a hidden layer, and an output layer. Each node in the hidden and output layer produces an output through a nonlinear activation function with updated weights. The update of weight is adjusted through a learning algorithm.

The performance of the MLP model is sensitive to the activation function applied to the nodes that defines their outputs, the number of nodes in the hidden layer, and the selection of learning patterns for weight optimization (Bui et al., 2020). Therefore, these hyperparameters were tuned to obtain an optimal MLP model.

Deep learning neural network

A deep learning neural network is a class of neural network with considerable depth. It normally consists of an input layer, several hidden layers, and an output layer. The configuration rules of DLNN architectures will not be explained here, as these have been repeatedly presented in many papers (Nhu et al., 2020). In this paper, a DLNN model was used to implement landslide analysis. In the model, the Rectified Linear Unit (ReLU) activation function was applied for nodes in hidden layers to produce outputs. As landslide prediction can be a binary classification, the sigmoid transfer function was used in the output layer to produce a prediction. The Binary Cross-Entropy loss function was used to estimate the loss of the model so that the weights of nodes could be updated and optimized to obtain an optimal model.

During the configuration of a DLNN model, some hyperparameters have a significant influence on its performance, including 1) the number of hidden layers; 2) the number of nodes in each layer; 3) the selection of an optimization algorithm; and 4) learning rate. Thus, these hyperparameters were tuned to obtain an optimal DLNN model for landslide analysis.

3.3.6. Frequency ratio analysis

FR analysis was carried out to quantitively explore the relationship between landslides and the input variables associated with kinematic analysis by using the data acquired from training and validation sets. The analysis assigned a weight coefficient to each class of analysed input variables. The weight coefficient expresses the probabilistic relationship of the class and landslides.

To obtain the RF values (weight coefficient) the following equations were used:

$$FR_i(j) = \frac{a_i(\mathrm{j})}{b_i(\mathrm{j})} \qquad (Eq.\ 3-2)$$

$$a_i(\mathrm{j}) = \frac{LS_i(j)}{LS} \qquad (Eq.\ 3-3)$$

$$b_i(\mathrm{j}) = \frac{P_i(j)}{P} \qquad (Eq.\ 3-4)$$

where $LS_i(j)$ is the number of pixels containing landslides in a class j of variable i; LS is the total number of pixels containing landslides; $P_i(j)$ is the total number of pixels of class i of variable j in the whole area; P is the total number of pixels in the whole area. In this research, P is 1020 and LS is 510.

3.4. Results

3.4.1. Frequency ratio analysis

In FR analysis, the analysed variables related to kinematic analysis were categorized into three different classes in accordance with their density values. On the basis of the results of FR analysis (Table 3-4), a common distribution characteristic for all analysed variables was revealed. Good consistency was observed between FR values and class values, whereby classes with high values possessed high FR values. In addition, quantitatively, most pixels in class 2 and class 3 are landslides points, but pixels in class 1 are mostly non-landslides points. Taking Planar_J4 as an example, 479 in 721 pixels in class 1 are non-landslide points, while 109 in 123 pixels and 159 in 176 pixels in class 2 and class 3, respectively, are landslide points.

Table 3-4. *The results of FR analysis of the discontinuity-related factors, including Planar_J1, Planar_J4, Wedge_J1/J4, Wedge_J2/J4, Wedge_J3/J4, and Flexural_J3.*

Mechanism	Class	LS_i	a_i	P_i	b_i	FR
Planar_J1	Class 1: [0, 0.05]	156	0.31	573	0.56	0.54
	Class 2: (0.05, 0.1]	213	0.42	283	0.28	1.51
	Class 3: (0.1, max]	141	0.28	164	0.16	1.72
Planar_J4	Class 1: [0, 0.02]	242	0.47	721	0.71	0.67
	Class 2: (0.02, 0.04]	109	0.21	123	0.12	1.77
	Class 3: (0.04, max]	159	0.31	176	0.17	1.81
Wedge_J1/J4	Class 1: [0, 0.1]	69	0.14	359	0.35	0.38
	Class 2: (0.1, 0.2]	208	0.41	364	0.36	1.14
	Class 3: (0.2, max]	233	0.46	297	0.29	1.57
Wedge_J2/J4	Class 1: [0, 0.03]	261	0.51	742	0.73	0.70
	Class 2: (0.03, 0.06]	119	0.23	132	0.13	1.80
	Class 3: (0.06, max]	130	0.25	146	0.14	1.78
Wedge_J3/J4	Class 1: [0,0.03]	307	0.60	794	0.78	0.77
	Class 2: (0.03, 0.06]	93	0.18	101	0.10	1.84
	Class 3: (0.06, max]	110	0.22	125	0.12	1.76
Flexural_J3	Class 1: [0, 0.03]	271	0.53	726	0.71	0.75
	Class 2: (0.03, 0.06]	188	0.37	233	0.23	1.61
	Class 3: (0.06, max]	51	0.10	61	0.06	1.67

3.4.2. ML analysis

Parameter tuning was carried out using several trial and error runs to obtain the most accurate prediction and to optimize the hyperparameters of the ML models involved in the initial (without discontinuity-related variables) and second series (with

discontinuity-related variables) of modelling. The parameters in the initial (second) modelling were tuned as below:

1) For the RF model, ntree was assigned as 500 (500), and mtry was 3 (4).
2) For the SVM model, the kernel was specified as the radial basis function ('rbf'), and the regularization parameter C was assigned as 100 (100).
3) For the MLP model, the activation function was specified as being 'logistic' ('logistic'); the weight optimization algorithm was specified as 'lbfgs' ('lbfgs'); the regularization parameter alpha was assigned as 0.1 (0.1); 10 (9) nodes were contained in the hidden layer.
4) For the DLNN model, a Keras sequential model with 3 (3) hidden layers was configured. Each layer contained 64 (128) neurons. The optimizer used in this model was 'Adadelta' for the adaptive learning rate. An EarlyStopping callback was used in conjunction with model training to save optimal epoch the batch size of 1 to prevent overfitting.

The assessment results of classification capability using the confusion matrix are presented in Fig. 3-8. From the perspective of 'vertical comparison', the integration of discontinuity-related input variables significantly reduces cases of the misclassification of landslide absence (0) as well as landslide presence (1). This is also reflected by the increase in overall classification accuracy, from 85% to 93% for DLNN modelling, from 87% to 96% for MLP modelling, from 87% to 94% for RF modelling, and from 88% to 94% for SVM modelling.

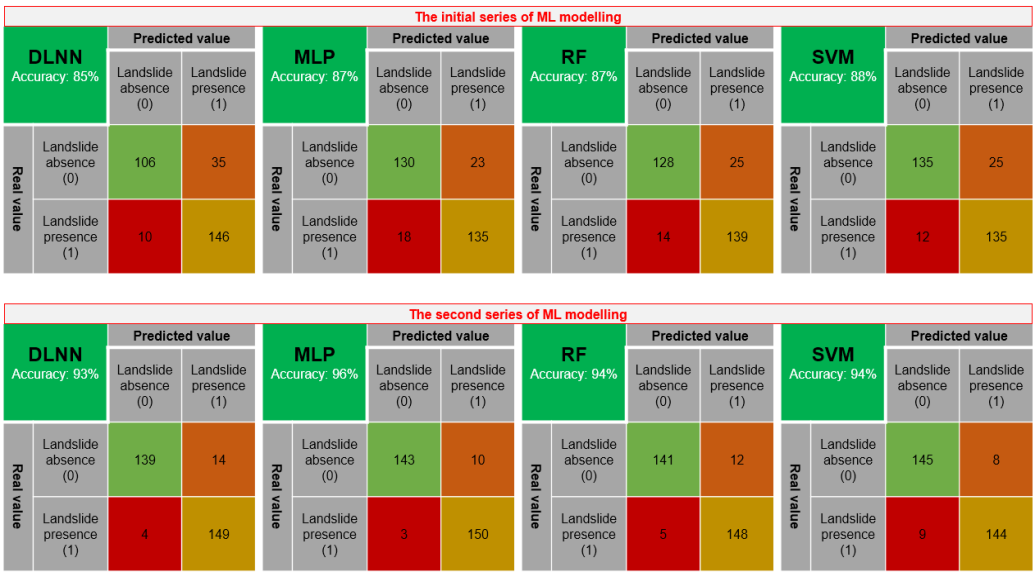

Fig. 3-8. *Confusion matrices showing the assessment results of binary classification capability of the four models involved in the initial (without considering discontinuities) and second (including discontinuities) series of ML modelling.*

The assessment results of LSM capability by ROC curves are presented in Fig. 3-9. Comparative analysis of the curves from the two modelling series shows that with respect to each model, the curve obtained from the second series of modelling overrides that from the initial series of modelling. This distribution characteristic is confirmed by the higher AUC values obtained for the second series of modelling.

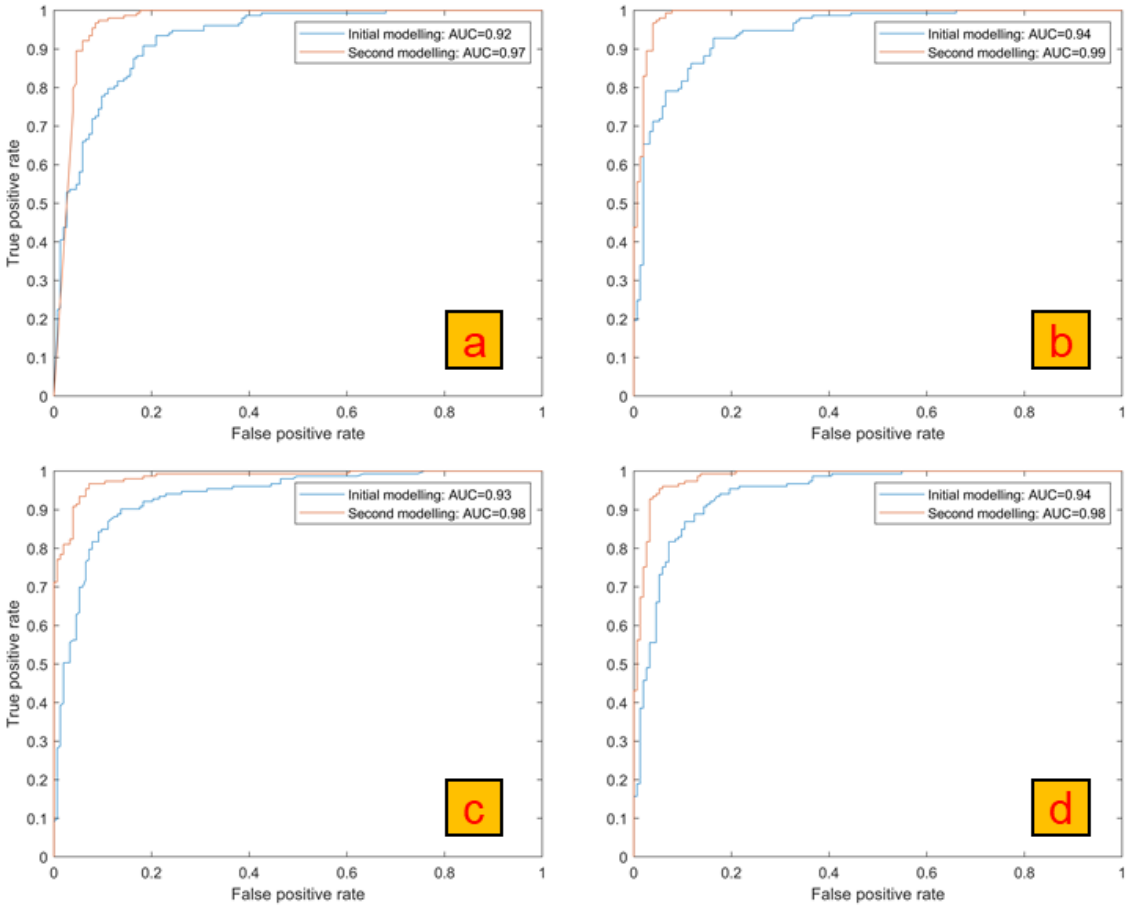

Fig. 3-9. *The assessment of the ML model performance by ROC curves with and without the involvement of discontinuity-related factors: (a) DLNN models, (b) MLP models, (c) RF models, and (d) SVM models.*

The ML analysis provides a variable importance analysis, as shown in Fig. 3-10. The importance indicates the importance of each variable to landslide prediction in the second series of modelling. For all four of the models selected, the discontinuity-

related input variable Wedge_J2/J4, obtained from GIS-based kinematic analysis, exclusively takes the highest importance among the 13 variables.

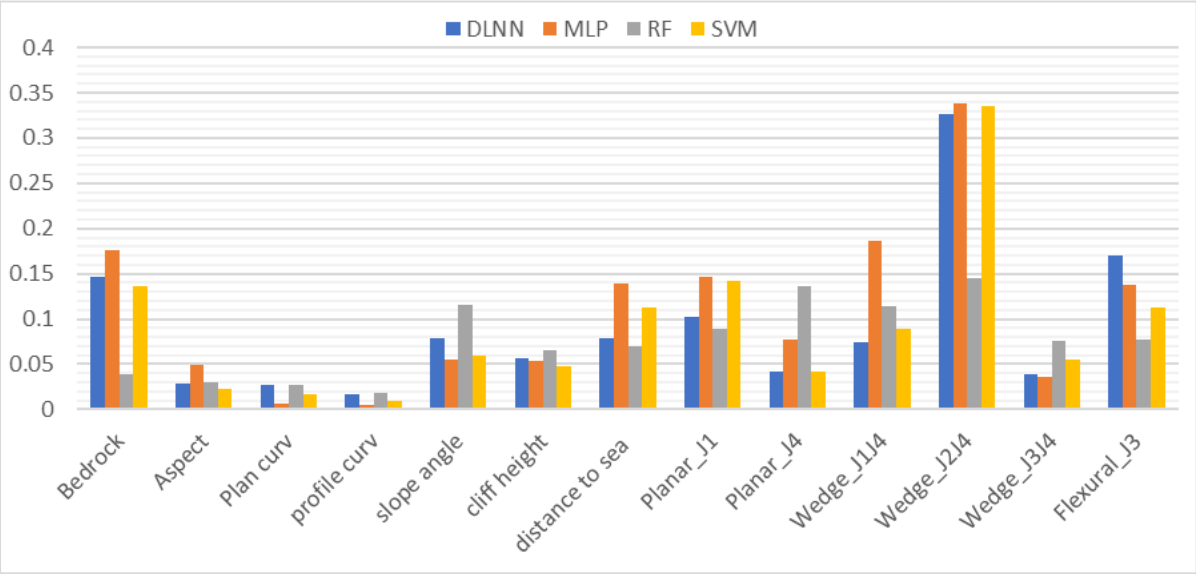

Fig. 3-10. *The results of variable importance, showing the importance of each of the influencing factors in landslide prediction.*

3.5. Discussion and Conclusions

In this research, discontinuities were introduced into ML-based landslide prediction as a controlling factor of rock mass instability by using the method of GIS-based kinematic analysis. The analysis assessed the potential of slopes to be prone to kinematic instabilities, including planar, wedge, direct toppling, and flexural toppling instability modes. GIS-based kinematic analysis is likely to provide effective clues to future landslide occurrence. Fig. 3-11 highlights six regions prone to wedge failures caused by J2/J4, which coincide with locations of previous landslides occurring in the study area. The highlighted landslides have a similar direction, dipping toward W or WNW. Some other landslides in slopes dipping towards N or NNW in the middle of the study area are proposed to be influenced by planar sliding kinematic analysis associated with J1 and wedge sliding kinematic analysis associated with J1/J4 (see Fig. 3-7).

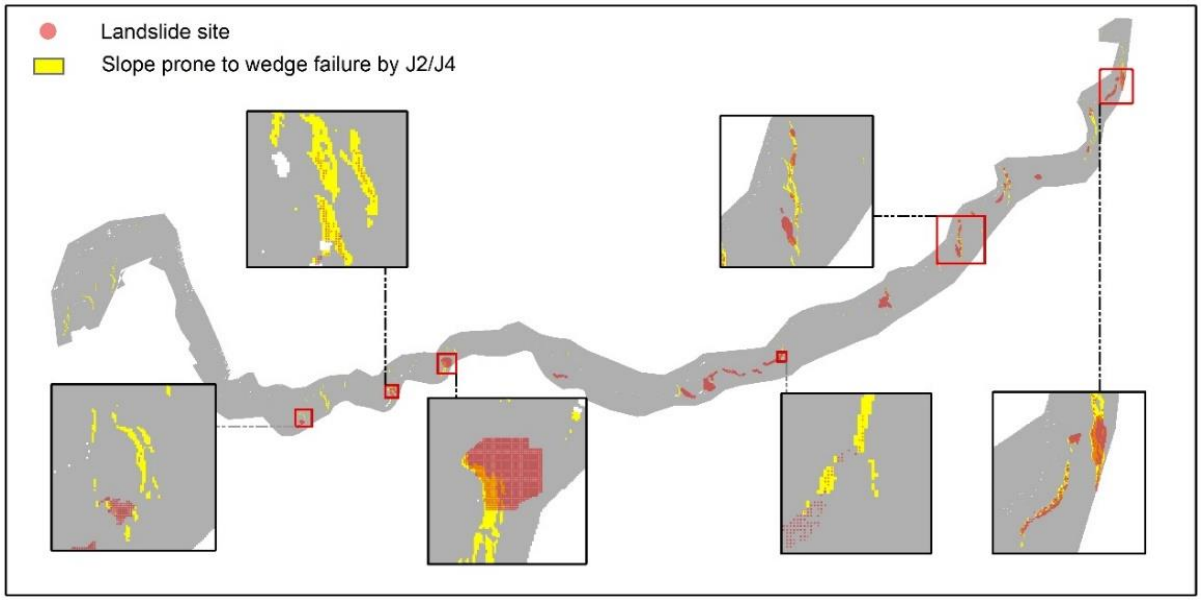

Fig. 3-11. *The comparison of locations of landslide sites of slope prone to wedge failures caused by J2/J4, highlighting the coincidence of the results of the kinematic analysis with real landslide sites.*

In addition, there was a catastrophic landslide in 2011 in the study area with an estimated volume of 100,000 m^3 (Hell's Mouth landslide) (Francioni et al., 2018a). By using the data in 2008, the GIS-based kinematic analysis effectively indicates the risk of possible kinematic failures at this location (Fig. 3-12). The analysis is a result of binary classification that indicates the unstable condition of the slope toe and the

stable condition of the slope crown. If the binary results (0/1) were to be applied as input variables in machine learning models, they would provide misleading information at the slope crown, where instability occurred. However, density mapping, transformed from binary classification, solved this problem by accounting for the unstable points in a 50 m circle range, considering that toe removal may trigger the development of instability at the slope crown (namely local effects).

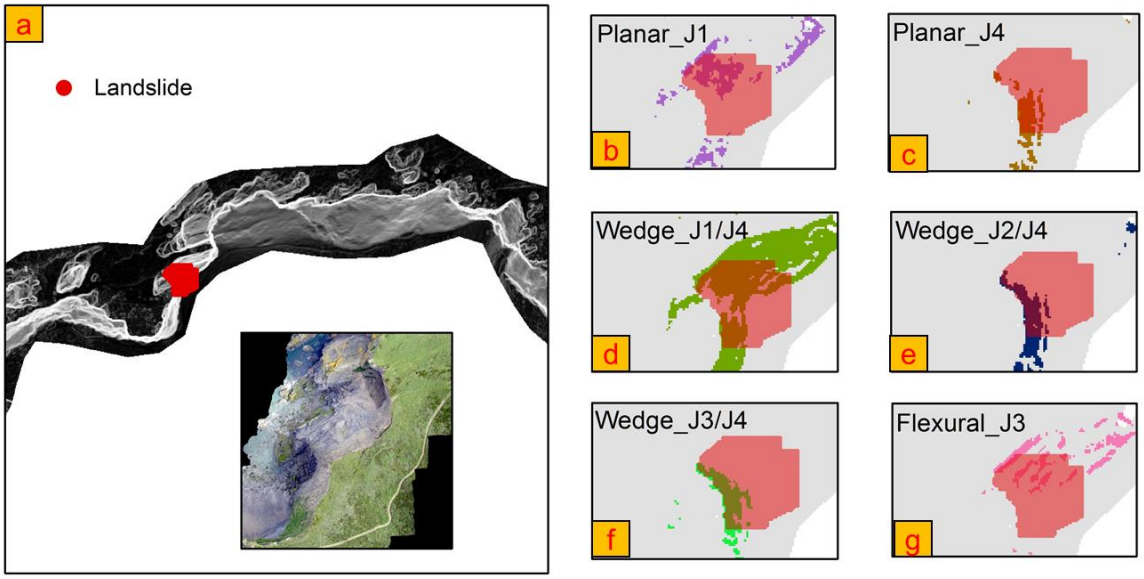

Fig. 3-12. *Results of GIS-based kinematic analysis and their comparison with the Hell's Mouth landslide, a) the extent of the Hell's Mouth landslide, b) potential planar sliding caused by J1, c) planar sliding caused by J4, d) wedge sliding caused by J1/J4, e) wedge sliding caused by J2/J4, f) wedge sliding caused by J3/J4 and g) flexural toppling caused by J3.*

The result of FR analysis provided evidence to support the effects of the GIS-based kinematic analysis. The results showed that high FR values only appear in the classes with high density (class 2 and 3), with respect to variables obtained from kinematic analysis. In addition, quantitively, most pixels in class 2 and 3 are landslides points, and most pixels in class 1 are non-landslide points. These distribution characteristics indicate that discontinuity-related factors with high density are likely to be an indicator of landslide occurrence.

With the inclusion of discontinuity-related variables, the landslide prediction accuracy of the four ML models improved dramatically, which is supported by the results of the two validation methods (Fig. 3-8 and Fig. 3-9). The increase in prediction accuracy was due to the decrease in the misclassification rate of landslide absence cases as

well landslide presence cases. The contrasting predictive capability highlights that these discontinuity-related variables are essential for landslide prediction. The results of variable importance analysis, showing that the factor Wedge_J2/J4 is the most important variable in ML landslide analysis, also supports the above conclusion.

However, the results of the kinematic analysis cannot be used as a standalone criterion for landslide prediction since it only considers the influences of unfavourable orientations of discontinuities. Without consideration of some other factors, such as rock mass strength and sea erosion conditions, kinematic analysis is likely to overestimate the extent of slopes prone to coastal rock slides in this study. This overestimation is reflected in Fig. 3-11, where some stable slopes are misclassed as unstable ones. From this perspective, in ML modelling, variables associated with bedrock, geometric conditions and sea erosion conditions potentially act as limiting conditions to refine landslide prediction by kinematic analysis.

Although less important than discontinuity-related variables in ML modelling, the variables related to bedrock, geometric conditions and sea erosion conditions may facilitate the occurrence of landslides and contribute to the landslide prediction. For example, the distance from the sea shows reasonable importance for landslide prediction, potentially indicating that different distances from the sea could result in various stability conditions. Slopes with less distance from the sea likely have more opportunity to interact with the sea and waves; therefore, they are more likely to be prone to sea erosion. It has been evidenced that the formation of a gully at Hell's Mouth was pre-conditioned by erosion-induced sea caves, on which discontinuities could be daylighted and stress from overburden concentrated. Finally, a gully formed as a result of these conditions. Another important variable is the material of the bedrock. The bedrock map shows that the Porthtowan Formation is more prone to landslides (Fig. 3-13), potentially due to the conditions of the rocks (metamudstone and mudstone/mudstone and sandstone) in the Porthtowan Formation being conducive to landslides with respect to the geometrical arrangement of outcrops, strength, weathering, grain size, etc. However, individual variables/factors would not solely trigger landslides, but rather would interact with each other to reduce the strength of rock masses, consequently resulting in instability.

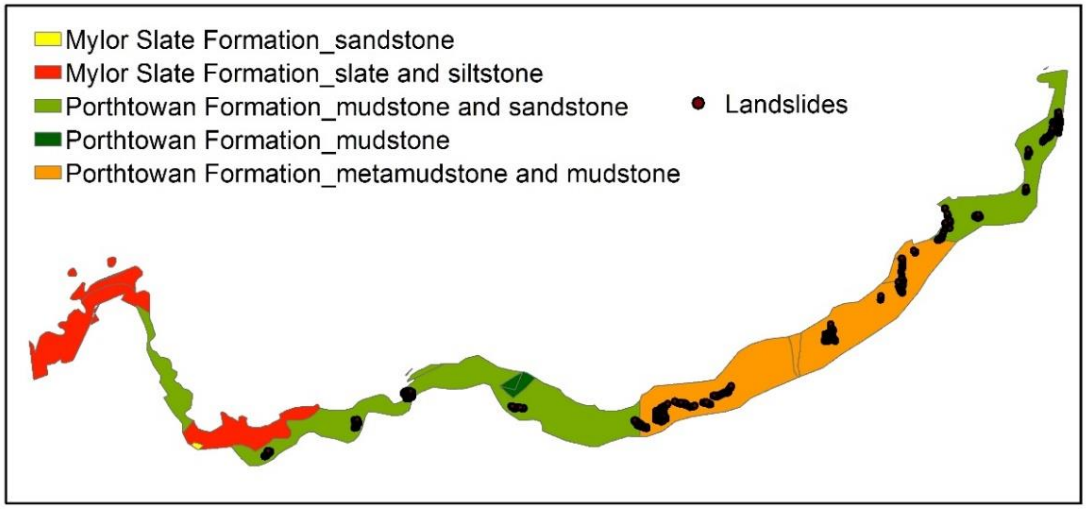

Fig. 3-13. *The component of bedrock over the study area, which is dominated by the Porthtowan Formation, with a small portion of the Mylor Slate Formation in the east.*

This paper provides guidelines for the generalization of the proposed method to other regions in order to perform extensive rock slope stability surveys. This can be implemented by incorporating local discontinuity information into machine learning modelling, including the detection of local discontinuities using remote sensing techniques, the processing of the discontinuity data through GIS-based kinematic analysis for the assessment of slopes prone to different modes of instability, the digitalization of the results of GIS-based kinematic analysis from binary classification to continuous values that are more applicable to ML models, and the combined use of discontinuity-related variables and other appropriate landslide preconditioning factors to train ML models and predict landslides.

It is noteworthy that even without the involvement of discontinuity-related factors, the prediction accuracy of ML models based on the seven common factors was still rather high, achieving approximately 87% of ACC and 0.94 of AUC. This is likely caused by the high sampling density of 30 pixels being selected from each landslide site. The 30 pixels from same site will potentially have had similar characteristics, such as similar bedrock material. The 70%:30% strategy for splitting the acquired data for model construction and model validation means that the validation data, to some extent, will resemble the training data, which could cause the high prediction accuracy. However, the involvement of discontinuity-related variables was still able to improve the prediction accuracy to a higher level, which demonstrates the reliable application of these variables in ML-based landslide prediction.

This case study may have limitations induced by landslide detection in the coastal cliff. Landslides occurred in the overhanging portion of the cliff are difficult to be detected using LiDAR DEM data due to occlusion of overlying slope material. Undetected landslide sites were accordingly regarded as stable sites in this case study. These misclassifications may produce data bias and provide unpredictable impacts on ML modelling and following analysis. In addition, the specific date and type of each landslide are not able to be mapped through this landslide detection method, these may also increase uncertainties for landslide analysis.

Discontinuities, and especially their orientations, have rarely been considered in ML landslide prediction. In this context, this section of research proposes a novel application of unfavourably orientated discontinuities in ML landslide analysis. Six discontinuity sets were detected within the study area through photogrammetric and aerial LiDAR surveys. These structural features were applied to assess the potential of slopes to be prone to different modes of rock instability (planar, wedge, direct toppling, and flexural topping) by GIS-based kinematic analysis. In order to consider local effects, the binary results of the kinematic analysis were transformed into density maps for subsequent FR analysis and ML analysis. Six density maps were obtained based on the results of GIS-based kinematic analysis associated with different rock instability mechanisms, including planar sliding controlled by J1 and J4, wedge sliding controlled by J1/J4, J2/J4 and J3/J4, and flexural topping controlled by J3. These density variables, as well as some commonly used landslide influencing factors, were then considered as input variables in ML models to predict landslides.

To validate the results of the GIS-based kinematic analysis, comparisons were made with previous landslide sites. The comparison results indicate that the slopes prone to kinematic failures presented in Figure 10 and Figure 11 were identified as the sites of previous landslides. This highlights the reliable application of GIS-based kinematic analysis in landslide prediction.

Good consistency was observed, through FR analysis, between landslide probability, which was characterized by FR values, and discontinuity-related variables, showing that classes with higher values possessed higher FR values. The coincidence with respect to their distribution characteristics indicates a close correlation between them.

The results of model assessment on the basis of confusion matrix and ROC curves showed that the inclusion of discontinuity-related input variables significantly improved the prediction accuracy of the four ML models. In addition, variable importance analysis revealed that discontinuity-related variables took the highest importance in landslide prediction in the four ML models.

The above findings highlight the reliable application of GIS-based kinematic analysis for assessing slopes prone to landslides. In addition, the novel application of unfavourably orientated discontinuities in ML models improves landslide prediction.

Chapter 4. Modelling discontinuity control on the origin and development of Hell's Mouth landslide (adapted from the paper (He et al., 2021b))

4.1. Introduction

Discontinuities (such as joints, cleavages, bedding, foliation, faults, and folds) produce weak planes in a rock mass that may contribute to the occurrence of landslides under unfavourable conditions associated with orientation, size, intensity, and strength of discontinuities (Hutchinson, 1989). Discontinuities can also behave as release surfaces at varying scales, along which failures can occur, allowing for sliding/fall from the main slope. There are numerous examples of discontinuity control on slope instability at varying scales in the literature. For example, the upper part of the La Valette landslide was shown to be structurally controlled at a regional scale with an estimated failure volume of 500,000 m^3 (Travelletti et al., 2013). Weidinger et al. (2014) noted that the occurrence of catastrophic landslides is likely related to relatively large-scale structures (e.g., tectonic faults). The gigantic 1999 Chiu-fen-erh-shan landslide developed along a pre-existing bedding fault that was formed during flexural slip folding, and its development was significantly influenced by the properties of the discontinuities (Wu et al., 2005). Inherited structures associated with slope-scale folding in Eastern Switzerland controlled the extent and mechanism of an ongoing deep-seated gravitational slope deformation with a volume of 1.85 km^3 (Agliardi et al., 2019).

Further examples of discontinuity-controlled instability include the 2010 Qiyangou landslide that involved a wedge-planar failure where the failed rock mass was displaced along a basal surface and was bounded by discontinuities (i.e., a thrust fault and a series of aligned joints belonging to the same set) (Fan et al., 2019). A recent earthquake-induced massive landslide (2017) in China occurred in a complex geological environment where two active faults intersected to form a compressive stress concentration zone, with the interface between metamorphic sandstone and slate allowed sliding of the rock mass (Shao et al., 2019). Donati et al. (2019, 2020, 2021a, 2021b) used a combined remote sensing (RS) and numerical modelling approach to highlight the importance of faults and shear zones in controlling the failure mechanisms at the Hope Slide, BC., the Downie Slide BC., and the San Leo

Rockslide, Italy. At a smaller scale, toppling failure that occurred in a granite slope of the Melbur Pit was shown to be controlled by unfavourably oriented discontinuities (Vanneschi et al., 2019).

Different methods have been used for the analysis of slope instability or landslides in jointed rock masses. The kinematic analysis provides a preliminary estimation of the kinematic potential of a rock slope prone to different mechanisms of instabilities within the rock mass (i.e., planar sliding, wedge sliding and toppling) (Hoek and Bray, 1981; Stead and Wolter, 2015; Francioni et al., 2018a). For relatively simple scenarios, limit equilibrium methods are usually adopted and can consider potential influences such as pseudo-static, earthquake acceleration, groundwater conditions and anisotropy. They can determine the factor of safety depending on an assumed failure mode (Huang and Yamasaki, 1993). In more complicated situations, 2D/3D numerical modelling methods can provide a comprehensive understanding of the stability conditions and mechanical behaviour of the slope, and allow simulation of progressive displacement and/or deformation involving the unstable slope prior to collapse (Jing, 2003; Stead et al., 2006). In the context of jointed rock slopes, discontinuum modelling methods offer a significant advantage in modelling deformable or rigid body movements by treating the rock slope as a discontinuous rock mass. The simulated rock mass comprises an assemblage of deformable or rigid blocks, with defined structural-related contacts between them. Among discontinuum methods, distinct element methods (DEM) (Corkum and Martin, 2004; Brideau et al., 2007, 2011; Dong et al., 2018; Agliardi et al., 2019), and discontinuous deformation analysis (DDA) (Kveldsvik et al., 2009; Huang et al., 2016; C. Liu et al., 2019; Xia et al., 2021) are two frequently adopted approaches for the analysis of structurally controlled landslides.

Where landslides have occurred in a rock mass, discontinuities are usually related to the propagation of tension cracks (Bovis and Evans, 1996; Brideau et al., 2007; Zhang, M. et al., 2018). Brideau et al. (2007) found that the onset of tension cracks in the Dawson City Landslide was related to the pre-existing discontinuity sets, where the distribution of tension cracks could be used for defining areas of unstable ground. Zhang, M. et al. (2018) showed that interpreting tension cracks developed along a series of aligned joints contributed to defining the boundary of the landslide.

Therefore, the analysis of visible tension cracks may be beneficial to the interpretation of discontinuities as well as providing further understanding into the development of a landslide. However, the onset and opening of tension cracks, has to date had limited consideration in the numerical analysis of a landslide. A virtual joint was introduced by Wang, J. et al. (2021) to simulate the propagation of cracks in intact rock masses in a 2D DDA (discontinuous deformation analysis). A 2D discrete element model was used to understand crack initiation, propagation, and coalescence within a rock mass during an earthquake-induced rock avalanche (G. Gao et al., 2020). Simplified geometry of joints was used in a 3D distinct element simulation using 3DEC (Itasca Consulting Group, Inc., 2017), to investigate the displacement of rock masses along the joints forming the tension cracks (Corkum and Martin, 2004).

In this case study, numerical modelling and back analysis of the Hell's Mouth landslide is used to provide an improved understanding of the evolution of a section of the North Coast of Cornwall, UK. The modelling uses a 3D distinct element approach that includes a representative discrete fracture network. The analysis provides further insight into the formation of an inlet and the influence of the discontinuities on the landslide and subsequent tension crack formation behind the cliff crest. The modelling results have been verified by observations obtained from remote sensing (RS) surveys and evidence from analysis of a video taken of the initial landslide. A sensitivity analysis has also been undertaken to demonstrate the effects of key discontinuity parameters (i.e., dip, dip direction, persistence, and friction angle) on the modelled landslide behaviour. This paper provides further insight into coastal evolution in blocky rock masses that are susceptible to discontinuity-controlled instabilities.

4.2. Study area description

The study area is located close to Hell's Mouth (Fig. 1), on the North Coast of Cornwall in the southwest of England, UK. At this location, two successive landslides occurred in 2011 within a three-month period. The area experiences a warm and temperate climate with average yearly temperature of 10 °C and average annual rainfall of 1062 mm. The cliffs in the vicinity of Hell's Mouth have an average height of approximately 70 m. The landslides occurred on the eastern side of a V-shaped cove (Hudder Cove which is directly east of Hell's Mouth). The eastern end of the V-shaped cove is characterized by a north-south striking near vertical scarp. An east-west fault-controlled striking 'zawn' is present at the northern edge of the cove (it is referred as 'inlet' in Fig. 4-1). A 'zawn' can be described as a deep and narrow sea-inlet in the British Isles, especially Cornwall and the south-west, cut by erosion into sea-cliffs, with steep or near vertical sidewalls. In addition, shallow caves can be observed at the toe of the cliff which suggests that the slope is susceptible to sea erosion or block removal by wave attack.

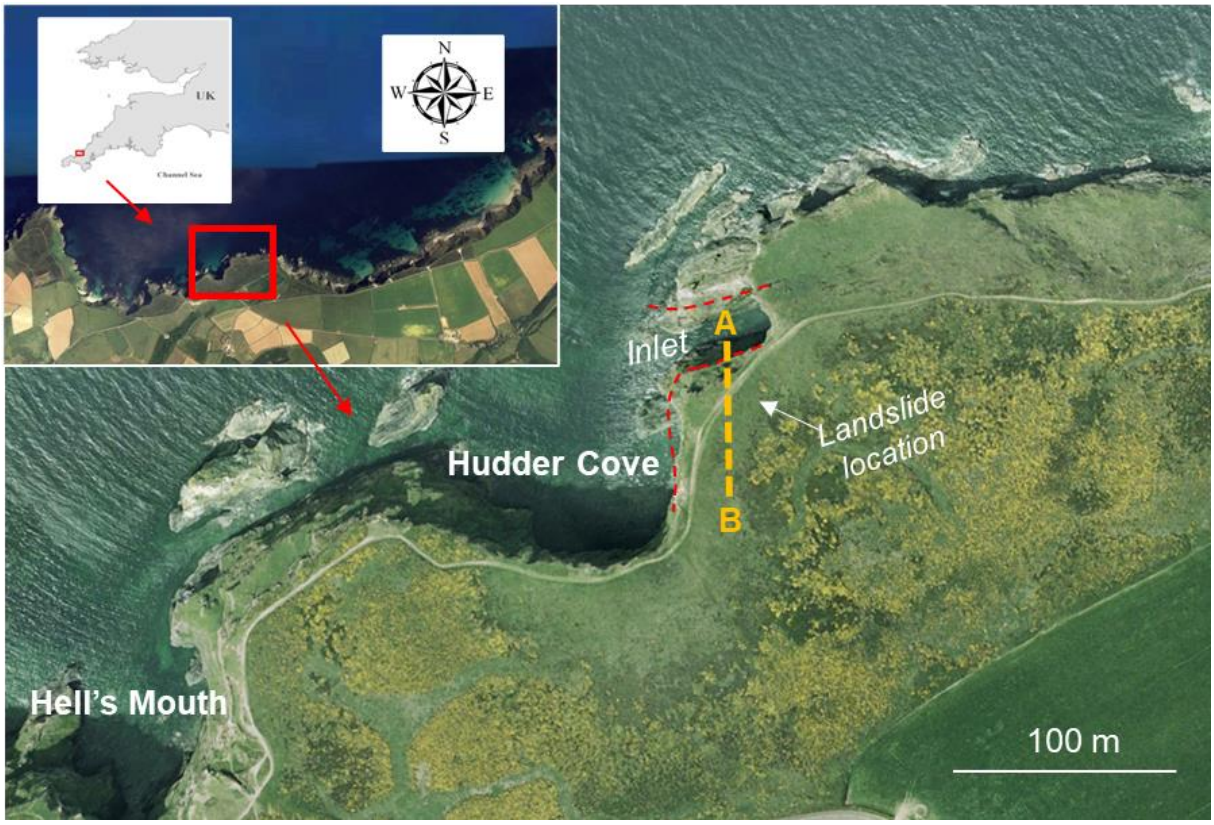

Fig. 4-1. *3D Google Earth image in 2001 showing the location of the study area which is close to Hell's Mouth on the North Coast of Cornwall, UK.*

4.2.1. Geological setting

Geologically, the analysed slope is located in the Gramscatho Basin and dominated by the Porthtowan Formation (Gramscatho Group) (see Fig. 3-2). Porthtowan formation comprises of alternating beds of strong to moderately strong, medium to thinly bedded dark grey mudstone, interbedded with strong to moderately strong, thick to thinly bedded pale grey fine sandstone, which may locally have a silt and mud component (Hollick et al., 2006; Francioni et al., 2018a).

Five discontinuity sets have been previously recognized by Francioni et al. (2018a) over the study area through interrogation of point cloud data provided by remote sensing techniques (Table 4-1). The identified sets mainly follow two trends (northwest-southeast and northeast-southwest) and significantly contribute to the geological evolution of the area, as the trends of the coastline closely follow these directions (Francioni et al., 2018a). Bedding (S0) is slightly inclined and has the highest persistence among the identified discontinuity sets. Joints associated with set J3 have a dip direction parallel to the bedding but are more steeply inclined. Joint sets J2 and J4 are sub-vertical and have a dip direction sub-orthogonal to each other. Joint set J1, has the lowest persistence of the mapped discontinuities, and is sub-parallel to J2. J1, however, dips towards the north-west and therefore has the potential to form a basal surface for planar sliding that daylights in the cliff face. Importantly, field mapping and previous analysis of remotely captured point cloud data indicates that major fault systems (F1, F2, F3 and F4) are associated with the joint sets (as introduced in Table 4-1). The location and presence of these features dictate the potential for cliff instability and are directly associated with previous landslide activity within the immediate section of coastline (Francioni et al., 2018a). The listric fault F1, for example, is frequently associated with major planar and wedge failures along the coastline and has formed the basal feature of previous coastal landslides.

Table 4-1. *Characteristics of 5 discontinuity sets and faulting identified by Francioni et al. (2018a), including dip, dip direction and associated descriptions of surface conditions.*

Discontinuity	Dip (°) / Dip Direction (°)	Bedding/Joint Description
S0	18/142	Bedding. Smooth, undulating, planar
J1/F1	34/320	Rough, undulating, stepped
J2/F2	87/336	Smooth, undulating, planar
J3/F3	64/143	Rough, undulating, planar

J4/F4	87/069	Smooth, undulating, planar

A geological section is presented in Fig 4-2 which is created along the profile AB (as previously depicted in Fig. 4-1), highlighting the dominant rock component of Porthtowan formation and 3 faults (F1, F2 and F3) in the slope. F4 is excluded from the geological model as it is sub-parallel to the cross section.

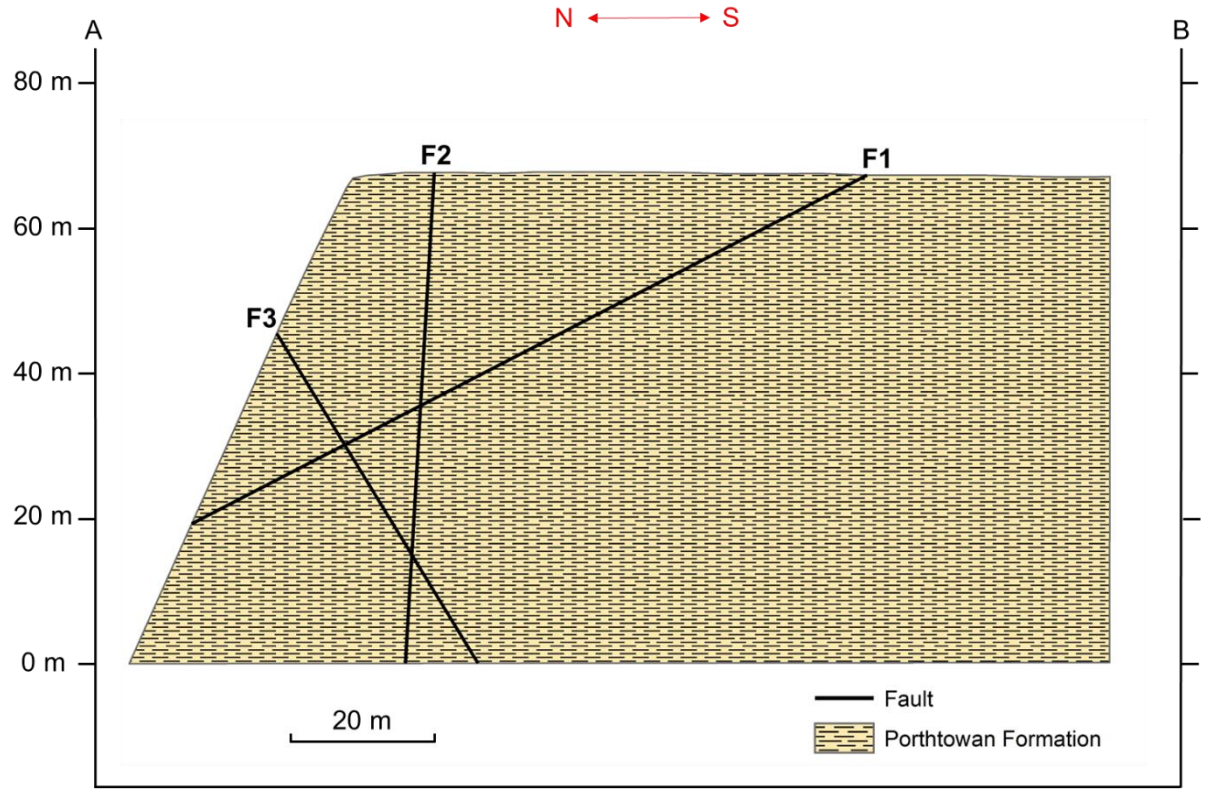

Fig. 4-2. *Simplified 2D geological section along the profile AB that is previously depicted in Fig 4-1.*

Fig. 4-3a shows the stereonet representation of discontinuities identified in the slope (Francioni et al., 2018a). Using mean values of each identified joint set orientation and an initial friction angle of 30°, preliminary kinematic analysis associated with planar sliding (Fig. 4-3b), wedge sliding (Fig. 4-3c) and flexural toppling (Fig. 4-3d) was undertaken. This analysis indicates that the north-western facing sidewall of the 'zawn' or inlet with an orientation (70°/330°) has the potential to fail through planar sliding controlled by J1, wedge sliding dominated by intersections of J1/J4 and J1/J2, and flexural toppling associated with J3. An evaluation of the potential variation of discontinuity set orientations suggests that direct and oblique toppling may also be possible, resulting from basal planes formed by J1 and steeply inclined block edges

formed by intersections of J2/J4 or J3/J4.

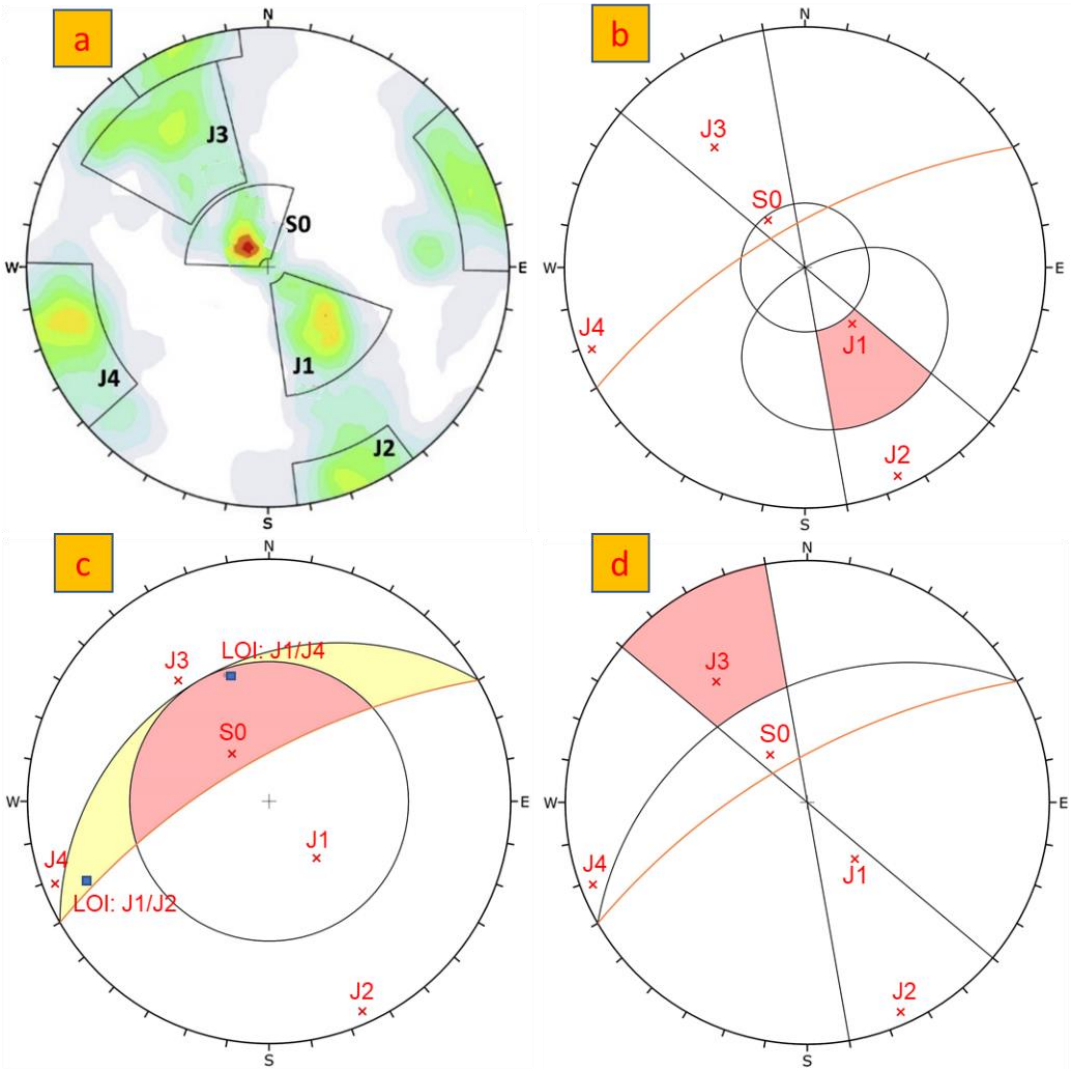

***Fig. 4-3**. a) Lower hemisphere stereonet showing contours of joint poles and 5 joint sets identified in the study area (Francioni et al., 2018a), b) kinematic overlay for planar sliding in the cliff (70°/330°) using the mean sets identified in part (a) and Table 4-1 c) wedge sliding kinematic analysis, d) flexural toppling kinematic analysis.*

4.2.2. Inlet formation

The north-east south-west trending fault (associated with F3) highlighted in Fig. 4-4a is identified as a major feature in the local geology of the area (Digimap, 2020). It has a critical influence on the cliff orientation and geomorphology of the immediate area. Fig. 4-4a and b show resulting stacks created at the northern edge of Hell's Mouth and the influence of the fault on inlet formation in the study area. Preferential erosion due to wave action, block release and erosion induced caves can be

observed at the toe of the cliff along this section of coastline (Fig. 4-4b). The cliff geomorphology prior to and after the two landslide events can be seen in Fig. 4-5 and Fig. 4-6. Two fault-related surfaces (70°/330° and 75°/160°) associated with F2 and F3 form the edges of the inlet. The discolouration of the rock within the vicinity of the inlet suggests an alteration zone that may be more susceptible to preferential erosion.

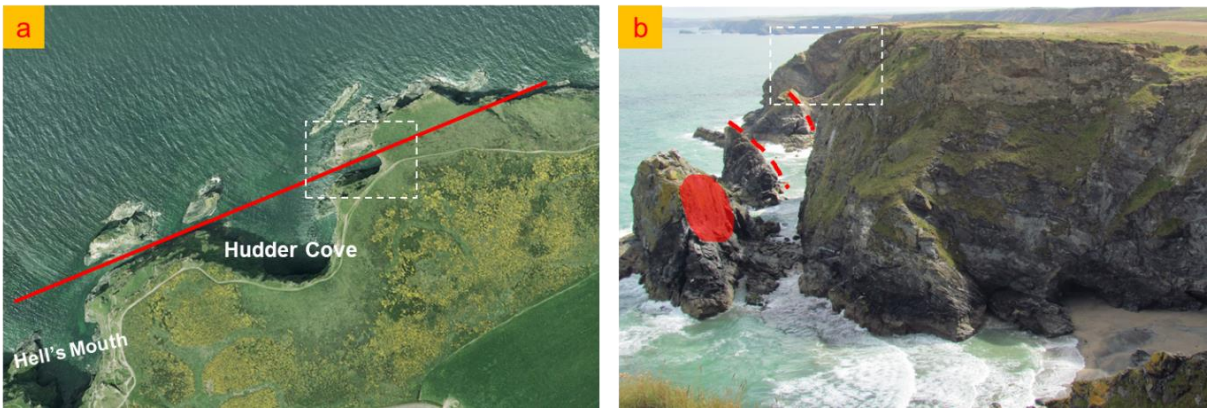

Fig. 4-4. *a) 2001 Google Earth Image showing that F3 (red line) has influenced development of Hell's Mouth landslide and inlet formation in the study area (white rectangle zone), b) image showing the geomorphology of the cliff and fault related (F3) scarps highlighted in red.*

4.2.3. Previous landsliding activities

This section of coast is susceptible to landslides of various sizes (Shail et al., 1998; Francioni et al., 2018a; He et al., 2021a). A significant landslide episode was videoed by engineers from Cornwall Council on the afternoon of Friday 23 September 2011 and is part of the British Geology Survey landslide database (British Geological Survey, 2020).

A video-frame analysis of the failure undertaken by Stead (2021) is provided in Fig. 4-5. Prior to major failure, initial development of wedge fractures, opening of fractures and soil flows were evident from the cliff face (Fig. 4-5a). This was followed by further fracture propagation, buckling of slabs and formation of an active-passive wedge near the toe of the slope (Fig. 4-5b). The fractures appear to propagate along pre-existing discontinuity orientations. Further sliding and wedge detachment occurs, with subsequent breakup of the rock mass during failure. The video shows the potential control of discontinuities on the propagation of the landslide.

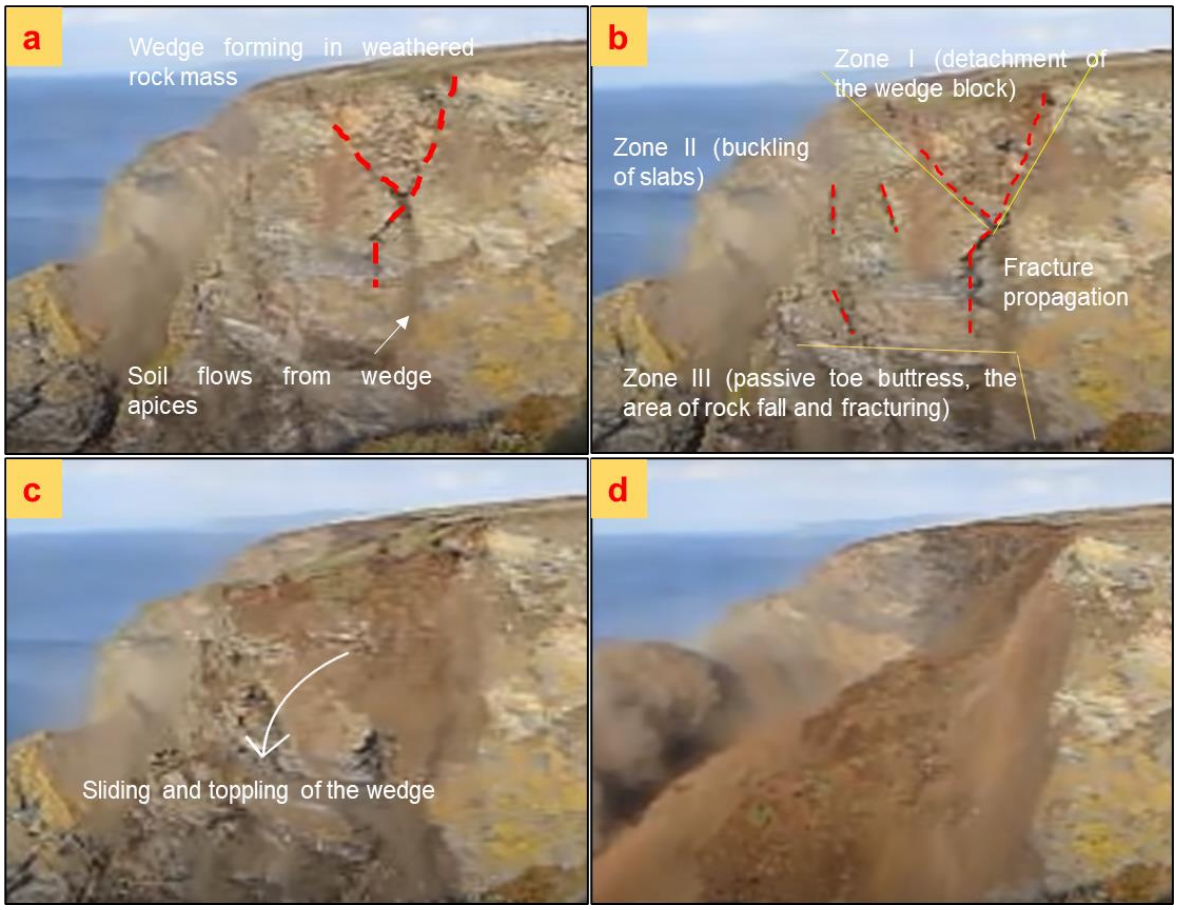

Fig. 4-5. *Preliminary video-frame analysis of the initial landslide at Hell's Mouth from Stead (2021), with images looking towards east.*

Following the first landslide detailed above, in September 2011 a second landslide occurred immediately to the south of the first landslide, prior to a visit to the site by the second author in October 2011. The slope geometries prior to the two landslide episodes, after the first episode, and after the second episode have been presented in Fig. 4-6. It can be seen from Fig. 4-6c that the extent of the second slide was smaller than the first.

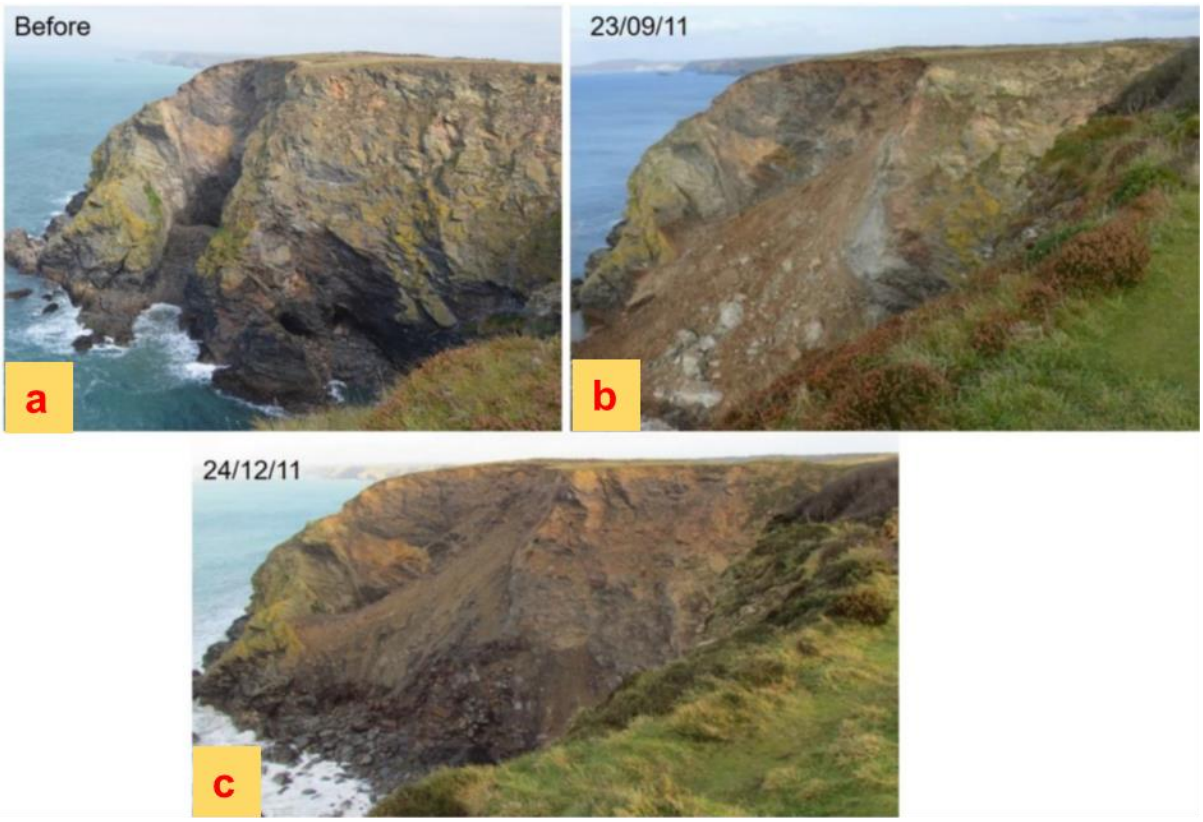

Fig. 4-6. *Pre-landslide and post-landslide images obtained from (Francioni et al., 2018a), showing the geomorphology of the analysed slope looking towards east at different time periods, a) prior to the landslide, b) after the first landslide episode, c) after the second landslide episode.*

4.2.4. Post-landslide features

In view of the lack of safe access, remote sensing techniques were used to detect and characterise post-landslide features. Francioni et al. (2018a) reported initial use of terrestrial LiDAR and photogrammetry to generate three-dimensional point clouds for extraction of discontinuity orientation data and comparison of aerial LiDAR data for estimations of slide volumes. More recent analysis in June 2018 used a Panasonic DMC-GH4 camera mounted on an DJI M600 UAV to capture overlapping stereo photographic images (resolution: 4608 x 3456). These images were georeferenced using eight ground control points (GCPs) derived from 180 corrected observations using a Trimble R10 RTK GNSS that provided an accurate model to detect landslide features, including landslide scars and tension crack development behind the crest of the cliff.

Fig. 4-7a presents an orthoimage constructed using the Metashape software (Agisoft, 2016) from a series of overlapped UAV stereo photographic images and shows the landslide scarps of the two landslides in plan view. These scarps define the boundaries of the two landslide episodes and are denoted by solid-coloured lines (red: the first landslide; pink: the second landslide). The scarps of the first and second landslides are both sub-vertical, striking northeast-southwest and approximately north-south, respectively. The rear and lateral release surfaces for the two landslide events are associated with J2/F2 and J4/F4 orientations.

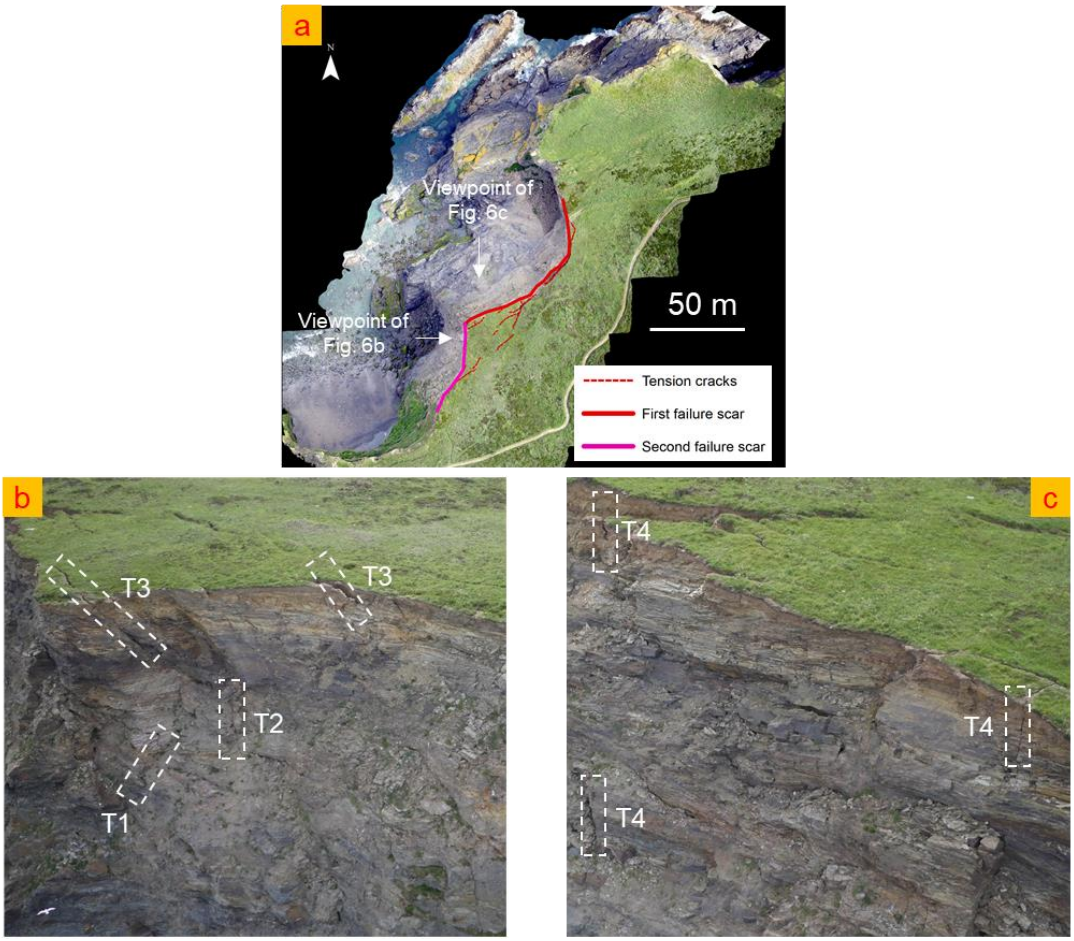

Fig. 4-7. *Images of the post-failure slope at Hell's Mouth: a) An orthoimage showing landslide scars of the two failures and tension cracks behind the scars; b) An UAV image presenting tension cracks that daylighted at the slope surface looking towards east; c) Tension cracks in slope looking towards south.*

Open tension cracks can be observed on slope surfaces (Fig. 4-7) as well as behind the crest of the slope. The cracks, developed on and behind the crest of the slope, show some regularity in orientation and appear to begin and propagate along pre-

existing discontinuities. Specifically, tilted cracks T1 (Fig. 4-7b) dipping out the slope may be related to discontinuity set J1 (34◦/320◦); The sub-vertical cracks T2 are likely to be associated with discontinuity J2 (87°/336◦); Northeast-southwest striking cracks T3 that dip into the slope appear to be developed along discontinuity set J3 (64◦/143◦); Sub-vertical and north-south striking cracks T4 (Fig. 4-7c) are related to set J4 (87◦/69◦).

4.2.5. Slope zone subdivision

The RS survey was used to subdivide the slope into six zones (Fig. 4-8) for modelling purposes. Zone A-1 represents currently stable areas, covering most of the slope; Zone A-2 represents the triangular rock prism forming the cliff geometry on the northern side of the inlet; the first landslide occurred in zone A-3; the second landslide occurred in zone A-4; zone A-5 represents the currently unstable blocks in which tension cracks are detected and Zone A-6 forms the region associated with the formation of the inlet. The formation of the inlet provides the kinematic freedom for the first landslide episode in zone A-3. Instability associated with zones A-3 and A-4 result in tension crack development in zone A-5.

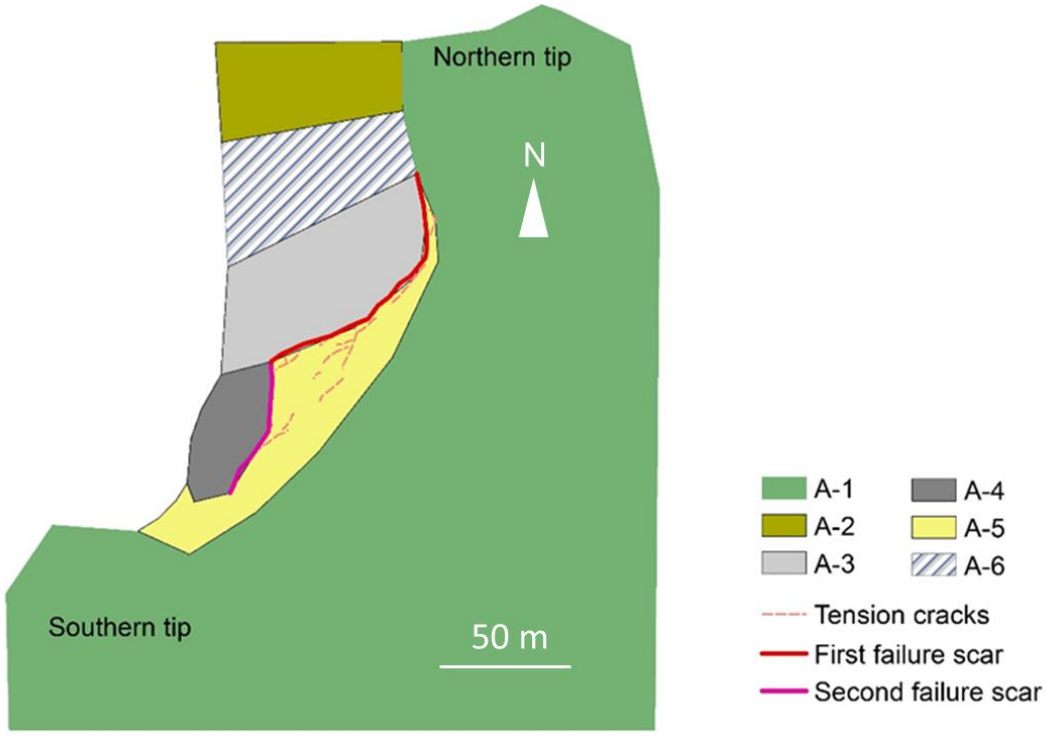

Fig. 4-8. *Plan view showing subdivision of the slope into six zones, including A-1 for currently stable area, A-2 for the triangular rock prism, A-3 for the first landslide area, A-4 for the second landslide*

area, A-5 for the currently unstable area, and A-6 for the inlet.

4.3. Numerical modelling

To analyse the slope instability of a jointed rock mass, a 3D DEM method assuming elastic-perfectly plastic joints was used for the modelling. Validation of the model was undertaken comparing the modelling results (e.g., tension cracks, landslide scars and rock mass damage) with corresponding observations from field surveys.

4.3.1. Model geometry and properties

The construction of two models

Three-dimensional models that consist of discrete and interconnected triangular meshes were constructed for the numerical modelling analysis by using Rhino software (Robert McNeel & Associates, 2012). The construction process for the models are presented as follows.

1) As shown in Fig. 4-9a, a point cloud (year 2008) was acquired from the open-source Channel Coastal Observatory (CCO) (Channel Coastal Observatory, 2020) to provide the slope geometry after the inlet formation and prior to the Hell's Mouth landslide.

2) Fig. 4-9b-d show the construction of a 3D meshed model from a point cloud. Fig. 4-9e presents the geometry of the modelled slope formed before the occurrence of the Hell's Mouth landslide and after the formation of the inlet for the numerical analysis of two landslide episodes

3) To assess the evolution of the inlet and its influence on proximal slope stability, a second model was constructed. This was performed by manually plotting the complementary section in zone A-6 (Fig. 4-9f), to represent the slope prior to inlet formation.

The two generated models (Fig. 4-9e and f) are defined by a global Cartesian coordinate system, where the X axis refers to the east, Y axis indicates the north direction, and Z axis coincides with the vertical direction. A fixed boundary condition

was applied to the base, east wall, west wall, and south wall of the model, whilst the north surface was kinematically free to allow simulation of landsliding. Boundaries were extended from the zone the of interest to ensure no boundary effects (model was 250m * 270m * 70m). During the modelling any detached blocks could freely drop so as not to allow accumulation at the base of the slope (to simulate the removal of blocks by wave action).

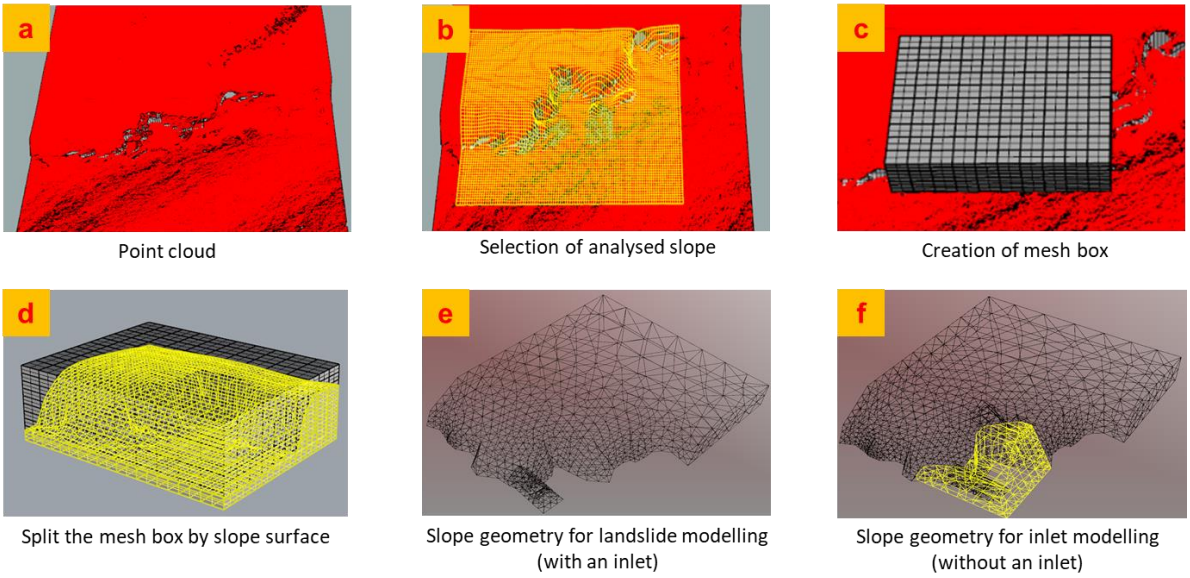

Fig. 4-9*. Construction of three-dimensional models of analysed slope, a) the point cloud of the coast in year 2008, b) the selection of the analysed slope, c) creation of a mesh box covering the extent of the slope, d) splitting the meshed slope model from the entire coast, e) the model for the simulation of two episodes of the Hell's Mouth landslide and f) the model for the simulation of inlet formation.*

Two observed sub-vertical faults (F2 and F3), shown in Fig. 4-4, were plotted crossing through the model to act as release surfaces constraining the geometry of the inlet. In addition, five previously identified discontinuity sets were also created in the model with their retrospective orientations, spacing and persistence.

Model setting

As previously indicated, the 3D DEM code 3DEC (Itasca Consulting Group, Inc., 2017) was used for numerical analysis. The code uses an explicit time-stepping system to solve equations of motion, simulating the response of rock mass that is subject to either static or dynamic loading (Itasca Consulting Group Inc., 2017). Individual blocks can behave as rigid or deformable, depending on specific situations. In this paper, rigid blocks were assumed as the analysed slope is

representative of a relatively stiff rock mass. The joint constitutive model used for the modelling adopted elastic-plastic contact mechanics through the Mohr-Coulomb slip failure criterion.

During application of in-situ stresses in the slope, the model was brought to initial equilibrium by applying high friction angle values to discontinuities. Under these conditions, the in-situ vertical stress at each point can be calculated from the weight of overlying material. The horizontal stresses were proportional to that of the vertical. The mechanical behaviour of the slope was simulated following equilibrium by reducing the discontinuity friction angle to the values provided in Table 4-2. An adaptive global damping strategy was applied at the first stage so that the model was able to reach a force equilibrium state as quickly as possible, by adjusting the viscosity such that the power absorbed by damping is a constant proportion of the rate of change of kinetic energy in the system (Hart et al., 1988). However, global damping was not considered appropriate for all localized case studies associated with DEM modelling to solve static solutions (Itasca Consulting Group, Inc., 2017). Therefore, a local damping mode was adopted after the model was brought to equilibrium for the slope failure analysis.

Table 4-2 provide discontinuity properties assumed for the model. Where possible, field data was used to determine the material parameters. This was supported with data from related publications and previous work (Hobbs et al., 2002; Vanneschi et al., 2019). Note that persistence used in 3DEC refers the probability that any given block lying in the path of a joint will be split on average (i.e., if persistence = 50%, then 50% of the blocks will be split) (Itasca Consulting Group Inc., 2017). Lower shear strength and material properties were assigned to the faults, compared with joints, i.e., lower cohesion and friction angle values. A higher value of cohesion was assumed for J1 during inlet formation to ensure the representative cliff geometry was established prior to modelling of the landslide. A reduced cohesion (0 MPa) was used to simulate strength deterioration potentially caused by weathering (Martin et al., 2011; Mousavi et al., 2019), rock bridge failure (Kemeny, 2003) and time-dependent deterioration (Aydan et al., 2012).

***Table 4-2**. Properties of discontinuities applied in 3DEC modelling, including geometry parameters (spacing and persistence) and deformation/strength parameters (normal stiffness, shear stiffness, friction angle and cohesion).*

Discontinuity		Spacing (m)	Persistence (%)	Normal stiffness (MPa/m)	Shear stiffness (MPa/m)	Friction angle (°)	Cohesion (MPa)
Joint sets	S0	5	80	100	10	30	1/0
	J1		50			32	
	J2		80			30	
	J3					32	
	J4					30	
Faults	F2	(none)	100			20	0
	F3						

4.3.2. Model simulations

Inlet formation

The model as previously shown in Fig. 4-9f was used for modelling the inlet formation. To simulate the impact of block removal through toe erosion on the inlet formation and investigate the influence of the progressive development of the inlet on adjacent slope stability, two modelling strategies were implemented.

1) Method 1: toe erosion characterized by the removal of rock blocks at the toe of the slope was carried out to investigate its effect on the stability of overlying rock mass. The sequence of the toe removal is presented in Fig. 4-10a.
2) Method 2: a simplified progression of the inlet, as shown in Fig. 4-10b was conducted to investigate its influence on the proximal slope stability. In the modelling, the gradual progressive formation of the inlet was simulated by sequential removal of rock blocks 1, 2, and 3, respectively.

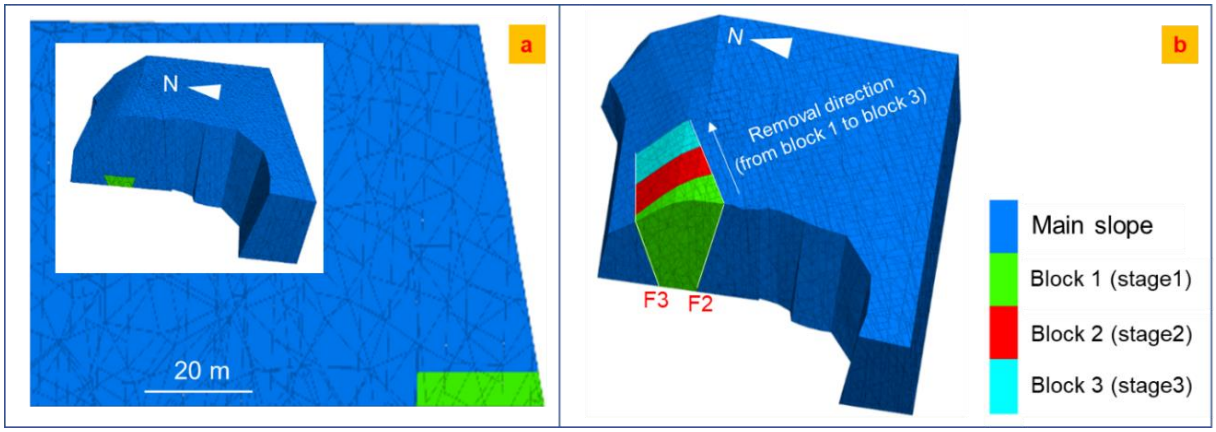

Fig. 4-10. *Different strategies for modelling the inlet formation: a) Method 1 for investigating the effect of toe erosion on the stability of overlying rock blocks, b) method 2 for investigating the effect of sequential removal of inlet blocks on the stability of adjacent zones.*

Landslide development and tension crack formation

The formation of the inlet provided daylighting conditions for discontinuities exposed on the inlet sidewalls. A three-dimensional model generated from LiDAR point cloud data (year 2008) was applied (as shown in Fig. 4-9e) to restore the pre-landslide geometry of the slope. The two 2011 failure episodes were then modelled in a single simulation. The modelling results were then compared with observations of tension crack formation and scar location/extent resulting from the two failures. These observations were taken from remote sensing survey data and aerial photographs of the site location. Cross sections through the 3DEC model were taken to monitor the modelled tension crack development, providing a comparison between the simulated tension cracks and the observed tension cracks behind the cliff with respect to their orientations and locations. The model results were then used to investigate the failure mechanism of the two landslides through the evaluation of cross sections taken through the 3DEC model in different directions.

In addition, further insight into the potential opening of a modelled tension crack developed upon a J3 plane (64°/143°) is provided by using the differential displacement analysis of two adjoining rock blocks. The displacements of two blocks in the X, Y, Z direction provides a basis to analyse the movement directions of the blocks, characterized by mean plunge and azimuth of block displacements in the model every 1000 calculation timesteps.

4.3.3. Sensitivity analysis

Francioni et al. (2018a) identified five discontinuity sets within the rock mass which exhibit data dispersion of orientations (Fig. 4-3). A sensitivity analysis was carried out to assess the potential impact of variations in orientation of key discontinuities on slope behaviour. Considering that the two landslide episodes were principally controlled by J1 (Francioni et al., 2018a), this was selected as the critical discontinuity for further sensitivity analysis.

Table 4-3. *Variations in dip, dip direction, persistence, friction angle of J1 set that were characterized by mean, minimum and maximum values.*

J1 property	Mean value	Minimum	Maximum
Dip (°)	34	24	44
Dip direction (°)	320	300	340
Persistence (%)	50	30	70
Friction angle (°)	32	22	42

The sensitivity analysis concentrated on dip, dip direction, persistence, and friction angle of joint set J1. Variations in these parameters were characterized by mean value, minimum and maximum, as shown in Table 4-3. A series of models were undertaken using a control variate method by which each discontinuity parameter is individually and sequentially varied (Vanneschi et al., 2019), to investigate the effects of variation of each parameter alone by the comparison of the related modelling results. For each analysed parameter, a sensitivity analysis was conducted by varying its value from the minimum, the mean, to the maximum and analysing the effect of this change.

4.4. Results

4.4.1. Simulation of toe erosion and inlet formation

With respect to modelling method 1, for investigating the influence of block removal and potential wave erosion, the results presented in Fig. 4-11 show that toe removal causes the collapse of overlying blocks. This is constrained by the F2, F3 and joints in set J4, which act as lateral (F2 and F3) and rear (J4) release surfaces, respectively. In addition, minor planar failures are observed in the proximity of the inlet in zone A-2, sliding along J1 planes resulting from kinematic release associated with the newly formed inlet face and daylighting features.

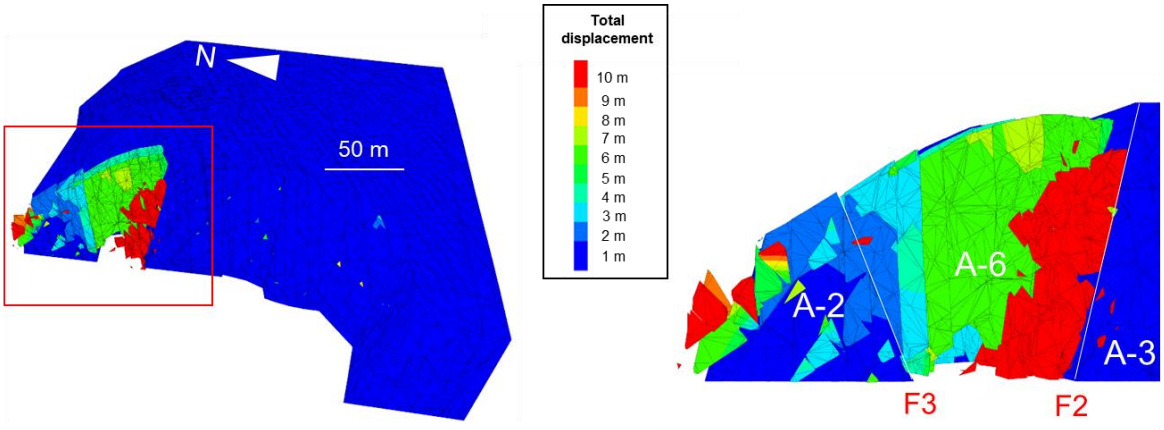

Fig. 4-11. *Results of modelling method 1, showing total displacements developed in the vicinity of the inlet caused by wave erosion.*

Regarding modelling method 2, for understanding influences of the progressive inlet formation on proximal slopes, the results presented in Fig. 4-12 indicate that the removal of the three blocks leads to progressive displacement of the proximal blocks in zone A-3, directly adjacent to the inlet sidewalls. Displacements within the southern inlet sidewall are greater at the western edge of the inlet than those simulated at the eastern edge. This reflects the sequence of block removal and progressive formation of the inlet. In addition, minor displacements were also detected in the scarp of zone A-4, as well as in the southern scarp of zone A-2.

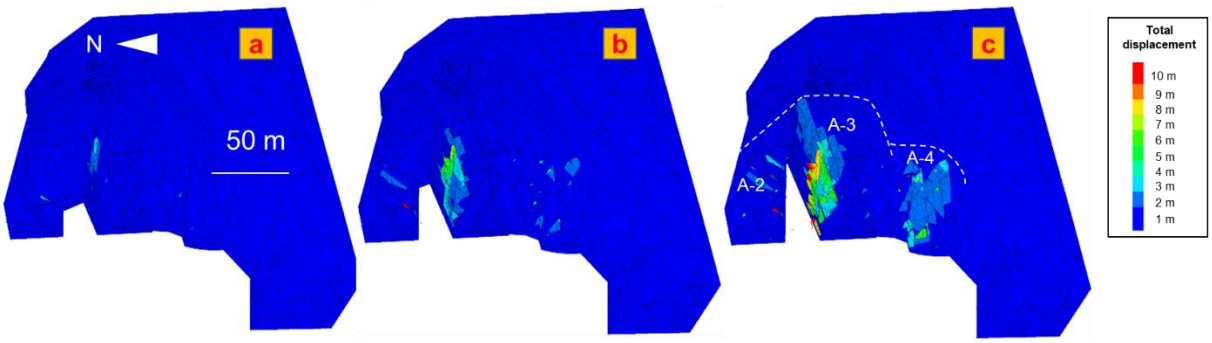

Fig. 4-12. *Results of modelling method 2, showing total displacements of blocks occurred in the three model stages: a) stage 1; b) stage 2: c) stage 3.*

4.4.2. Simulation of the two landslides

The results for the modelled landslides at timestep 5000 are presented in Fig. 4-13 and highlight two regions of increased deformation for both the northern and western faces of the cliff. Major displacements occur within zone A-3 and A-4 (representing the two landslide episodes) with minor displacements in zone A-5 (the region of current tension crack development). The scars for both landslide events and the observed field tension crack development are superimposed on the modelling results shown in Fig. 4-13a. A good agreement can be observed between the modelled results and field observations. Vectors of block resultant displacement are presented in Fig. 4-13b, which confirms that displacements in zone A-3 and A-4 are greater than that in zone A-5, with all three regions showing a general displacement trend towards the northwest.

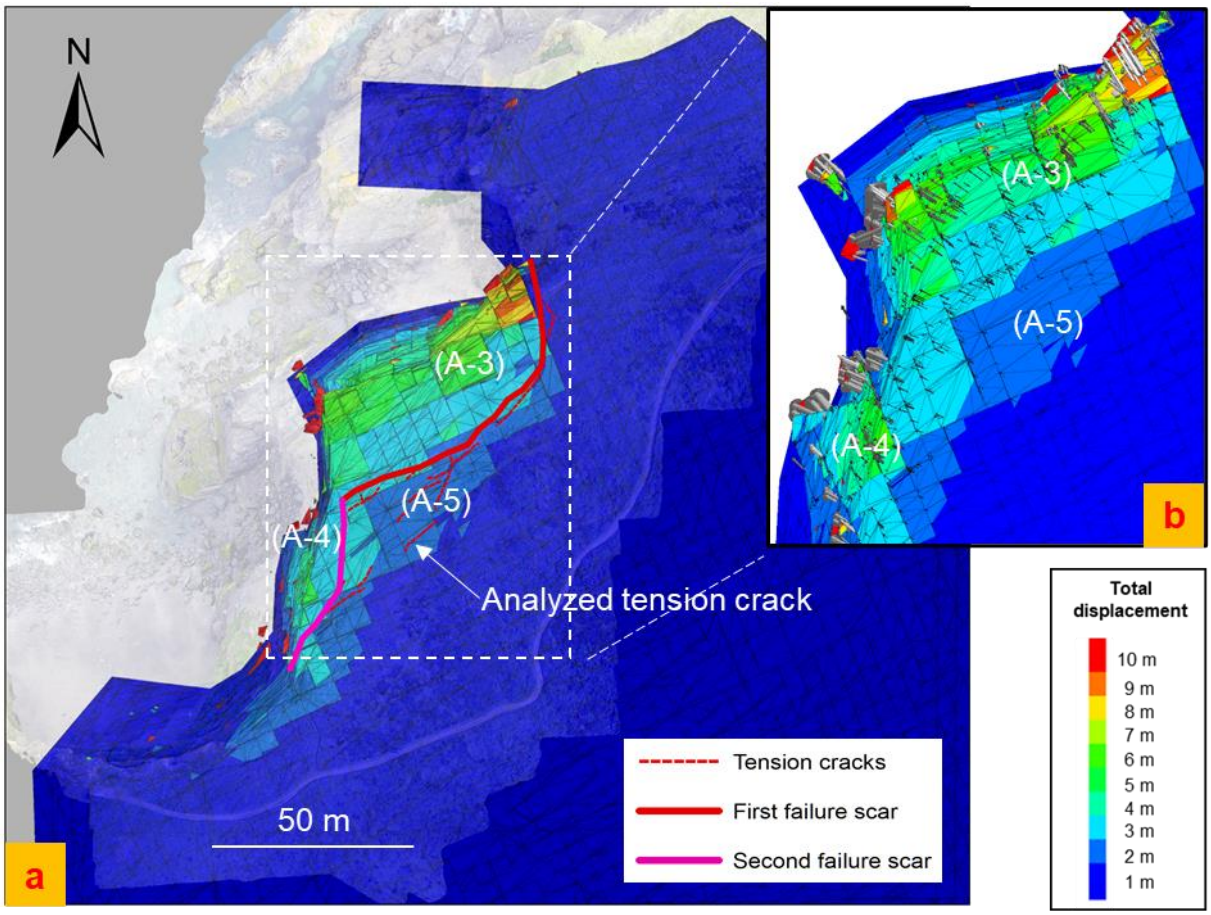

Fig. 4-13. *3DEC modelling results: a) Plan view showing comparison of modelled total displacement contours with field observations of landslide scars and tension crack development behind the crest of the cliff; b) Plan view of modelled total displacement contours with displacement vectors included.*

In order to provide further understanding of the modelled block interaction and landslide development, cross sections were taken through the 3DEC model in different directions. For the first landslide location, a north-south and an east-west cutting plane were created, as depicted in Fig. 4-14. This shows the total displacement of blocks along the selected cross sections. Fig. 4-14a provides a north-south cross-section that highlights the controlling influence of discontinuity set J1 which dips out of the face and forms a potential basal sliding plane. Increased deformation towards the top of the cross-section suggests the potential influence of toppling which is controlled by the aspect ratio of rock columns formed by discontinuity sets J2, J3 and J4. Fig. 4-14b provides an east-west cross-section and shows the development of an active-passive wedge at the base of the slope and further potential for toppling. These observations support the findings from the video-frame analysis described in section 4.2.3. The video was taken from the adjacent cliff

looking towards north-east, so Fig. 4-14b and Fig. 4-15a provide the closest matching views. Both Figs. 4-14a and b show potential tension crack opening behind the modelled slope crest, with the specific discontinuity orientations highlighted. Note the label ‘T’ is used to depict a tension crack formed from a particular discontinuity orientation (i.e., T1 associated with J1 etc.)

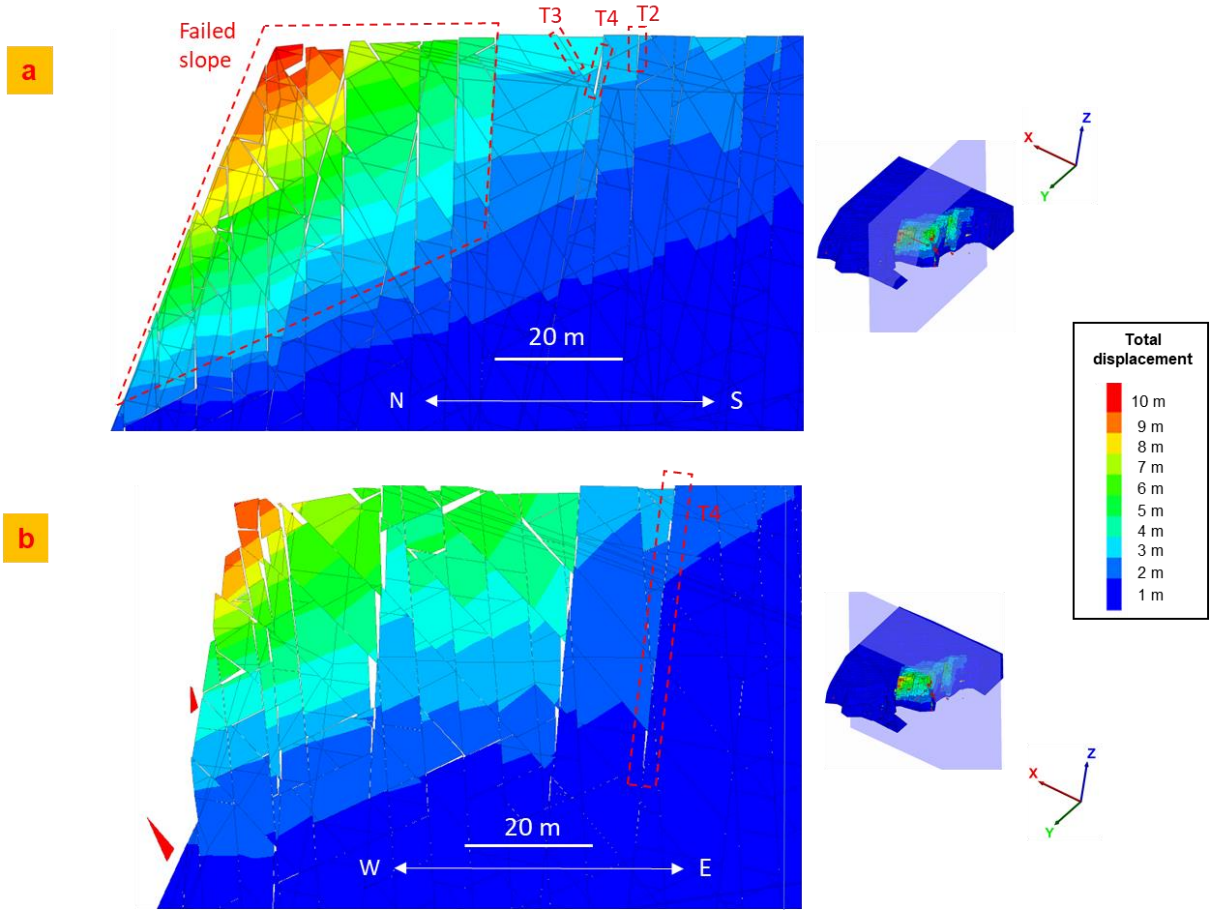

Fig. 4-14. *Cross sections of 3DEC analysis for the region of the first landslide episode showing the total displacement of blocks: a) north-south, b) east-west.*

Fig. 4-15 shows cross sections taken through the 3DEC model in the area of the second landslide. Again, the influence of potential basal features and toppling can be observed, particularly in Fig. 4-15a, where the active passive wedge and toppling observed in the video-frame analysis is replicated.

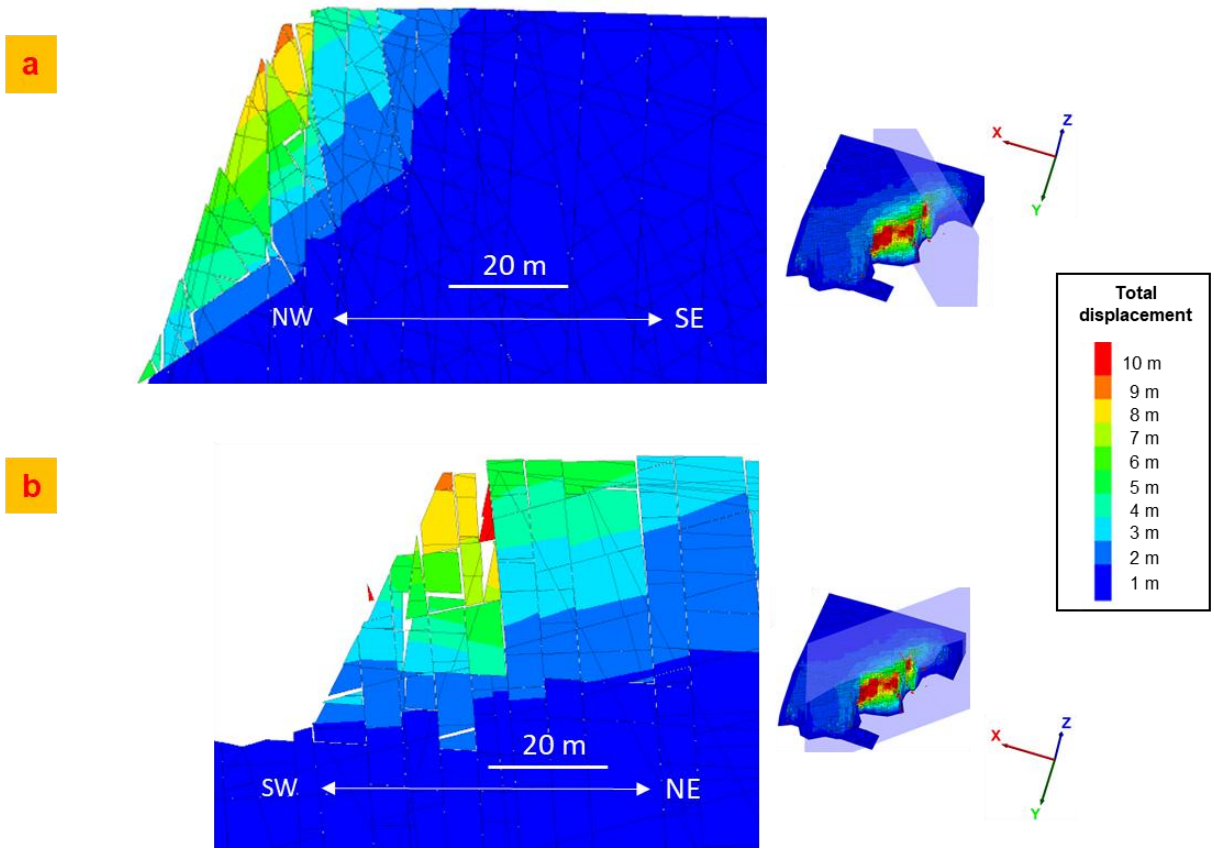

Fig. 4-15. *Cross sections of 3DEC analysis for the region of the second landslide episode showing the total displacement of blocks: a) northwest-southeast, b) northeast-southwest.*

4.4.3. Opening of tension cracks

The opening of internal joints within the model slope has been investigated, by identifying joint opening on the north-south cross-section shown in Fig. 4-14a for different calculation time steps using the software Fiji (ImageJ based) (Schindelin et al., 2012). It can be seen from Fig. 4-16 that opening of joints in the unstable zone (A-5) is less noticeable than that in the failure zone (A-3), which is more obvious in Fig. 4-16c and d. The analysis allows quantification of opening of modelled joints.

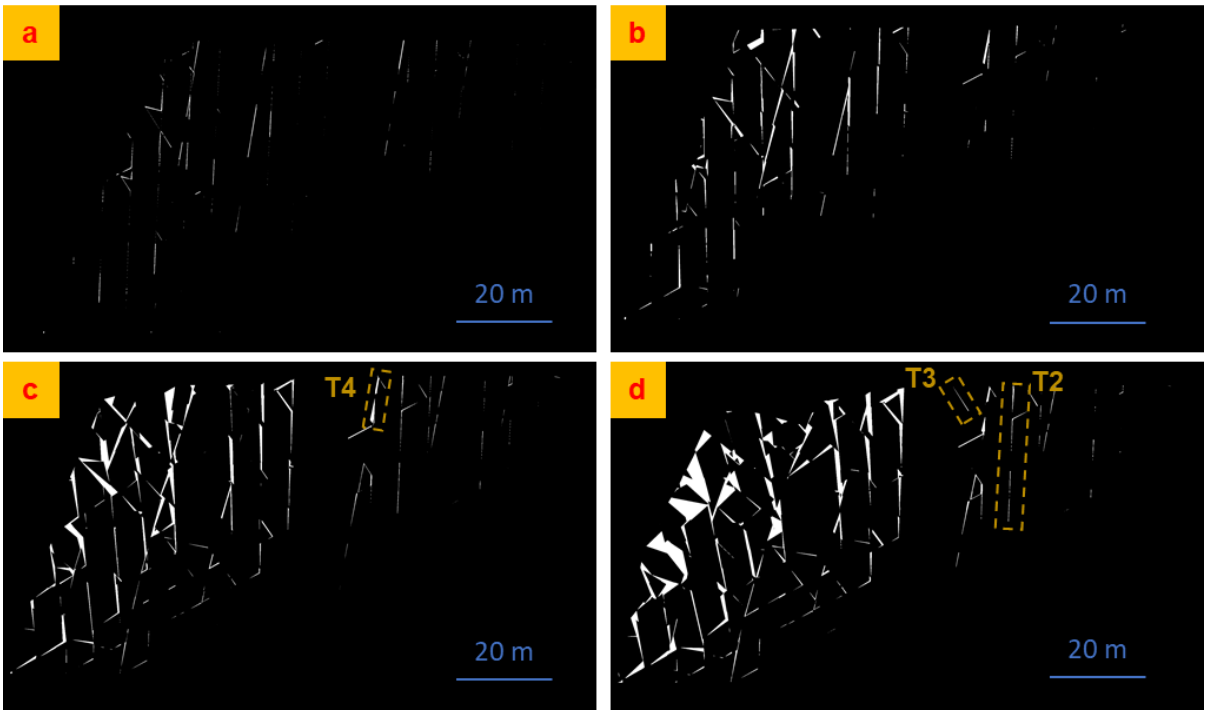

Fig. 4-16. *Identified joint opening (joint-cracks) on the north-south cross section (shown in Fig. 13a) at different timesteps, a) timestep 1000, b) timestep 5000, c) timestep 9000, d) timestep 13000.*

A north-south cross-section (presented in Fig. 4-13a, Fig. 4-14a and Fig. 4-16d) of the tension crack, T3, have been recorded at steps 6000, 11000, and 14000 to provide the visualization of the tension crack development (Fig. 4-17). In Fig. 4-17b ground depression is observed with relatively lowering of block 2.

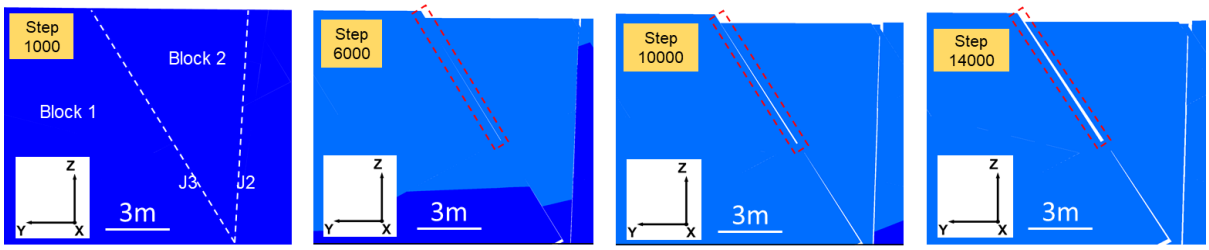

Fig. 4-17. *North-south cross sections through the 3DEC model at different calculation timesteps, showing the development of a tension crack associated with opening along a J3 plane and relatively lowering of the block 2.*

The lowering of blocks behind the crest of the cliff is also observed in the field, as shown in Fig. 4-18, which shows recent photographs taken of the region of tension cracks formed behind the crest of the cliff section.

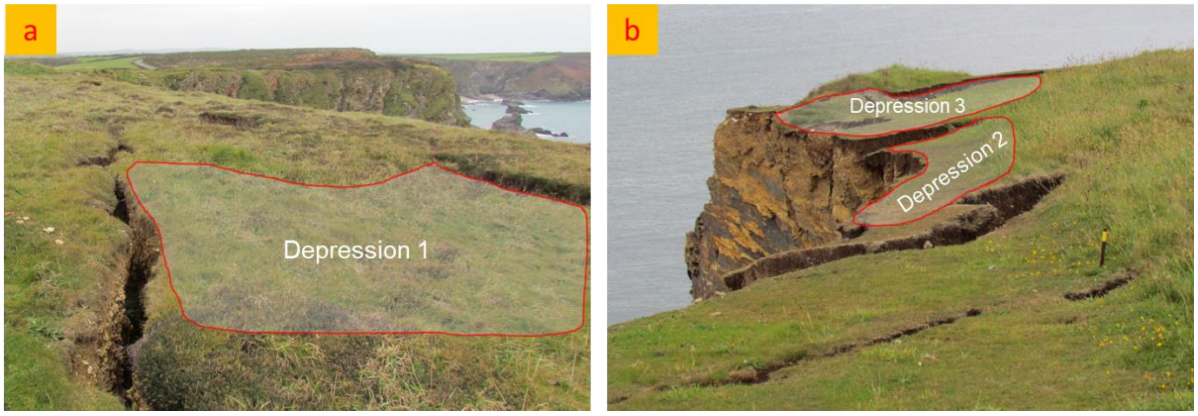

Fig. 4-18. *Depressions occurred along with the opening of tension cracks in the unstable slope. a) An image looking towards west, b) an image looking towards north.*

In order to analyze movement of the modelled joints or cracks, T3 is used to record the displacements of the two adjoining rock blocks. A differential displacement behavior in X, Y, Z directions can be observed between blocks 1 and 2. Specifically, during the development of the joint-controlled tension crack,T3, block 1 is displaced preceding block 2 in X and Y directions with gradually increased opening (Figs. 4-19a and b). However, with respect to the Z direcion, more displacement of block 2 is observed (Fig. 4-19c).

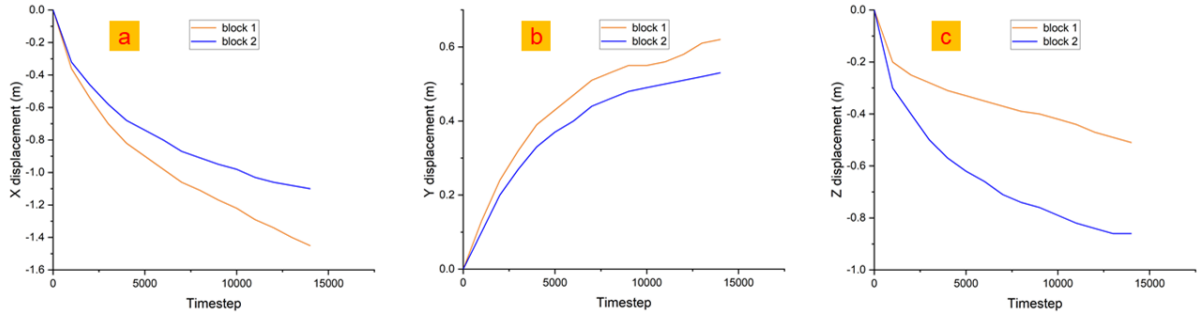

Fig. 4-19. *Displacement curves of block 1 (orange lines) and 2 (blue lines): a) block displacements in X direction, b) block displacements in Y direction, c) block displacements in Z direction.*

Displacement directions of the two blocks can be assessed by mean plunge angles and azimuth angles for every 1000 calculation timesteps (Fig. 4-20). The azimuth curves fluctuate between 270° and 310° (Fig. 4-20a), lower than the landslide sliding direction (320°) controlled by J1, as well as the toppling direction (323°) controlled by J3 (as indicated in Fig. 4-2). In general, the plunge of block 2 is greater than that of block 1, resulting from significantly more z-direction displacement (Fig. 4-20b). The

plunge of block 2 is zero at step 14000, as a result of no displacement of block 2 in the Z direction at that time.

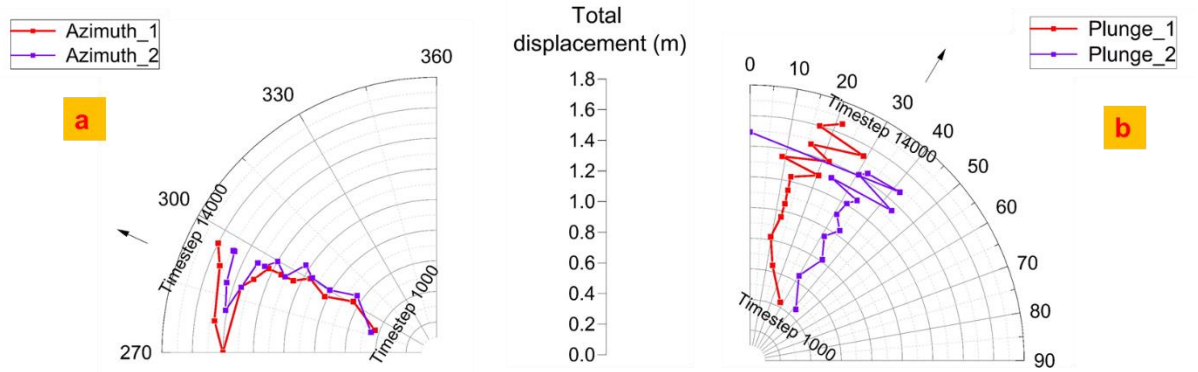

***Fig. 4-20**. Hodographs of mean movement directions of the two blocks with block total displacement in each 1000 timesteps: a) the azimuth of the trajectory; b) the plunge of the trajectory.*

4.4.4. Sensitivity analysis for J1

Fig. 4-21 shows the influence of variation in the dip of J1 on the modelled results in plan view. When the dip of J1 is reduced to 24° from its original value (34°), less displacement and reduced extent of slope deformation is observed. As expected, greater deformation and a larger region of instability is formed when the dip of J1 is increased to 44°.

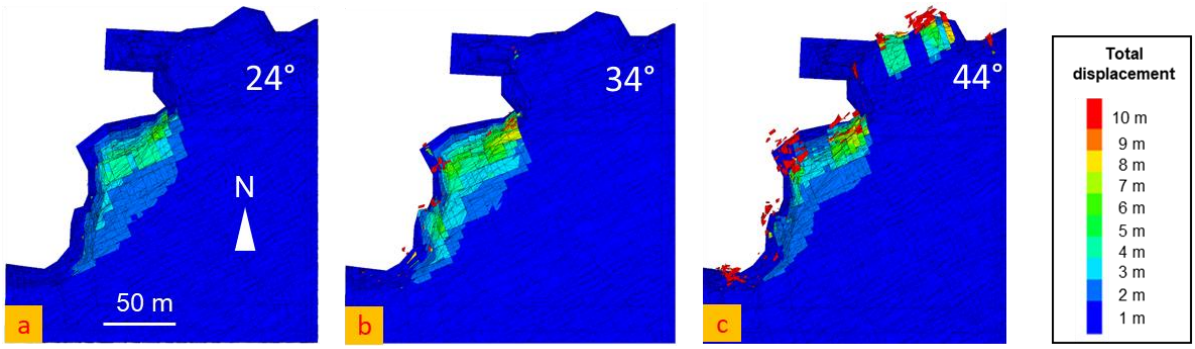

***Fig. 4-21.** Sensitivity analysis of J1 dip angle by varying from 24° to 44° in plan view, a) 24°, b) 34° and c) 44°.*

The results shown in Fig. 4-22 clearly show the influence of dip direction of J1 on the slope stability. When the dip direction is reduced to 300°, modelling shows that west-dipping slopes in zone A-2 and A-3 are more prone to failure. Whereas an increase in the dip direction causes more potential for north-dipping slopes, particularly at the eastern tip of the inlet to become unstable. This is also reflected in stereonet plots

that when the dip direction of J1 varies from 300° to 340°, the displacement directions of potential instabilities, caused by J1 set or its interaction with other sets, generally change from west to a more northerly direction (as depicted in Fig. 4-23).

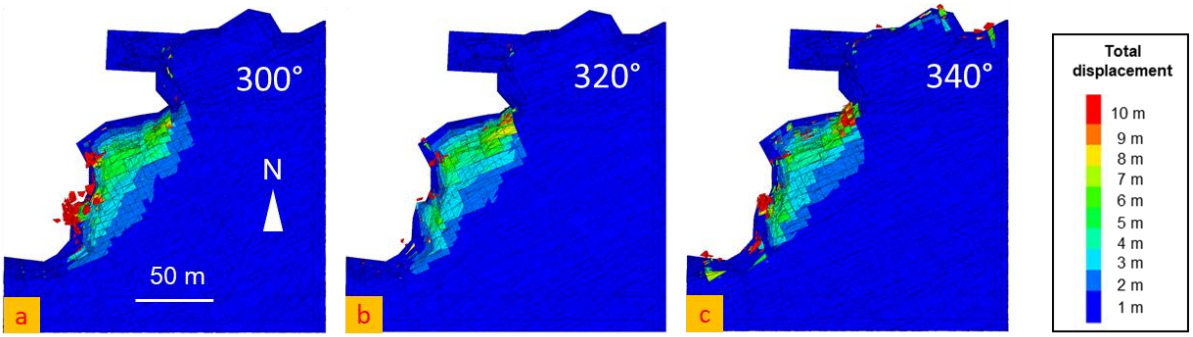

Fig. 4-22. *Sensitivity analysis of J1 dip direction by varying from 300° to 340° in plan view, a) 300°, b) 320° and c) 340°.*

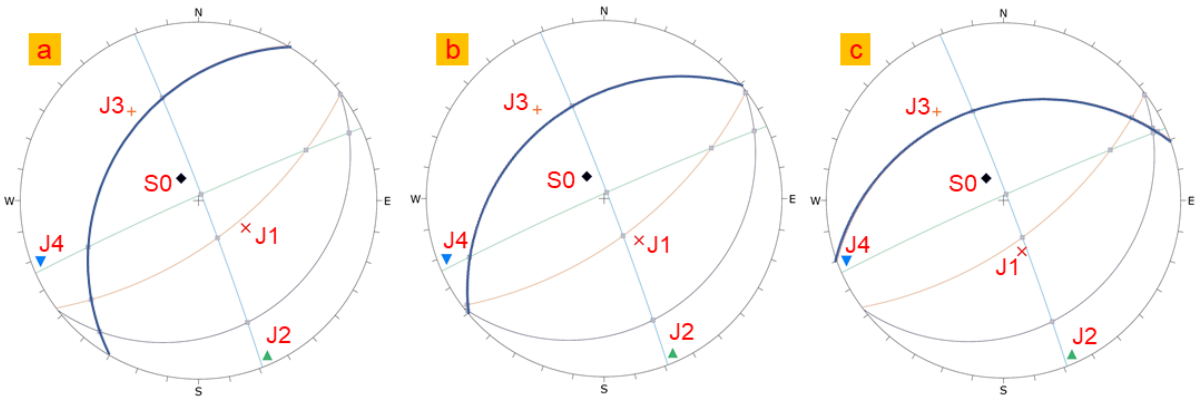

Fig. 4-23. *Stereonet plots showing orientations of joint sets and intersections with variations in J1 dip direction from a) 300°, b) 320°, c) 340°.*

The effect of persistence is presented in Fig. 4-24. This indicates that the persistence has a critical influence on the extent of potential instability. An increase in discontinuity persistence from 30% to 70% results in the enlargement of the failed zone, particularly at the eastern end of the north-dipping slope and more deformation/influence in the region of the second landslide event on the west-dipping slope.

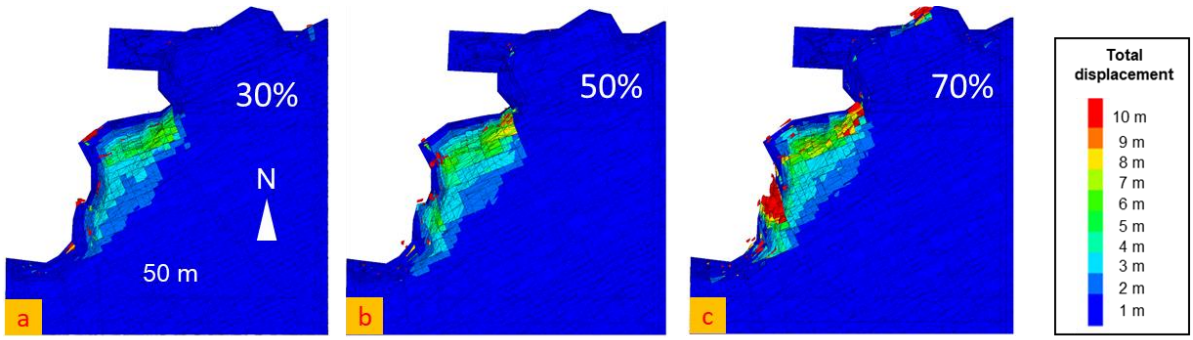

Fig. 4-24. *Sensitivity analysis of J1 persistence by varying from 30% to 70% in plan view, a) 30%, b) 50% and c) 70%.*

When evaluating the influence of modelled friction angle, the extent of the first and second landslide appear not to be significantly influenced by variations of friction angle. However, as would be expected, when the friction angle is decreased from 32° to 22°, the total displacement of the unstable rock blocks rises, which is shown in Fig. 4-25.

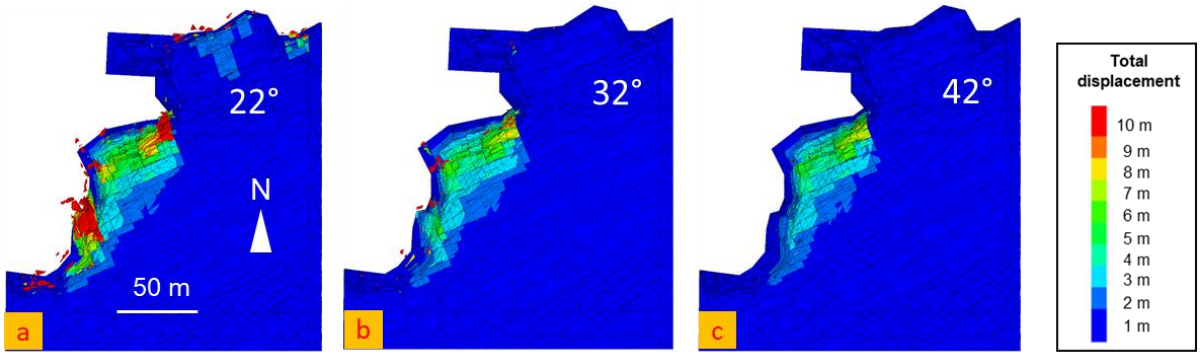

Fig. 4-25. *Sensitivity analysis of J1 friction angle by varying from 22° to 42° in plan view, a) 22°, b) 32° and c) 42°.*

4.5. Discussion and Conclusions

This case study presents the results of a back analysis of a landslide that occurred at Hell's Mouth on the north coast of Cornwall, to provide further understanding of the coastal cliff erosion processes and the kinematics of the slope failure mechanisms involved. The landslide occurred as two separate events over a three-month period. In view of the discontinuity-controlled nature of the failures 3DEC modelling was undertaken. Modelling included the evolution and formation of an inlet, and the influence of discontinuities on potential landslide failure mechanisms and tension crack development behind the crest of the slope. A video recording of the initial failure was used to constrain the interpretation of the modelled results. Due to potential variations of discontinuity properties associated with the potential basal plane associated with planar sliding, wedge sliding and topping failure, a series of sensitivity analyses were undertaken to investigate the effects of these uncertainties on slope stability analysis. The key conclusions arising from the study are:

1) The simulation of inlet formation shows that block removal (from wave erosion) would result in sequential instability of overlying blocks confined by two sub-vertical faults, consequently forming the inlet. During progressive inlet formation, modelling shows the potential for daylighting features in the newly exposed inlet sides to form, resulting in potential for discontinuity related instability from the southern inlet sidewall.
2) Numerical modelling of the landslide events highlights the controlling influence of the potential basal feature (J1), which is also influenced by lateral release surfaces associated with J2 and rear release surfaces associated with J4. J3 may also contribute to toppling failures.
3) The sequence of events captured in the video taken during the initial failure are effectively reproduced by the 3DEC model. This includes the development of an active-passive wedge near the base of the slope, together with evidence of wedge and toppling failure.
4) 3DEC modelling was also able to effectively capture the opening of tension cracks on pre-existing discontinuities behind the crest of the slope. Modelled tension crack formation was detected behind the crest of the landslide zones. Cross-sections taken through the 3DEC model strongly suggests that the

observed tension cracks formed along pre-existing discontinuities. The tension cracks appear to be primarily associated with more steeply inclined discontinuities (J2, J3, J4) with visible daylighting on the slope surface.

5) Sensitivity analysis highlighted the importance of fracture network orientations relative to slope geometry on potential landslide failure mechanisms with respect to the size and spatial distribution. The sensitivity analysis also highlighted the effect of dip, dip direction and persistence of the basal feature on the extent and spatial distribution of potential slope instability.
6) Use of a hodographic interpretation of block displacements in association with stereographs can aid in interpreting complex rock slope failure mechanisms.

Chapter 5. Modelling the influence of geological structures in paleo rock avalanche failures using field and remote sensing data (adapted from the paper (He et al., 2022))

5.1. Introduction

Catastrophic rock avalanche can involve rock failures of million cubic meters in size (Geertsema et al., 2006; Runqiu, 2009; Singeisen et al., 2020), that lead to high velocity flows of fragmented rocks with the release of enormous energy that can be highly destructive (Zhuang et al., 2019; Gao et al., 2020). In addition, rock avalanche may cause indirect hazards related to their debris flow deposition (e.g., upstream flooding induced by river obstruction) (Allen et al., 2016; Pandey et al., 2022). Unfavourably oriented discontinuities are deemed to be one of the critical preconditioning factors for rock avalanches (Hutchinson, 1989; Nicoletti et al., 1993; Agliardi et al., 2001; Bianchi-Fasani et al., 2011; Della Seta et al., 2017). It has been found that catastrophic rock avalanches are usually related to the presence of large and persistent discontinuities (e.g., faults and bedding), which is emphasized by the cases of translational sliding (Borrelli and Gullà, 2017; Mihalić Arbanas et al., 2017), wedge sliding (Chigira et al., 2013), and toppling failures (Nichol et al., 2002). The influence of the local fracture network has also been observed in catastrophic landslides, contributing to the disintegration of the failed rock mass and the formation of release surfaces (Fan et al., 2019; Donati et al., 2021a).

For rock slide analysis, the interpretation of on-site discontinuity orientation and persistence is critical as it can provide the basis for rock mass characterization, estimation of rock mass properties, and the prediction of possible failure mechanisms (Goodman, 1980). Discontinuity characterisation has been conventionally performed through traditional manual surveys used to collect important information on discontinuity geometry, orientation and strength properties (Hoek and Bray, 1981). However, the use of traditional surveys is limited in hazardous or inaccessible sites (e.g., coastal cliffs, unstable slopes, and steep slopes). Recent advancements in remote sensing (RS) techniques can provide 3D topographic mapping of outcrops at these sites, thus allowing remote discontinuity detection. These include utilization of aerial/terrestrial light detection and ranging

(LiDAR) mapping to directly acquire a 3D point cloud (or TIN mesh) of an outcropping rock mass (Jaboyedoff et al., 2012). Digital photogrammetry can also be deployed to acquire a series of stereo images to construct 3D topography of outcrops by using a structure-from-motion (SfM) algorithm (Martino and Mazzanti, 2014; Kong et al., 2021a). The application of optical sensors mounted on unmanned aerial vehicles (UAV) for digital photogrammetry, termed UAV remote sensing (UAV-RS), becomes a low-cost, lightweight, time-saving, and user-friendly option to map rocky outcrops where discontinuities daylight (Kong et al., 2021a).

Following the interpretation of on-site discontinuities, stability analysis can then be undertaken. Initial evaluation of potential instability is typically undertaken through kinematic analysis to predict potential failure modes of discontinuous rock slopes. The inclusion of internal (weight) and/or external stresses (e.g., pore-water pressure), can be undertaken using 2D and/or 3D limit equilibrium (LE) analysis to evaluate the factor of safety (FoS) of a rock block that is constrained by a simple geometrical representation of the identified discontinuities (Kumar et al., 2018). Both kinematic and LE analysis can provide an initial estimation of the stability condition of a rock slope. However, they are not applicable for the analysis of slope displacement and other complex situations, e.g., anisotropic rocks, and complicated discontinuity networks (Stead and Wolter, 2015). Numerical modelling, especially based on discontinuum methods and hybrid methods, can be used to provide further insight into landslide failure mechanisms, particularly where the discrete fracture network has a controlling influence on potential failure (Kawamoto and Aydan, 1999). For example, discontinuum modelling has been preferentially employed to investigate the displacement and/or deformation of rock blocks (He et al., 2021b), and used for the analysis of rockfalls and the mobility or run-out of landslides as large displacements and rotation of blocks are allowed in the modelling (Bao et al., 2020; Mao et al., 2021).

It is therefore clear that rock mass characterization plays a key role in the analysis of rock failures. Another crucial aspect in such types of analyses is represented by the geological and evolutional model of the area. During numerical simulation the geological models are often simplified to facilitate the modelling process. However, the structural/geological model can play a key role in understanding of the evolution

of the rock avalanche failure mechanism (Hutchinson, 1989; Francioni et al., 2019).

In this context, this paper presents the representative case study of the Lettopalena rock avalanche to examine the influence of an anticline on a catastrophic translational landslide in sedimentary rocks. The Lettopalena rock avalanche occurred approximately 4.8 kyr BP (Scarascia-Mugnozza et al., 2006) and it is located in the Italian Apennines, where the influence of structural/tectonic features play a key role in the evolution/triggering of such large phenomena. The rock avalanche, which volume was estimated around $30x10^6$ m^3 (Bianchi Fasani et al., 2005), has been studied in the years by several authors who have analysed both the ancient rock avalanche mechanisms and evolution (Scarascia-Mugnozza et al., 2006; Bianchi Fasani et al., 2011) and the most recent rock fall events. In fact, several rockfalls event have been documented in recent decades (Paolucci et al., 2001) with the most recent one dated 2005 and estimated around 2000 m^3 by Bianchi-Fasani et al. (Bianchi Fasani et al., 2005). Such rockfalls events are mainly controlled by the unfavourable orientation of structural features (bedding and joints) and by water infiltration along discontinuities (Bianchi Fasani et al., 2005). Such minor events has to be studied in a more general context which involve the structural-morphotectonic evolution of the area which has led to failures varying from a few cubic meters to millions of cubic meters (such as the Lettopale rock avalanche (Scarascia-Mugnozza et al., 2006; Bianchi Fasani et al., 2011).

Scarascia-Mugnozza et al. (2006) performed a comprehensive study of morphological, structural and lithological constraints on the rock avalanche slope. A geological and numerical model of the rupture developed by the authors highlighted the key role of the pre-existing topography/geomorphic features and the high deformability of the out-cropping Mio-Pliocene formation.

Most recently, further studies in the area have been carried out by Bianchi Fasani et al. (2011), who developed a morpho-structural evolution model by the integration of detailed geological–structural and geomorphological surveys. Based on this model, the authors performed numerical simulations through Finite Difference Method (FEM) with the goal of evaluating the effect of the uplift-related morphological changes of the valley–slope system and the role of the horizontal/vertical stress ratio variations due to geodynamic regime shifts. The results presented by the authors confirmed the

presence of stress–strain conditions in the massive rock slope failures.

In this context, this research aims to integrate the existing studies with a different type of numerical simulation/model, carried out using discrete element method to highlight the role of the structural setting (bedding inclination) and potential river erosion in the Lettopalena rock avalanche. Various RS techniques (i.e., UAV-RS and satellite RS) have been combined to detect structural features and post-landslide features. Subsequent 2D modelling was employed to simulate, as mentioned above, the development of the landslide following river erosion at the toe of slope. The remotely captured data was used to constrain and validate the numerical modelling undertaken. It will be highlighted how the geological model and the interpretation of the geological-geostructural evolution of the area can play a key role in the results of rock avalanche numerical back analyses. The use of distinct element analysis, combined with previous FEM simulation (Scarascia-Mugnozza et al., 2006; Bianchi Fasani et al., 2011), can represent a further tool for landslide interpretation.

5.2. Study area description

The study area is located in the Central Apennines of Italy, at 40° 00'35''N 14° 09'56''E, on the NW side of Lettopalena in Chieti, at an altitude in the range of approximately 500 m a.s.l. to 1200 m a.s.l. (Fig. 5-1). The valley where the rock avalanche is sited is the Caramanico Valley, a north–south-oriented tectonic depression located on the SE of Monte Amaro and about 40 km west of the Adriatic Sea. The area is still monitored for potential instability due to the hazard posed to a village built up adjacent to landslide deposits and the section of a state road (SS84) constructed along the landslide scar. A recent landslide, which occurred on the 20th April 2005, that resulted in a 2000 m^3 rock block failure highlights the ongoing risk. The run-out from the failure blocked the SS84 state road, destroyed a private house along the route, and led to the death of one resident.

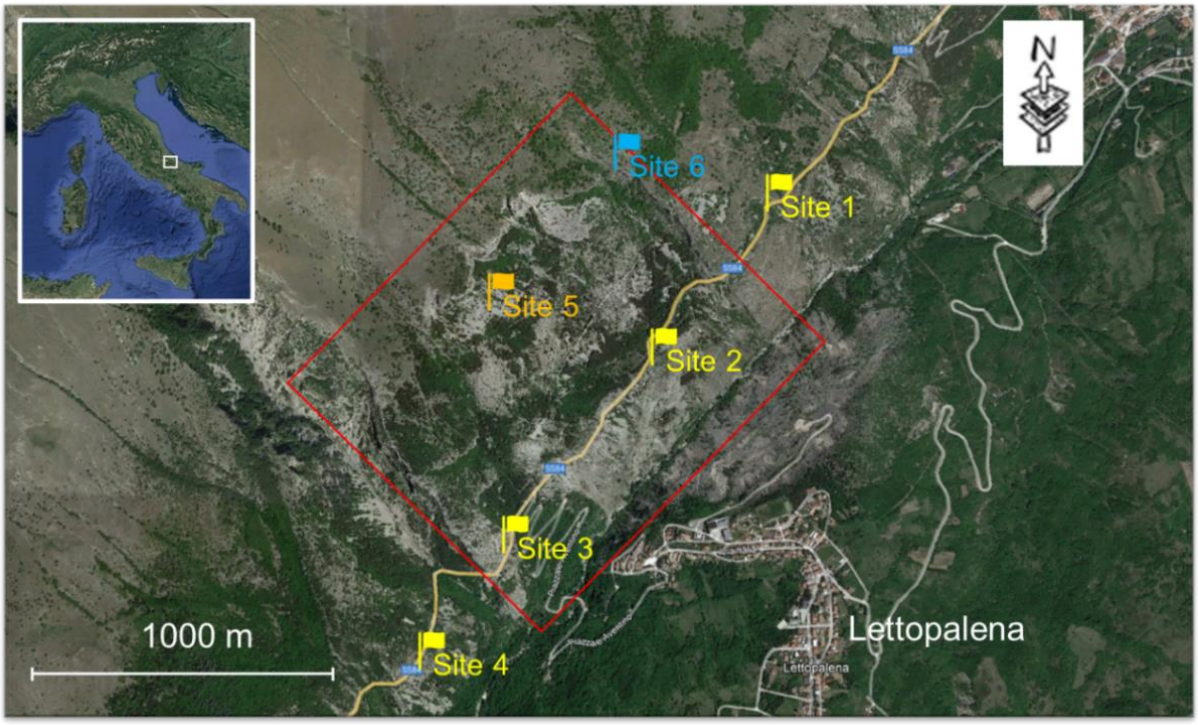

Fig. 5-1. *Location of the study area, showing the rough boundary of the analysed landslide (in red) and the sampling sites (site 1-4) of structural identification through traditional survey and UAV mapping, site 5 of structural identification using satellite map.*

5.2.1. Geological setting

Geologically, the study area is situated on the southeast side of the Majella anticline on a carbonate platform succession (Vecsei et al., 1999). The platform is characterized by a N–S oriented anticline with a steeply-dipping forelimb, and a thrust fault underlying the Majella unit at the E margin (Vecsei et al., 1999; Aydin et al., 2010). The sedimentary record of the platform comprises of a wide time interval from the Late Jurassic to the late Miocene (Vecsei et al., 1999). The undeformed platform was initially formed transecting approximately 20 km long to the adjacent northern basin, which was separated by a 1000-metre-high non-depositional escarpment trending E-W (Vecsei et al., 1999). During the Cretaceous period, basinal sedimentary rocks buried the escarpment causing the gradual decrease of the slope angle (Vecsei et al., 1999). At the end of the Campanian, the basin was almost filled, and the Maastrichtian sequences were deposited onto the platform, consequently forming a distally steepened ramp (Mutti et al., 1997; Vecsei et al., 1999; Brandano et al., 2016). A carbonate ramp, consisting of Bolognano formation, was subsequently developed overlying the shallow water deposits during the late Rupelian to early Messinian interval (Brandano et al., 2016). The schematic platform-basin cross section has been provided by (Vecsei et al., 1999).

On a local scale, a primary geological characteristic is the Molise unit overlying the younger Majella unit which was caused by overthrust faulting. The major component of the Molise unit is the Argille Policrome (APO) that is comprised of the alternation of pinkish-reddish to greenish marly claystone, chert, and calcilutite. The Majella unit, in the order of the depositional sequence from the bottom to top, is composed of Morrone di Pacentro Formation (MOR), Monte Acquaviva Formation (ACQ), Scaglia Formation (SCZ), Orfento Formation (OR), Santo Spirito Formation (FFS), Bolognano Formation (BOL), Gessoso-Solfifera Formation (GES), and Majella Flysch (MAJ) (Festa et al., 2014). The characteristics of these formations has been summarized in Table 5-1. In addition, Talus Deposits are distributed in the valleys adjacent to the analysed slope, consisting of well-sorted centimetres-to-decimetres sized rock fragments that are characterized by openwork to partially openwork texture (Festa et al., 2014). Fig. 5-2a shows the geological map of the area after Vezzani and Ghisetti (Vezzani and Ghisetti, 1998) and Miccadei et al. (Miccadei et al.,

2013). The base digital elevation data used in the map is the 10x10 meter resolution digital elevation data available from Abruzzo Region GIS portal (Abruzzo council, 2022). The slope profiles 1-4 in the geological map have been created to highlight landslide geometry. Profile 2 has been used to create the 2D geological section of Fig. 5-2b. Profiles 1,3 and 4 will be shown and discussed in section 5.4.1.

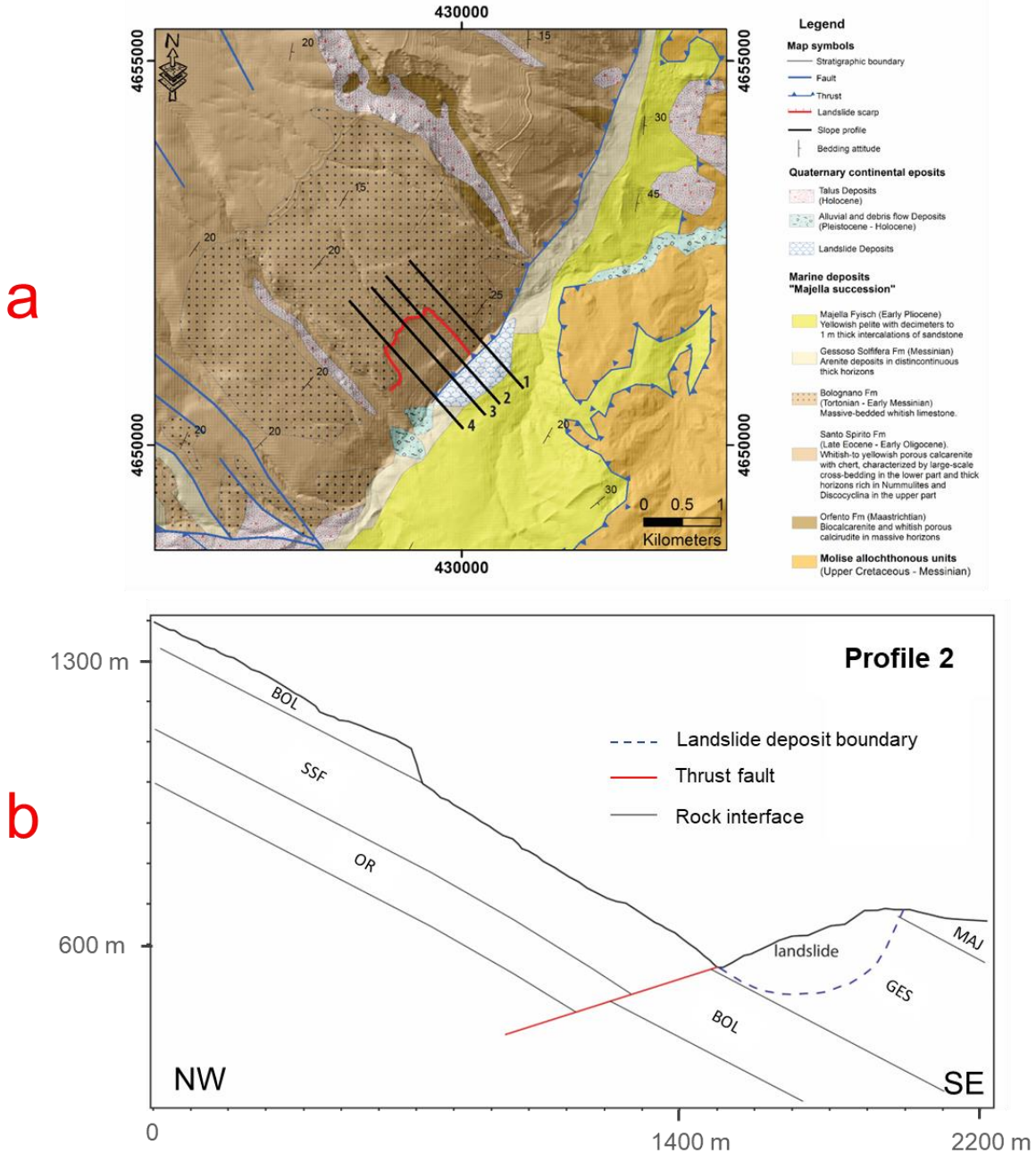

Fig. 5-2. *a) the geological map of the study area after Vezzani and Ghisetti (1998) and Miccadei et al., (2013), and b) 2D section (along Profile 2) of the analysed slope, showing the lithology, distribution of discontinuity and landslide deposits.*

In respect of the structural geology, the slope is characterized by the convex relief of the bedding as the presence of an anticline, whose bedding inclination undergoes a gradual increase from sub-horizontal angles (10° - 20°) on the crest of the slope to tilted angles (25° - 30°) in the medium-low part of the slope (Fig. 5-2). There are two thrust faults in the analysed slope (Fig. 5-2a), one is dipping towards SE and causing the Molise unit overlying the Majella unit (as aforementioned) and the second dipping towards NW and resulting in uplift of hanging wall of Majella unit.

Table 5-1. *Characteristics of the formations that constitute the Majella unit (Festa et al., 2014).*

Formation		Lithology	Thickness
MAJ		Yellowish pelite with decimetres-to-metres thick intercalations of sandstone	> 900 m
GES		Gypsum and gypsumarenite deposits intercalated in alternating grayish marl and siltstone	30 m – 100 m
BOL	BOL1	Marly limestone and cherty limestone	0 – 20 m
	BOL2	Bryozoan-rich calcarenite	0 – 70 m
	BOL3	Massive-bedded whitish limestone with rodolites of coralline algae, bryozoan, echinoids, molluscs, macroforaminifera	30 m – 60 m
FSS	FSS1	Whitish calcilutite with chert alternating with calciturbidites	20 m – 50 m
	FSS2	Whitish-to yellowish porous calcarenite with chert	100 m -300 m
OR		Biocalcarenite and whitish porous calcirudite	60 m - 200 m
SCZ		White hemipelagic calcilutite, in decimetres thick beds, with red-to violet chert, alternating with porous bioclastic calcisiltite and calcarenite	50 m - 400m
ACQ		White fine-grained biocalcarenite and calcirudite rich in Rudists	200 m - 300 m
MOR		Massive micritic limestone and oolitic and oncolitic calcarenite	> 400 m

5.2.2. The Lettopalena Paleolandslide

The Lettopalena Paleolandslide (sometimes named Taranta-Peligna Paleolandslide) is a historic landslide, with the delineated boundary (shown in Fig. 5-3a) which probably occurred in the Mid- Holocene (Paolucci et al., 2001). The landslide features an elongated headscarp characterised by a ‘Z’ shape on the SW side (Fig. 5-3d) and a right-angle corner on the NE side (Fig. 5-3e). Landslide deposits, composed of scree and talus with various sizes of fragmented rocks (Fig. 5-3b), are observed at the toe of the slope and on the opposite side of the valley where the village of Lettopalena has been built. Some blocks, tens of metres in size, are still visible at the toe slope and along the river, which testify the heterogeneity of the paleo-landslide deposits. An example of such blocks is shown in Fig. 5-3c; the planar condition of the block surface facing the camera implies the block was detached

along a highly persistent geological structure.

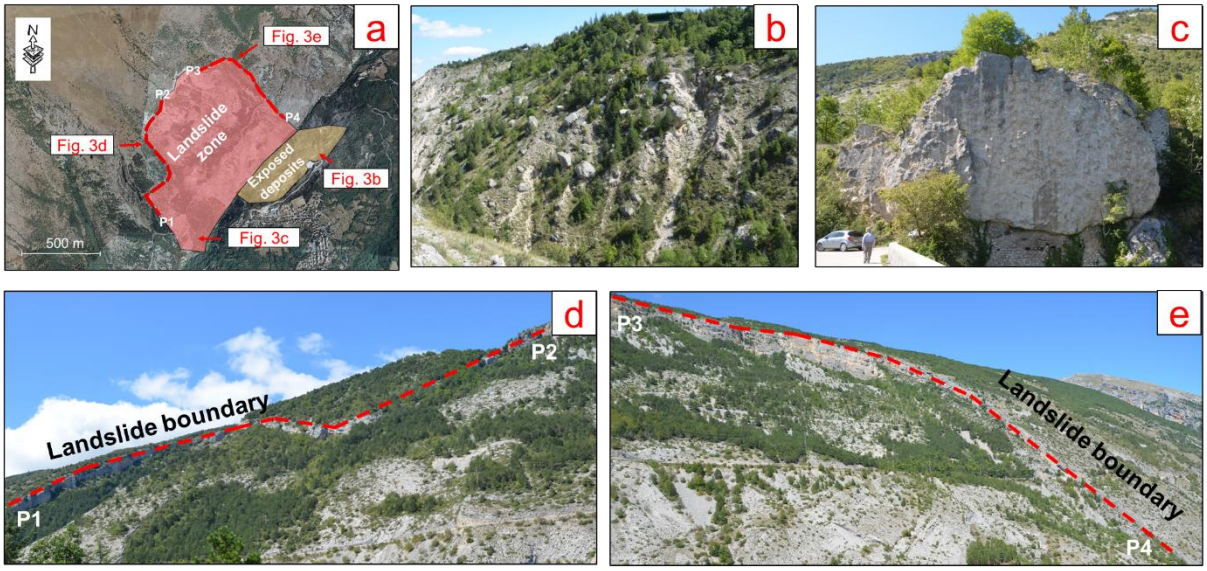

Fig. 5-3. *Landslide scar and deposits, a) the extent of the ancient landslide and the deposit, b) landslide deposits characterized by scree and talus, c) an isolated rock block located by the river, d) the SW headscarp of the landslide, e) the NE headscarp of the landslide, e) the NE headscarp of the landslide.*

Although there is scarcity of additional detail for the ancient landslide, a recent small-scale landslide in 2005 (Bianchi Fasani et al., 2005), adjacent to the study site, can be a useful indicator of potential triggers for the ancient landslide. The two landslides are located in identical geological environments and have a similar mechanism that is controlled by the bedding and the lateral and rear release surfaces and were defined by the discrete fracture network. For the 2005 landslide, rainfall was suggested as a contributing trigger factor (Bianchi Fasani et al., 2005). This may also be applicable to the catastrophic landslide, because of the fact that water saturation is effective to reduce shear strength of discontinuities (Pellet et al., 2013; Noël et al., 2021). Paolucci et al. also suggested that the paleolandslide may have been triggered by an earthquake (Paolucci et al., 2001), as for other paleolandslide in the region (e.g., Scanno Paleolandslide, (Francioni et al., 2019)).The high mobility of the landslide is evidenced by the distribution of landslide deposits in proximity to the village (see Fig. 5-3a and b), with the presence of talus deposits on the opposite flank of the valley that ran out 150 metres away from the toe of the slope.

5.3. Material and methods

5.3.1. Interpretation of geological structures and kinematic analysis

Geological structures were interpreted through the combination of traditional manual surveys and RS mapping to investigate the potential mechanism and kinematics of the landslide. More precisely, in relation to the 6 survey sites shown in Fig. 5-1 (site 1-6), traditional manual surveys and terrestrial photogrammetry have been carried out at accessible sites (sites 1-2-3-4 of Fig. 5-1) between 2019 and 2021. In regard to the sites 5 and 6, these were investigated using Google Earth satellite imagery from 2009 (site 5) and a UAV survey (site 6). This provided a method to gather further structural information in the inaccessible upper part of landslide scar and therefore verify that main lineaments have a constant orientation along the entire slope.

At sites 1-4 a scanline survey was conducted at each location to detect on-site discontinuities with the measurement of their properties, including orientations (dip and dip direction), estimated joint wall compressive strength (JCS), spacing, persistence, surface weathering condition, surface shape and joint roughness coefficient (JRC). Where, persistence is measured by the exposed trace length of a discontinuity.

Additional discontinuity data was collected at sites 1-2-3-4 through terrestrial photogrammetric mapping, to complement and verify the results of manual surveys. Terrestrial photogrammetry provides a series of stereo images to construct a 3D point of rock outcrops by using a SfM technique, which was carried out by using the Agisoft Metashape software (Agisoft, 2016). Based on the point cloud, local geological structures (joints and fractures) were manually identified by using the Compass plugin (Thiele et al., 2017), provided by CloudCompare software (CloudCompare, 2017). The plane tool of the Compass plugin was used to measure the orientation of an exposed planar structure where its plane was fitted to all points sitting within the circle (using least squares). This method provides an orientation estimate (dip/dip direction) for the fitted plane. Using this software, it was possible to plot the data on a stereonet for comparison with the conventional engineering geology data.

A 2019 satellite image at site 5 (Fig. 5-1) was obtained from Google Earth, orientated towards the north. Using this image, it was possible to determine the strike of daylighting discontinuities.

Site 6 is a representative section of the landslide scarp at the upper right corner of the failure zone, this area was surveyed using UAV photogrammetric mapping in October 2019. A total of 92 photographs were acquired with a lateral and vertical overlap of 70/80%. The aircraft used for the survey was a DJI Mavic 2 Pro and the final resolution of the extracted point cloud was between 3 and 4 cm.

Using the features and discontinuities identified at the 6 sites described above, an analysis was undertaken to evaluate the kinematic potential of the slope (dip/dip direction: 40°/110°) for planar sliding, wedge sliding and direct toppling.

Finally, satellite digital elevation data (10x10 metres resolution, provided by Abruzzo Region) was used to identify the post-landslide features for the entire slope. Various thematic maps have been generated using the DEM data, including a *slope* map to delineate the inclination of the slope, a *hillshape* map to produce a grayscale 3D representation of the terrain surface, and an *aspect* map to quantify the slope direction. A 2022 Google Earth image (0.5x0.5 metres) was used to interpret the geometric characteristics of failure scar at the toe of the slope.

5.3.2. Numerical analysis of the landslide

In view of the landslide characteristics (i.e., a structurally-controlled mechanism and relatively simple geometry) the 2D distinct element code, Universal Distinct Element Code (UDEC) (Itasca Consulting Group Inc., 2019), was used to model the landslide. The code uses an explicit time-stepping system to solve equations of motion, simulating the response of rock mass that is subject to either static or dynamic loading. In the model, a rock slope is represented as an assemblage of discrete blocks separated by discontinuities which are treated as boundary conditions between blocks. In this case study, individual blocks behave as deformable and deformation behaviours are defined by the Mohr-Coulomb failure

criterion. Typical limestone property values, as provided in Table 5-2, were used for landslide modelling (Lama and Vutukuri, 1978).

Table 5-2. *Rock properties associated with Mohr-Coulomb failure criterion.*

Density	Shear modulus	Bulk modulus	Friction angle	Cohesion	Tensile strength
2750 (kg/m3)	30 (GPa)	50 (GPa)	40 (°)	8 (MPa)	2.5 (MPa)

5.3.2.1. Landslide back numerical analysis

Using the geological section in Fig. 5-2 and post-landslide slope geometry that was delineated using satellite DEM data (10 × 10 metres resolution, provided by Abruzzo Region), pre-landslide scenarios have been constructed along profile 2 (Fig. 5-4). The models highlight how the thrust fault at the toe of the slope generates the contact between the BOL and the GES formations. The BOL formation, being made of limestone materials, has higher erosion resistance compared with the GES formation. Therefore, we have indicated that the Aventino River erodes the GES formation at the toe of the slope, daylighting the bedding planes of the BOL formation. The erosional evolution (pre-failure) has been illustrated in Fig. 5-4a. Fig. 5-4b shows the current slope profile (post-failure) with landslide deposits at the toe of the slope and on the opposite side of the valley.

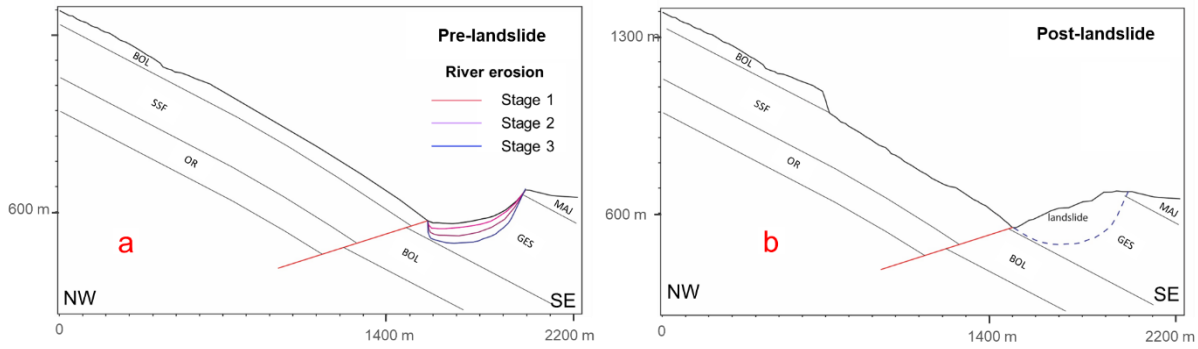

Fig. 5-4. *Geological models of the analysed slope with the consideration of the effect of sequential river incisions, a) pre-landslide, b) post-landslide.*

Using the assumed pre-landslide slope geometry (as shown in Fig. 5-4a) the 2D distinct element model in UDEC (Fig. 5-5) was created. The model incorporates the identified discontinuity network (i.e., S0 and J1) with the properties listed in Table 5-3, but with sets J2 and J3 excluded from the modelling as they are sub-parallel to the cross section. Generic properties of discontinuity and rock were used for numerical

modelling. The values of these parameters were determined within reference to relevant literature (Antolini et al., 2016), and calibrated through back analysis. The thrust fault is considered with the uplift of hanging wall in which a folded bedding plane is configured by a curve of 20° inclination at the crest of the slope and 25° inclination at the toe of the slope.

Gradual river erosion is also incorporated into the modelling through the sequential removal of rock blocks in three stages. Note that the folded bedding plane at the base of the modelled slope does not daylight until the third stage of erosion is completed. The modelling sequence took place between 2021 and 2022 and consisted of 4 simulation intervals (interval 1-4). Interval 1 simulates the mechanical behaviour of the slope before river erosion); Interval 2 models the mechanical behaviour of the slope in response to stage 1 of the simulated river erosion; Interval 3 is associated with the mechanical behaviour of the slope in response to stage 2 of the simulated river erosion; Interval 4 models the mechanical behaviour of the slope in response to stage 3 of the simulated river erosion.

Table 5-3. *The property of discontinuities used in numerical modelling.*

Normal stiffness	Shear stiffness	Friction angle	Cohesion
10 (GPa/m)	5 (GPa/m)	22 (°)	25 (KPa)

A fixed boundary condition was applied to sidewalls and the base of the model. To ensure no boundary effects on the zone of interest, boundaries (sidewalls and the base) were extended 200 m from the zone of interest. Three representative history points (H1, H2 and H3) were placed in BOL rocks within the model to monitor the displacement of BOL in the lower, middle, and upper parts (see Fig. 5-5) of the modelled slope.

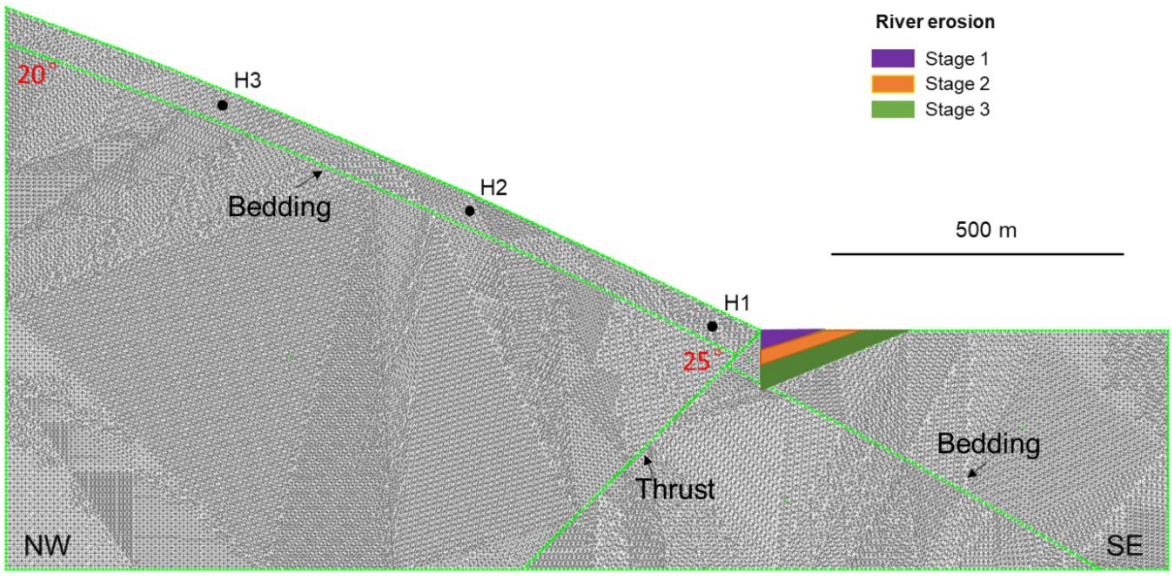

Fig. 5-5. *Model geometry used for numerical modelling of the landslide, highlighting gradual river erosion characterized by sequential removal of rock blocks, thrust faulting of a bedding plane, and the location of 3 history points (H1, H2 and H3).*

5.3.2.2. Sensitivity analysis

In numerical simulations material properties are usually the most difficult parameters to determine. In this context, a sensitivity analysis was carried out to assess the potential impact of variations in the material properties on the modelling of the landslide. Considering that the catastrophic landslide was most likely associated with translational sliding along bedding planes, the sensitivity analysis focused on the variation of the friction angle and cohesion of S0, as shown in Table 5-4. For each parameter, a sensitivity analysis was performed by varying its value from the minimum, the mean, to the maximum using a control variate method (He et al., 2021b), in order to examine the influence of the uncertainties on the slope stability analysis.

Table 5-4. *Variations in dip, dip direction, persistence, friction angle of the folded bedding plane were characterized by mean, minimum and maximum values.*

J1 Property	Mean Value	Minimum	Maximum
Friction angle (°)	22	17	27
Cohesion (Pa)	2.5×10^4	0	5×10^4

5.4. Results

5.4.1. The characteristics of geological structures and result of kinematic analysis

5.4.1.1. The characteristics of geological structures

As discussed in section 3, the characteristics of the geological structures have been investigated through different survey methods. Traditional manual surveys and terrestrial photogrammetry have been performed at sites 1-2-3-4. A total of 79 discontinuities were measured using the traditional manual approach and further 81 through photogrammetric analysis. Fig. 5-6a shows a lower hemisphere stereonet plot representing the poles of 76 discontinuities (joints and bedding planes) collected from traditional manual surveys at sites 1-2-3-4, where 4 main discontinuity sets (S0, J1, J2 and J3) were identified. Fig. 5-6b presents a stereonet representation of the poles of 81 discontinuities measured from the terrestrial and UAV photogrammetric surveys at sites 1-2-3-4-6. Both results are generally consistent, although J3 is less pronounced.

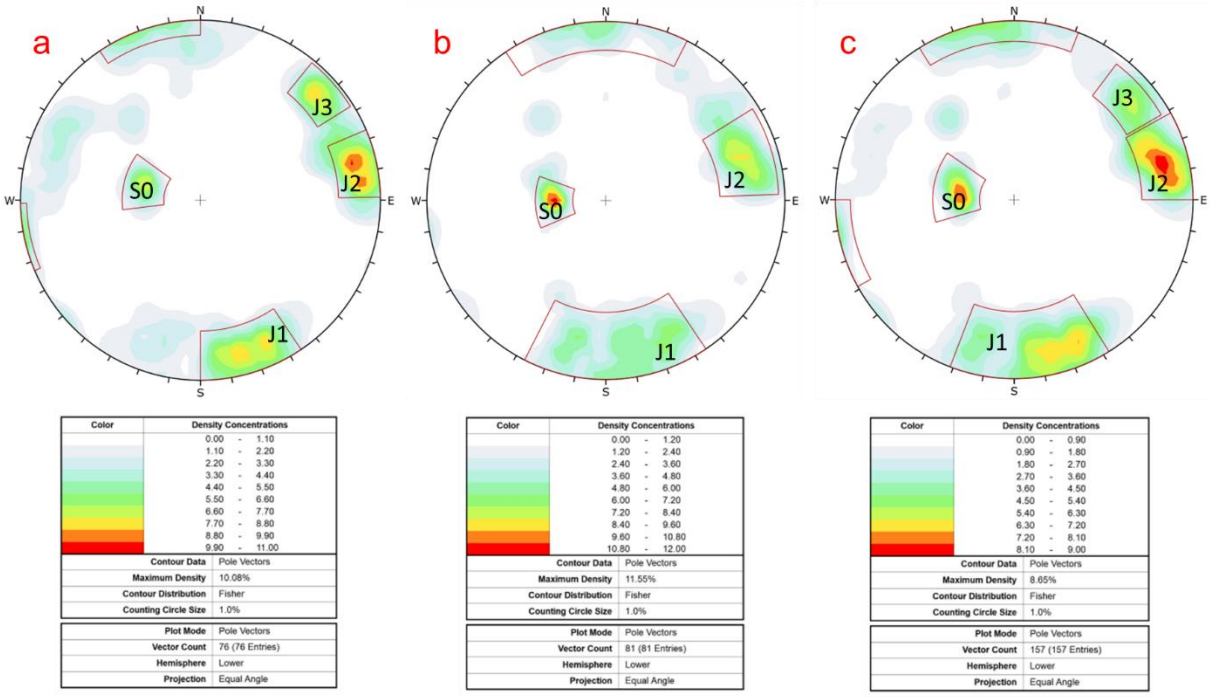

Fig. 5-6. *Lower hemisphere stereonet plots of discontinuity poles measured from: a) engineering geological mapping, b) photogrammetric surveys, c) combination of engineering geological mapping*

and photogrammetric surveys.

The two datasets were then combined (Fig. 5-6c). The relatively low-angle discontinuities dipping towards SE in set S0 is related to bedding of Majella rock units, with a mean orientation (35°/099°) and high persistence (more than 20 m); J2 (81°/257°) and J3 (80°/230°) are sub-parallel with J2 being the predominant one; joints in sets J1 (80°/348°) and J2 are sub-vertical and sub-orthogonal to each other. J1, J2 and J3 are less persistent compared with S0, whilst they have similar degrees of spacing (approximately 0.4 m) throughout the four sampling sites (Table 5-5). The spatial relationship between S0, J1 and J2 and their geometric characteristics are presented in Fig. 5-7 which shows a terrestrial photogrammetric built 3D model for a roadside section of the analysed slope.

Table 5-5. *Discontinuity properties, including the mean orientations obtained from the traditional manual survey, mean orientations obtained from photogrammetric surveys, mean orientations obtained from the combination of both surveys, mean discontinuity spacing and mean discontinuity persistence.*

Set	Mean orientation (Dip°/Dip Direction°)			Mean spacing (m)	Mean persistence (m)	Mean Infilling (mm)
	From traditional manual survey	From 3D model	Combined			
S0	36/105	33/93	35/99	0.4	> 20	Hard filling < 5
J1	84/341	74/356	80/348	0.3	1-3	Hard filling < 5
J2	83/257	78/255	81/257	0.4	1-3	Hard filling < 5
J3	80/230	(Nah)	80/230	0.4	1-3	Hard filling < 5

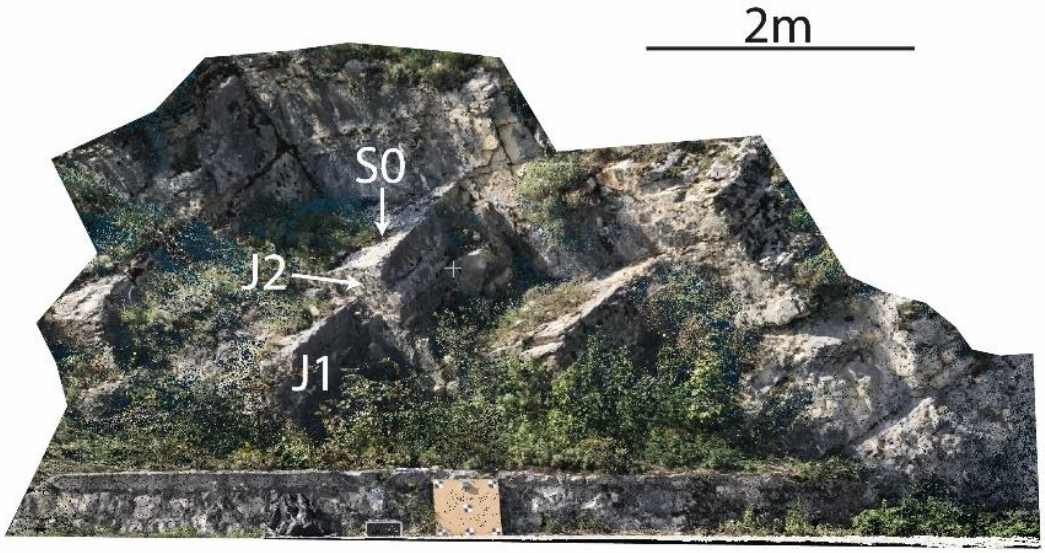

Fig. 5-7. *A terrestrial photogrammetric 3D model of a roadside section of the analysed slope.*

Table 5-6 summarizes geomechanical discontinuity properties (i.e., JCS, weathering condition, surface shape condition and JRC) at sites 1-2-3-4 (where traditional manual survey was conducted). Discontinuity properties measured at site 2 differ from the properties detected at other sites. For example, for the 4 sets, the JCS measured at site 2 is lower than the one measured at sites 1, 3 and 4. Less weathering and increased undulation of discontinuity surfaces was observed at site 2.

Table 5-6. *Site-dependent discontinuity properties (site 1/ site 2/ site3/ site 4), including UCS, surface weathering condition, surface shape and JRC.*

Set	JCS (MPa)	Weathering	JRC
S0	50/32/48/44	moderately/slightly/moderately/moderately	3/7/3/1
J1	44/30/50/48	moderately/slightly/moderately/moderately	3/7/3/3
J2	50/30/44/50	moderately/slightly/moderately/moderately	3/9/5/3
J3	48/30/(Nah)/50	moderately/slightly/(Nah)/moderately	3/9/(Nah)/3

With regards to sites 5 and 6, as mentioned in section 3, they have been investigated using Google Earth satellite images (site 5) and UAV survey (site 6). This provided a basis to validate the results gathered from the traditional manual surveys and terrestrial photogrammetry and, more importantly, to confirm that the orientation of major lineaments at the crest of landslide scarp were similar to the ones measured along the state road (SS84). Fig. 5-8a shows the strikes of

daylighting discontinuities on a Google Earth at site 5, where the observed discontinuities are delineated by blue and red lines. From the rosette plot of strikes of the features (Fig. 5-8b), the discontinuities highlighted in blue are SSW-NNE trending and discontinuities highlighted in red are SSE-NNW trending, implying their close relation with J1 and J2/J3, respectively (Fig. 5-6). However, discontinuities related to S0 are absent in the image as S0 is parallel to the slope surface and has less potential to daylighting in the slope.

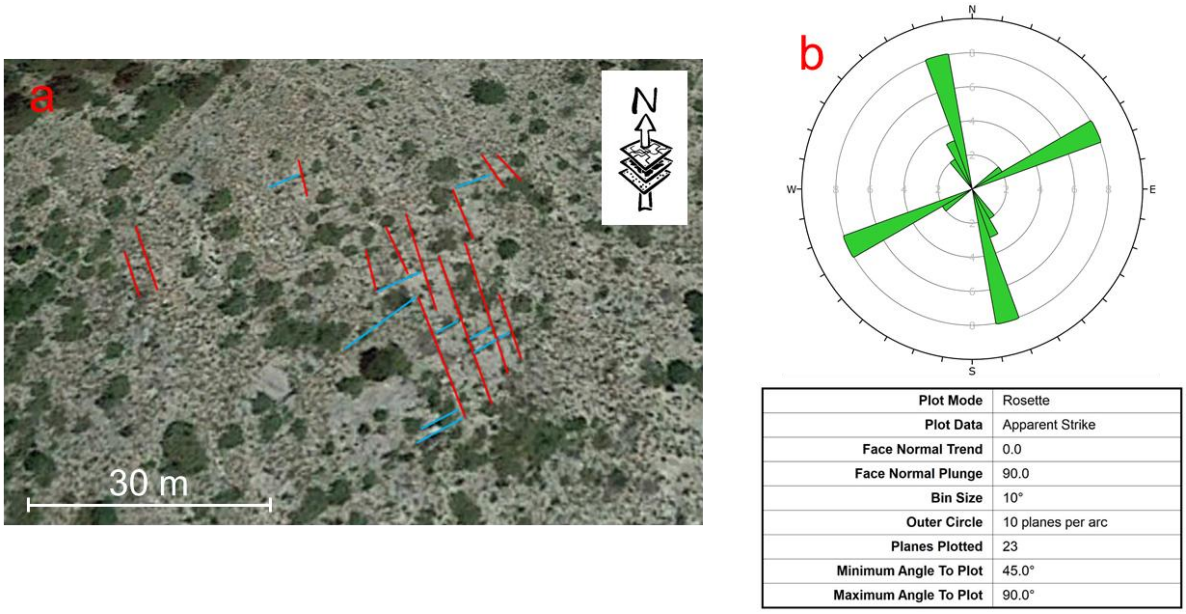

Plot Mode	Rosette
Plot Data	Apparent Strike
Face Normal Trend	0.0
Face Normal Plunge	90.0
Bin Size	10°
Outer Circle	10 planes per arc
Planes Plotted	23
Minimum Angle To Plot	45.0°
Maximum Angle To Plot	90.0°

Fig. 5-8. *a) the detection of strikes of daylighting discontinuities from a 2019 Google Earth image high-lighted by red and blue lines, b) a rosette plot showing the strike of detected discontinuities.*

The UAV photogrammetry at site 6, with a flight plan depicted in Fig. 5-9a generated a 3D point cloud, consisting of approximately 36 million points with spatial resolution between 3 and 4 cm, to delineate the section of the escarpment. Where X indicates E direction, Y points towards N direction and Z infers the vertical (Fig. 5-9b). The survey was unable to map the entire base of the valley due to occlusion caused by vegetation. However, two sections of the escarpment related to the rear and lateral release surfaces of the landslide are clearly presented. It shows that two sections of escarpment are characterized by near-vertical limestone cliffs of 60-metre height. The rear release surface is formed by major features (88°/155°) belonging to J1 while the lateral release surface by two features (79°/202° and 85°/038°) belonging to J2/J3. The bare slope (slip surface) underlying the escarpment also exhibits a low-angle planar surface related to bedding.

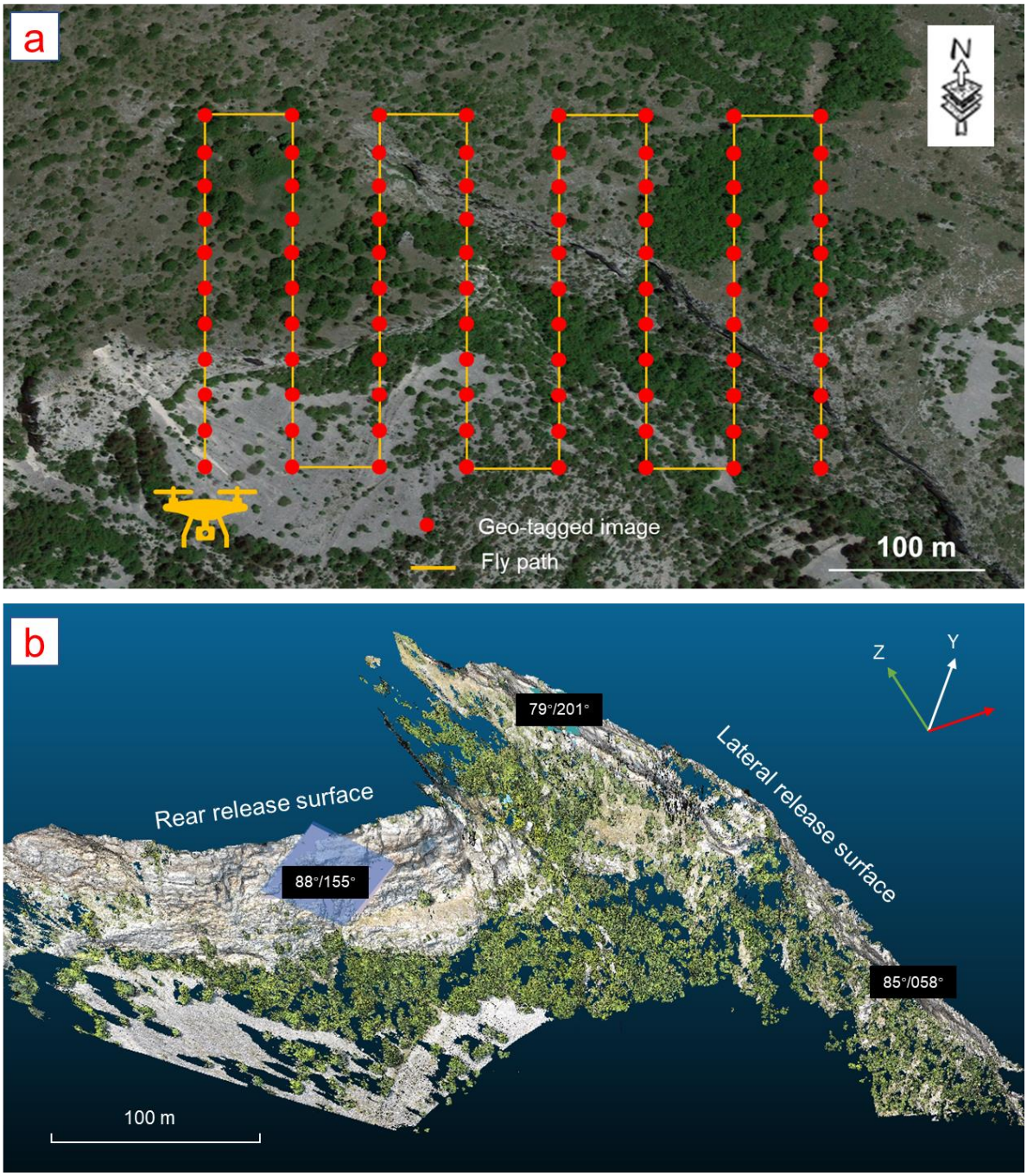

Fig. 5-9. *UAV photogrammetry, a) UAV flight plan over the upper right corner of the failure zone, b) point cloud showing the topography of the upper right escarpment of the landslide zone with highlighted 3 discontinuities that define the rear and release surfaces.*

With regards to the 10x10 DEM analysis, the raster data presents a clear topographic contrast between the carbonate reliefs of the NW slope, with altitudes exceeding 1700 m a.s.l., and the predominantly clayey hilly landscape of the SE foothills, with average altitudes of less than 900 m a.s.l. (Fig. 5-10a). The contact between the two parts is marked by the deep incision of the NE-SW trending

Aventino river valley (Fig. 5-10b). The SE slope underlying the Lettopalena village exhibits a flat terrain represented by low slope angles in Fig. 5-10c and a white colour on the *hillshade* map (Fig. 5-10d). Compared with the SE slope, the NW slope is relatively steep, characterized by a convex terrain where the inclination, in general, increases from the crest to the toe (Fig. 5-10c). In addition, the slope where the landslide occurred is constrained by two valleys (the NE-SW trending Aventino river valley and an NW-SE trending valley).

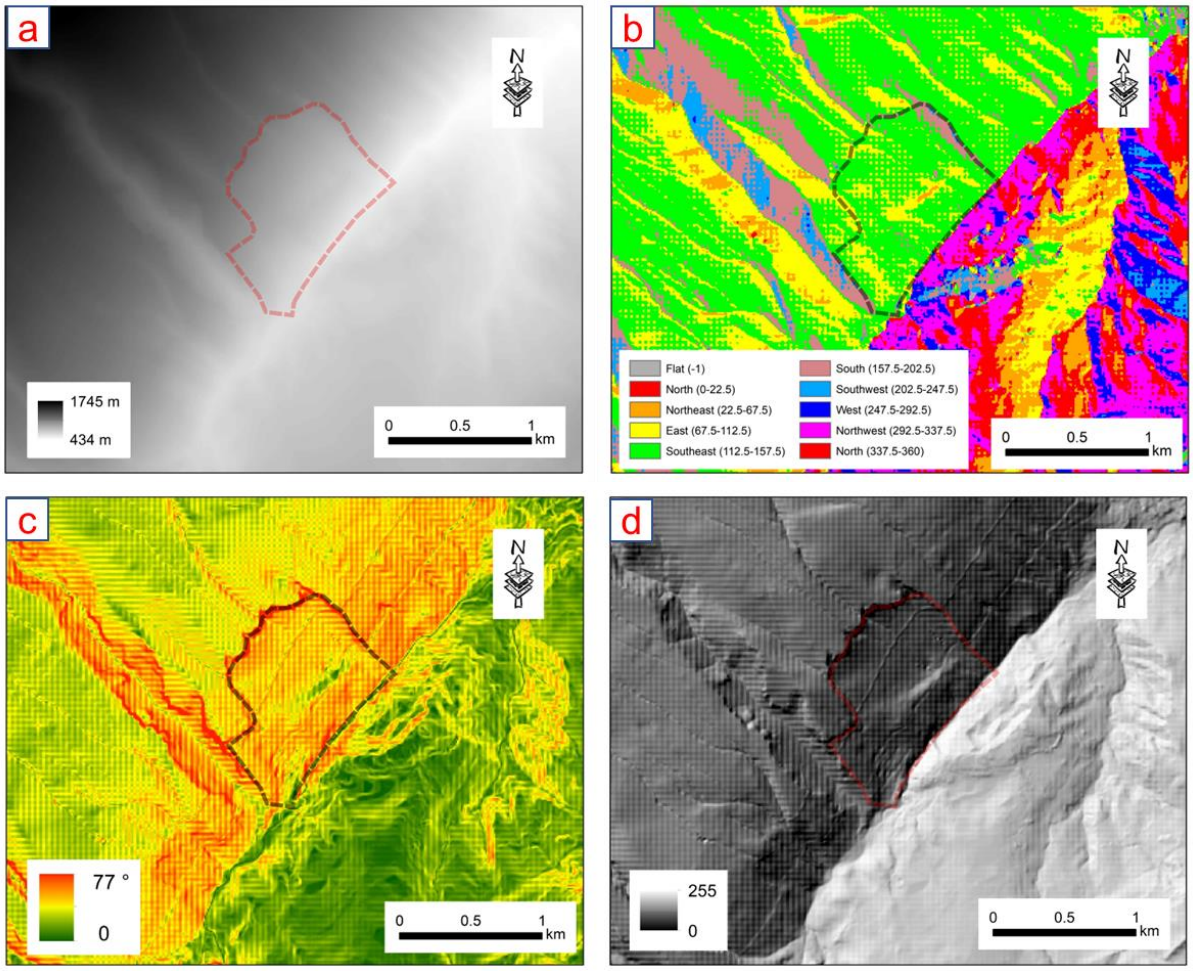

Fig. 5-10. *Topography of the analysed slope, showing the information on a) elevation, b) aspect c) inclination, and d) hillshade.*

The landslide scar is also clearly visible in these maps. For example, the elevation map (Fig. 5-10a) and the *hillshade* map (Fig. 5-10d) identify the landslide zone through a sudden colour change. The high slope angle values (approximately 70°) highlighted in red along the upper landslide boundary indicate the presence of an escarpment, connecting the NW-SE trending valley at the lower sector of the slope

(as shown in Fig. 5-10c).

The landslide extent is depicted in the high-resolution satellite image (Fig. 5-3a) and the thematic maps (Fig. 5-10) with a measured area of 0.94 million m^2. In addition, the thickness of the BOL rock layer (failure body) is approximately 50 m according to the height of the escarpment (Fig. 5-9b). It is estimated that the failure volume of the catastrophic landslide was approximately 4.7 million m^3.

Using the DEM data, 2D geometric models have been generated along the 4 slope profiles of Figure 2a to highlight the terrain change associated with the landslide (Fig. 5-11). Profile 1 is out of the landslide zone, while profiles 2-4 pass across the landslide zone and capture the geometry of the landslide scar. It can also be seen in profiles 2-4 that the upper boundary of the landslide is marked by the presence of an escarpment and located at approximately 1000 m a.s.l. In addition, the height of the escarpment gradually reduces from profile 2 to profile 4 (from NE to SW).

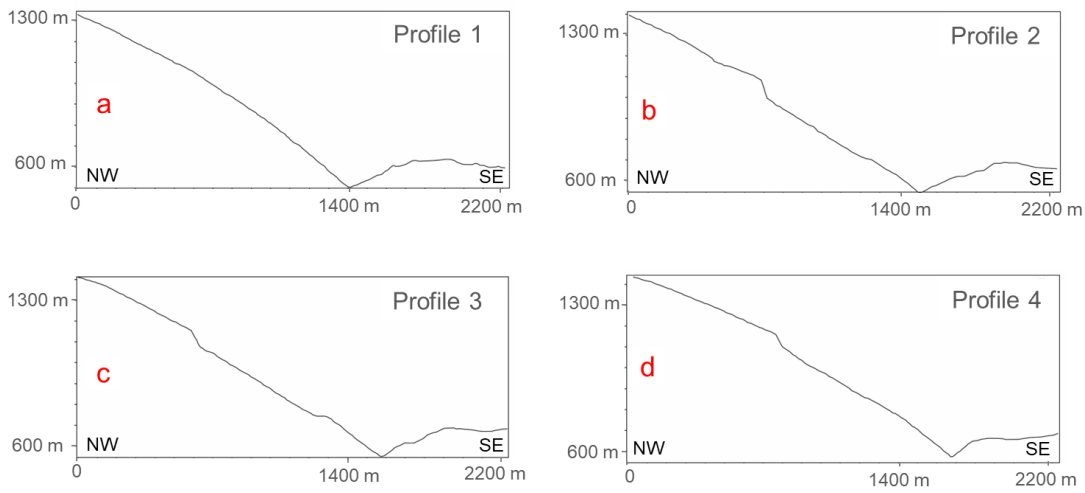

Fig. 5-11. *Slope profiles along the four cutting planes highlighted in Figure 2, a) profile 1, b) profile 2, c) profile 3 and d) profile 4.*

5.4.1.2. Results of kinematic analysis

Kinematic analysis highlighted that the slope is prone to planar sliding along a subset of the set S0/bedding (Fig. 5-12a). Wedge sliding is also possible, constrained by S0/J1 and S0/J2 and slides along S0 (Fig. 5-12b). Concerning potential direct toppling, J1 and J2 could intersect to form block edges dipping into the slope and S0 acts as the potential basal sliding surface (Fig. 5-12c). The results of kinematic

analysis highlight the dominant influence of bedding (set S0) on the potential for planar sliding, wedge sliding and direct toppling.

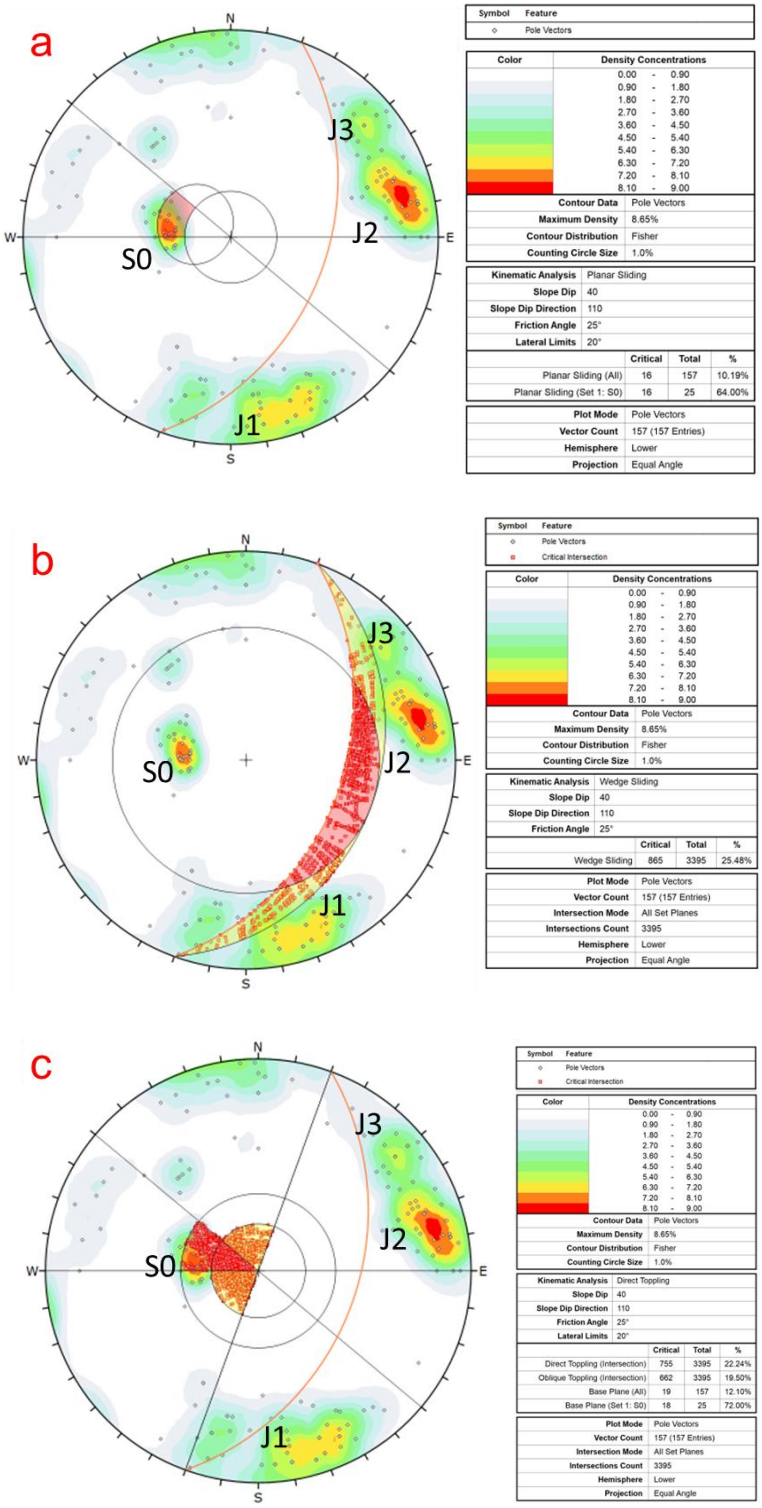

Fig. 5-12. *Kinematic analysis of the translational landslide, a) planar sliding, b) wedge sliding, and c) direct toppling.*

The topographic mapping highlights that the slope exhibits a convex terrain, with

increasing slope angle towards the toe (Fig. 5-10c). Furthermore, at the toe of the slope during the phases of river erosion, the slope face alongside the river could reach an inclination much higher than 20-25°. In this context, kinematic analysis examined the kinematic potential of the slope for planar sliding with different values of slope angle (Table 5-7). When the slope angle is 40°, 59% of joints in S0 can behave as a slip surface for potential planar sliding. This percentage was calculated based on the total number of the surveyed planes of S0. Increasing the slope angle allows higher probability of planar sliding. When the slope angle increases above 50°, the probability of failure achieved a convergence.

Table 5-7. *Probability of planar sliding along S0 with different slope angles.*

Slope angle	40°	50°	60°
Probability for all joints	10.19%	14.01%	14.01%
Probability for S0	59.26%	81.48%	81.48%

5.4.2. Landslide numerical modelling and sensitivity analysis

5.4.2.1. Landslide numerical modelling

Fig. 5-13 shows a modelling result associated with slope displacement in the X direction after river erosion. The modelling successfully simulates the large translational sliding along the bedding plane. The result supports field observations and the depicted evolution of the area (Fig. 5-11) with the lower and middle section of the slope being susceptible to failure. The landslide is characterized by a step-path slip surface at the toe of the slope, as highlighted in the close-up image 2 in Fig. 5-13. At the NW tip, the failure terminates in the upper-middle section of the slope, and the headscarp is defined by the interaction and connection of S0 and J1, as highlighted in the close-up image 1 in Fig. 5-13.

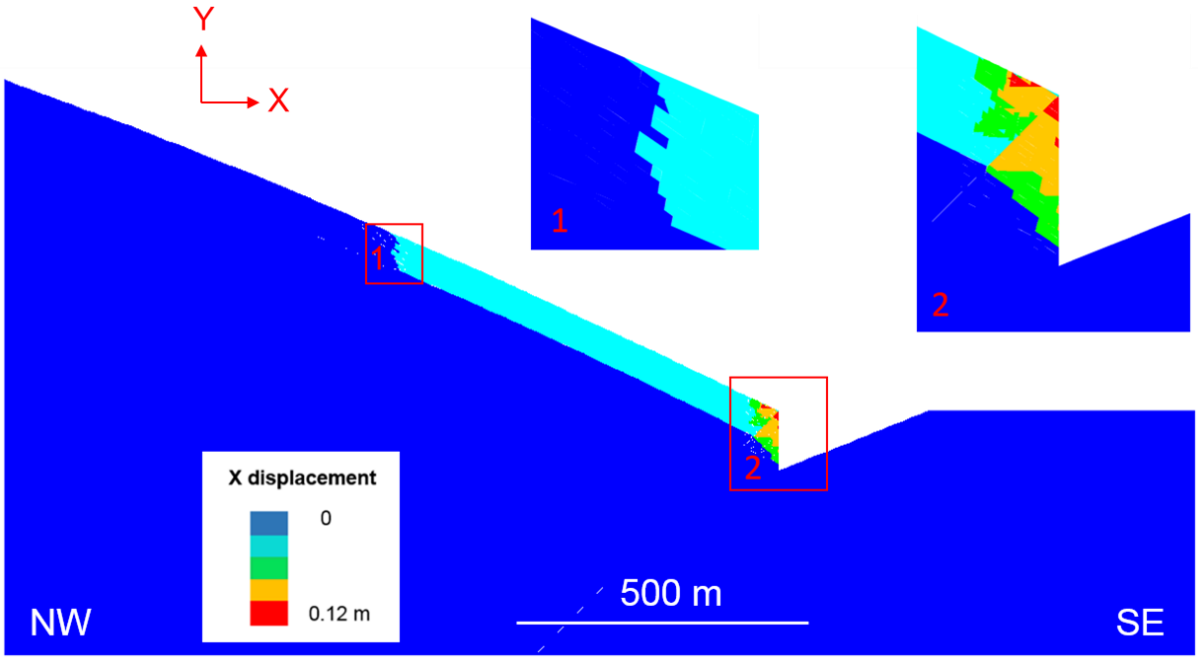

Fig. 5-13. *The result of numerical stability analysis showing the contour of X displacement with the close-up of structurally defined landslide scarp and step-path slip surface at the toe of the slope in the modelling.*

The X displacement of the history points has been recorded with the advancement of the modelling sequence (Fig. 5-14). The modelled sequence consists of 4 temporal intervals of calculation timesteps.

1) Interval 1 (timestep 0-100,000): The 3 history points all achieve a limit equilibrium state, that is characterized by the convergence of X displacement. During this interval, H3 experiences more X displacement than H2/H1.

2) Interval 2 (timestep 100,000-180,000): During this interval, H1/H2/H3 are stable and experienced a minor increase in X displacement which is caused by the debuttressing induced by river erosion. This debuttressing provides a gradually attenuated impact on the slope from H1 to H3, showing that H1 has increased X displacement of 0.3 mm.

3) Interval 3 (timestep 180,000-260,000): Similar to interval 2, H1/H2/H3 remain stable. Additional increases in X displacement of the 3 history points can be observed. During interval 3, the debuttressing effect is more noticeable than in interval 2, which is reflected by increased X displacement of H1/H2/H3.

4) Interval 4 (timestep 260,000-340,000): When river erosion advances to stage 3, the displacement of H1/H2 sharply increases, whilst H3 approaches stable convergence. This infers that the daylighting of the bedding plane caused by river erosion in stage 3 creates kinematic freedom for translational sliding of the layered rocks. The contrasting displacement behaviours between H1/H2 and H3 is potentially caused by the folded bedding plane (associated with the anticline) that has an inclination of 20° on the crest of the slope and of 25° at the toe of the slope (valley). This is consistent with the interpretation of field observation and that the translational landslide occurred in the lower section of the slope whilst the upper section of the slope remains stable (Figure 3a and Figure 11).

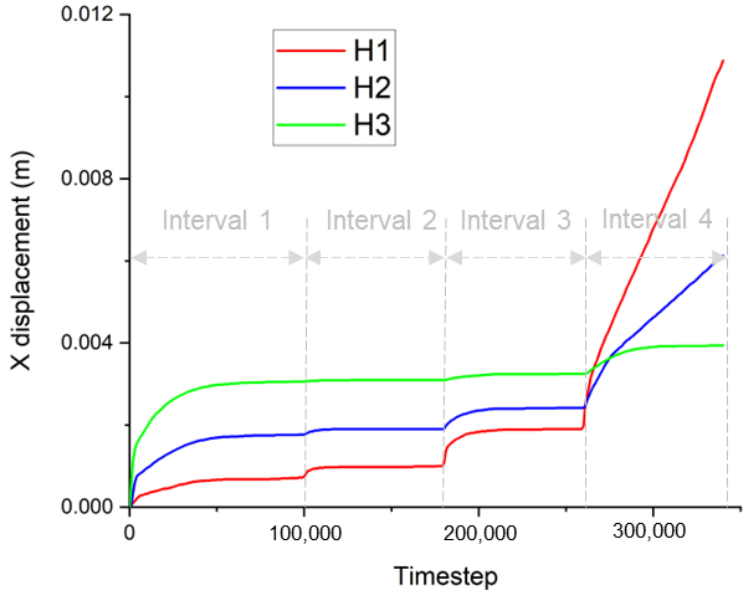

Fig. 5-14. X displacement of 3 history points (H1, H2 and H3) against calculation timestep.

At a local scale, the modelling indicates that the development of river erosion promotes rock failures in the vicinity of the valley, as shown in Fig. 5-15a–c. After the erosion of stage 1, a planar instability occurs along a single slip surface related to S0 (Fig. 5-15a). The erosion of stage 2 causes further sliding on a step-path surface defined by the connection of S0 and J1 (Fig. 5-15b); and finally, when the erosion advances to stage 3, a second step-path surface forms connecting the bedding plane in the hanging wall of the thrust fault to generate the entire slip surface of the catastrophic landslide (Fig. 5-15c), which is also highlighted in Fig. 5-4.

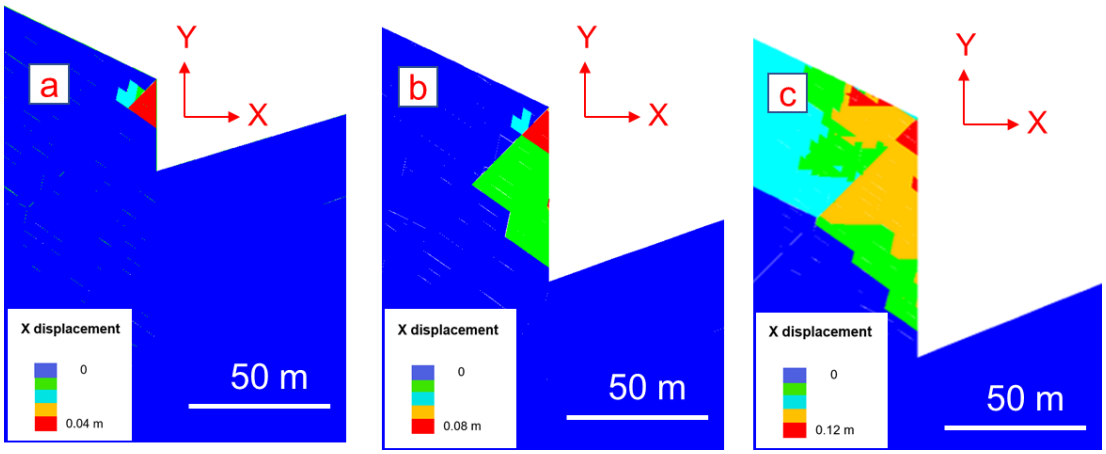

Fig. 5-15. *Close-up view of the contour of X displacement in the valley during sequential removal of rock blocks caused by the staged river erosion, a) stage 1, b) stage 2 and c) stage 3.*

The same step-path geometry highlighted in the simulation is still visible in the field. The Google Earth image shows a step-path failure geometry at the toe of the slope (Fig. 5-16). The step-path geometry is mainly constrained by multiple bedding planes and joints related to J1.

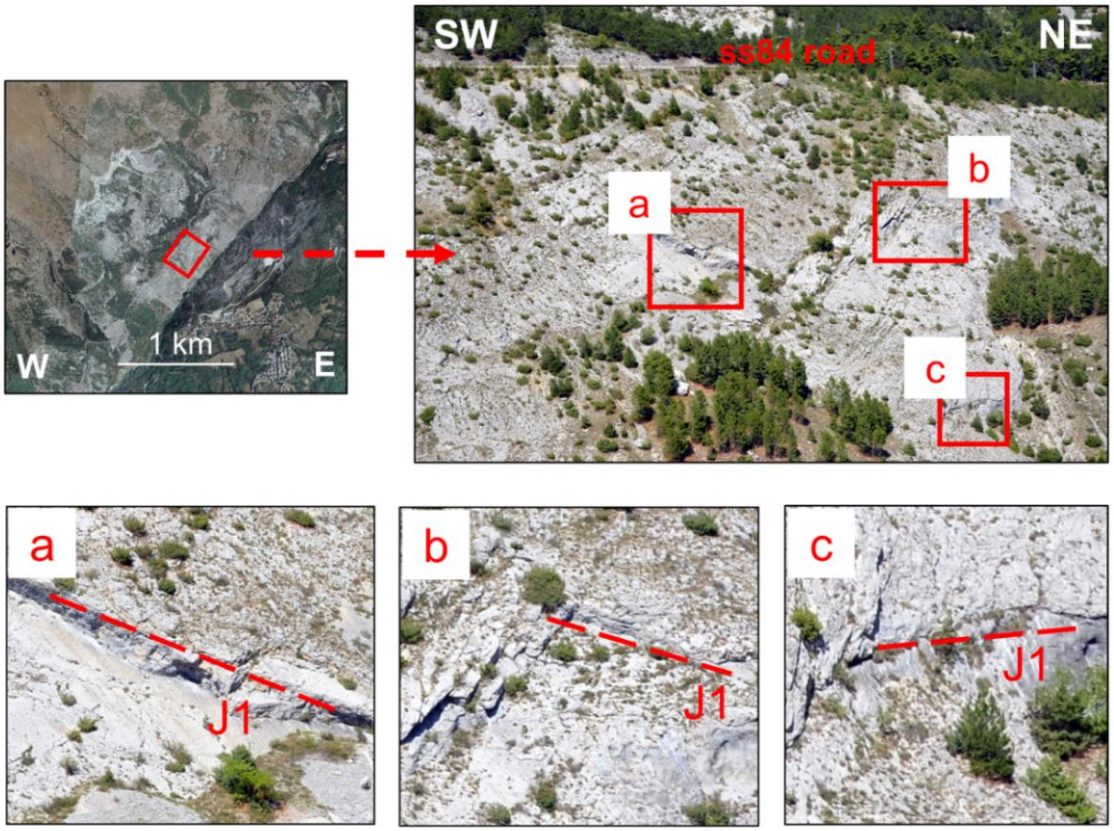

Fig. 5-16. *Topography of the analysed slope at the toe showing the scar of a step-path failure constrained by multiple bedding planes and joints related to J1.*

5.4.2.2. Sensitivity analysis

A sensitivity analysis of the bedding friction angle was then undertaken. It can be seen from Fig. 5-17 that three history points maintain a stable state after the staged river erosion when the friction angle increases to 27°. This indicates that when the friction angle of S0 is higher than 27°, translational sliding is unlikely to occur. The reduction of friction angle to 17° shows that the three modelled history points become unstable, implying the translational sliding could impact the lower, middle and upper sections of the analysed slope. As would be expected, a reduction in the friction angle causes more displacement of failed blocks.

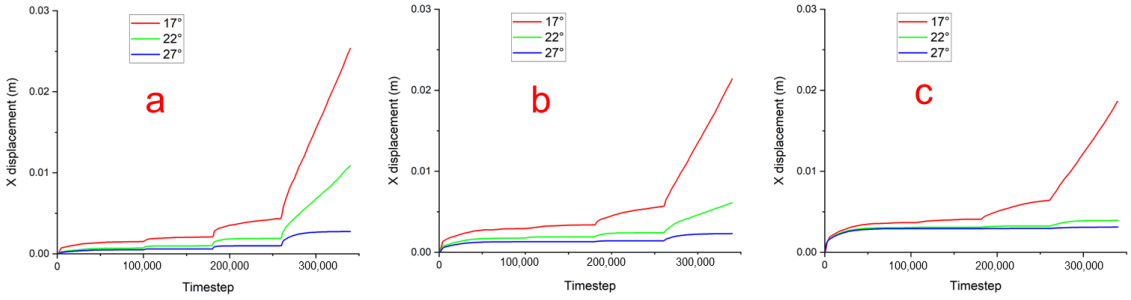

Fig, 5-17. *Sensitivity analysis of S0 friction angle by varying from 17° to 27°, showing the displacement of history points in X direction (a) H1, (b) H2 and (c) H3.*

The effect of cohesion is presented in Fig. 5-18. A decrease in cohesion from 25 kPa to 0 results in further displacement of H3 and demonstrates the development of a larger failed zone from the middle section to the upper section of the slope. When the cohesion increases to 50 kPa, the X displacement of the three history points approaches convergence, indicating a stable condition of the BOL slope. The sensitivity analysis demonstrates that slope stability is highly sensitive to the modelled friction angle and cohesion of the potential slip surface (bedding).

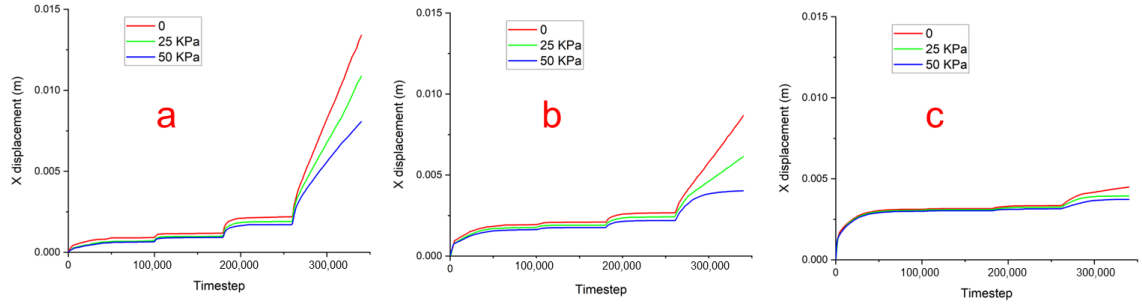

Fig. 5-18. *Sensitivity analysis of S0 cohesion by varying from 0 to 50 KPa, showing the displacement of history points in X direction (a) H1, (b) H2, and (c) H3.*

5.5. Discussion and Conclusions

This research has presented the combined use and application of RS techniques (e.g., terrestrial and UAV photogrammetry and satellite RS) and numerical modelling for landslide investigation.

The use of the Google Earth satellite images has demonstrated its effectiveness for extraction of large-scale landslide features (e.g., post-landslide slope topography and entire landslide boundary) as well as the identification of the strike of daylighting discontinuities in this study. Therefore, the combined use of UAV-RS and satellite RS can provide data for multi-scale landslide investigation: from large-scale mapping of the entire slope to small-scale mapping of the escarpment.

The data acquired from RS has been combined with the geological interpretation of landslide area to develop a basis for landslide numerical modelling. As reported by Agliardi et al., (2001), Stead and Wolter (2015), Bianchi Fasani et al., (2011) geological structures can control slope instabilities through the interaction with slope and discontinuity networks in different ways. In particular, referring to this specific case study, Scarascia Mugnozza et al. (Scarascia-Mugnozza et al., 2006) and Bianchi Fasani et al. (2011) presented the analysis, modelling and evolutional model of the area of the Caramanico Valley. The evolutional model was based on the studies from Patacca et al. (Patacca et al., 2008) and has been simulated through the use of FEM analysis. These studies demonstrated the role that the tectonic activity in producing local stress regimes that lead to large-scale slope instabilities and slope movements, especially in case of high-rate tectonic uplift in a short time interval and consequent releasing effects.

In agreement with what showed by these authors, this research attempted to model the behaviour of Lettopalena rock avalanche using numerical distinct element analysis. Diversely from previous study, in this case the numerical simulation was mainly focused on the role of anticline structures, structural setting of the slope (bedding variation) and river erosion.

Although previous studies have investigated the role of anticlines in slope instabilities using field investigations (Cui et al., 2018; Nilforoushan et al., 2021), the simulation of landslide behaviour in anticline limbs through numerical modelling has not been

well documented. Neither has the potential role of river erosion on removal of the toe and subsequent development of instability.

In this context, traditional manual surveys and RS mapping were employed to construct pre- and post-landslide geological models of the Lettopalena Paleolandslide. The geological models were then used to constrain numerical modelling, with the bedding inclination varying within the model in relation to the structural evidence extracted from field observations and RS analyses. It is highlighted that geological models and the interpretation of the geological-geostructural evolution of the area under study can play a key role in the rock avalanche back analyses, in agreement with what showed by Scarascia-Mugnozza et al. (Scarascia-Mugnozza et al., 2006) and Bianchi Fasani et al., (Bianchi Fasani et al., 2011). It is also pointed out how the integration of geological models and numerical analyses can provide an improved understanding of the landslide behaviour and factors controlling landslide triggering, such as the influence of river erosion and folded bedding with increasing inclination. Although river erosion may have been one of the predisposing factors, the modelling confirms that folded bedding (with inclination increasing at the toe of the slope) controlled the geometry of the failure, with the upper part of the slope (less inclined) remaining stable (in agreement with field observation and current landslide scar).

In addition, numerical modelling also infers a step-path sliding surface in the proximity to the river valley at the toe of the slope, which agrees with the field observation depicted in Fig. 5-16.

This paper presents the results of the back analysis of a catastrophic historic landslide that occurred in the province of Chieti, Italy, to provide a further understanding of the slope failure mechanisms. Various methods (e.g., UAV-RS, satellite RS, and traditional manual surveys) were combined to identify geological structures and interpret post-landslide features. Given the structurally controlled characteristics of the landslide, UDEC modelling was undertaken to determine the role of structural geology (e.g., folded bedding due to the presence of an anticline, discrete fracture network, and a thrust fault) and the influence of river erosion on slope stability. Due to potential variations in material properties associated with the potential basal slip surface, a series of sensitivity analyses were undertaken to

investigate the effects of these uncertainties on slope stability analysis.

The key conclusions arising from the study are:

1) Satellite images can be useful to improve data acquired from engineering geological and photogrammetric surveys.
2) Lidar data was able to effectively provide information on elevation, slope angle, and aspect from the topography of the post-landslide slope. This also allowed to depict the variation of the dip of S0 along the slope.
3) The point cloud generated by a series of UAV stereo images showed that the formation of a section of landslide escarpment was controlled by the discrete fracture network, where the upper boundary was related to the set J1 and the left boundary was related to sets J2/J3.
4) UDEC modelling was able to recreate the translational landslide failure mechanism, highlighting the fundamental role of gradual river erosion, which daylighted the bedding planes providing kinematic release for the landslide to occur.
5) The modelling suggests that termination of the landslide rear release surface was influenced by the presence of an anticline which provides variation in the inclination of folded bedding planes.
6) The investigation highlights the important role of the geological and geostructural model in numerical landslide simulations, both in term of predisposing factors and landslide geometry.
7) The modelling highlights the influence of step-path failure in the vicinity of the toe of the slope.
8) The sensitivity analysis emphasises the influence of discontinuity strength properties (i.e., friction angle and cohesion) of the basal slip surface on the extent of potential slope instability.

Chapter 6. Modelling discontinuity control on slope instability of a large open-pit mine in South America

6.1. Introduction

Discontinuities are critical to rock stability as they may behave as the plane of weakness along which instabilities may occur (Hutchinson, 1989). Under low stress environments, slope instability may be controlled by potential failure and movemnet along persistent discontinuites or interconnection of the discrete fracture network providing kinematic release of rock blocks (He et al., 2021b). However, if potential failure occurs in either large-scale slopes or underground excavations it can be more complex as rock deformation and fracturing may also occur when the principal stresses approach or exceed rock strength. In these cases, the configuration of fracture networks and estimation of rock mass strength have to be taken into account to perform stability analysis. When estimating rock mass strength, non-persistent discontinuities are evaluated as rock bridges between adjacent discontinuities improve rock mass quality improving stability (Stead and Wolter, 2015). Therefore, to generate more realistic representations of fracture networks, some researchers produce stochastic discrete fracture networks (DFN), whilst this increases computational complexity it is considered more robust when assessing rock mass strength and deformation properties (Gao et al., 2014; Wang et al., 2017; Cui et al., 2021).

To date, various methods have been developed to investigate the role of structural features in controlling rock slope stability and failure modes. At the laboratory level, due to the difficulties involved in replicating the rock properties (e.g., structural arrangement), rock-like specimens with artificially created fractures were created to analyse rock mass behaviour (Cheng et al., 2019; Zhang, Y. et al., 2020). Numerical methods upon a continuum, discontinuum and hybrid analysis are another principal measure to simulate the mechanical behaviour of rock mass in response to different stress conditions (Stead and Wolter, 2015). This allows discontinuity properties to be freely assigned accounting for different geological conditions in comparison to

laboratory tests. When numerical modelling is undertaken using a jointed rock mass, discontinuum and hybrid analysis are preferentially adopted as they are more capable of modelling discontinuous bodies with the inclusion of complex discontinuity networks (Stead and Wolter, 2015). A range of methods have been developed and are usually grouped as Discrete Element Methods (DEM) in which discontinuities, treated as boundary conditions, discretize a model into joint-bounded blocks where displacement and/or deformation (depending on intact rock blocks are deformable or rigid) of the blocks is allowed (Stead and Coggan, 2012). In addition, grain-based DEM methods, such as bonded-particle models (BPM) (Potyondy and Cundall, 2004) and Voronoi tessellation based models (Lorig and Cundall, 1989; Gao and Stead, 2014), are ultlised when modelling brittle rock fracturing. These models are composed of an assembly of variably-sized rigid particles and simulate independent movement (translation and rotation) and interaction of the particles that occur on their contacts. FDEM has been developed to provide reliable investigation of rock deformation, displacement, and fracturing, with integrated advantages of continuum and disconttinuum analysis (Munjiza et al., 1995b; Munjiza, 2004b).

In the field, discontinuities generally have geometrical variatiability (e.g., size, orientation, position and aperture), influencing the rock mass properties (Meyer and Einstein, 2002; Jimenez-Rodriguez et al., 2006). The variability is usually defined by the DFN to explicitly depict the geometry of each discontinuity, which is generated through different probability distributions (Miyoshi et al., 2018; Pan et al., 2019; Zhang et al., 2021). Coupled with numerical modelling, DFNs built upon the field mapping data has been used for a small-scale investigation in rock engineering, e.g., tunnel stability analysis (Lei et al., 2017c; Vazaios et al., 2019; Wang and Cai, 2020b). In large-scale slope engineering, such as large open-pit mines, DFN has been rarely considered because when complexity of incorporating a DFN into a discontinuum or hybrid numerical model, as it can dramatically increase computational time and power. Further research is still expected to advance to a comprehensive understanding of discontinuity control on large-scale slope instability.

This study investigates discontinuity control on a large open-pit mine slope instability incorporating the use of a DFN built from point cloud data that was acquired using remote sensing techniques. A 2D FDEM approach and a 3D DEM approach has

been used to provide an improved understanding of the slope instability. Modelling results were validated through in person observations and remote sensing surveys.

6.2. Study area description

The research study is focused on a large-scale mine slope instability that occurred within an open pit in South America. The mine is situated at an altitude in a range of 4,200 m to 4,600 m asl. The slope is characterized by approximately 30° overall slope angle and a 220-metre-high west slope in which a non-daylighting wedge deformation and multiple smaller bench failures have been observed and recorded.

6.2.1. Geological setting

The mine has a well-developed supergene enrichment profile of oxide copper and secondary chalcocite that overlies hypogene sulfide (chalcopyrite-molybdenite) mineralization. Geologically, the mine is situated at the southern end of the Maricunga mineral belt and originated in a cluster of monzogranites and dacitic porphyry intrusions along with associated hydrothermal-contact breccias. The lithology of the mine consists of monzogranites, dacite porphyries, breccias, diorites and epithermal deposits. The property of rocks associated with the Hoek-Brown failure criterion has been listed in Table 6-1 including unit weight (γ), material constant (mi), uniaxial compressive strength (σ_{ci}), Young's modulus (E_i) and Poisson's ration (v_i).

Table 6-1. *Intact rock properties associated with Hoek-Brown criterion.*

Rock	γ(t/m3)	mi	σci (MPa)	Ei (GPa)	Vi
Monzogranite	2.56	16.7	85.5	12.56	0.24
Dacite porphyry	2.5	21.1	66.58	30.86	0.22
Breccia	2.58	16	98.7	44.73	0.25
Diorite	2.64	10.4	89.29	46.41	0.18
Epithermal deposits	2.57	25	60	21.27	0.18

6.2.2. Landslide events

Slope instability is a critical safety concern during mining excavation phases throughout the pit but of higher risk on the west slope. Previous evidence of instability is visible on the west slope, and these have been monitored and recorded.

These include a number of closely distributed small-scale bench failures and a larger area associated with ongoing inter-ramp deformation. Fig. 6-1 highlights the boundary of the inter-ramp deformation by a white dash line and the 4 representative bench failures labelled 1-4.

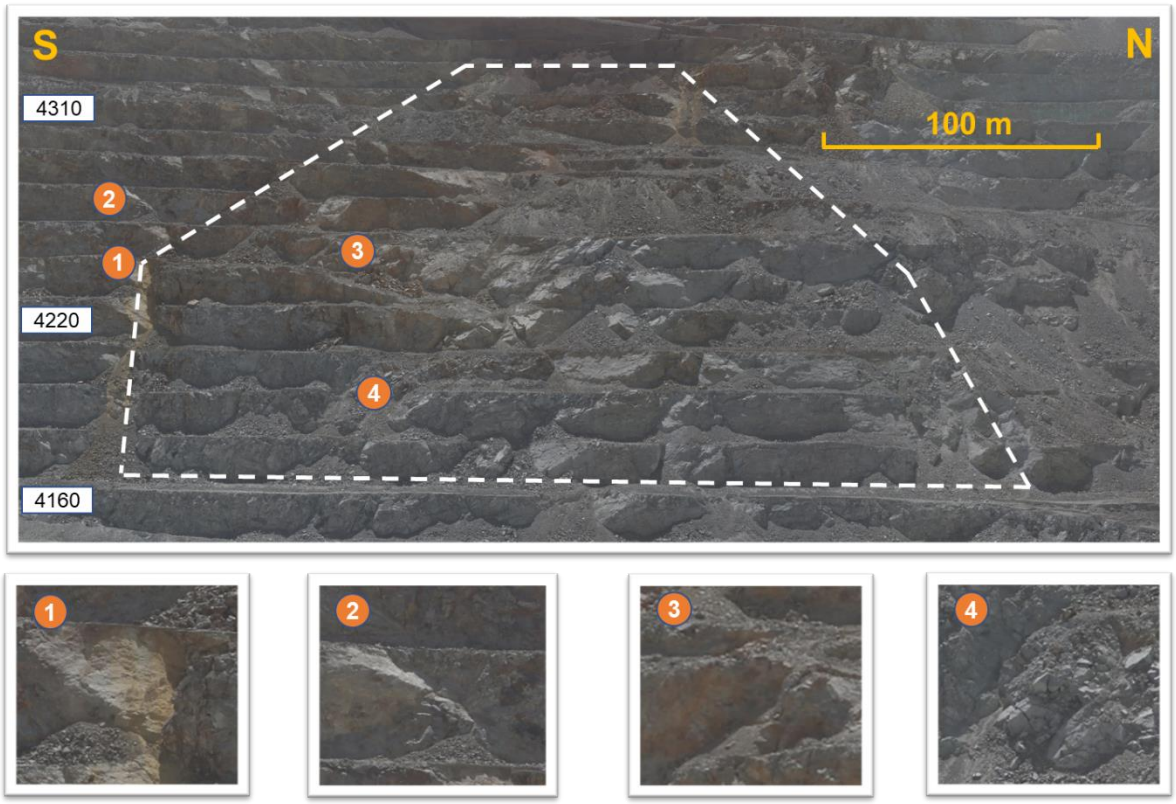

Fig. 6-1. *The west slope of the mine with highlighting a rough boundary of the inter-ramp instability in white and 4 bench failures for analysis.*

Both Fig. 6-1 and Fig. 6-2 indicate that the bench failures are structurally controlled and characterized by planar and/or stepped surface geometry. It can be seen in Fig. 6-2 a-c, failures are typically constrained by two discontinuity planes. In addition, Fig. 6-2d shows a stepped failure scar related to damaged bedding planes. After the occurrence of small-scale bench failures, an inter-ramp deformation over 12 benches, was detected by an SSR-323XT radar monitoring system, and the monitoring results are shown in Fig. 6-3. The first signs of movement were observed on May 29, 2020, with a peak velocity of 3.3 mm/h, and occurred after blasting activity on May 28, 2020. Increased movement was detected on June 6, 2020, with a peak velocity of 4-5 mm/h, as shown in Fig. 6-4. The deformation rate achieved the highest velocity of more than 9.1 mm/h on June 10 at 5:10 p.m. Following this the movement rate was

maintained at velocity magnitude of 0.2-0.3 mm/h in a transgressive/ regressive trend on the west slope.

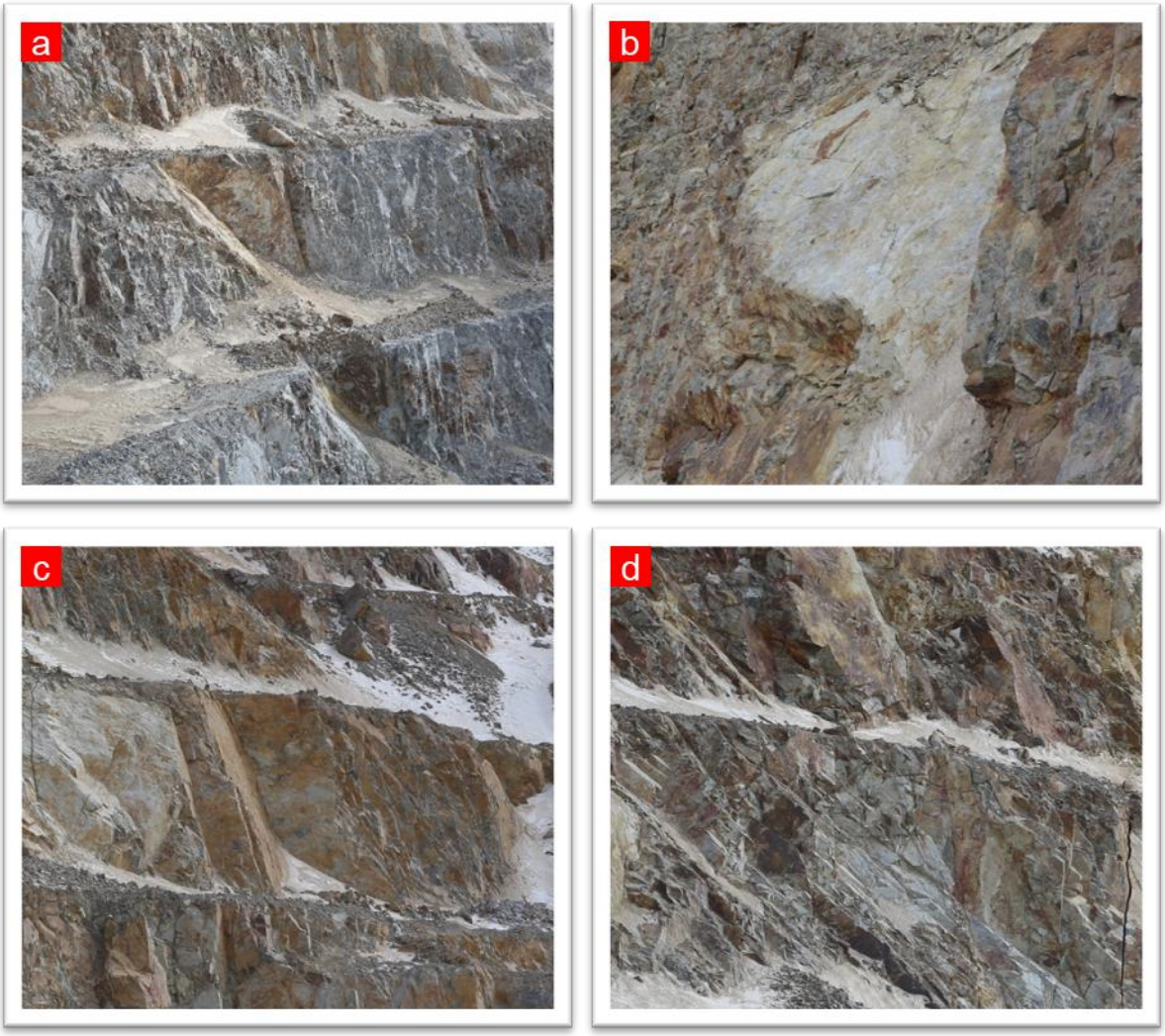

Fig. 6-2. *The scar of other bench failures in the west slope, showing the geometric characteristic of failure planes.*

The inter-ramp deformation is believed to be resulting from a non-daylighting wedge instability, contributing to rock bridge damage within the slope, allowing the displacement of the block moving inwards to the excavation. A superimposed effect of de-buttressing induced by sequential excavations at the bottom of the slope and accumulated blast damage may have potentially contributed to rock bridge damage and the observed slope deformation.

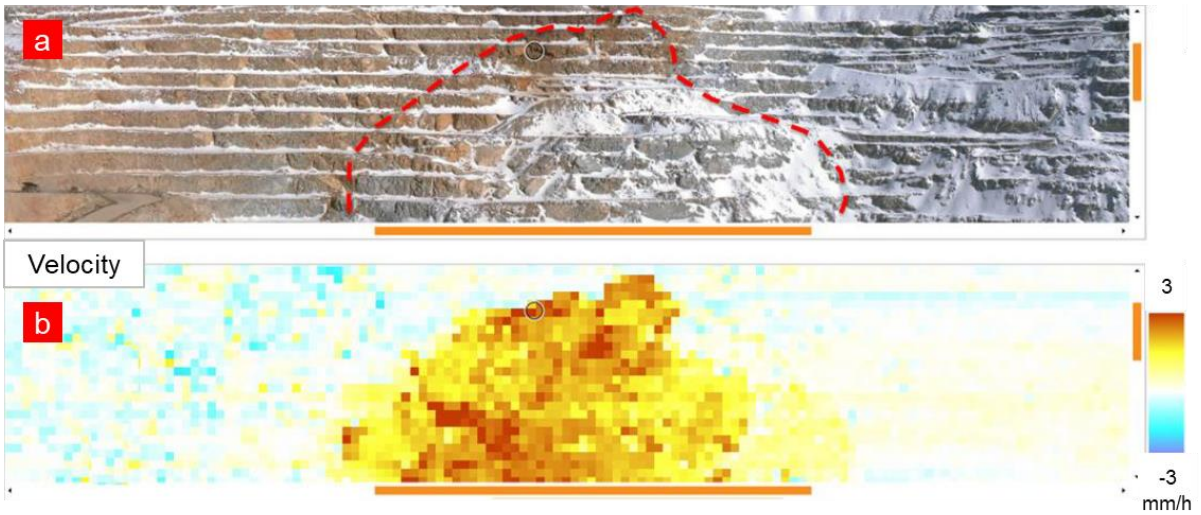

Fig. 6-3. *Inter-ramp deformation, a) an image depicts extent (with red) of the instability, b) displacement velocity obtained from radar data.*

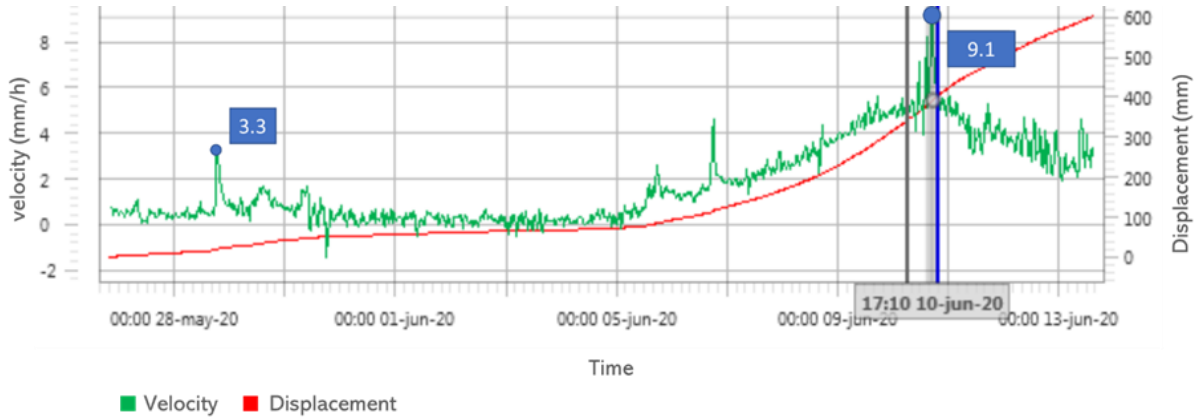

Fig. 6-4. *Radar data showing the velocity curve of the west slope in green and the curve of accumulated displacement in red.*

6.3. Methodology

This aspect of the research contains three sections: discontinuity characterisation based on RS data, simulation based on limit equilibrium analysis of bench failures, and the numerical modelling of the observed inter-ramp deformation. The primary objective of the work is to provide an improved understand of the mechanical properties of the rock mass and the underlying instability mechanism.

6.3.1. Data preparation

RS mapping was carried out at the west slope to acquire the digital terrain model (DTM) comprising of triangular meshes of 0.25-metre resolution. The derived DTM was then used to generate a 3D point cloud to provide data basis for identifying geological structures (faults and joints) using the Compass plugin (Thiele et al., 2017), provided by the software CloudCompare (CloudCompare, 2017). This is a manual process to determine the orientation of an exposed structure plane on which the size of a structure is measured with the maximum length of the plane. In addition, an index of a real fracture intensity (P_{21}), expressed as the total length of fracture traces per unit area, was used to evaluate the 2D intensity of joints used to generate a DFN for the rock mass.

In total, 923 joints were detected from the RS mapping. Three discontinuity sets (S0, J1 and J2) were identified, as shown in the stereonet plot (Fig. 6-5). Joints in set J1 can be related to bedding, with the mean orientation (50°/124°), and have the highest persistence (mean continuity: 2.8 m); Joints in set J2 have a mean orientation (51°/066°), being of less continuity and spacing compared with J1; Joints in J3 are sub-vertical and have a dip direction parallel to the slope face.

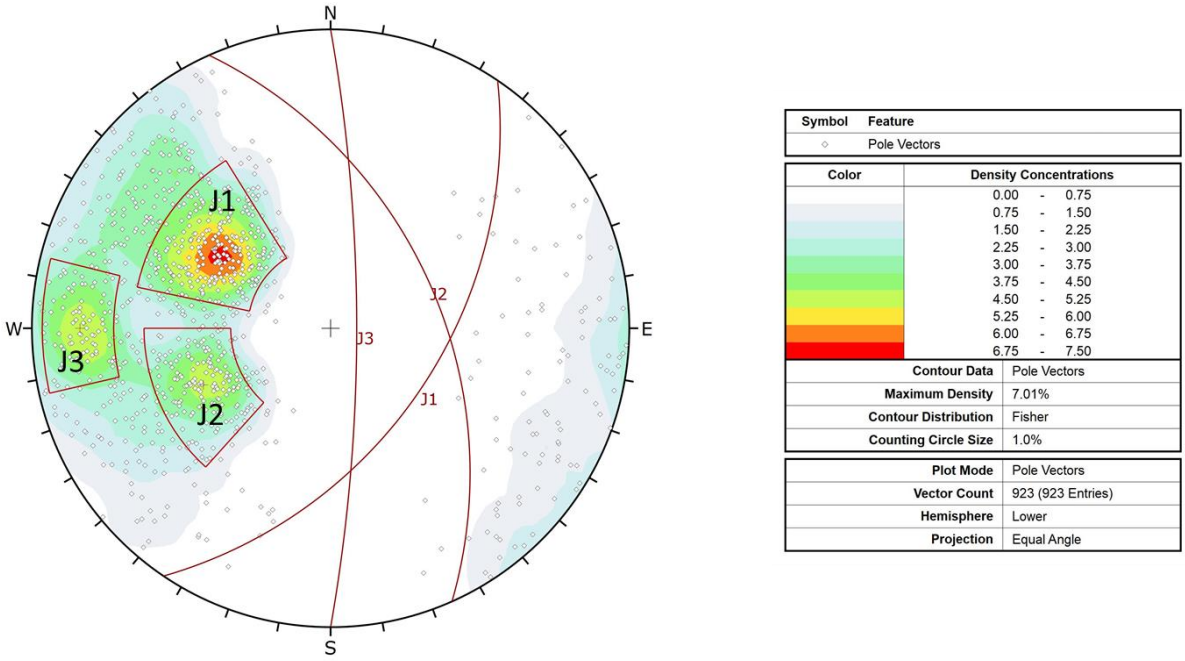

Fig. 6-5. *Lower hemisphere stereonet showing contours of 923 joint poles and 4 joint sets identified in the study area.*

Fig. 6-5 shows the amount of data dispersion of joint orientation that exists within the identified sets. In this context, a DFN model was generated in which 3 joint sets are defined by separate statistical distributions. The DFN properties (i.e., orientation, size and intensity) and their statistical distributions are listed in Table 6-2.

Table 6-2. *Properties of the 3 joint sets in the DFN model, including orientation, size, and intensity.*

Joint set	Orientation				size		Intensity
	Normal distribution				Log-normal distribution		constant
	dip		Dip direction				
	u (°)	σ	u (°)	σ	u (m)	σ	P21 (m/m2)
J1	50	9	124	12	0.68	0.61	0.36
J2	51	8	066	12	0.64	0.59	0.2
J3	80	5	090	70	0.65	0.6	0.16

In addition, six highly persistent joints/faults have been recognized in the west slope, their spatial positions and orientations are highlighted in Fig. 6-6. It is important to note that faults F1_1 and F1_2 are associated with J1 and faults F2_1, F2_2 and F2_3 are associated with J2 based on their orientation. The extent of the landslide depicted in Fig. 6-1 and Fig. 6-3 indicates that the observed slope deformation is likely to be constrained by the interaction of F1-1, F1-2, F2-1 and F2-3.

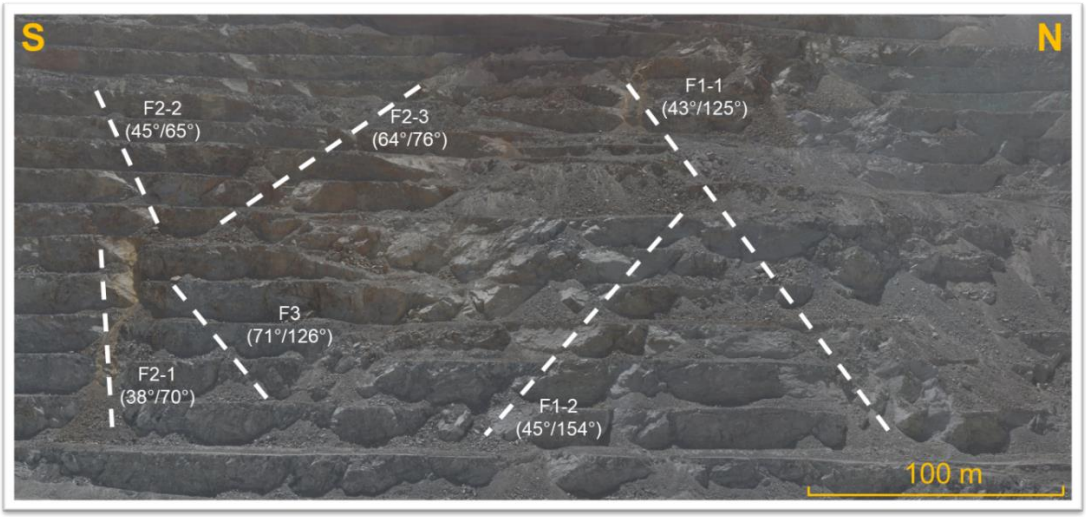

Fig. 6-6. *Six faults identified in the slope with their positions and orientations.*

Discontinuity strength (cohesion and friction angle) and elastic (normal stiffness and shear stiffness) properties used within the modelling have been provided in Table 6-3. Note that discontinuity strength properties were obtained by experiments, provided by the mining company, and deformation properties were determined based on field data.

Table 6-3. *Discontinuity properties associated with strength (i.e., cohesion and friction angle) and deformation (normal stiffness and shear stiffness).*

Type	Cohesion (KPa)	Friction angle (°)	Normal stiffness (Pa/m)	Shear stiffness (Pa/m)
Joint	50	35	$2e^{10}$	$1e^{10}$
Fault	30	25	$5e^{9}$	$2.5e^{9}$

6.3.2. Bench failure analysis

Four representative bench failures with clearly identified release surfaces were selected for kinematic and limit equilibrium analysis (Fig. 6-1). The release surfaces defined by joints or faults was measured from the point cloud data to identify their orientations and spatial locations. Based on the detected boundary information, geometric models of the bench failures were constructed. Limit equilibrium analysis was then carried out using discontinuity properties provided in Table 6-3, aiming to:

1) provide the 3D geometric model of the bench failures for better visualization.
2) approximate the volume of the bench failures.
3) Identify the kinematics and movement of these failures.

4) assess the factor of safety (FoS) values of the blocks.

The analysis estimate the FoS of each rock block defined as the ratio of resuting stresses to resisting stresses induced by its weight. This would provide a basis to determine if external factors were involved to trigger the occurred bench failures, e.g., potentially requiring additional external stresses if a calculated FoS > 1.

6.3.3. Numerical analysis

Two types of numerical analysis have been carried out, including 2D FDEM modelling and 3D DEM modelling, to estimate the mechanical property of rock mass and investigate the mechanism and development of the deformation, respectively.

6.3.3.1. 2D FDEM modelling

A trial version of the 2D FDEM code, Irazu (Geomechanica Inc., 2021), was used to conduct numerical uniaxial compressive tests to assess the rock mass strength and elasticity modulus. This methodology permits the dynamic simulation of multiple interacting bodies which can deform elastically, translate, rotate, interact, and fracture upon satisfying fracture criterion. The theory and principle of the method has been explained in previous publications (Munjiza et al., 1995, 2004), therefore it is not discussed in detail in this study.

The capacity of FDEM for simulation of rock mechanical behaviours associated with brittle rock fracturing has been extensively tested and validated, which is supported by high consistency between numerical results and corresponding experimental results (Rougier et al., 2014; Euser et al., 2019; Chau et al., 2020; Wang, W. et al., 2020).

Estimation of rock mass properties

Assessing rock mass properties promotes the understanding of the mechanical behaviour influenecing rock instability. Generalized Hoek-Brown failure criterion has been a preferred method to evaluate a rock masses properties, where a disturbance factor represents the degree of damage caused by blasting and/or stress relaxation (Li et al., 2011; Shen et al., 2013; Yang et al., 2020). Although the geological strength

index (GSI) was introduced to link the failure criterion to the geological conditions in the field, it is inadequate to account for the anisotropy of strength and deformation of rock mass. This is because it regards the rock mass as a homogeneous and isotropic material, which is not realistic (Eberhardt, 2012).

In this study, numerical uniaxial compression tests have been conducted to evaluate the rock mass properties (i.e., uniaxial compressive strength and Young's modulus). By varing the size of DFN embedded SRM, compression tests were carried out on it to obtain the representative elementary volume (REV) (Lei et al., 2017b; Ma et al., 2020; Wang and Cai, 2020). Note that the REV describes the minimum volume beyond which any submass behaves essentially like the whole rock mass.

6 models were constructed with the width of 10m, 20m, 30m, 40m, 50m, and 60m, respectively, and a height to width ratio of 2.5. For numerical uniaxial compression tests, a low constant loading velocity (CLV) was applied on the horizontal boundaries of models. The loading velocity was controlled in such a way that models were not loaded faster than the velocity with which the stresses can be transferred numerically through the entire tested model. In addition, compression was also applied to the REV model in other 3 directions (i.e., E-W, NW-SE, and NE-SW) to estimate the anisotropy of rock mass properties induced by stochastic joints (Fig. 6-7).

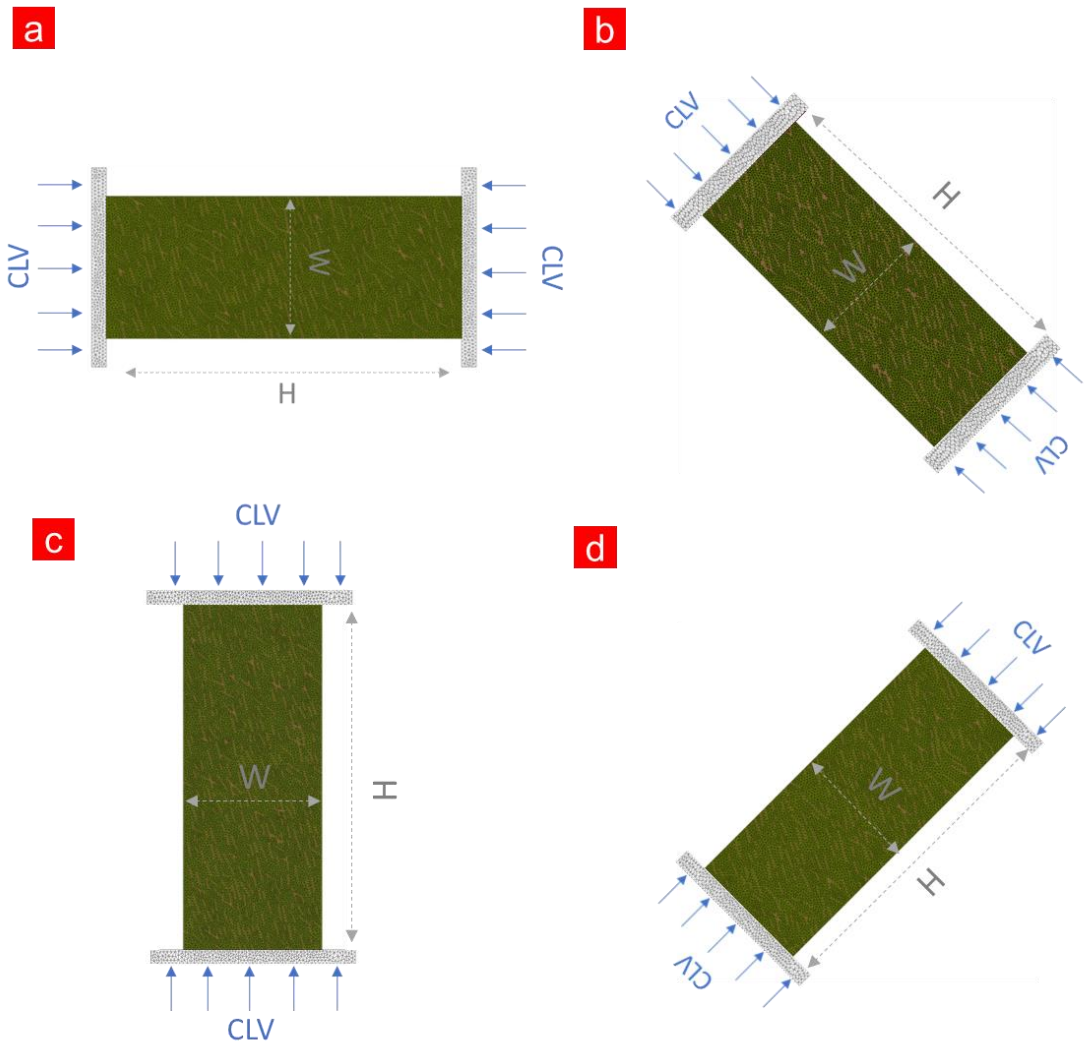

Fig. 6-7. *Numerical uniaxial compression tests on a DFN embedded SRM with a boundary condition of constant loading velocity in different directions, a) E-W, b) NW-SE, c) N-S and d) NE-SW.*

6.3.3.2. 3D DEM modelling

The 3D DEM code 3DEC (Itasca Consulting Group, Inc., 2017) was used for numerically simulating the inter-ramp deformation. For the details associated with model setup (such as selection of constitutive models for rocks and discontinuities, the damping strategy, and modelling procedures), please refer to the paper (He et al., 2021b). Unlike the previous case study, In this modelling deformable blocks were assumed considering the fact that rock bridge damage has been observed in the field.

A simplified slope geometry was constructed for modelling, with the overall slope angle of 30°, the bench angle of 75°, and the bench height of 15 metres (Fig. 6-8). In

the modelling, the jointed rock mass was considered equivalent continuum material (Wang and Cai, 2020), and only the large critical discontinuities (i.e., F1-1, F1-2, F2-1 and F2-3) were included in the model to reduce complexity and computational efficiency. The properties of the equivalent intact rock were assessed through the aforementioned numerical compression tests. A fixed boundary condition was applied to the base and sidewalls of the model and boundaries were extended from the zone of interest to ensure no boundary effects.

Table 6-4. *Property of blasting-induced weak zones related to the Mohr-Coulomb failure criterion.*

Density	Young's Modulus	Cohesion	Friction angle	Poisson's ration
2.58 t/m^3	5 GPa	0.3 MPa	20 °	0.25

The research aims to understand the influences of sequential excavations and blasting on the development of the deformation. In this context, two series of modelling have been carried out: modelling 1 incorporating sequential excavations from excavation 1 to 3 (shown in Fig. 6-8a) and modelling 2 considering sequential excavations and the creation of a blasting-induced weak zone (shown in Fig. 6-8b, c and d). The weak zone was extended 15 metres from each excavation to simulate a damage zone caused by poor blasting. The property of the weak zone has been summarized in Table 6-4 which is associated with the Mohr-Coulomb failure criterion. A representative history point was placed on the slope to monitor rock bridge failures and record the development of velocity magnitude and total displacement within the model.

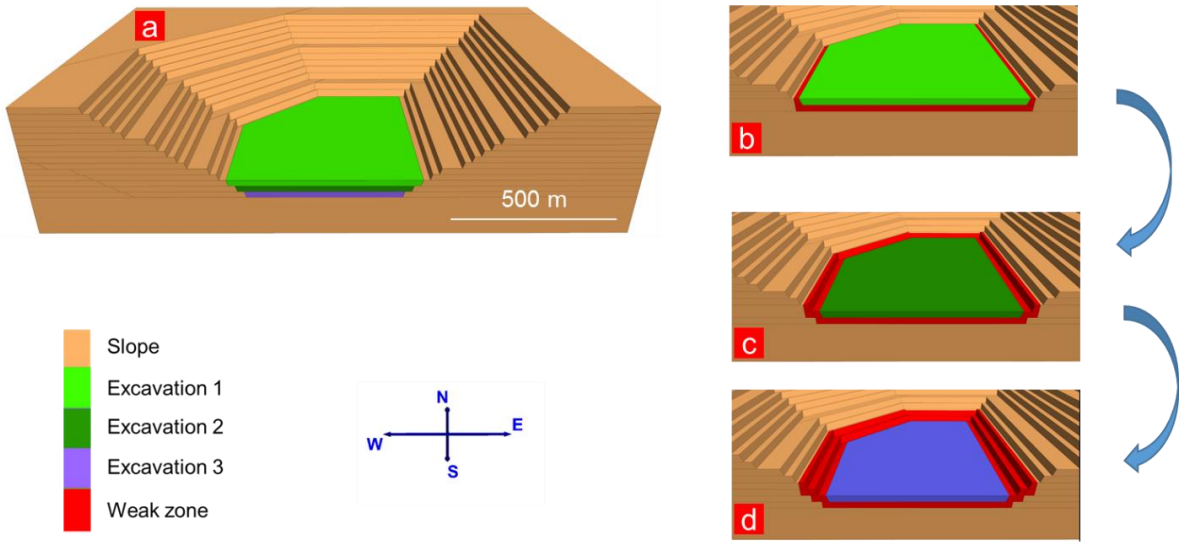

***Fig. 6-8**. 3DEC modelling strategy, a) method 1 incorporating sequential excavations from excavation 1 to 3, b) method 2 incorporating sequential excavations and blasting-induced weak zones.*

6.4. Results

6.4.1. Interpretation of bench failures

Fig. 6-9 presents a 3D geometric model of failure 1 that is constrained by F1 (45°/70°) and a joint in set J2 (83°/135°). The bench was defined by a 75° face inclination and 15-metre slope height. A failure volume of 423 m^3 was estimated, and FoS is approximately 0.71 for failure 1. In addition, Table 6-5 summarizes the results of the analysis associated with these 4 bench failures, highlighting discontinuities that define the boundary, estimated volume, the sliding direction and calculated FoS values of failures. It can be seen that failure 3 is in a marginally unstable state and failure 4 is in a marginally stable state based on the input geometry and the modelled discontinuity shear strength properties.

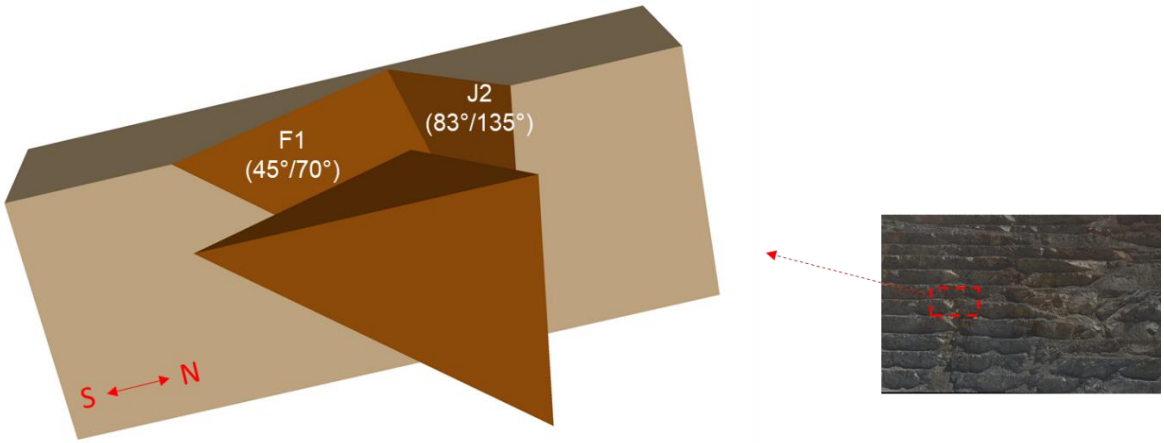

***Fig. 6-9.** A representative wedge sliding shows a structural control on constraining the geometry.*

***Table 6-5.** The result of bench failure analysis including involved structures, estimated volume, sliding direction and FoS value.*

Bench failure	Involved structures	Volume (m^3)	Sliding direction	FoS
1	F1(45°/070°) / (83°/135°)	423	45°/70°	0.71
2	F2-2(38°/056°) / J1(71°/111°)	172	38°/56°	0.61
3	J3(81°/78°) / J1(63°/150°) Basal: J1 (38°/131°)	226	38°/131°	0.95
4	J1(44°/154°)/J2(63°/056°/)	481	39°/121°	1.04

6.4.2. Rock mass properties

Fig. 6-10 presents 6 stress-strain curves derived from numerical uniaxial compressive tests implemented on a SRM of different sizes. Size-dependent characteristics of rock mass properties are observed when the model is smaller than 40m * 100m and they become size-independent when the model size is larger than 40m * 100m. For example, the value of UCS reduces with the increase of the model size, achieving a convergence (14 MPa) at the size 40m * 100m. The result indicates that the SRM (40m * 100m in size) is more representative of on-site rock mass and may be used for estimation of rock mass properties.

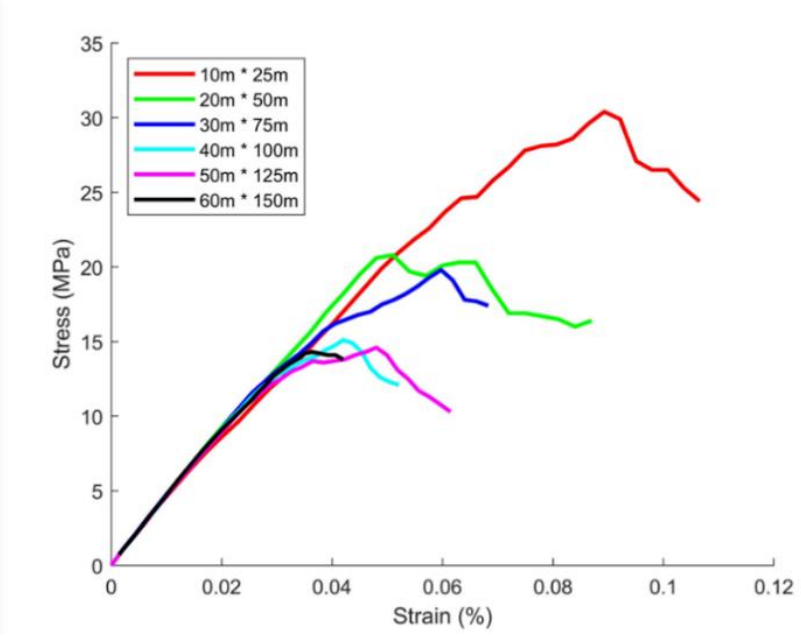

Fig. 6-10. *representative axial stress-strain curves for a SRM of different sizes (width*length).*

In respect of rock anisotropy, Fig. 6-11a shows axial stress-strain curves derived from uniaxial compression tests in response to different loading directions, highlighting a direction-dependent characteristic of strength and elastic properties. Specifically, UCS of the rock mass has the maximum strength (34 MPa) in the NE-SW direction and the minimum strength (8 MPa) in the NW-SE direction (Fig. 6-11b). Concerning Young's modulus, it decreases to the minimum (33 GPa) when stress is loaded in the NW-SE direction (Fig. 6-11c).

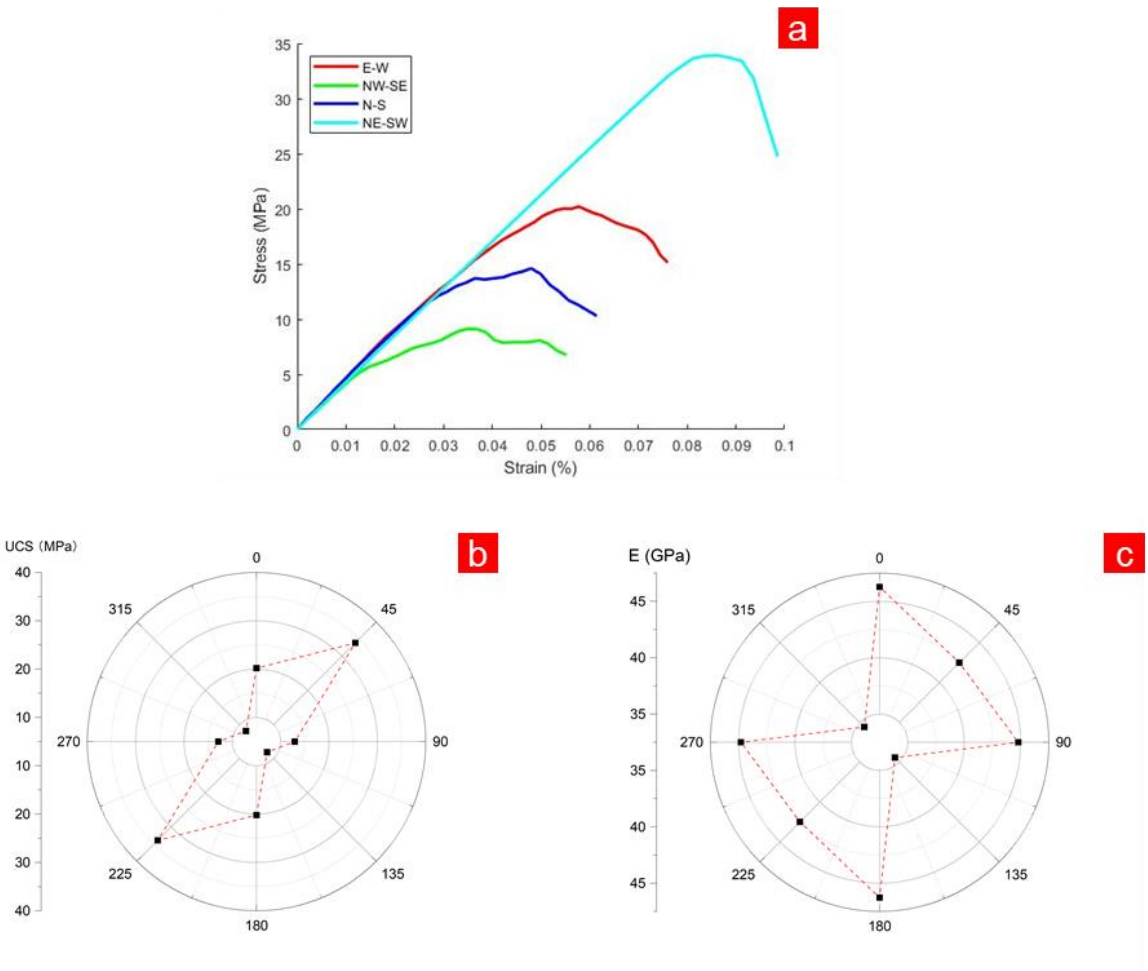

Fig. 6-11. *A) Axial stress-strain curves of a REV model under different loading directions, b) UCS values in different directions c) Young's modulus values in different directions.*

6.4.3. 3D DEM modelling results

6.4.4.1. Results of modelling 1

The results of modelling 1 have been presented in Fig. 6-12 (excavation 1), Fig. 6-13 (excavation 2) and Fig. 6-14 (excavation 3), showing the total displacement of the slope in response to sequential excavations. From excavation 1 to 3, minor displacements of rock blocks are observed, and there are limited increases in total displacements. This is also reflected in Fig. 6-15 where, the modelled history point attains 0.02 m of the maximum total displacement and then equilibrium is achieved.

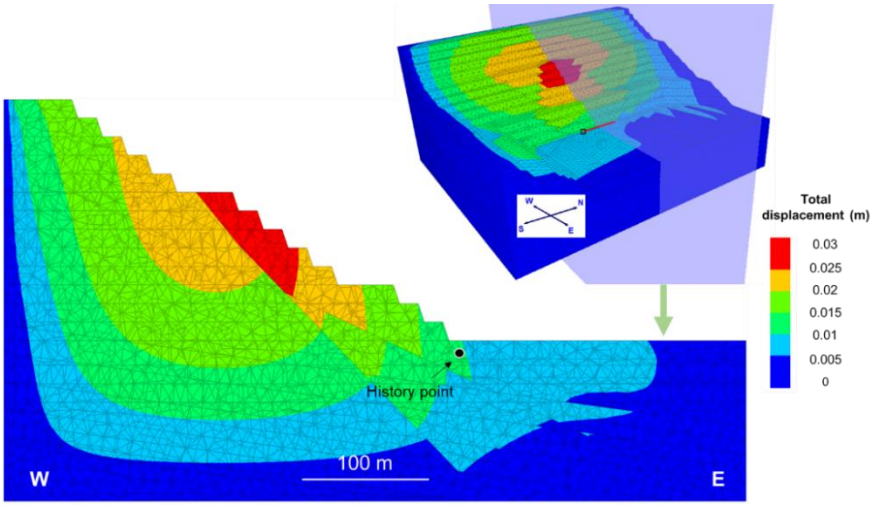

Fig. 6-12. *Result of modelling 1 after excavation 1 at timestep 20000, showing the total displacement of the slope.*

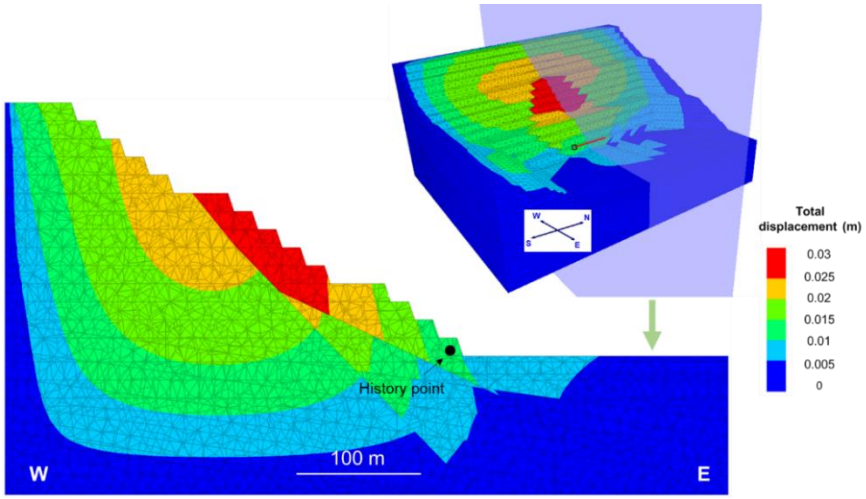

Fig. 6-13. *Result of modelling 1 after excavation 1 at timestep 25000, showing the total displacement of the slope.*

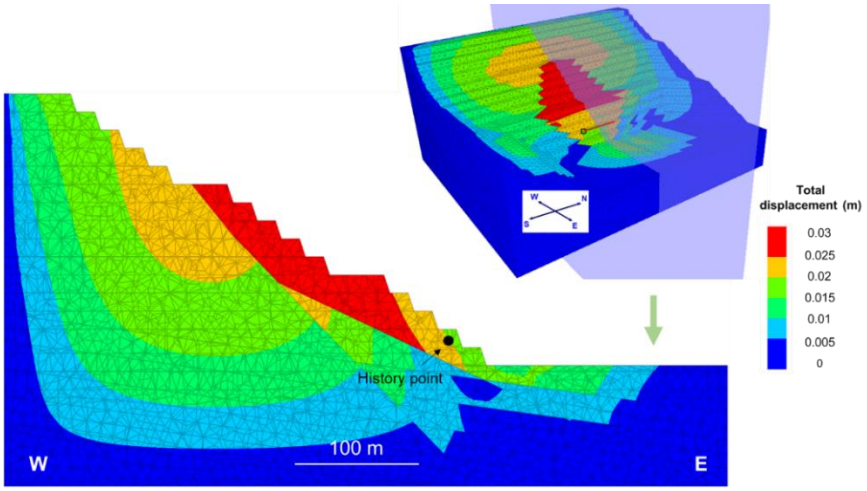

***Fig. 6-14**. Result of modelling 1 after excavation 1 at timestep 35000, showing the total displacement of the slope.*

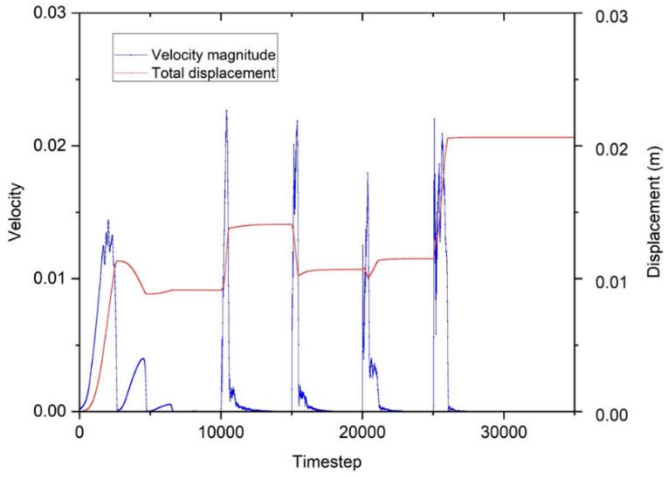

***Fig. 6-15.** Velocity and displacement curves of the history point against timestep from modelling 1.*

6.4.4.2. Results of modelling 2

The results of modelling 2 are presented in Fig. 6-16, Fig. 6-17 and Fig. 6-18. Few total displacements of the slope are observed as a result of excavation 1 (Fig. 6-16). However, from excavation 2 (Fig. 6-17) to excavation 3 (Fig. 6-18), differential displacements between the main slope and the wedge are distinct and magnified (approximately 0.08 m after excavation 2 and 0.3 m after excavation 3). The wedge undergoes significant displacement and is indicative of slope instability.

The modelled displacement of the history point is also recorded in modelling 2, as shown in (Fig. 6-19). The displacement involves 5 stages,

1) Stage 1 (timestep 0-10000): At this stage, high values of properties are assigned to rock mass for the estimation of in-situ stresses and an equilibrium state is achieved (velocity approaching 0).

2) Stage 2 (timestep 10001-15000): The original values of properties are assigned to rock masses. It can be seen that at the beginning of this stage a sudden increase in velocity and a slight increase in accumulated displacement is observed. After this, the velocity decreases to a negligibly small value indicating a stable state for the slope.

3) Stage 3 (timestep 15001-20000): In the beginning, like stage 2 a sudden increase in velocity is observed, then this rapidly drops to zero m/s. Although there is a slight change in the displacement, the slope is considered stable.

4) Stage 4 (timestep 20001-25000): Compared with stage 3, more peak velocity is achieved immediately after excavation 4. But the velocity drops to zero m/s consequently indicating that the slope is under a stable condition. During stage 4, the modelled history point has gained approximately 0.05 m of total displacement.

5) Stage 5 (timestep 25001-35000): Excavation 3 is performed at this stage. Like stage 4, a sudden increase in velocity is also experienced. The difference is that at this stage, the slope is no longer stable, and although the velocity drops and fluctuates around 0.025 m/s after timestep 29000, the displacement continues to increase which is representative of instability associated with the modelled geometry.

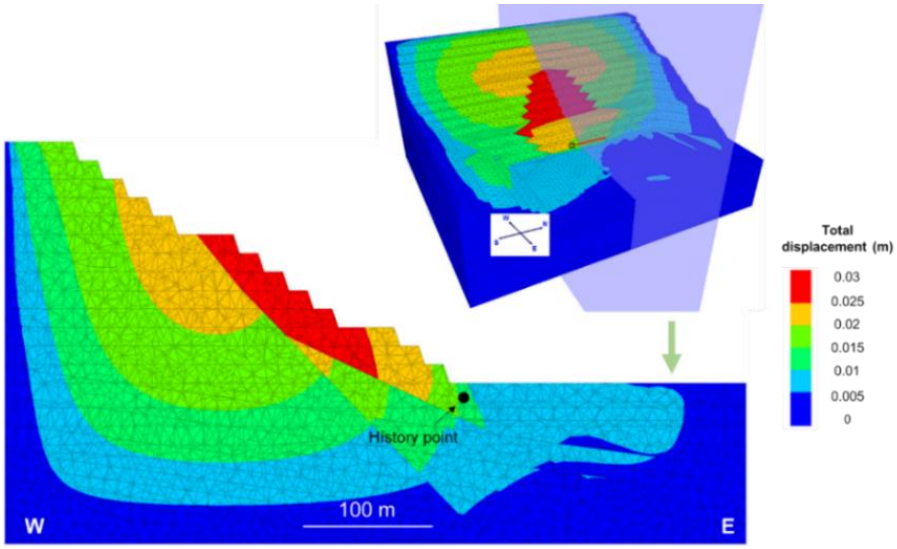

Fig. 6-16. *Result of modelling 2 after excavation 1 at timestep 20000, showing the total displacement of the slope.*

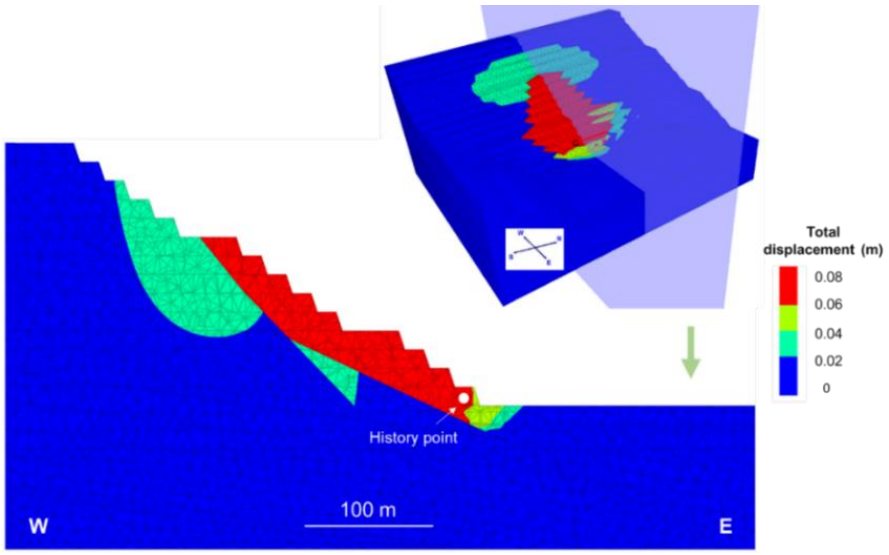

Fig. 6-17. *Result of modelling 2 after excavation 2 at timestep 25000, showing the total displacement of the slope.*

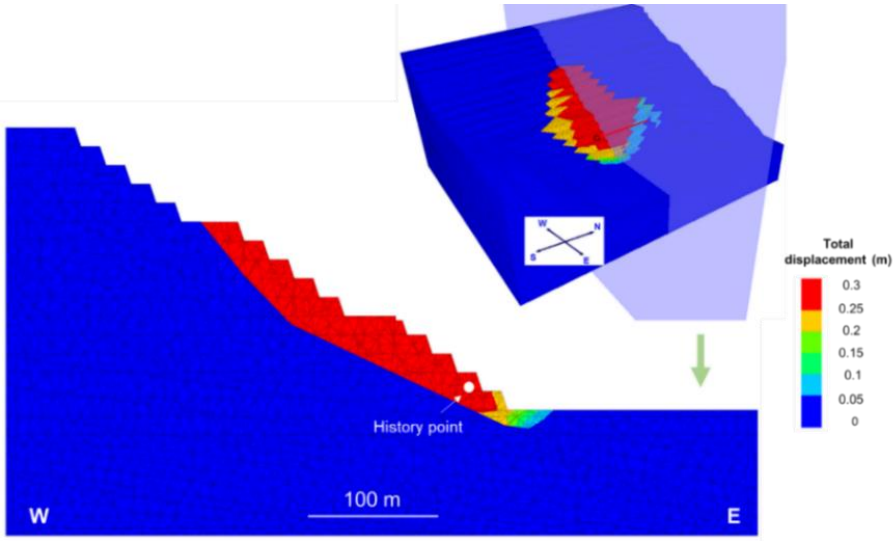

Fig. 6-18. *Result of modelling 2 after excavation 3 at timestep 35000, showing the total displacement of the slope.*

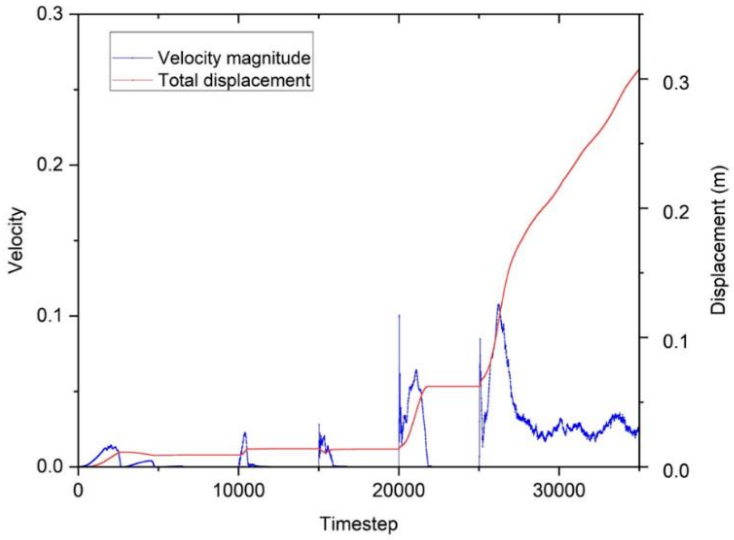

Fig. 6-19. *Velocity and displacement curves of the history point against timestep from modelling 2.*

6.5. Discussion and Conclusions

The limit equilibrium analysis has confirmed the controlling influences of discontinuity orientation and shear strength properties on the bench-related instabilities. However, one of the cases simulated had a calculated FoS value marginally greater than 1 (see Table 6-5). This suggests that additional driving forces may contribute to triggering the failures. It has been well recognized that repeated blasting can cause the progressive degradation of joint shear strength (e.g., reduction in the cohesion of discontinuities) (Kong, 2012; Siamaki et al., 2018), which might be the case in this mine, particularly for the ongoing larger-scale deformation and sequential extraction of the open pit.

Unlike some previous numerical tests using the SRM models with less than 1m in size (Laghaei et al., 2018; Liu et al., 2021), SRM samples used in the present study were tens of metres in size given the potential influence of joints in the west slope. Results of REV tests show that rock mass properties (i.e., UCS and Young's modulus) approach scale independence when the width of the SRM model increase from 10m to 40m. During this process, UCS decreases and then converges to a fixed value, whose trend is consistent with the findings in previous studies (Gao et al., 2014; Laghaei et al., 2018). The REV size is influenced by the geometry of DFN, and determined by the combination of DFN properties (e.g., fracture density, maximum trace length, and spacing). This has been investigated and demonstrated by previous studies (Pariseau et al., 2008; Schultz, 1996; Zhou et al., 2022), with the findings of empirical relationship between maximum trace length/spacing and REV size (e.g., REV size is 10 times the maximum joint spacing). Although a uniform result associated with the relationship was not obtained, these findings can provide critical basis to estimate REV size quickly and roughly from DFN properties.

The anisotropy of rock mass properties has been tested by a series of numerical uniaxial compression tests. The rock mass exhibits the lowest values of UCS and Young's modulus in the NW-SE direction that is approximately parallel to the dominant dip direction of joints (presented in Fig. 6-11). The result agrees with the findings obtained from previous investigations that UCS falls to a minimum when stress loading direction is paralleled to the orientation of geological structures (Hoek and Brown, 1980b; Nasseri et al., 2003; Kim et al., 2016; Cui et al., 2021). In addition,

it indicates that when the maximum principal stress is oriented in the NW-SE direction the rock mass is more prone to failure. In this case study, the maximum principal stress caused by topography overburden on the west slope is in such an unfavourable orientation, which may promote rock bridge failures.

Each excavation can cause a sudden increase in velocity magnitude, and this can be observed both in modelling 1 and 2. The difference is that in modelling 1 the slope remains stable constantly, but the slope becomes unstable in modelling 2. The result of modelling 2 is consistent with radar data of the slope deformation as presented in Fig. 6-4. The comparative analysis highlights that the weak zone associated with excavation 3 is the key aspect of triggering the slope deformation. The modelling result also emphasizes the controlling effect of the rock bridge constrained by F1-2 and F2-1 at the toe of the slope on the slope stability through resisting the stress from the overlying rock block. However, mining excavation as the pit deepens gradually removes rocks from the rock bridge and poor blasting may cause the fracturing and damage of the rock bridge. This superimposed effect may weaken the strength of the rock bridge and the induced de-buttressing effect may facilitate the observed inter-ramp deformation.

This research provides the back analysis of observed slope instability at an open pit case study in South America that is characterized by an ongoing inter-ramp instability and multiple bench failures. A series of 3D geometric models were constructed to represent bench failures. Based on these models, limit equilibrium analysis was conducted to estimate the FoS of rock blocks. In addition, numerical analysis based on a 2D FDEM approach and a 3D DEM approach has been carried out to provide an improved insight into potential mechanisms associated with the ongoing inter-ramp deformation. The key conclusions arising from the study are:

1) Limit equilibrium analysis confirms the controlling influence of discontinuity orientation and shear strength properties on bench instability and highlights that external factors (such as blasting) may also contribute to trigger bench failures in the west slope of mine case study.
2) Numerical compression tests based on 2D FDEM modelling examined the anisotropy of rock mass properties showing U-shaped UCS and Young's modulus curves against inclination where the trough was observed when

stress loading direction is parallel to the predominant direction of joints.

3) 3D DEM modelling is able to recreate the observed inter-ramp deformation, showing the control of rock bridge, constrained by F1-2 and F2-1 at the toe of the slope, on the deformation.
4) 3D DEM modelling highlights that blasting-induced weak zones and the effects of sequential extraction are potentially key triggers for the observed slope deformation.

Chapter 7. Discussion

Benefits of RS surveys for landslide analysis

This research has presented the combined use and application of RS techniques (e.g., terrestrial and UAV photogrammetry and satellite RS) for landslide investigation.

Photogrammetry can provide high-resolution stereo images from which a representative 3D point cloud can be generated using SfM algorithms. It has been demonstrated that the point cloud data acquired from UAV photogrammetry is comparable, in density and accuracy, to those generated by terrestrial and airborne laser scanning at a lower cost (Cook, 2017; Cooper et al., 2021). In addition, when compared with laser scanning, photogrammetric mapping provides better visual representation of textures, providing additional clues and insights to interpret the relationship between local joints and the formation of the escarpment.

Laser scanning techniques are also useful for large-scale landslide analysis due to their effectiveness of extracting slope elevation information. For example, it is possible to delineate the 3D geometry of a large-scale slope and construct a digital terrain model (DTM) through airborne laser scanning. The derived DTM then can be used for limit equilibrium analysis (Kargar et al., 2021), and numerical analysis (He et al., 2021b) of slope stability. In addition, considering that landslides result in mass movement and the change of slope topography, it is possible to use multi-temporal (pre- and post-landslide) lidar data to detect them (He et al., 2021a), and estimate failure volumes (Francioni et al., 2018a). Moreover, with the elevation information provided by lidar data, slope topographic features can be interpreted, including the interpretation of slope aspect, curvature, angle, and height. The results can provide the basis for kinematic analysis of slope stability (Brideau et al., 2012), and LSM (He et al., 2021a).

Although providing a relatively low resolution, satellite RS has demonstrated its effectiveness for extraction of large-scale landslide features (e.g., post-landslide slope topography and entire landslide boundary) as well as the identification of the strike of daylighting discontinuities in the case study of the catastrophic rock

avalanche in Italy.

Therefore, the combined use of UAV-RS and satellite RS can provide data for multi-scale landslide investigation: from large-scale mapping of the entire slope to small-scale mapping of the escarpment for comprehensive landslide investigations.

Precautions when conducting LSM

Machine learning and deep learning modelling are statistically based, and their modelling performance highly relies on input data. In landslide case studies, prejudging and identifying the fundamental relationships (e.g., logistic relation, spatial relation, and temporal relationships) between landslides and their factors (i.e., predisposing factors and triggering factors), and the scientific selection and deployment of these factors are critical for ML predictions. Therefore, this research has demonstrated the incorporation of discontinuities into ML models for landslide prediction.

Apart from the type of input variables, data quality is also critical when implementing ML. In some previous studies, temporal matches between landslides and their factors have not been analysed in detail. For example, factors associated with slope geometric conditions (e.g., slope angle, aspect, and slope height) derived from post-landslide LiDAR elevation data was used for LSM. Logistically this doesn't make sense because landsliding will alter the slope topography and transform the slope from an unstable condition to a stable condition, and the post-landslide features are not triggers of the landslide. This misleading information may result in unexpected modelling results and significantly reduce prediction accuracy. This is also the case associated with other changeable factors during landsliding occurring in a short period, such as LULC, NDVI, and rainfall.

In addition, a clear date of landslide occurrence is also required. In some case studies, landslide inventory provides accurate landslide locations, but information the events date is ignored, which could also cause uncertainty about the temporal match. Landslide detection using multi-temporal elevation data is a potential solution

to identify the location and size of landslides (as used in Chapter 3), with which the time of landslide occurrence can be interpreted within a timespan. From this point of view, it is critical to establish a comprehensive database with inclusion of legacy data, which is able to provide baseline information for a temporal analysis and opportunities for the understanding of long-term landscape evolution behaviours. The benefits from the comprehensive databases (i.e., Digimap and CCO databases) available in the UK, LSM for north cliff of SW England was implemented. It is also encouraged to establish regional (elsewhere) or global databases for LSM, which can include legacy data, current data and even future prediction data.

Benefits of the multi-level landslide investigation

Integrating LSM and numerical modelling analysis can establish a system that can be used for landslide investigations. In the system, ML-based LSM provides the estimation of the landslide probability for an extensive region. As seen from Chapter 3, information on most independent variables were directly or indirectly obtained from open-source databases, enabling ML landslide prediction to be readily carried out for regional-scale investigations. Following this, numerical modelling can be used to concentrate on specific slopes with high landslide risk, providing a more accurate and reliable prediction of slope stability conditions. In addition, more details can be obtained from numerical analysis, such as the deformation and displacement of rock mass, tension crack development, brittle rock fracturing.

The integration of manual and RS techniques have been used for landslide investigation, providing additional data for analysis. For example, engineering-geological mapping and RS mapping have been combined for discontinuity identification. The combination of them can supplement each other and provide a significant number of identified discontinuities. This provides a basis to more efficiently identify the discontinuity sets and characterise the variation of discontinuity geometry. In addition, the result of manual mapping and RS mapping can mutually be verified. This can largely increase the confidence to ensure the reliability of the results if comparable results are obtained from both surveys. However, when results are not comparable, the combination of them may cause higher data dispersion (e.g., dispersion of discontinuity orientation) and increase uncertainty of discontinuity

characterisation. This may require either experience to judge the reliability of each result or their combination with the consideration of their variations.

Considerations of 2D and 3D numerical modelling

This research has presented the use of different numerical methods, both 2D and 3D, for landslide simulation. The 3D analysis can incorporate additional characteristics (e.g., 3D slope geometry and 3D discontinuity characterisation), and provides the basis to evaluate additional influences on slope stability. This was demonstrated in the Hell's Mouth landslide case in which the unique slope topography and the formation of the inlet contributed to defining the boundary of the landslide. Compared with 2D modelling, 3D discontinuity characterisation is more able to characterize the geometry of rock mass, rock bridge and discontinuities (Elmo et al., 2018).

However, a major disadvantage of 3D DEM modelling, especially with the integration of complicated fracture networks, is excessive computational costs (Elmo et al., 2018). Some attempts have been proposed to simplify fracture networks and reduce computational costs. One representative method is the use of weak equivalent rock to characterize the jointed rock mass with the same values of the strength (UCS) and elasticity (Young's modulus and Poisson's ratio) properties obtained from numerical compression tests. Relying upon this, some other methods have been developed by eliminating small discontinuities and remaining relatively large discontinuities in equivalent rocks (Ma et al., 2019, 2020). However, these methods intrinsically use an equivalent continuum rock to replace a jointed rock mass, which may diminish mechanical anisotropy of rock mass. To solve this problem, the elastic anisotropy of rock masses can be defined by a compliance tensor in 3D dimensions, where deformation properties in all directions can be estimated through numerical triaxial compression tests (ISRM, 1983; Laghaei et al., 2018). Moreover, the micro and macro fracturing process, and the post-failure process cannot be fully characterised using these equivalent properties. Therefore, when analysing brittle rock fracturing the methods based on equivalent properties must be carefully used. Under high stress environments, rock deformation and fracturing may occur when the principal

stresses approach or exceed rock strength.

When deciding which model to use, one of the major considerations is whether a 2D model can represent the structural arrangement and the analysed domain (as seen in Fig. 7-1), as 2D modelling undoubtfully takes advantage of less computational costs. This is the reason for the application of the UDEC code to model the Italian landslide due to the simply identified failure geometry which is dominantly constrained by bedding as the basal sliding surface. Therefore, 2D modelling can effectively investigate the failure mechanism.

When failure geometry is complicated, 3D modelling is preferred. This is the case of Hell's Mouth landslide analysis and the analysis of the mine slope instability in South America, where 3DEC modelling was used to simulate rock mass behaviours. However, incorporating 3D modelling with complex fracture networks may result in high computational costs. In this context, model simplification is necessary in order to reduce computational time and resource. For different scenarios of slope instability, various simplification methods are readily available. Under low stress environments, slope instability may be controlled by potential failure and movement along persistent discontinuities or interconnection of the discrete fracture network. Model simplification can be undertaken by considering rocks as rigid materials. The model is discretized by discontinuities without meshing to reduce the number of discretized rock blocks, significantly minimizing computational costs (such as the one shown in Hell's Mouth case study). Under high stress environments, rock deformation and fracturing may also occur when the principal stresses approach or exceed rock strength. Model simplification can be carried out by using equivalent properties to characterize the rock mass that is composed of short-length fractures and reserving large discontinuities (as shown in mine slope instability analysis in South America).

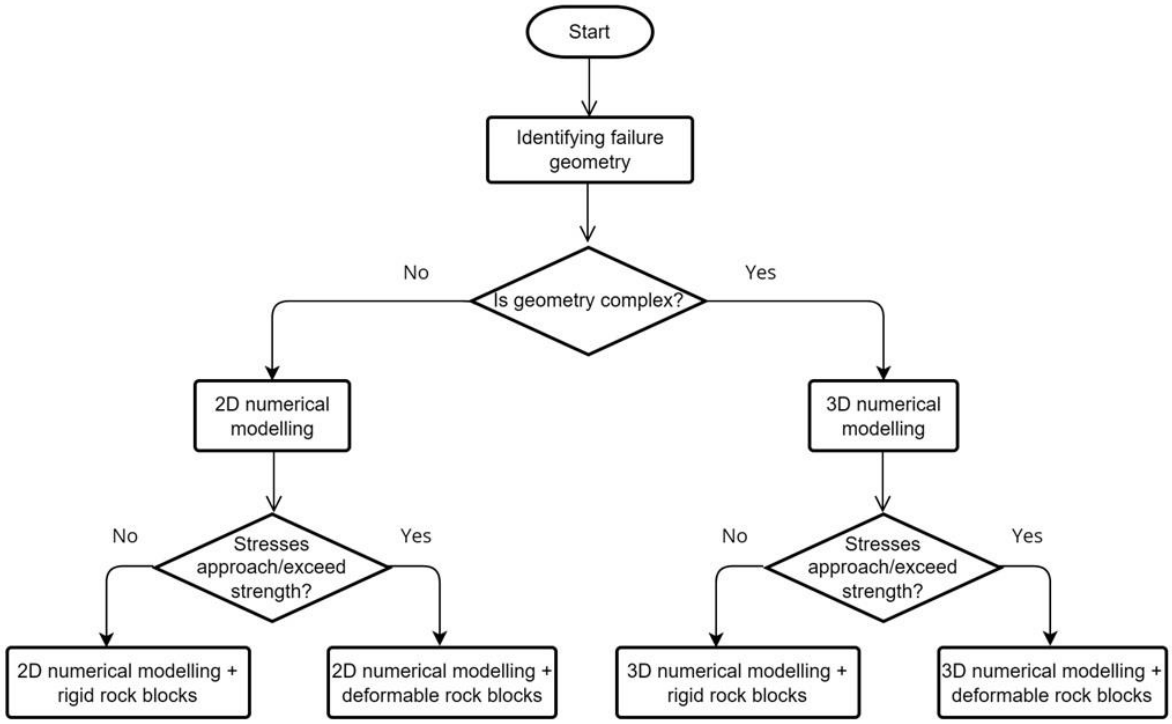

Fig. 7-1. *Flowchart on the selection of modelling methods for landslide analysis.*

Research limitations

In LSM analysis, landslides that occurred during the years 2008 to 2014 were detected for training and validation of ML models. From the perspective of temporal scales, the relatively short period (7 years) for landslide detection may cause inaccurate recognition of slopes that may be susceptible to landsliding after 2014, while they remained stable during 2008-2014 and were classified as permanently stable ground. To reduce or eliminate potential impacts, future research would extend the duration of time for as long as possible when detecting landslides.

In addition, using mean orientation to represent all joints in a set for slope stability analysis may produce misleading results due to variations in discontinuity orientations (Zheng et al., 2015). The GIS-based kinematic analysis is completed in such a way that may underestimate or overestimate landslide probabilities. Concerning DFN generation, the variation of discontinuity orientations can be characterized by discontinuity clustering that is defined by probability distribution laws. Built upon this method, probability analysis permits the estimation of slope stability with the consideration of the uncertainty of joint orientation (Song et al., 2001;

Zheng et al., 2017). Combining with GIS-based kinematic analysis, this method potentially reduces the impact of joint variation on slope stability analysis (Park et al., 2016). The derived probability index can be incorporated into ML models as an independent variable for landslide prediction.

The Hell's Mouth case study employs a rigid model to constrain rock mechanical behaviours, through which model complexity is significantly reduced. Modelling results are generally consistent with data obtained from field observations, highlighting kinematic controls of local joints on the landslide. However, the buckling of rock slabs (shown in Fig. 4-5b) cannot be recreated in the modelling as the deformation and brittle fracturing of intact rock are not permitted in a rigid model.

When modelling deformation and/or fracturing of rocks, the model must be deformable, and meshing is required. Issues related to meshing arise when the model changes to be deformable, which are more noticeable in 3D DEM and FDEM modelling that incorporate a DFN model and considers the variation of joint geometry. In the modelling meshing is used to produce good quality meshes (as seen in Fig. 7-2), avoiding 'bad block geometry' of considerably high aspect ratio (e.g., slender blocks) that can cause problems (e.g., 'negative volume zone') when deformation occurs. However, this is inevitable in the case where two sub-parallel joints intersect, and a low intersection angle must result in a bad quality of block geometry that is constrained by the two joint planes. In addition, sometimes small meshing sizes are required due to the presence of spatially closed joints or small-scale joints, which can bring significant computational costs. To solve these problems, methods are readily available to simplify fracture networks (Karimi Sharif et al., 2019; Ma et al., 2020; Wang and Cai, 2020), which are achieved by: 1) removing short-length fractures, 2) merging sub-parallel fractures that are spatially close, 3) adjusting the intersection angle of fractures, 4) using equivalent properties to characterize the rock mass that is composed of short-length fractures with the prerequisite of reserving large discontinuities, or 5) the combination of afore-mentioned ways.

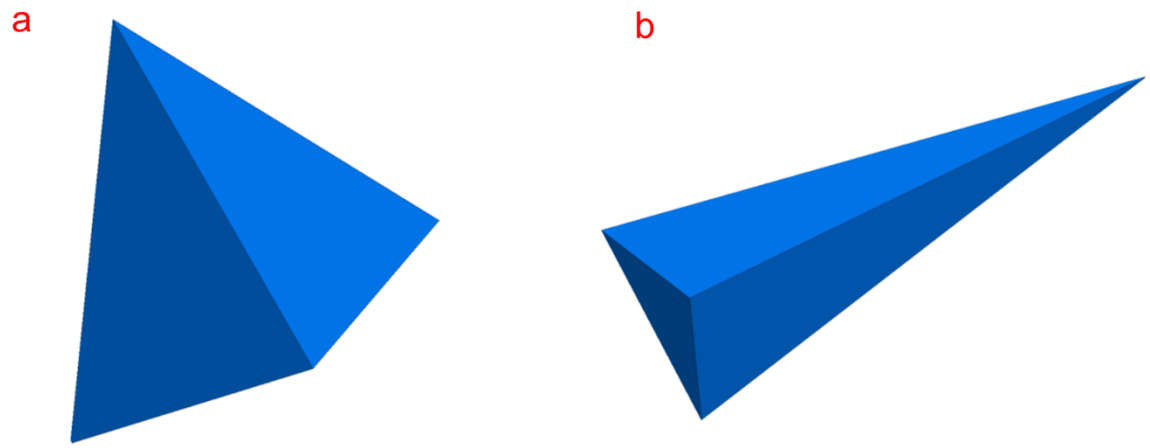

Fig. 7-2. *Block geometry, a) good block geometry, b) bad block geometry.*

The effectiveness of DFN simplification has been validated by the comparable properties of simplified rock mass compared with the original one. However, the reliability of DFN simplification regarding brittle fracturing patterns has yet to be investigated. This may result in uncertainties when dealing with problems related to brittle rock fracturing, which is the case of the South American mine instability. More attempts would concentrate on testing the reliability of DFN simplification methods through comparative studies to investigate the fracturing behaviour of rock mass before and after simplification.

Chapter 8. Conclusions, major contributions, and future work

Conclusions

This research has examined the role of discontinuities, at different scales, on the origin and development of rock slides. In the environment where rock strength exceeds the in-situ stresses, rock blocks exhibit a rigid characteristic and rock displacement along discontinuities is the predominant movement behaviour. With respect to large-scale discontinuities, an unfavourably oriented fault sometimes behaves as the sidling surface or release surface of a landslide, which is the case of Hell's Mouth landslide where two fault planes constrain the formation of the inlet, providing the kinematic freedom for the following landslide, and also the case of Italian rock avalanche where the bedding acted as the basal sliding surface. Small-scale discontinuities (i.e., joints and fractures) can also forms a release surface. However, compared with faults, joints with less persistence/continuity potentially form a step-path slip surface, as shown at the toe of the slope in the Italian rock avalanche case.

In the rock slope where stresses exceed rock strength, rock deformation would occur. With the presence of discontinuities, stress flow distributed in the slope is interrupted, and excessive stress concentration in the proximity to relatively large discontinuities can result in rock bridge damage. This has been presented in South America cause study in which the deformation of the rock bridge is modelled between two faults, which is validated by field and remote sensing data. Concerning non-persistent joints, they could weaken rock strength and cause the anisotropy of rock mass properties. The numerical compression tests, provided in chapter 6, have demonstrated that the presence of joint system causes the reduction of UCS of rocks from 98.7 MPa to 14 MPa. In addition, mechanical anisotropy of rock masses is also induced by joints. It is found that rock masses exhibits the lowest values of UCS and Young's modulus in the direction that is approximately parallel to the dominant dip direction of joints

In addition, the influence of discontinuity on rock slides is also assessed through GIS-based kinematic analysis and statistical analysis. The GIS-based kinematic analysis indicates slopes of high landslide risks, which is validated by field

observations. Furthermore, incorporating the results of GIS-based kinematic analysis effectively is able to improve the landslide prediction accuracy of machine learning models for LSM.

Major contributions

First, this thesis presents the application of a broad range of RS techniques for landslide investigations, which include airborne and spaceborne optical and laser scanning mapping. It demonstrates the fundamental role of RS mapping to identify features of landslides and slope topography, which can complement and/or replace conventional engineering-geological surveys in dangerous and inaccessible areas.

Second, the research has developed a novel method to incorporate discontinuity orientation for LSM, which was carried out through GIS-based kinematic analysis. The LSM analysis using data collected from the North cliffs of Cornwall, UK has demonstrated the improved landslide prediction accuracy due to the inclusion of discontinuity orientation. The analysis can provide a guideline for researchers to include discontinuities into ML modelling for LSM and might be applicable to other places for landslide prediction.

Third, the research presents a comprehensive understanding of the role of different-sized discontinuities (e.g., joints and faults) on rock slide development through 3 representative landslide case studies. The mechanical behaviour of individual discontinuities or multiple interacted discontinuities has been analysed. The associated work may provide a reference and analogue for scientists to investigate the mechanism of other rock slides effectively and rapidly.

Fourth, the role of folded bedding induced by the presence of an anticline has been investigated from the Lettopalena Paleolandslide case study. The work bridges a gap in simulation of landslide behaviour in anticline limbs through numerical modelling.

Fifth, the Lettopalena Paleolandslide case study also presents a representative example of using the integration of geological models and numerical modelling for landslide analysis, showing the benefit that can provide an improved understanding of the landslide behaviour and factors controlling landslide triggering.

Sixth, the influence of sea erosion on rock coast evolution has been investigated from the Hell's Mouth case study. The investigation shows that sea erosion behaves as one of primary triggers for coastal slope instability and accounts for coastal retreat and evolution. In addition, this research has also examined the effect of river erosion on slope stability from Lettopalena Paleolandslide case study. Both results highlight that toe removal has detrimental impacts on slope stability conditions.

Seventh, the research provides a typical example of modelling the opening of tension cracks on pre-existing discontinuities behind the crest of the slope, with the result being consistent with field observations.

Eighth, the deformation behaviour of a rock bridge in response to sequential excavations and blasting has been analysed in the South America case study, providing improved understanding of inter-ramp, non-daylighting wedge instability in the open pit mine.

Future work

Some adaptions, experiments, and tests have been left for future due to the lack of critical data and resources. Future works concern new proposals to try different methods and further investigation of particular mechanisms.

Chapter 4 highlights ongoing instability through opening of tension cracks on pre-existing discontinuities behind the crest of the slope. Tension cracks are a visible landslide precursor. The detection of tension cracks and identification of their distribution can promote the understanding of landslide development and the role of discontinuities in the process. In addition, the detection is also important for landslide early warning and risk reduction. In this context, future efforts will be endeavoured for the identification of tension cracks, which can be carried out using ML and RS techniques. With obtaining an adequate number of tension crack images (e.g., satellite images, UAV images, and other RS images), it is possible to train a robust ML/DL model (e.g., convolutional neural network) to detect cracks in a new image.

Brittle rock fracturing which occurred during the Hell's Mouth landslide (Chapter 4), and was related to the mine slope instability in South America (Chapter 6). Due to

the complex failure geometry of these two landslide cases, 2D FDEM method was not used for landslide analysis. Future works can involve the use of 3D FDEM methods and/or 3D grain-based DEM methods, incorporating complex DFNs and large-scale discontinuities (e.g., faults and bedding), to analyse mechanical behaviours of rock mass in a slope. The improved understanding of rock brittle fracturing in the slope promotes investigation of mechanism and development of large-scale landslides.

References

Abanades, J., Greaves, D., Iglesias, G., 2015. Coastal defence using wave farms: The role of farm-to-coast distance. Renewable Energy 75, 572–582. https://doi.org/10.1016/j.renene.2014.10.048

Abe, S., Van Tien, D., Ha, D.N., Hoshide, T., Nishitani, T., Miyagi, T., 2018. Topography and landslides in weathered granitic rock areas—Hai Van landslide in central Vietnam. Landslides 15, 1675–1689. https://doi.org/10.1007/s10346-018-1017-x

Abolfazli, M., Fahimifar, A., 2020. The effects of rock joint characteristics and normal stress level on the stiffness of rock joints. Arab J Geosci 13, 984. https://doi.org/10.1007/s12517-020-05934-2

Abruzzo council, 2022. Abruzzo Region GIS portal. URL http://geoportale.regione.abruzzo.it/Cartanet

Agisoft, 2016. Metashape.

Agliardi, F., Crosta, G., Zanchi, A., 2001. Structural constraints on deep-seated slope deformation kinematics. Engineering Geology 59, 83–102. https://doi.org/10.1016/S0013-7952(00)00066-1

Agliardi, F., Riva, F., Barbarano, M., Zanchetta, S., Scotti, R., Zanchi, A., 2019. Effects of tectonic structures and long-term seismicity on paraglacial giant slope deformations: Piz Dora (Switzerland). Engineering Geology 263, 105353. https://doi.org/10.1016/j.enggeo.2019.105353

Alberti, S., Wang, G., Dattola, G., Crosta, G.B., 2019. Physical mechanical characterization of a rockslide shear zone by standard and unconventional tests. Landslides 16, 739–750. https://doi.org/10.1007/s10346-018-01126-y

Aleotti, P., Chowdhury, R., 1999. Landslide hazard assessment: summary review and new perspectives. Bull Eng Geol Env 58, 21–44. https://doi.org/10.1007/s100640050066

Allen, S.K., Linsbauer, A., Randhawa, S.S., Huggel, C., Rana, P., Kumari, A., 2016. Glacial lake outburst flood risk in Himachal Pradesh, India: an integrative and anticipatory approach considering current and future threats. Nat Hazards 84,

1741–1763. https://doi.org/10.1007/s11069-016-2511-x

Anbalagan, R., 1992. Landslide hazard evaluation and zonation mapping in mountainous terrain. Engineering Geology 32, 269–277. https://doi.org/10.1016/0013-7952(92)90053-2

Antolini, F., Barla, M., Gigli, G., Giorgetti, A., Intrieri, E., Casagli, N., 2016. Combined Finite–Discrete Numerical Modeling of Runout of the Torgiovannetto di Assisi Rockslide in Central Italy. Int. J. Geomech. 16, 04016019. https://doi.org/10.1061/(ASCE)GM.1943-5622.0000646

Arabameri, A., Chandra Pal, S., Rezaie, F., Chakrabortty, R., Saha, A., Blaschke, T., Di Napoli, M., Ghorbanzadeh, O., Thi Ngo, P.T., 2021. Decision tree based ensemble machine learning approaches for landslide susceptibility mapping. Geocarto International 1–35. https://doi.org/10.1080/10106049.2021.1892210

Ayalew, L., Yamagishi, H., 2005. The application of GIS-based logistic regression for landslide susceptibility mapping in the Kakuda-Yahiko Mountains, Central Japan. Geomorphology 65, 15–31. https://doi.org/10.1016/j.geomorph.2004.06.010

Aydan, Ö., Uehara, F., Kawamoto, T., 2012. Numerical Study of the Long-Term Performance of an Underground Powerhouse Subjected to Varying Initial Stress States, Cyclic Water Heads, and Temperature Variations. Int. J. Geomech. 12, 14–26. https://doi.org/10.1061/(ASCE)GM.1943-5622.0000040

Aydin, A., Antonellini, M., Tondi, E., Agosta, F., 2010. Deformation along the leading edge of the Maiella thrust sheet in central Italy. Journal of Structural Geology 32, 1291–1304. https://doi.org/10.1016/j.jsg.2008.10.005

Baecher, G.B., Lanney, N.A., Einstein, H.H., 1977. Statistical description of rock fractures and sampling. Presented at the 18th U.S. Symposium on Rock Mechanics.

Baghbanan, A., Jing, L., 2007. Hydraulic properties of fractured rock masses with correlated fracture length and aperture. International Journal of Rock Mechanics and Mining Sciences 44, 704–719. https://doi.org/10.1016/j.ijrmms.2006.11.001

Ballabio, C., Sterlacchini, S., 2012. Support Vector Machines for Landslide Susceptibility Mapping: The Staffora River Basin Case Study, Italy. Math Geosci 44, 47–70. https://doi.org/10.1007/s11004-011-9379-9

Bao, Y., Zhai, S., Chen, J., Xu, P., Sun, X., Zhan, J., Zhang, W., Zhou, X., 2020. The

evolution of the Samaoding paleolandslide river blocking event at the upstream reaches of the Jinsha River, Tibetan Plateau. Geomorphology 351, 106970. https://doi.org/10.1016/j.geomorph.2019.106970

Barton, N., 1973. Review of a new shear-strength criterion for rock joints. Engineering Geology 7, 287–332. https://doi.org/10.1016/0013-7952(73)90013-6

Barton, N., Choubey, V., 1977. The shear strength of rock joints in theory and practice. Rock Mechanics 10, 1–54. https://doi.org/10.1007/BF01261801

Barton, N., Lien, R., Lunde, J., 1974. Engineering classification of rock masses for the design of tunnel support. Rock Mechanics 6, 189–236. https://doi.org/10.1007/BF01239496

Barton, Nicholas.R., Bandis, S., 1982. Effect of block size on the shear behavior of jointed rocks. Presented at the 23rd U.S. symp. on rock mechanics, Berkeley, US.

Barton, N.R., 1972. A model study of rock-joint deformation. International Journal of Rock Mechanics and Mining Sciences & Geomechanics Abstracts 9, 579–582. https://doi.org/10.1016/0148-9062(72)90010-1

Bastola, S., Cai, M., Damjanac, B., 2020. Slope stability assessment of an open pit using lattice-spring-based synthetic rock mass (LS-SRM) modeling approach. Journal of Rock Mechanics and Geotechnical Engineering 12, 927–942. https://doi.org/10.1016/j.jrmge.2019.12.019

Behnia, P., Blais-Stevens, A., 2018. Landslide susceptibility modelling using the quantitative random forest method along the northern portion of the Yukon Alaska Highway Corridor, Canada. Nat Hazards 90, 1407–1426. https://doi.org/10.1007/s11069-017-3104-z

BGS, 2015. UK3D. URL https://www.bgs.ac.uk/datasets/uk3d/

Bianchi Fasani, G., Di Luzio, E., Esposito, C., Martino, S., Scarascia-Mugnozza, G., 2011. Numerical modelling of Plio-Quaternary slope evolution based on geological constraints: a case study from the Caramanico Valley (Central Apennines, Italy). SP 351, 201–214. https://doi.org/10.1144/SP351.11

Bianchi Fasani, G., Esposito, C., Scarascia-Mugnozza, G., Stedile, L., 2005. La frana di Taranta Peligna (Chieti) del 20 Aprile 2005: un altro caso di morte annunciata per frana. Giornale di Geologia Applicata 20–26. https://doi.org/10.1474/GGA.2005–02.0–03.0029

Bianchi-Fasani, G., Esposito, C., Petitta, M., Scarascia-Mugnozza, G., Barbieri, M., Cardarelli, E., Cercato, M., Di Filippo, G., 2011. The Importance of Geological Models in Understanding and Predicting the Life Span of Rockslide Dams: The Case of Scanno Lake, Central Italy, in: Evans, S.G., Hermanns, R.L., Strom, A., Scarascia-Mugnozza, Gabriele (Eds.), Natural and Artificial Rockslide Dams, Lecture Notes in Earth Sciences. Springer Berlin Heidelberg, Berlin, Heidelberg, pp. 323–345. https://doi.org/10.1007/978-3-642-04764-0_11

Bieniawski, Z.T., 1989. Engineering rock mass classifications: a complete manual for engineers and geologists in mining, civil, and petroleum engineering. Wiley, New York.

Bonnet, E., Bour, O., Odling, N.E., Davy, P., Main, I., Cowie, P., Berkowitz, B., 2001. Scaling of fracture systems in geological media. Rev. Geophys. 39, 347–383. https://doi.org/10.1029/1999RG000074

Borrelli, L., Gullà, G., 2017. Tectonic constraints on a deep-seated rock slide in weathered crystalline rocks. Geomorphology 290, 288–316. https://doi.org/10.1016/j.geomorph.2017.04.025

Bovis, M.J., Evans, S.G., 1996. Extensive deformations of rock slopes in southern Coast Mountains, southwest British Columbia, Canada. Engineering Geology 44, 163–182. https://doi.org/10.1016/S0013-7952(96)00068-3

Bozzano, F., Lenti, L., Martino, S., Montagna, A., Paciello, A., 2011. Earthquake triggering of landslides in highly jointed rock masses: Reconstruction of the 1783 Scilla rock avalanche (Italy). Geomorphology 129, 294–308. https://doi.org/10.1016/j.geomorph.2011.02.025

Brandano, M., Cornacchia, I., Raffi, I., Tomassetti, L., 2016. The Oligocene–Miocene stratigraphic evolution of the Majella carbonate platform (Central Apennines, Italy). Sedimentary Geology 333, 1–14. https://doi.org/10.1016/j.sedgeo.2015.12.002

Brideau, M.A., Pedrazzini, A., Stead, D., Froese, C., Jaboyedoff, M., van Zeyl, D., 2011. Three-dimensional slope stability analysis of South Peak, Crowsnest Pass, Alberta, Canada. Landslides 8, 139–158. https://doi.org/10.1007/s10346-010-0242-8

Brideau, M.A., Stead, D., Roots, C., Orwin, J., 2007. Geomorphology and engineering geology of a landslide in ultramafic rocks, Dawson City, Yukon. Engineering Geology 89, 171–194.

https://doi.org/10.1016/j.enggeo.2006.10.004

Brideau, M.A., Sturzenegger, M., Stead, D., Jaboyedoff, M., Lawrence, M., Roberts, N.J., Ward, B.C., Millard, T.H., Clague, J.J., 2012. Stability analysis of the 2007 Chehalis lake landslide based on long-range terrestrial photogrammetry and airborne LiDAR data. Landslides 9, 75–91. https://doi.org/10.1007/s10346-011-0286-4

British Geological Survey, 2020. Hell's Mouth, Cornwall - landslide case study. British Geological Survey. URL https://www.bgs.ac.uk/case-studies/hells-mouth-cornwall-landslide-case-study/ (accessed 2.22.21).

British Geological Survey, 2018. How to classify a landslide. British Geological Survey. URL https://www.bgs.ac.uk/discovering-geology/earth-hazards/landslides/how-to-classify-a-landslide/ (accessed 8.29.21).

Bromhead, E.N., Ibsen, M.L., 2004. Bedding-controlled coastal landslides in Southeast Britain between Axmouth and the Thames Estuary. Landslides 1. https://doi.org/10.1007/s10346-004-0015-3

Budetta, P., De Luca, C., 2015. Wedge failure hazard assessment by means of a probabilistic approach for an unstable sea-cliff. Nat Hazards 76, 1219–1239. https://doi.org/10.1007/s11069-014-1546-0

Bui, D.T., Tsangaratos, P., Nguyen, V.T., Liem, N.V., Trinh, P.T., 2020. Comparing the prediction performance of a Deep Learning Neural Network model with conventional machine learning models in landslide susceptibility assessment. CATENA 188, 104426. https://doi.org/10.1016/j.catena.2019.104426

Bzdok, D., Altman, N., Krzywinski, M., 2018. Statistics versus machine learning. Nat Methods 15, 233–234. https://doi.org/10.1038/nmeth.4642

Bzdok, D., Krzywinski, M., Altman, N., 2017. Machine learning: a primer. Nat Methods 14, 1119–1120. https://doi.org/10.1038/nmeth.4526

Call, R.D., Savely, J.P., Nicholas, D.E., 1978. Estimation of joint set characteristics from surface mapping data. International Journal of Rock Mechanics and Mining Sciences & Geomechanics Abstracts 15, 64. https://doi.org/10.1016/0148-9062(78)90171-7

Cao, R., Cao, P., Fan, X., Xiong, X., Lin, H., 2016. An Experimental and Numerical Study on Mechanical Behavior of Ubiquitous-Joint Brittle Rock-Like Specimens Under Uniaxial Compression. Rock Mech Rock Eng 49, 4319–4338. https://doi.org/10.1007/s00603-016-1029-6

Cao, R.H., Cao, P., Lin, H., Ma, G.W., Fan, X., Xiong, X.G., 2018. Mechanical behavior of an opening in a jointed rock-like specimen under uniaxial loading: Experimental studies and particle mechanics approach. Archives of Civil and Mechanical Engineering 18, 198–214. https://doi.org/10.1016/j.acme.2017.06.010

Catani, F., Lagomarsino, D., Segoni, S., Tofani, V., 2013. Landslide susceptibility estimation by random forests technique: sensitivity and scaling issues. Nat. Hazards Earth Syst. Sci. 13, 2815–2831. https://doi.org/10.5194/nhess-13-2815-2013

Cerri, R.I., Reis, F.A.G.V., Gramani, M.F., Rosolen, V., Luvizotto, G.L., Giordano, L. do C., Gabelini, B.M., 2018. Assessment of landslide occurrences in Serra do Mar mountain range using kinematic analyses. Environ Earth Sci 77, 325. https://doi.org/10.1007/s12665-018-7508-1

Changwei, Y., Xinmin, L., Jianjing, Z., Zhiwei, C., Cong, S., Hongbo, G., 2014. Analysis on mechanism of landslides under ground shaking: a typical landslide in the Wenchuan earthquake. Environ Earth Sci 72, 3457–3466. https://doi.org/10.1007/s12665-014-3251-4

Channel Coastal Observatory, 2020. Channel Coastal Observatory. URL https://www.channelcoast.org/

Chau, V., Rougier, E., Lei, Z., Knight, E.E., Gao, K., Hunter, A., Srinivasan, G., Viswanathan, H., 2020. Numerical analysis of flyer plate experiments in granite via the combined finite–discrete element method. Comp. Part. Mech. 7, 1005–1016. https://doi.org/10.1007/s40571-019-00300-w

Chauhan, S., Sharma, M., Arora, M.K., Gupta, N.K., 2010. Landslide Susceptibility Zonation through ratings derived from Artificial Neural Network. International Journal of Applied Earth Observation and Geoinformation 12, 340–350. https://doi.org/10.1016/j.jag.2010.04.006

Chen, W., Li, Y., 2020. GIS-based evaluation of landslide susceptibility using hybrid computational intelligence models. CATENA 195, 104777. https://doi.org/10.1016/j.catena.2020.104777

Chen, W., Peng, J., Hong, H., Shahabi, H., Pradhan, B., Liu, J., Zhu, A.X., Pei, X., Duan, Z., 2018. Landslide susceptibility modelling using GIS-based machine learning techniques for Chongren County, Jiangxi Province, China. Science of The Total Environment 626, 1121–1135.

https://doi.org/10.1016/j.scitotenv.2018.01.124

Chen, W., Pourghasemi, H.R., Kornejady, A., Zhang, N., 2017. Landslide spatial modeling: Introducing new ensembles of ANN, MaxEnt, and SVM machine learning techniques. Geoderma 305, 314–327. https://doi.org/10.1016/j.geoderma.2017.06.020

Chen, X.L., Liu, C.-G., Chang, Z.F., Zhou, Q., 2016. The relationship between the slope angle and the landslide size derived from limit equilibrium simulations. Geomorphology 253, 547–550. https://doi.org/10.1016/j.geomorph.2015.01.036

Cheng, Y., Jiao, Y.Y., Tan, F., 2019. Numerical and Experimental Study on the Cracking Behavior of Marble with En-Echelon Flaws. Rock Mech Rock Eng 52, 4319–4338. https://doi.org/10.1007/s00603-019-01849-x

Cheng, Y.M., 1998. Advancements and improvement in discontinuous deformation analysis. Computers and Geotechnics 22, 153–163. https://doi.org/10.1016/S0266-352X(98)00002-0

Chigira, M., Tsou, C.Y., Matsushi, Y., Hiraishi, N., Matsuzawa, M., 2013. Topographic precursors and geological structures of deep-seated catastrophic landslides caused by Typhoon Talas. Geomorphology 201, 479–493. https://doi.org/10.1016/j.geomorph.2013.07.020

Choi, J., Oh, H.J., Won, J.S., Lee, S., 2010. Validation of an artificial neural network model for landslide susceptibility mapping. Environ Earth Sci 60, 473–483. https://doi.org/10.1007/s12665-009-0188-0

Clague, J.J., Stead, D., 2012. Landslides : types, mechanisms and modeling. Cambridge : Cambridge University Press.

Clark, R.M., Cox, S.J.D., 1996. A modern regression approach to determining fault displacement-length scaling relationships. Journal of Structural Geology 18, 147–152. https://doi.org/10.1016/S0191-8141(96)80040-X

CloudCompare, 2017. 3D point cloud and mesh processing software.

Colkesen, I., Sahin, E.K., Kavzoglu, T., 2016. Susceptibility mapping of shallow landslides using kernel-based Gaussian process, support vector machines and logistic regression. Journal of African Earth Sciences 118, 53–64. https://doi.org/10.1016/j.jafrearsci.2016.02.019

Collins, B.D., Znidarcic, D., 2004. Stability Analyses of Rainfall Induced Landslides. J. Geotech. Geoenviron. Eng. 130, 362–372. https://doi.org/10.1061/(ASCE)1090-0241(2004)130:4(362)

Cook, K.L., 2017. An evaluation of the effectiveness of low-cost UAVs and structure from motion for geomorphic change detection. Geomorphology 278, 195–208. https://doi.org/10.1016/j.geomorph.2016.11.009

Cooper, H.M., Wasklewicz, T., Zhu, Z., Lewis, W., LeCompte, K., Heffentrager, M., Smaby, R., Brady, J., Howard, R., 2021. Evaluating the Ability of Multi-Sensor Techniques to Capture Topographic Complexity. Sensors 21, 2105. https://doi.org/10.3390/s21062105

Corkum, A.G., Martin, C.D., 2004. Analysis of a rock slide stabilized with a toe-berm: a case study in British Columbia, Canada. International Journal of Rock Mechanics and Mining Sciences 41, 1109–1121. https://doi.org/10.1016/j.ijrmms.2004.04.008

Cowie, P.A., Scholz, C.H., 1992. Physical explanation for the displacement-length relationship of faults using a post-yield fracture mechanics model. Journal of Structural Geology 14, 1133–1148. https://doi.org/10.1016/0191-8141(92)90065-5

Cruden, D.M., 1977. Describing the size of discontinuities. International Journal of Rock Mechanics and Mining Sciences & Geomechanics Abstracts 14, 133–137. https://doi.org/10.1016/0148-9062(77)90004-3

Cui, S., Pei, X., Huang, R., 2018. Effects of geological and tectonic characteristics on the earthquake-triggered Daguangbao landslide, China. Landslides 15, 649–667. https://doi.org/10.1007/s10346-017-0899-3

Cui, Z., Sheng, Q., Luo, Q., Zhang, G., 2021. Investigating the Anisotropy of Mechanical Parameters of Schist Rock with Practical Numerical Methods. Sustainability 13, 725. https://doi.org/10.3390/su13020725

Cundall, P.A., 1988. Formulation of a three-dimensional distinct element model—Part I. A scheme to detect and represent contacts in a system composed of many polyhedral blocks. International Journal of Rock Mechanics and Mining Sciences & Geomechanics Abstracts 25, 107–116. https://doi.org/10.1016/0148-9062(88)92293-0

Cundall, P.A., 1971. A computer model for simulating progressive large-scale movements in blocky rock systems. Presented at the Proceedings of the Symposium of the International Society for Rock Mechanics.

Dahal, R.K., Bhandary, N.P., Hasegawa, S., Yatabe, R., 2014. Topo-stress based probabilistic model for shallow landslide susceptibility zonation in the Nepal

Himalaya. Environ Earth Sci 71, 3879–3892. https://doi.org/10.1007/s12665-013-2774-4

Dai, F.C., Lee, C.F., 2002. Landslide characteristics and slope instability modeling using GIS, Lantau Island, Hong Kong. Geomorphology 42, 213–228. https://doi.org/10.1016/S0169-555X(01)00087-3

Dao, D.V., Jaafari, A., Bayat, M., Mafi-Gholami, D., Qi, C., Moayedi, H., Phong, T.V., Ly, H.-B., Le, T.-T., Trinh, P.T., Luu, C., Quoc, N.K., Thanh, B.N., Pham, B.T., 2020. A spatially explicit deep learning neural network model for the prediction of landslide susceptibility. CATENA 188, 104451. https://doi.org/10.1016/j.catena.2019.104451

Darcel, C., Davy, P., Le Goc, R., Mas Ivars, D., 2018. Rock mass effective properties from a DFN approach. Presented at the Second International Discrete Fracture Network Engineering Conference, Seattle, USA.

Davy, P., Le Goc, R., Darcel, C., 2013. A model of fracture nucleation, growth and arrest, and consequences for fracture density and scaling: A DISCRETE FRACTURE NETWORK MODEL. J. Geophys. Res. Solid Earth 118, 1393–1407. https://doi.org/10.1002/jgrb.50120

de Dreuzy, J.R., Davy, P., Bour, O., 2002. Hydraulic properties of two-dimensional random fracture networks following power law distributions of length and aperture: PERMEABILITY OF HETEROGENEOUS FRACTURE NETWORKS. Water Resour. Res. 38, 12-1-12–9. https://doi.org/10.1029/2001WR001009

Della Seta, M., Esposito, C., Marmoni, G.M., Martino, S., Scarascia Mugnozza, G., Troiani, F., 2017. Morpho-structural evolution of the valley-slope systems and related implications on slope-scale gravitational processes: New results from the Mt. Genzana case history (Central Apennines, Italy). Geomorphology 289, 60–77. https://doi.org/10.1016/j.geomorph.2016.07.003

Dershowitz, W.S., Herda, H.H., 1992. Interpretation of fracture spacing and intensity, in: International Journal of Rock Mechanics and Mining Sciences & Geomechanics Abstracts. Santa Fe, p. 757 - 766.

Digimap, 2020. Digimap. URL https://digimap.edina.ac.uk/lidar

Dilley, M., Chen, R., Deichmann, U., Lerner-Lam, A., Arnold, M., Agwe, J., Yetman, G., 2005. Natural Disaster Hotspots: A Global Risk. Washington, D.C.

Donati, D., Stead, D., Brideau, M.-A., Ghirotti, M., 2021a. Using pre-failure and post-

failure remote sensing data to constrain the three-dimensional numerical model of a large rock slope failure. Landslides 18, 827–847. https://doi.org/10.1007/s10346-020-01552-x

Donati, D., Stead, D., Elmo, D., Borgatti, L., 2019. A Preliminary Investigation on the Role of Brittle Fracture in the Kinematics of the 2014 San Leo Landslide. Geosciences 9, 256. https://doi.org/10.3390/geosciences9060256

Donati, D., Stead, D., Stewart, T.W., Marsh, J., 2020. Numerical modelling of slope damage in large, slowly moving rockslides: Insights from the Downie Slide, British Columbia, Canada. Engineering Geology 273, 105693. https://doi.org/10.1016/j.enggeo.2020.105693

Donati, D., Westin, A.M., Stead, D., Clague, J.J., Stewart, T.W., Lawrence, M.S., Marsh, J., 2021b. A reinterpretation of the Downie Slide (British Columbia, Canada) based on slope damage characterization and subsurface data interpretation. Landslides 18, 1561–1583. https://doi.org/10.1007/s10346-020-01601-5

Dong, M., Kulatilake, P.H.S.W., Zhang, F., 2018. Deformation and stability investigations in 3-D of an excavated rock slope in a hydroelectric power station in China. Computers and Geotechnics 96, 132–149. https://doi.org/10.1016/j.compgeo.2017.10.019

Dou, J., Yunus, A.P., Tien Bui, D., Merghadi, A., Sahana, M., Zhu, Z., Chen, C.-W., Khosravi, K., Yang, Y., Pham, B.T., 2019. Assessment of advanced random forest and decision tree algorithms for modeling rainfall-induced landslide susceptibility in the Izu-Oshima Volcanic Island, Japan. Science of The Total Environment 662, 332–346. https://doi.org/10.1016/j.scitotenv.2019.01.221

Duman, T.Y., 2009. The largest landslide dam in Turkey: Tortum landslide. Engineering Geology 104, 66–79. https://doi.org/10.1016/j.enggeo.2008.08.006

Dunning, S.A., Mitchell, W.A., Rosser, N.J., Petley, D.N., 2007. The Hattian Bala rock avalanche and associated landslides triggered by the Kashmir Earthquake of 8 October 2005. Engineering Geology 93, 130–144. https://doi.org/10.1016/j.enggeo.2007.07.003

Dunning, S.A., Rosser, N.J., Petley, D.N., Massey, C.R., 2006. Formation and failure of the Tsatichhu landslide dam, Bhutan. Landslides 3, 107–113. https://doi.org/10.1007/s10346-005-0032-x

Eberhardt, E., 2012. The Hoek–Brown Failure Criterion. Rock Mech Rock Eng 45,

981–988. https://doi.org/10.1007/s00603-012-0276-4

Edil, T.B., Vallejo, L.E., 1980. Mechanics of coastal landslides and the influence of slope parameters. Engineering Geology 16, 83–96. https://doi.org/10.1016/0013-7952(80)90009-5

Einstein, H.H., Veneziano, D., Baecher, G.B., O'Reilly, K.J., 1983. The effect of discontinuity persistence on rock slope stability. Int. J. Rock Mech. Min. Sci. Geomech. Abstr. 20, 227–236. https://doi.org/10.1016/0148-9062(83)90003-7

Eiras, C.G.S., Souza, J.R.G. de, Freitas, R.D.A. de, Barella, C.F., Pereira, T.M., 2021. Discriminant analysis as an efficient method for landslide susceptibility assessment in cities with the scarcity of predisposition data. Nat Hazards 107, 1427–1442. https://doi.org/10.1007/s11069-021-04638-4

Elmo, D., Donati, D., Stead, D., 2018. Challenges in the characterisation of intact rock bridges in rock slopes. Engineering Geology 245, 81–96. https://doi.org/10.1016/j.enggeo.2018.06.014

Elmo, D., Rogers, S., Stead, D., Eberhardt, E., 2014. Discrete Fracture Network approach to characterise rock mass fragmentation and implications for geomechanical upscaling. Mining Technology 123, 149–161. https://doi.org/10.1179/1743286314Y.0000000064

Euser, B., Rougier, E., Lei, Z., Knight, E.E., Frash, L.P., Carey, J.W., Viswanathan, H., Munjiza, A., 2019. Simulation of Fracture Coalescence in Granite via the Combined Finite–Discrete Element Method. Rock Mech Rock Eng 52, 3213–3227. https://doi.org/10.1007/s00603-019-01773-0

Fadakar Alghalandis, Y., 2017. ADFNE: Open source software for discrete fracture network engineering, two and three dimensional applications. Computers & Geosciences 102, 1–11. https://doi.org/10.1016/j.cageo.2017.02.002

Fan, W., Lv, J., Cao, Y., Shen, M., Deng, L., Wei, Y., 2019. Characteristics and block kinematics of a fault-related landslide in the Qinba Mountains, western China. Engineering Geology 249, 162–171. https://doi.org/10.1016/j.enggeo.2018.12.019

Fang, Z., Wang, Y., Peng, L., Hong, H., 2020. Integration of convolutional neural network and conventional machine learning classifiers for landslide susceptibility mapping. Computers & Geosciences 139, 104470. https://doi.org/10.1016/j.cageo.2020.104470

Feng, S., Wu, Y., Liu, Y., Li, X., Wang, X., Chen, P., 2021. A fractal analysis of radon

migration in discrete fracture network model. Chemosphere 266, 129010. https://doi.org/10.1016/j.chemosphere.2020.129010

Ferrero, A.M., Migliazza, M.R., Pirulli, M., Umili, G., 2016. Some Open Issues on Rockfall Hazard Analysis in Fractured Rock Mass: Problems and Prospects. Rock Mech Rock Eng 49, 3615–3629. https://doi.org/10.1007/s00603-016-1004-2

Festa, A., Accotto, C., Coscarelli, F., Malerba, E., Palazzin, G., 2014. Geology of the Aventino River Valley (eastern Majella, central Italy). Journal of Maps 10, 584–599. https://doi.org/10.1080/17445647.2014.899524

Francioni, Calamita, Coggan, Nardis, Eyre, Miccadei, Piacentini, Stead, Sciarra, 2019. A Multi-Disciplinary Approach to the Study of Large Rock Avalanches Combining Remote Sensing, GIS and Field Surveys: The Case of the Scanno Landslide, Italy. Remote Sensing 11, 1570. https://doi.org/10.3390/rs11131570

Francioni, M., Coggan, J., Eyre, M., Stead, D., 2018a. A combined field/remote sensing approach for characterizing landslide risk in coastal areas. International Journal of Applied Earth Observation and Geoinformation 67, 79–95. https://doi.org/10.1016/j.jag.2017.12.016

Francioni, M., Salvini, R., Stead, D., Coggan, J., 2018b. Improvements in the integration of remote sensing and rock slope modelling. Nat Hazards 90, 975–1004. https://doi.org/10.1007/s11069-017-3116-8

Friedli, B., Hauswirth, D., Puzrin, A.M., 2017. Lateral earth pressures in constrained landslides. Géotechnique 1–16. https://doi.org/10.1680/jgeot.16.P.158

Furuki, H., Chigira, M., 2019. Structural features and the evolutionary mechanisms of the basal shear zone of a rockslide. Engineering Geology 260, 105214. https://doi.org/10.1016/j.enggeo.2019.105214

Gao, F., Stead, D., Kang, H., 2014. Numerical investigation of the scale effect and anisotropy in the strength and deformability of coal. International Journal of Coal Geology 136, 25–37. https://doi.org/10.1016/j.coal.2014.10.003

Gao, F.Q., Stead, D., 2014. The application of a modified Voronoi logic to brittle fracture modelling at the laboratory and field scale. International Journal of Rock Mechanics and Mining Sciences 68, 1–14. https://doi.org/10.1016/j.ijrmms.2014.02.003

Gao, G., Meguid, M.A., Chouinard, L.E., Xu, C., 2020. Insights into the Transport and Fragmentation Characteristics of Earthquake-Induced Rock Avalanche:

Numerical Study. Int. J. Geomech. 20, 04020157. https://doi.org/10.1061/(ASCE)GM.1943-5622.0001800

Gao, Y., Li, B., Gao, H., Chen, L., Wang, Y., 2020. Dynamic characteristics of high-elevation and long-runout landslides in the Emeishan basalt area: a case study of the Shuicheng “7.23”landslide in Guizhou, China. Landslides 17, 1663–1677. https://doi.org/10.1007/s10346-020-01377-8

Geertsema, M., Clague, J.J., Schwab, J.W., Evans, S.G., 2006. An overview of recent large catastrophic landslides in northern British Columbia, Canada. Engineering Geology 83, 120–143. https://doi.org/10.1016/j.enggeo.2005.06.028

Genuer, R., Poggi, J.M., Tuleau-Malot, C., 2010. Variable selection using random forests. Pattern Recognition Letters 31, 2225–2236. https://doi.org/10.1016/j.patrec.2010.03.014

Geomechanica Inc., 2021. Irazu. URL https://www.geomechanica.com/ (accessed 12.21.21).

Geoslope, 2021. SLOPE/W [WWW Document]. URL https://www.geoslope.com/products/slope-w (accessed 10.18.21).

Glueer, F., Loew, S., Manconi, A., Aaron, J., 2019. From Toppling to Sliding: Progressive Evolution of the Moosfluh Landslide, Switzerland. J. Geophys. Res. Earth Surf. 124, 2899–2919. https://doi.org/10.1029/2019JF005019

Goetz, J.N., Brenning, A., Petschko, H., Leopold, P., 2015. Evaluating machine learning and statistical prediction techniques for landslide susceptibility modeling. Computers & Geosciences 81, 1–11. https://doi.org/10.1016/j.cageo.2015.04.007

Golder Associates Ltd., 2018. FracMan, version 7.9.

Gonzalez-Ollauri, A., Mickovski, S.B., 2017. Hydrological effect of vegetation against rainfall-induced landslides. Journal of Hydrology 549, 374–387. https://doi.org/10.1016/j.jhydrol.2017.04.014

Goodman, R.E., 1980. Introduction to rock mechanics. Wiley, New York.

Goodman, R.E., Taylor, R.L., Brekke, T.L., 1968. A Model for the Mechanics of Jointed Rock. J. Soil Mech. and Found. Div. 94, 637–659. https://doi.org/10.1061/JSFEAQ.0001133

Goodman, Richard.E., Bray, J.W., 1976. Topppling of rock slopes. Presented at the Proceedings of the specialty conference on rock engineering for fundations and

slopes, ASCE/Boulder, Colorado, USA, pp. 201–234.

Gorokhovich, Y., Vustianiuk, A., 2021. Implications of slope aspect for landslide risk assessment: A case study of Hurricane Maria in Puerto Rico in 2017. Geomorphology 391, 107874. https://doi.org/10.1016/j.geomorph.2021.107874

Gu, D., Huang, D., 2016. A complex rock topple-rock slide failure of an anaclinal rock slope in the Wu Gorge, Yangtze River, China. Engineering Geology 208, 165–180. https://doi.org/10.1016/j.enggeo.2016.04.037

Guo, L., Li, X., Zhou, Y., Zhang, Y., 2015. Generation and verification of three-dimensional network of fractured rock masses stochastic discontinuities based on digitalization. Environ Earth Sci 73, 7075–7088. https://doi.org/10.1007/s12665-015-4175-3

Haakon Fossen, 2016. Structural Geology.

Han, X., Chen, J., Wang, Q., Li, Y., Zhang, W., Yu, T., 2016. A 3D Fracture Network Model for the Undisturbed Rock Mass at the Songta Dam Site Based on Small Samples. Rock Mech Rock Eng 49, 611–619. https://doi.org/10.1007/s00603-015-0747-5

Hart, R., Cundall, P.A., Lemos, J., 1988. Formulation of a three-dimensional distinct element model—Part II. Mechanical calculations for motion and interaction of a system composed of many polyhedral blocks. International Journal of Rock Mechanics and Mining Sciences & Geomechanics Abstracts 25, 117–125. https://doi.org/10.1016/0148-9062(88)92294-2

He, L., Coggan, J., Francioni, M., Eyre, M., 2021a. Maximizing Impacts of Remote Sensing Surveys in Slope Stability—A Novel Method to Incorporate Discontinuities into Machine Learning Landslide Prediction. IJGI 10, 232. https://doi.org/10.3390/ijgi10040232

He, L., Coggan, J., Stead, D., Francioni, M., Eyre, M., 2021b. Modelling discontinuity control on the development of Hell’s Mouth landslide. Landslides. https://doi.org/10.1007/s10346-021-01813-3

He, L., Francioni, M., Coggan, J., Calamita, F., Eyre, M., 2022. Modelling the Influence of Geological Structures in Paleo Rock Avalanche Failures Using Field and Remote Sensing Data. Remote Sensing 14, 4090. https://doi.org/10.3390/rs14164090

Healy, D., Rizzo, R.E., Cornwell, D.G., Farrell, N.J.C., Watkins, H., Timms, N.E., Gomez-Rivas, E., Smith, M., 2017. FracPaQ: A MATLABTM toolbox for the

quantification of fracture patterns. Journal of Structural Geology 95, 1–16. https://doi.org/10.1016/j.jsg.2016.12.003

Hekmatnejad, A., Crespin, B., Opazo, A., Emery, X., Hitschfeld-Kahler, N., Elmo, D., 2020. Investigating the impact of the estimation error of fracture intensity (P32) on the evaluation of in-situ rock fragmentation and potential of blocks forming around tunnels. Tunnelling and Underground Space Technology 106, 103596. https://doi.org/10.1016/j.tust.2020.103596

Hess, D.M., Leshchinsky, B.A., Bunn, M., Benjamin Mason, H., Olsen, M.J., 2017. A simplified three-dimensional shallow landslide susceptibility framework considering topography and seismicity. Landslides 14, 1677–1697. https://doi.org/10.1007/s10346-017-0810-2

Highland, L.M., Bobrowsky, P., 2008. The Landslide Handbook - A Guide to Understanding Landslides, Geological Survey Circular 1325. Reston, Virginia, U.S.

Hobbs, P.R.N., Hallam, J.R., Forster, A., Entwisle, D.C., Jones, L.D., Cripps, A.C., Northmore, K.J., Self, S.J., Meakin, J.K., 2002. Engineering geology of British rocks and soils, Mudstones of the Mercia, Mudstone Group (Research report).

Hoek, E., 1994. Strength of rock and rock masses. ISRM News Journal 2, 4–16.

Hoek, E., Bray, J.W., 1981. Rock Slope Engineering, 3rd edition. ed. The Institute of Mining and Metallurgy, London, England.

Hoek, E., Brown, E.T., 1980a. Empirical Strength Criterion for Rock Masses. J. Geotech. Engrg. Div. 106, 1013–1035. https://doi.org/10.1061/AJGEB6.0001029

Hoek, E., Brown, T., 1980b. Underground Excavations in Rock, 1st Edition. ed. The Institution of Mining and Metallurgy, London.

Hollick, L., Shail, R., Leveridge, B., 2006. Devonian rift-related sedimentation and Variscan tectonics – new data on the Looe and Gramscatho basins from the resurvey of the Newquay District. Presented at the Geosci. South-West England.

Hsieh, Y.C., Chan, Y.C., Hu, J.C., Chen, Y.Z., Chen, R.F., Chen, M.M., 2016. Direct Measurements of Bedrock Incision Rates on the Surface of a Large Dip-slope Landslide by Multi-Period Airborne Laser Scanning DEMs. Remote Sensing 8, 900. https://doi.org/10.3390/rs8110900

Hua, Y., Wang, X., Li, Y., Xu, P., Xia, W., 2021. Dynamic development of landslide

susceptibility based on slope unit and deep neural networks. Landslides 18, 281–302. https://doi.org/10.1007/s10346-020-01444-0

Huang, D., Li, Y.Q., Song, Y.X., Xu, Q., Pei, X.J., 2019. Insights into the catastrophic Xinmo rock avalanche in Maoxian county, China: Combined effects of historical earthquakes and landslide amplification. Engineering Geology 258, 105158. https://doi.org/10.1016/j.enggeo.2019.105158

Huang, D., Song, Y., Cen, D., Fu, G., 2016. Numerical Modeling of Earthquake-Induced Landslide Using an Improved Discontinuous Deformation Analysis Considering Dynamic Friction Degradation of Joints. Rock Mech Rock Eng 49, 4767–4786. https://doi.org/10.1007/s00603-016-1056-3

Huang, F., Cao, Z., Guo, J., Jiang, S.-H., Li, S., Guo, Z., 2020. Comparisons of heuristic, general statistical and machine learning models for landslide susceptibility prediction and mapping. CATENA 191, 104580. https://doi.org/10.1016/j.catena.2020.104580

Huang, J., Zhao, M., Xu, C., Du, X., Jin, L., Zhao, X., 2018. Seismic stability of jointed rock slopes under obliquely incident earthquake waves. Earthq. Eng. Eng. Vib. 17, 527–539. https://doi.org/10.1007/s11803-018-0460-y

Huang, N., Jiang, Y., Liu, R., Li, B., Sugimoto, S., 2019. A novel three-dimensional discrete fracture network model for investigating the role of aperture heterogeneity on fluid flow through fractured rock masses. International Journal of Rock Mechanics and Mining Sciences 116, 25–37. https://doi.org/10.1016/j.ijrmms.2019.03.014

Huang, S.L., Yamasaki, K., 1993. Slope Failure Analysis Using Local Minimum Factor‐of‐Safety Approach. Journal of Geotechnical Engineering 119, 1974–1989. https://doi.org/10.1061/(ASCE)0733-9410(1993)119:12(1974)

Huang, Y., Zhao, L., 2018. Review on landslide susceptibility mapping using support vector machines. CATENA 165, 520–529. https://doi.org/10.1016/j.catena.2018.03.003

Hutchinson, J.N., 1989. Morphological and geotechnical parameters of landslides in relation to geology and hydrogeology. International Journal of Rock Mechanics and Mining Sciences & Geomechanics Abstracts 26, 88. https://doi.org/10.1016/0148-9062(89)90310-0

Indraratna, B., Jayanathan, M., Brown, E.T., 2008. Shear strength model for

overconsolidated clay-infilled idealised rock joints. Géotechnique 58, 55–65. https://doi.org/10.1680/geot.2008.58.1.55

Indraratna, B., Oliveira, D.A.F., Brown, E.T., 2010. A shear-displacement criterion for soil-infilled rock discontinuities. Géotechnique 60, 623–633. https://doi.org/10.1680/geot.8.P.094

Indraratna, B., Premadasa, W., Brown, E.T., Gens, A., Heitor, A., 2014. Shear strength of rock joints influenced by compacted infill. International Journal of Rock Mechanics and Mining Sciences 70, 296–307. https://doi.org/10.1016/j.ijrmms.2014.04.019

Indraratna, B., Thirukumaran, S., Brown, E.T., Zhu, S.P., 2015. Modelling the Shear Behaviour of Rock Joints with Asperity Damage Under Constant Normal Stiffness. Rock Mech Rock Eng 48, 179–195. https://doi.org/10.1007/s00603-014-0556-2

ISRM, 1983. Suggested methods for determining the strength of rock materials in triaxial compression: Revised version. International Journal of Rock Mechanics and Mining Sciences & Geomechanics Abstracts 20, 285–290. https://doi.org/10.1016/0148-9062(83)90598-3

ISRM, 1978. Suggested methods for the quantitative description of discontinuities in rock masses: International Society for Rock Mechanics. Int. J. Rock Mech. Min. Sci.

Itasca Consulting Group, Inc., 2021. PFC — Particle Flow Code.

Itasca Consulting Group, Inc., 2019. UDEC — Universal Distinct Element Code.

Itasca Consulting Group, Inc., 2017. 3DEC | US Minneapolis - Itasca Consulting Group, Inc.

Jaboyedoff, M., Oppikofer, T., Abellán, A., Derron, M.-H., Loye, A., Metzger, R., Pedrazzini, A., 2012. Use of LIDAR in landslide investigations: a review. Nat Hazards 61, 5–28. https://doi.org/10.1007/s11069-010-9634-2

Jennings, J.E., 1970. A mathematical theory for the calculation of the stability of slopes in open cast mines, in: Proceedings. Presented at the Planning Open Pit Mines, Johannesburg, pp. 87–102.

Jimenez-Rodriguez, R., Sitar, N., Chacón, J., 2006. System reliability approach to rock slope stability. International Journal of Rock Mechanics and Mining Sciences 43, 847–859. https://doi.org/10.1016/j.ijrmms.2005.11.011

Jing, L., 2003. A review of techniques, advances and outstanding issues in numerical

modelling for rock mechanics and rock engineering. International Journal of Rock Mechanics and Mining Sciences 40, 283–353. https://doi.org/10.1016/S1365-1609(03)00013-3

Jing, L., Nordlund, E., Stephansson, O., 1994. A 3-D constitutive model for rock joints with anisotropic friction and stress dependency in shear stiffness. International Journal of Rock Mechanics and Mining Sciences & Geomechanics Abstracts 31, 173–178. https://doi.org/10.1016/0148-9062(94)92808-8

Joshi, M., Rajappan, S., Rajan, P.P., Mathai, J., Sankar, G., Nandakumar, V., Kumar, V.A., 2018. Weathering Controlled Landslide in Deccan Traps: Insight from Mahabaleshwar, Maharashtra. J Geol Soc India 92, 555–561. https://doi.org/10.1007/s12594-018-1067-7

Kamp, U., Growley, B.J., Khattak, G.A., Owen, L.A., 2008. GIS-based landslide susceptibility mapping for the 2005 Kashmir earthquake region. Geomorphology 101, 631–642. https://doi.org/10.1016/j.geomorph.2008.03.003

Kargar, P., Osouli, A., Stark, T.D., 2021. 3D analysis of 2014 Oso landslide. Engineering Geology 287, 106100. https://doi.org/10.1016/j.enggeo.2021.106100

Karimi Sharif, L., Elmo, D., Stead, D., 2019. Improving DFN-geomechanical model integration using a novel automated approach. Computers and Geotechnics 105, 228–248. https://doi.org/10.1016/j.compgeo.2018.10.005

Karimzade, E., Sharifzadeh, M., Zarei, H.R., Shahriar, K., Cheraghi Seifabad, M., 2017. Prediction of water inflow into underground excavations in fractured rocks using a 3D discrete fracture network (DFN) model. Arab J Geosci 10, 206. https://doi.org/10.1007/s12517-017-2987-z

Kavzoglu, T., Sahin, E.K., Colkesen, I., 2014. Landslide susceptibility mapping using GIS-based multi-criteria decision analysis, support vector machines, and logistic regression. Landslides 11, 425–439. https://doi.org/10.1007/s10346-013-0391-7

Kawamoto, T., Aydan, Ö., 1999. A review of numerical analysis of tunnels in discontinuous rock masses. Int. J. Numer. Anal. Meth. Geomech. 23, 1377–1391. https://doi.org/10.1002/(SICI)1096-9853(199911)23:13<1377::AID-NAG932>3.0.CO;2-S

Kayastha, P., Dhital, M.R., De Smedt, F., 2013. Evaluation of the consistency of landslide susceptibility mapping: a case study from the Kankai watershed in

east Nepal. Landslides 10, 785–799. https://doi.org/10.1007/s10346-012-0361-5

Kemeny, J., 2003. The Time-Dependent Reduction of Sliding Cohesion due to Rock Bridges Along Discontinuities: A Fracture Mechanics Approach. Rock Mechanics and Rock Engineering 36, 27–38. https://doi.org/10.1007/s00603-002-0032-2

Kim, B.H., Cai, M., Kaiser, P.K., Yang, H.S., 2007. Estimation of Block Sizes for Rock Masses with Non-persistent Joints. Rock Mech. Rock Engng. 40, 169–192. https://doi.org/10.1007/s00603-006-0093-8

Kim, K.Y., Zhuang, L., Yang, H., Kim, H., Min, K.B., 2016. Strength Anisotropy of Berea Sandstone: Results of X-Ray Computed Tomography, Compression Tests, and Discrete Modeling. Rock Mech Rock Eng 49, 1201–1210. https://doi.org/10.1007/s00603-015-0820-0

Kim, M.K., Sohn, H.G., Kim, S., 2020. Incorporating the effect of ALS-derived DEM uncertainty for quantifying changes due to the landslide in 2011, Mt. Umyeon, Seoul. GIScience & Remote Sensing 57, 287–301. https://doi.org/10.1080/15481603.2019.1687133

Kong, D., Saroglou, C., Wu, F., Sha, P., Li, B., 2021a. Development and application of UAV-SfM photogrammetry for quantitative characterization of rock mass discontinuities. International Journal of Rock Mechanics and Mining Sciences 141, 104729. https://doi.org/10.1016/j.ijrmms.2021.104729

Kong, D., Wu, F., Saroglou, C., Sha, P., Li, B., 2021b. In-Situ Block Characterization of Jointed Rock Exposures Based on a 3D Point Cloud Model. Remote Sensing 13, 2540. https://doi.org/10.3390/rs13132540

Kong, W., 2012. Blasting assessment of slopes and risks planning. AJCE 10. https://doi.org/10.7158/C11-706.2012.10.2

Kul Yahşi, B., Ersoy, H., 2018. Site characterization and evaluation of the stability of the Yesilyurt Landslide (Trabzon, NE Turkey) using back analysis method. J. Geophys. Eng. 15, 927–937. https://doi.org/10.1088/1742-2140/aaa9c3

Kulatilake, P.H.S.W., Shreedharan, S., Sherizadeh, T., Shu, B., Xing, Y., He, P., 2016. Laboratory Estimation of Rock Joint Stiffness and Frictional Parameters. Geotech Geol Eng 34, 1723–1735. https://doi.org/10.1007/s10706-016-9984-y

Kulatilake, P.H.S.W., Wu, T.H., 1984. Estimation of mean trace length of discontinuities. Rock Mech Rock Engng 17, 215–232.

https://doi.org/10.1007/BF01032335

Kumar, N., Verma, A.K., Sardana, S., Sarkar, K., Singh, T.N., 2018. Comparative analysis of limit equilibrium and numerical methods for prediction of a landslide. Bull Eng Geol Environ 77, 595–608. https://doi.org/10.1007/s10064-017-1183-4

Kumar, S., Pandey, H.K., Singh, P.K., Venkatesh, K., 2019. Demarcation of probable failure zones based on SMR and kinematic analysis. Geomatics, Natural Hazards and Risk 10, 1793–1804. https://doi.org/10.1080/19475705.2019.1618399

Kutlug Sahin, E., Colkesen, I., 2021. Performance analysis of advanced decision tree-based ensemble learning algorithms for landslide susceptibility mapping. Geocarto International 36, 1253–1275. https://doi.org/10.1080/10106049.2019.1641560

Kveldsvik, V., Einstein, H.H., Nilsen, B., Blikra, L.H., 2009. Numerical Analysis of the 650,000 m2 Åknes Rock Slope based on Measured Displacements and Geotechnical Data. Rock Mech Rock Eng 42, 689–728. https://doi.org/10.1007/s00603-008-0005-1

Laghaei, M., Baghbanan, A., Hashemolhosseini, H., Dehghanipoodeh, M., 2018. Numerical determination of deformability and strength of 3D fractured rock mass. International Journal of Rock Mechanics and Mining Sciences 110, 246–256. https://doi.org/10.1016/j.ijrmms.2018.07.015

Lama, R.D., Vutukuri, V.S., 1978. Handbook on mechanical properties of rocks. 2, 1. print. ed, Series on rock and soil mechanics. Trans Tech Publications, Clausthal.

Lantuit, H., Pollard, W.H., 2008. Fifty years of coastal erosion and retrogressive thaw slump activity on Herschel Island, southern Beaufort Sea, Yukon Territory, Canada. Geomorphology 95, 84–102. https://doi.org/10.1016/j.geomorph.2006.07.040

Lato, M., Diederichs, M.S., Hutchinson, D.J., Harrap, R., 2009. Optimization of LiDAR scanning and processing for automated structural evaluation of discontinuities in rockmasses. International Journal of Rock Mechanics and Mining Sciences 46, 194–199. https://doi.org/10.1016/j.ijrmms.2008.04.007

LeCun, Y., Bengio, Y., Hinton, G., 2015. Deep learning. Nature 521, 436–444. https://doi.org/10.1038/nature14539

Lee, D.H., Kim, Y.T., Lee, S.R., 2020. Shallow Landslide Susceptibility Models Based

on Artificial Neural Networks Considering the Factor Selection Method and Various Non-Linear Activation Functions. Remote Sensing 12, 1194. https://doi.org/10.3390/rs12071194

Lee, E., Meadowcroft, I., Hall, J., Walkden, M., 2002. Coastal landslide activity: a probabilistic simulation model. Bulletin of Engineering Geology and the Environment 61, 347–355. https://doi.org/10.1007/s10064-001-0146-x

Lee, S., 2005. Application of logistic regression model and its validation for landslide susceptibility mapping using GIS and remote sensing data. International Journal of Remote Sensing 26, 1477–1491. https://doi.org/10.1080/01431160412331331012

Lee, S., Pradhan, B., 2006. Probabilistic landslide hazards and risk mapping on Penang Island, Malaysia. J Earth Syst Sci 115, 661–672. https://doi.org/10.1007/s12040-006-0004-0

Lee, S., Ryu, J.H., Won, J.S., Park, H.J., 2004. Determination and application of the weights for landslide susceptibility mapping using an artificial neural network. Engineering Geology 71, 289–302. https://doi.org/10.1016/S0013-7952(03)00142-X

Lei, Q., Latham, J.-P., Tsang, C.-F., 2017a. The use of discrete fracture networks for modelling coupled geomechanical and hydrological behaviour of fractured rocks. Computers and Geotechnics 85, 151–176. https://doi.org/10.1016/j.compgeo.2016.12.024

Lei, Q., Latham, J.P., Xiang, J., Tsang, C.F., 2017b. Role of natural fractures in damage evolution around tunnel excavation in fractured rocks. Engineering Geology 231, 100–113. https://doi.org/10.1016/j.enggeo.2017.10.013

Lei, Q., Latham, J.P., Xiang, J., Tsang, C.F., 2017c. Role of natural fractures in damage evolution around tunnel excavation in fractured rocks. Eng. Geol. 231, 100–113. https://doi.org/10.1016/j.enggeo.2017.10.013

Leveridge, B.E., Shail, R.K., 2011. The Gramscatho Basin, south Cornwall, UK: Devonian active margin successions. Proceedings of the Geologists' Association 122, 568–615. https://doi.org/10.1016/j.pgeola.2011.03.004

Levin, N., Kidron, G.J., Ben-Dor, E., 2006. The spatial and temporal variability of sand erosion across a stabilizing coastal dune field. Sedimentology 53, 697–715. https://doi.org/10.1111/j.1365-3091.2006.00787.x

Li, A.J., Merifield, R.S., Lyamin, A.V., 2011. Effect of rock mass disturbance on the

stability of rock slopes using the Hoek–Brown failure criterion. Computers and Geotechnics 38, 546–558. https://doi.org/10.1016/j.compgeo.2011.03.003

Li, H., Li, X., Li, W., Zhang, S., Zhou, J., 2019. Quantitative assessment for the rockfall hazard in a post-earthquake high rock slope using terrestrial laser scanning. Engineering Geology 248, 1–13. https://doi.org/10.1016/j.enggeo.2018.11.003

Li, L., Wu, W., El Naggar, M.H., Mei, G., Liang, R., 2019. Characterization of a jointed rock mass based on fractal geometry theory. Bull Eng Geol Environ 78, 6101–6110. https://doi.org/10.1007/s10064-019-01526-x

Li, W., Fang, Z., Wang, Y., 2021. Stacking ensemble of deep learning methods for landslide susceptibility mapping in the Three Gorges Reservoir area, China. Stoch Environ Res Risk Assess. https://doi.org/10.1007/s00477-021-02032-x

Li, W.C., Dai, F.C., Wei, Y.Q., Wang, M.L., Min, H., Lee, L.M., 2016. Implication of subsurface flow on rainfall-induced landslide: a case study. Landslides 13, 1109–1123. https://doi.org/10.1007/s10346-015-0619-9

Li, Z., He, Y., Li, H., Wang, Y., 2017. Antecedent rainfall induced shallow landslide-A case study of Yunnan landslide, China. Scientia Iranica 0, 0–0. https://doi.org/10.24200/sci.2017.4234

Lisjak, A., Mahabadi, O.K., He, L., Tatone, B.S.A., Kaifosh, P., Haque, S.A., Grasselli, G., 2018. Acceleration of a 2D/3D finite-discrete element code for geomechanical simulations using General Purpose GPU computing. Computers and Geotechnics 100, 84–96. https://doi.org/10.1016/j.compgeo.2018.04.011

Liu, C., Liu, X., Peng, X., Wang, E., Wang, S., 2019. Application of 3D-DDA integrated with unmanned aerial vehicle–laser scanner (UAV-LS) photogrammetry for stability analysis of a blocky rock mass slope. Landslides 16, 1645–1661. https://doi.org/10.1007/s10346-019-01196-6

Liu, J., Xu, Q., Wang, S., Siva Subramanian, S., Wang, L., Qi, X., 2020. Formation and chemo-mechanical characteristics of weak clay interlayers between alternative mudstone and sandstone sequence of gently inclined landslides in Nanjiang, SW China. Bull Eng Geol Environ 79, 4701–4715. https://doi.org/10.1007/s10064-020-01859-y

Liu, R., Li, B., Jiang, Y., 2016. A fractal model based on a new governing equation of fluid flow in fractures for characterizing hydraulic properties of rock fracture

networks. Computers and Geotechnics 75, 57–68. https://doi.org/10.1016/j.compgeo.2016.01.025

Liu, R., Zhu, T., Jiang, Y., Li, B., Yu, L., Du, Y., Wang, Y., 2019. A predictive model correlating permeability to two-dimensional fracture network parameters. Bull Eng Geol Environ 78, 1589–1605. https://doi.org/10.1007/s10064-018-1231-8

Liu, X., Zhang, Z., 2010. Drainage network extraction using LiDAR-derived DEM in volcanic plains: Drainage network extraction. Area no-no. https://doi.org/10.1111/j.1475-4762.2010.00955.x

Liu, Z., Wang, H., Zhang, C., Zhou, B., Zhou, H., 2021. Size dependences of the mechanical behaviors of basalt rock blocks with hidden joints analyzed using a hybrid DFN–FDEM model. Engineering Fracture Mechanics 258, 108078. https://doi.org/10.1016/j.engfracmech.2021.108078

Lorig, L.J., Cundall, P.A., 1989. Modeling of Reinforced Concrete Using the Distinct Element Method, in: Shah, S.P., Swartz, S.E. (Eds.), Fracture of Concrete and Rock. Springer New York, New York, NY, pp. 276–287. https://doi.org/10.1007/978-1-4612-3578-1_28

Lucchese, L.V., de Oliveira, G.G., Pedrollo, O.C., 2020. Attribute selection using correlations and principal components for artificial neural networks employment for landslide susceptibility assessment. Environ Monit Assess 192, 129. https://doi.org/10.1007/s10661-019-7968-0

Ma, G., Li, M., Wang, H., Chen, Y., 2020. Equivalent discrete fracture network method for numerical estimation of deformability in complexly fractured rock masses. Engineering Geology 277, 105784. https://doi.org/10.1016/j.enggeo.2020.105784

Ma, G., Li, T., Wang, Y., Chen, Y., 2019. The equivalent discrete fracture networks based on the correlation index in highly fractured rock masses. Engineering Geology 260, 105228. https://doi.org/10.1016/j.enggeo.2019.105228

Mahabadi, O.K., Lisjak, A., Munjiza, A., Grasselli, G., 2012. Y-Geo: New Combined Finite-Discrete Element Numerical Code for Geomechanical Applications. Int. J. Geomech. 12, 676–688. https://doi.org/10.1061/(ASCE)GM.1943-5622.0000216

Manda, A.K., Mabee, S.B., 2010. Comparison of three fracture sampling methods for layered rocks. International Journal of Rock Mechanics and Mining Sciences 47, 218–226. https://doi.org/10.1016/j.ijrmms.2009.12.004

Mao, J., Liu, X., Zhang, C., Jia, G., Zhao, L., 2021. Runout prediction and deposit characteristics investigation by the distance potential-based discrete element method: the 2018 Baige landslides, Jinsha River, China. Landslides 18, 235–249. https://doi.org/10.1007/s10346-020-01501-8

Marcotte, D., Henry, E., 2002. Automatic joint set clustering using a mixture of bivariate normal distributions. International Journal of Rock Mechanics and Mining Sciences 39, 323–334. https://doi.org/10.1016/S1365-1609(02)00033-3

Martin, C.D., Alzo'ubi, A.K., Cruden, D., 2011. Progressive Failure Mechanisms in a Slope Prone to Toppling. Presented at the International Symposium on Rock Slope Stability in Open Pit Mining and Civil Engineering, Vancouver, Canada.

Martino, S., Mazzanti, P., 2014. Integrating geomechanical surveys and remote sensing for sea cliff slope stability analysis: the Mt. Pucci case study (Italy). Nat. Hazards Earth Syst. Sci. 14, 831–848. https://doi.org/10.5194/nhess-14-831-2014

Massey, C.I., Petley, D.N., McSaveney, M.J., 2013. Patterns of movement in reactivated landslides. Engineering Geology 159, 1–19. https://doi.org/10.1016/j.enggeo.2013.03.011

Mateos, R.M., García-Moreno, I., Azañón, J.M., 2012. Freeze–thaw cycles and rainfall as triggering factors of mass movements in a warm Mediterranean region: the case of the Tramuntana Range (Majorca, Spain). Landslides 9, 417–432. https://doi.org/10.1007/s10346-011-0290-8

Mauldon, M., 1998. Estimating Mean Fracture Trace Length and Density from Observations in Convex Windows. Rock Mechanics and Rock Engineering 31, 201–216. https://doi.org/10.1007/s006030050021

Maurer, J., Rupper, S., 2015. Tapping into the Hexagon spy imagery database: A new automated pipeline for geomorphic change detection. ISPRS Journal of Photogrammetry and Remote Sensing 108, 113–127. https://doi.org/10.1016/j.isprsjprs.2015.06.008

Mehranpour, M.H., Kulatilake, P.H.S.W., Xingen, M., He, M., 2018. Development of New Three-Dimensional Rock Mass Strength Criteria. Rock Mech Rock Eng 51, 3537–3561. https://doi.org/10.1007/s00603-018-1538-6

Merghadi, A., Yunus, A.P., Dou, J., Whiteley, J., ThaiPham, B., Bui, D.T., Avtar, R., Abderrahmane, B., 2020. Machine learning methods for landslide susceptibility studies: A comparative overview of algorithm performance. Earth-Science

Reviews 207, 103225. https://doi.org/10.1016/j.earscirev.2020.103225

Meyer, T., Einstein, H.H., 2002. Geologic Stochastic Modeling and Connectivity Assessment of Fracture Systems in the Boston Area. Rock Mechanics and Rock Engineering 35, 23–44. https://doi.org/10.1007/s006030200007

Miccadei, E., Piacentini, T., Pozzo, A.D., Corte, M.L., Sciarra, M., 2013. Morphotectonic map of the Aventino-Lower Sangro valley (Abruzzo, Italy), scale 1:50,000. Journal of Maps 9, 390–409. https://doi.org/10.1080/17445647.2013.799050

Micheletti, N., Foresti, L., Robert, S., Leuenberger, M., Pedrazzini, A., Jaboyedoff, M., Kanevski, M., 2014. Machine Learning Feature Selection Methods for Landslide Susceptibility Mapping. Math Geosci 46, 33–57. https://doi.org/10.1007/s11004-013-9511-0

Mihalić Arbanas, S., Sečanj, M., Bernat Gazibara, S., Krkač, M., Begić, H., Džindo, A., Zekan, S., Arbanas, Ž., 2017. Landslides in the Dinarides and Pannonian Basin—from the largest historical and recent landslides in Croatia to catastrophic landslides caused by Cyclone Tamara (2014) in Bosnia and Herzegovina. Landslides 14, 1861–1876. https://doi.org/10.1007/s10346-017-0880-1

Miyoshi, T., Elmo, D., Rogers, S., 2018. Influence of data analysis when exploiting DFN model representation in the application of rock mass classification systems. Journal of Rock Mechanics and Geotechnical Engineering 10, 1046–1062. https://doi.org/10.1016/j.jrmge.2018.08.003

Mokhtarian, H., Moomivand, Hassan, Moomivand, Hussamuddin, 2020. Effect of infill material of discontinuities on the failure criterion of rock under triaxial compressive stresses. Theoretical and Applied Fracture Mechanics 108, 102652. https://doi.org/10.1016/j.tafmec.2020.102652

Montrasio, L., Valentino, R., Losi, G.L., 2009. Rainfall-induced shallow landslides: a model for the triggering mechanism of some case studies in Northern Italy. Landslides 6, 241–251. https://doi.org/10.1007/s10346-009-0154-7

Mousavi, S.Z.S., Tavakoli, H., Moarefvand, P., Rezaei, M., 2019. Assessing the effect of freezing-thawing cycles on the results of the triaxial compressive strength test for calc-schist rock. International Journal of Rock Mechanics and Mining Sciences 123, 104090. https://doi.org/10.1016/j.ijrmms.2019.104090

Mugagga, F., Kakembo, V., Buyinza, M., 2012. Land use changes on the slopes of

Mount Elgon and the implications for the occurrence of landslides. CATENA 90, 39–46. https://doi.org/10.1016/j.catena.2011.11.004

Munjiza, A., 2004a. The Combined Finite-Discrete Element Method: Munjiza/Discrete Element Method. John Wiley & Sons, Ltd, Chichester, UK. https://doi.org/10.1002/0470020180

Munjiza, A., 2004b. The Combined Finite-Discrete Element Method: Munjiza/Discrete Element Method. John Wiley & Sons, Ltd, Chichester, UK. https://doi.org/10.1002/0470020180

Munjiza, A., Owen, D.R.J., Bicanic, N., 1995a. A combined finite‐discrete element method in transient dynamics of fracturing solids. Engineering Computations 12, 145–174. https://doi.org/10.1108/02644409510799532

Munjiza, A., Owen, D.R.J., Bicanic, N., 1995b. A combined finite‐discrete element method in transient dynamics of fracturing solids. Engineering Computations 12, 145–174. https://doi.org/10.1108/02644409510799532

Mutlu, B., Nefeslioglu, H.A., Sezer, E.A., Akcayol, M.A., Gokceoglu, C., 2019. An Experimental Research on the Use of Recurrent Neural Networks in Landslide Susceptibility Mapping. IJGI 8, 578. https://doi.org/10.3390/ijgi8120578

Mutti, M., Bernoulli, D., Stille, P., 1997. Temperate carbonate platform drowning linked to Miocene oceanographic events: Maiella platform margin, Italy. Terra Nova 9, 122–125. https://doi.org/10.1046/j.1365-3121.1997.d01-19.x

Nasseri, M.H.B., Rao, K.S., Ramamurthy, T., 2003. Anisotropic strength and deformational behavior of Himalayan schists. International Journal of Rock Mechanics and Mining Sciences 40, 3–23. https://doi.org/10.1016/S1365-1609(02)00103-X

Neuhäuser, B., Damm, B., Terhorst, B., 2012. GIS-based assessment of landslide susceptibility on the base of the Weights-of-Evidence model. Landslides 9, 511–528. https://doi.org/10.1007/s10346-011-0305-5

Nhu, V.-H., Hoang, N.-D., Nguyen, H., Ngo, P.T.T., Thanh Bui, T., Hoa, P.V., Samui, P., Tien Bui, D., 2020. Effectiveness assessment of Keras based deep learning with different robust optimization algorithms for shallow landslide susceptibility mapping at tropical area. CATENA 188, 104458. https://doi.org/10.1016/j.catena.2020.104458

Nichol, S.L., Hungr, O., Evans, S.G., 2002. Large-scale brittle and ductile toppling of

rock slopes. Can. Geotech. J. 39, 773–788. https://doi.org/10.1139/t02-027

Nicoletti, G., Prestininzi, P.G., Miccadei, E., 1993. The Scanno rock avalanche (Abruzzi, South-Central Italy). Boll. Soc. Geol. Ital. 112, 523–535.

Nilforoushan, A., Khamehchiyan, M., Nikudel, M.R., 2021. Investigation of the probable trigger factor for large landslides in north of Dehdasht, Iran. Nat Hazards 105, 1891–1921. https://doi.org/10.1007/s11069-020-04382-1

Noël, C., Baud, P., Violay, M., 2021. Effect of water on sandstone's fracture toughness and frictional parameters: Brittle strength constraints. International Journal of Rock Mechanics and Mining Sciences 147, 104916. https://doi.org/10.1016/j.ijrmms.2021.104916

Odling, N.E., 1997. Scaling and connectivity of joint systems in sandstones from western Norway. Journal of Structural Geology 19, 1257–1271. https://doi.org/10.1016/S0191-8141(97)00041-2

Oh, H.J., Lee, S., 2011. Cross-application used to validate landslide susceptibility maps using a probabilistic model from Korea. Environ Earth Sci 64, 395–409. https://doi.org/10.1007/s12665-010-0864-0

Ohlmacher, G.C., 2007. Plan curvature and landslide probability in regions dominated by earth flows and earth slides. Engineering Geology 91, 117–134. https://doi.org/10.1016/j.enggeo.2007.01.005

Olson, J.E., 2003. Sublinear scaling of fracture aperture versus length: An exception or the rule?: SUBLINEAR SCALING OF FRACTURE APERTURE VERSUS LENGTH. J. Geophys. Res. 108. https://doi.org/10.1029/2001JB000419

Ozdemir, A., Altural, T., 2013. A comparative study of frequency ratio, weights of evidence and logistic regression methods for landslide susceptibility mapping: Sultan Mountains, SW Turkey. Journal of Asian Earth Sciences 64, 180–197. https://doi.org/10.1016/j.jseaes.2012.12.014

Packulak, T.R.M., Day, J.J., Ahmed Labeid, M.T., Diederichs, M.S., 2021. New Data Processing Protocols to Isolate Fracture Deformations to Measure Normal and Shear Joint Stiffness. Rock Mech Rock Eng. https://doi.org/10.1007/s00603-021-02632-7

Pahl, P.J., 1981. Estimating the mean length of discontinuity traces. International Journal of Rock Mechanics and Mining Sciences & Geomechanics Abstracts 18, 221–228. https://doi.org/10.1016/0148-9062(81)90976-1

Painter, S., Cvetkovic, V., Selroos, J.-O., 1998. Transport and retention in fractured

rock: Consequences of a power-law distribution for fracture lengths. Phys. Rev. E 57, 6917–6922. https://doi.org/10.1103/PhysRevE.57.6917

Palma, B., Parise, M., Reichenbach, P., Guzzetti, F., 2012. Rockfall hazard assessment along a road in the Sorrento Peninsula, Campania, southern Italy. Nat Hazards 61, 187–201. https://doi.org/10.1007/s11069-011-9899-0

Pan, D., Li, S., Xu, Z., Zhang, Y., Lin, P., Li, H., 2019. A deterministic-stochastic identification and modelling method of discrete fracture networks using laser scanning: Development and case study. Engineering Geology 262, 105310. https://doi.org/10.1016/j.enggeo.2019.105310

Pandey, V.K., Kumar, R., Singh, R., Kumar, R., Rai, S.C., Singh, R.P., Tripathi, A.K., Soni, V.K., Ali, S.N., Tamang, D., Latief, S.U., 2022. Catastrophic ice-debris flow in the Rishiganga River, Chamoli, Uttarakhand (India). Geomatics, Natural Hazards and Risk 13, 289–309. https://doi.org/10.1080/19475705.2021.2023661

Pánek, T., Hradecký, J., Minár, J., Šilhán, K., 2010. Recurrent landslides predisposed by fault-induced weathering of flysch in the Western Carpathians. Geological Society, London, Engineering Geology Special Publications 23, 183–199. https://doi.org/10.1144/EGSP23.11

Paolucci, G., Pizzi, R., Scarascia Mugnozza, G., 2001. Analisi preliminare della frana di Lettopalena (Abruzzo). Mem. Soc. Geol. It. 131–137.

Papaliangas, T., Hencher, S.R., Lumsden, A.C., Manolopoulou, S., 1993. The effect of frictional fill thickness on the shear strength of rock discontinuities. International Journal of Rock Mechanics and Mining Sciences & Geomechanics Abstracts 30, 81–91. https://doi.org/10.1016/0148-9062(93)90702-F

Pariseau, W.G., Puri, S., Schmelter, S.C., 2008. A new model for effects of impersistent joint sets on rock slope stability. International Journal of Rock Mechanics and Mining Sciences 45, 122–131. https://doi.org/10.1016/j.ijrmms.2007.05.001

Park, H.J., 2005. A new approach for persistence in probabilistic rock slope stability analysis. Geosci J 9, 287–293. https://doi.org/10.1007/BF02910589

Park, H.J., Lee, J.H., Kim, K.M., Um, J.G., 2016. Assessment of rock slope stability using GIS-based probabilistic kinematic analysis. Engineering Geology 203, 56–69. https://doi.org/10.1016/j.enggeo.2015.08.021

Patacca, E., Scandone, P., Di Luzio, E., Cavinato, G.P., Parotto, M., 2008. Structural

architecture of the central Apennines: Interpretation of the CROP 11 seismic profile from the Adriatic coast to the orographic divide: CROP 11 SEISMIC PROFILE. Tectonics 27, n/a-n/a. https://doi.org/10.1029/2005TC001917

Patton, F.D., 1966. Multiple Modes of Shear Failure In Rock. Presented at the Proc. 1st congr. Int. Soc. Rock Mech., Lisbon, Portugal.

Pellet, F.L., Keshavarz, M., Boulon, M., 2013. Influence of humidity conditions on shear strength of clay rock discontinuities. Engineering Geology 157, 33–38. https://doi.org/10.1016/j.enggeo.2013.02.002

Pham, B.T., Prakash, I., Singh, S.K., Shirzadi, A., Shahabi, H., Tran, T.-T.-T., Bui, D.T., 2019. Landslide susceptibility modeling using Reduced Error Pruning Trees and different ensemble techniques: Hybrid machine learning approaches. CATENA 175, 203–218. https://doi.org/10.1016/j.catena.2018.12.018

Pham, Q.B., Achour, Y., Ali, S.A., Parvin, F., Vojtek, M., Vojteková, J., Al-Ansari, N., Achu, A.L., Costache, R., Khedher, K.M., Anh, D.T., 2021. A comparison among fuzzy multi-criteria decision making, bivariate, multivariate and machine learning models in landslide susceptibility mapping. Geomatics, Natural Hazards and Risk 12, 1741–1777. https://doi.org/10.1080/19475705.2021.1944330

Poli, S., Sterlacchini, S., 2007. Landslide Representation Strategies in Susceptibility Studies using Weights-of-Evidence Modeling Technique. Nat Resour Res 16, 121–134. https://doi.org/10.1007/s11053-007-9043-8

Poluga, S.L., Shakoor, A., Bilderback, E.L., 2018. Rock Mass Characterization and Stability Evaluation of Mount Rushmore National Memorial, Keystone, South Dakota. Environmental and Engineering Geoscience 24, 385–412. https://doi.org/10.2113/EEG-2042

Ponomareva, V.V., Melekestsev, I.V., Dirksen, O.V., 2006. Sector collapses and large landslides on Late Pleistocene–Holocene volcanoes in Kamchatka, Russia. Journal of Volcanology and Geothermal Research 158, 117–138. https://doi.org/10.1016/j.jvolgeores.2006.04.016

Potyondy, D.O., Cundall, P.A., 2004. A bonded-particle model for rock. International Journal of Rock Mechanics and Mining Sciences 41, 1329–1364. https://doi.org/10.1016/j.ijrmms.2004.09.011

Pourghasemi, H.R., Sadhasivam, N., Kariminejad, N., Collins, A.L., 2020. Gully erosion spatial modelling: Role of machine learning algorithms in selection of

the best controlling factors and modelling process. Geoscience Frontiers 11, 2207–2219. https://doi.org/10.1016/j.gsf.2020.03.005

Priest, S.D., 1993. Discontinuity Analysis for Rock Engineering. Springer Netherlands, Dordrecht. https://doi.org/10.1007/978-94-011-1498-1

Priest, S.D., Hudson, J.A., 1981. Estimation of discontinuity spacing and trace length using scanline surveys. International Journal of Rock Mechanics and Mining Sciences & Geomechanics Abstracts 18, 183–197. https://doi.org/10.1016/0148-9062(81)90973-6

Pritchard, M.A., Savigny, K.W., 1991. The Heather Hill landslide: an example of a large scale toppling failure in a natural slope. Can. Geotech. J. 28, 410–422. https://doi.org/10.1139/t91-051

Qi, S., Zou, Y., Wu, F., Yan, C., Fan, J., Zang, M., Zhang, S., Wang, R., 2017. A Recognition and Geological Model of a Deep-Seated Ancient Landslide at a Reservoir under Construction. Remote Sensing 9, 383. https://doi.org/10.3390/rs9040383

Reddy, G.P.O., Kumar, N., Sahu, N., Singh, S.K., 2018. Evaluation of automatic drainage extraction thresholds using ASTER GDEM and Cartosat-1 DEM: A case study from basaltic terrain of Central India. The Egyptian Journal of Remote Sensing and Space Science 21, 95–104. https://doi.org/10.1016/j.ejrs.2017.04.001

Regmi, A.D., Yoshida, K., Cui, P., Hatano, N., 2017. Development of Taprang landslide, West Nepal. Landslides 14, 929–946. https://doi.org/10.1007/s10346-016-0752-0

Regmi, A.D., Yoshida, K., Nagata, H., Pradhan, A.M.S., Pradhan, B., Pourghasemi, H.R., 2013. The relationship between geology and rock weathering on the rock instability along Mugling–Narayanghat road corridor, Central Nepal Himalaya. Nat Hazards 66, 501–532. https://doi.org/10.1007/s11069-012-0497-6

Reid, M.E., Christian, S.B., Brien, D.L., 2015. Scoops3D—software to analyze three-dimensional slope stability throughout a digital landscape (Techniques and Methods), Techniques and Methods.

Renshaw, C.E., Park, J.C., 1997. Effect of mechanical interactions on the scaling of fracture length and aperture. Nature 386, 482–484. https://doi.org/10.1038/386482a0

Robert McNeel & Associates, 2012. Rhino.

Robiati, Eyre, Vanneschi, Francioni, Venn, Coggan, 2019. Application of Remote Sensing Data for Evaluation of Rockfall Potential within a Quarry Slope. IJGI 8, 367. https://doi.org/10.3390/ijgi8090367

Rocscience, 2021. Slope Stability Software | Powerful Slope Stability Analysis. URL https://www.rocscience.com/software/slope-stability (accessed 10.18.21).

Rogers, S., Elmo, D., Webb, G., Catalan, A., 2015. Volumetric Fracture Intensity Measurement for Improved Rock Mass Characterisation and Fragmentation Assessment in Block Caving Operations. Rock Mech Rock Eng 48, 633–649. https://doi.org/10.1007/s00603-014-0592-y

Rosi, A., Peternel, T., Jemec-Auflič, M., Komac, M., Segoni, S., Casagli, N., 2016. Rainfall thresholds for rainfall-induced landslides in Slovenia. Landslides 13, 1571–1577. https://doi.org/10.1007/s10346-016-0733-3

Rougier, E., Knight, E.E., Broome, S.T., Sussman, A.J., Munjiza, A., 2014. Validation of a three-dimensional Finite-Discrete Element Method using experimental results of the Split Hopkinson Pressure Bar test. International Journal of Rock Mechanics and Mining Sciences 70, 101–108. https://doi.org/10.1016/j.ijrmms.2014.03.011

Runqiu, H., 2009. Some catastrophic landslides since the twentieth century in the southwest of China. Landslides 6, 69–81. https://doi.org/10.1007/s10346-009-0142-y

Saha, S., Sarkar, R., Roy, J., Hembram, T.K., Acharya, S., Thapa, G., Drukpa, D., 2021. Measuring landslide vulnerability status of Chukha, Bhutan using deep learning algorithms. Sci Rep 11, 16374. https://doi.org/10.1038/s41598-021-95978-5

Sameen, M.I., Pradhan, B., Lee, S., 2020. Application of convolutional neural networks featuring Bayesian optimization for landslide susceptibility assessment. CATENA 186, 104249. https://doi.org/10.1016/j.catena.2019.104249

Santangelo, M., Marchesini, I., Cardinali, M., Fiorucci, F., Rossi, M., Bucci, F., Guzzetti, F., 2015. A method for the assessment of the influence of bedding on landslide abundance and types. Landslides 12, 295–309. https://doi.org/10.1007/s10346-014-0485-x

Scarascia-Mugnozza, G., Bianchi-Fasani, G., Esposito, C., Martino, S., Saroli, M., Di Luzio, E., Evans, S.G., 2006. ROCK AVALANCHE AND MOUNTAIN SLOPE

DEFORMATION IN A CONVEX DIP-SLOPE: THE CASE OF THE MAIELLA MASSIF, CENTRAL ITALY, in: Evans, Stephen G., Mugnozza, G.S., Strom, A., Hermanns, R.L. (Eds.), Landslides from Massive Rock Slope Failure, NATO Science Series. Springer Netherlands, Dordrecht, pp. 357–376. https://doi.org/10.1007/978-1-4020-4037-5_19

Schindelin, J., Arganda-Carreras, I., Frise, E., Kaynig, V., Longair, M., Pietzsch, T., Preibisch, S., Rueden, C., Saalfeld, S., Schmid, B., Tinevez, J.-Y., White, D.J., Hartenstein, V., Eliceiri, K., Tomancak, P., Cardona, A., 2012. Fiji: an open-source platform for biological-image analysis. Nat Methods 9, 676–682. https://doi.org/10.1038/nmeth.2019

Schultz, R.A., 1996. Relative scale and the strength and deformability of rock masses. Journal of Structural Geology 18, 1139–1149. https://doi.org/10.1016/0191-8141(96)00045-4

Schultz, R.A., Soliva, R., Fossen, H., Okubo, C.H., Reeves, D.M., 2008. Dependence of displacement–length scaling relations for fractures and deformation bands on the volumetric changes across them. Journal of Structural Geology 30, 1405–1411. https://doi.org/10.1016/j.jsg.2008.08.001

Schulz, W.H., 2007. Landslide susceptibility revealed by LIDAR imagery and historical records, Seattle, Washington. Engineering Geology 89, 67–87. https://doi.org/10.1016/j.enggeo.2006.09.019

Seguí, C., Tauler, E., Planas, X., Moya, J., Veveakis, M., 2021. The interplay between phyllosilicates fabric and mechanical response of deep-seated landslides. The case of El Forn de Canillo landslide (Andorra). Landslides 18, 145–160. https://doi.org/10.1007/s10346-020-01492-6

Seno, S., Thüring, M., 2006. Large landslides in Ticino, Southern Switzerland: Geometry and kinematics. Engineering Geology 83, 109–119. https://doi.org/10.1016/j.enggeo.2005.06.027

Shail, R.K., Coggan, J.S., Stead, D., 1998. Coastal landsliding in Cornwall, UK: Mechanisms, modelling and implications. Presented at the 8th International Congress of the International-Association-for-Engineering-Geology-and-the-Environment, VANCOUVER, CANADA, pp. 1323–1330.

Shang, J., Hencher, S.R., West, L.J., 2016. Tensile Strength of Geological Discontinuities Including Incipient Bedding, Rock Joints and Mineral Veins. Rock Mech Rock Eng 49, 4213–4225. https://doi.org/10.1007/s00603-016-

1041-x

Shang, J., Hencher, S.R., West, L.J., Handley, K., 2017. Forensic Excavation of Rock Masses: A Technique to Investigate Discontinuity Persistence. Rock Mech Rock Eng 50, 2911–2928. https://doi.org/10.1007/s00603-017-1290-3

Shang, J., West, L.J., Hencher, S.R., Zhao, Z., 2018a. Geological discontinuity persistence: Implications and quantification. Engineering Geology 241, 41–54. https://doi.org/10.1016/j.enggeo.2018.05.010

Shang, J., West, L.J., Hencher, S.R., Zhao, Z., 2018b. Tensile strength of large-scale incipient rock joints: a laboratory investigation. Acta Geotech. 13, 869–886. https://doi.org/10.1007/s11440-017-0620-7

Shao, C., Li, Y., Lan, H., Li, P., Zhou, R., Ding, H., Yan, Z., Dong, S., Yan, L., Deng, T., 2019. The role of active faults and sliding mechanism analysis of the 2017 Maoxian postseismic landslide in Sichuan, China. Bull Eng Geol Environ 78, 5635–5651. https://doi.org/10.1007/s10064-019-01480-8

Sharma, R.H., 2013. Evaluating the effect of slope curvature on slope stability by a numerical analysis. Australian Journal of Earth Sciences 60, 283–290. https://doi.org/10.1080/08120099.2013.762942

Shen, J., Karakus, M., Xu, C., 2013. Chart-based slope stability assessment using the Generalized Hoek–Brown criterion. International Journal of Rock Mechanics and Mining Sciences 64, 210–219. https://doi.org/10.1016/j.ijrmms.2013.09.002

Shi, G., 1992. DISCONTINUOUS DEFORMATION ANALYSIS: A NEW NUMERICAL MODEL FOR THE STATICS AND DYNAMICS OF DEFORMABLE BLOCK STRUCTURES. Engineering Computations 9, 157–168. https://doi.org/10.1108/eb023855

Siamaki, A., Esmaieli, K., Mohanty, B., 2018. Degradation of a discrete infilled joint shear strength subjected to repeated blast-induced vibrations. International Journal of Mining Science and Technology 28, 561–571. https://doi.org/10.1016/j.ijmst.2018.04.015

Singeisen, C., Ivy-Ochs, S., Wolter, A., Steinemann, O., Akçar, N., Yesilyurt, S., Vockenhuber, C., 2020. The Kandersteg rock avalanche (Switzerland): integrated analysis of a late Holocene catastrophic event. Landslides 17, 1297–1317. https://doi.org/10.1007/s10346-020-01365-y

Singh, Y., Bhat, G.M., Sharma, V., Pandita, S.K., Thakur, K.K., 2012. Reservoir induced landslide at Assar, Jammu and Kashmir: A case study. J Geol Soc

India 80, 435–439. https://doi.org/10.1007/s12594-012-0162-4

Snow, D.T., 1970. The frequency and apertures of fractures in rock. International Journal of Rock Mechanics and Mining Sciences & Geomechanics Abstracts 7, 23–40. https://doi.org/10.1016/0148-9062(70)90025-2

Song, H., Cui, W., 2016. A large-scale colluvial landslide caused by multiple factors: mechanism analysis and phased stabilization. Landslides 13, 321–335. https://doi.org/10.1007/s10346-015-0560-y

Song, J.-J., Lee, C.-I., 2001. Estimation of joint length distribution using window sampling. International Journal of Rock Mechanics and Mining Sciences 38, 519–528. https://doi.org/10.1016/S1365-1609(01)00018-1

Song, J.-J., Lee, C.-I., Seto, M., 2001. Stability analysis of rock blocks around a tunnel using a statistical joint modeling technique. Tunnelling and Underground Space Technology 16, 341–351. https://doi.org/10.1016/S0886-7798(01)00063-3

Split Engineering LLC, 2016. Split-FX.

Stead, D., 2021. ISRM. 34th ISRM Online Lecture. URL https://www.isrm.net/gca/index.php?id=1588 (accessed 7.7.21).

Stead, D., Coggan, J., 2012. Numerical modeling of rock-slope instability, in: Clague, J.J., Stead, D. (Eds.), Landslides. Cambridge University Press, Cambridge, pp. 144–158. https://doi.org/10.1017/CBO9780511740367.014

Stead, D., Eberhardt, E., Coggan, J.S., 2006. Developments in the characterization of complex rock slope deformation and failure using numerical modelling techniques. Engineering Geology 83, 217–235. https://doi.org/10.1016/j.enggeo.2005.06.033

Stead, D., Wolter, A., 2015. A critical review of rock slope failure mechanisms: The importance of structural geology. Journal of Structural Geology 74, 1–23. https://doi.org/10.1016/j.jsg.2015.02.002

Stokes, A., Atger, C., Bengough, A.G., Fourcaud, T., Sidle, R.C., 2009. Desirable plant root traits for protecting natural and engineered slopes against landslides. Plant Soil 324, 1–30. https://doi.org/10.1007/s11104-009-0159-y

Sturzenegger, M., Stead, D., Elmo, D., 2011. Terrestrial remote sensing-based estimation of mean trace length, trace intensity and block size/shape. Engineering Geology 119, 96–111. https://doi.org/10.1016/j.enggeo.2011.02.005

Sujatha, E.R., Kumaravel, P., Rajamanickam, G.V., 2014. Assessing landslide susceptibility using Bayesian probability-based weight of evidence model. Bull Eng Geol Environ 73, 147–161. https://doi.org/10.1007/s10064-013-0537-9

Sujatha, E.R., Rajamanickam, V., Kumaravel, P., Saranathan, E., 2013. Landslide susceptibility analysis using probabilistic likelihood ratio model—a geospatial-based study. Arab J Geosci 6, 429–440. https://doi.org/10.1007/s12517-011-0356-x

Sun, B., 2021. A Combined Discrete Element-Finite Difference Model for Simulation of Double Shield TBM excavation in Jointed Rocks. Rock Mech Rock Eng. https://doi.org/10.1007/s00603-021-02560-6

Sun, H.Y., Pan, P., Lü, Q., Wei, Z.L., Xie, W., Zhan, W., 2019. A case study of a rainfall-induced landslide involving weak interlayer and its treatment using the siphon drainage method. Bull Eng Geol Environ 78, 4063–4074. https://doi.org/10.1007/s10064-018-1365-8

Sun, J., Wang, X., Liu, H., Yuan, H., 2021. Effects of the attitude of dominant joints on the mobility of translational landslides. Landslides 18, 2483–2498. https://doi.org/10.1007/s10346-021-01668-8

Tang, Y., Bossard, C., Reidhead, J., 2015. Effects of percent cover of Japanese cedar in forests on slope slides in Sichuan, China. Ecological Engineering 74, 42–47. https://doi.org/10.1016/j.ecoleng.2014.09.040

Tehrany, M.S., Pradhan, B., Mansor, S., Ahmad, N., 2015. Flood susceptibility assessment using GIS-based support vector machine model with different kernel types. CATENA 125, 91–101. https://doi.org/10.1016/j.catena.2014.10.017

Teza, G., Marcato, G., Pasuto, A., Galgaro, A., 2015. Integration of laser scanning and thermal imaging in monitoring optimization and assessment of rockfall hazard: a case history in the Carnic Alps (Northeastern Italy). Nat Hazards 76, 1535–1549. https://doi.org/10.1007/s11069-014-1545-1

Thai Pham, B., Tien Bui, D., Prakash, I., 2018. Landslide susceptibility modelling using different advanced decision trees methods. Civil Engineering and Environmental Systems 35, 139–157. https://doi.org/10.1080/10286608.2019.1568418

Thiele, S.T., Grose, L., Samsu, A., Micklethwaite, S., Vollgger, S.A., Cruden, A.R., 2017. Rapid, semi-automatic fracture and contact mapping for point clouds,

images and geophysical data. Solid Earth 8, 1241–1253. https://doi.org/10.5194/se-8-1241-2017

Thiery, Y., Lacquement, F., Marçot, N., 2019. Landslides triggered in weathered crystalline rocks of moderate latitudes: A case study in Mediterranean environment (The Maures Massif, France). Engineering Geology 248, 164–184. https://doi.org/10.1016/j.enggeo.2018.12.002

Tommasi, P., Baldi, P., Chiocci, F.L., Coltelli, M., Marsella, M., Pompilio, M., Romagnoli, C., 2005. The Landslide Sequence Induced by the 2002 Eruption at Stromboli Volcano, in: Sassa, K., Fukuoka, H., Wang, F., Wang, G. (Eds.), Landslides. Springer-Verlag, Berlin/Heidelberg, pp. 251–258. https://doi.org/10.1007/3-540-28680-2_32

Travelletti, J., Malet, J.-P., Samyn, K., Grandjean, G., Jaboyedoff, M., 2013. Control of landslide retrogression by discontinuities: evidence by the integration of airborne- and ground-based geophysical information. Landslides 10, 37–54. https://doi.org/10.1007/s10346-011-0310-8

Tsangaratos, P., Benardos, A., 2014. Estimating landslide susceptibility through a artificial neural network classifier. Nat Hazards 74, 1489–1516. https://doi.org/10.1007/s11069-014-1245-x

Tu, G., Deng, H., Shang, Q., Zhang, Y., Luo, X., 2020. Deep-Seated Large-Scale Toppling Failure: A Case Study of the Lancang Slope in Southwest China. Rock Mech Rock Eng 53, 3417–3432. https://doi.org/10.1007/s00603-020-02132-0

Turichshev, A., Hadjigeorgiou, J., 2015. Experimental and Numerical Investigations into the Strength of Intact Veined Rock. Rock Mech Rock Eng 48, 1897–1912. https://doi.org/10.1007/s00603-014-0690-x

Turner, D., Lucieer, A., de Jong, S., 2015. Time Series Analysis of Landslide Dynamics Using an Unmanned Aerial Vehicle (UAV). Remote Sensing 7, 1736–1757. https://doi.org/10.3390/rs70201736

USGS, 2004. Landslide types and processes.

Vanneschi, C., Eyre, M., Venn, A., Coggan, J.S., 2019. Investigation and modeling of direct toppling using a three-dimensional distinct element approach with incorporation of point cloud geometry. Landslides 16, 1453–1465. https://doi.org/10.1007/s10346-019-01192-w

Varnes, D.J., 1978. Slope movement types and processes, in Schuster, R.L., and Krizek, R.J., eds., Landslides—Analysis and control, Special report -

Transportation Research Board, National Research Council. Washington : National Academy of Sciences.

Vazaios, I., Vlachopoulos, N., Diederichs, M.S., 2019. Assessing fracturing mechanisms and evolution of excavation damaged zone of tunnels in interlocked rock masses at high stresses using a finite-discrete element approach. Journal of Rock Mechanics and Geotechnical Engineering 11, 701–722. https://doi.org/10.1016/j.jrmge.2019.02.004

Vecsei, A., Sanders, D.G.K., Bernoulli, D., Eberli, G.P., Pignatti, J.S., 1999. Cretaceous to Miocene Sequence Stratigraphy and Evolution of the Maiella Carbonate Platform Margin, Italy, in: Mesozoic and Cenozoic Sequence Stratigraphy of European Basins. SEPM Society for Sedimentary Geology. https://doi.org/10.2110/pec.98.02.0053

Vezzani, L., Ghisetti, F., 1998. Carta geologica dell'Abruzzo: S.EL.CA., Firenze.

Wang, J., Zhang, Y., Chen, Y., Wang, Q., Xiang, C., Fu, H., Wang, P., Zhao, J.X., Zhao, L., 2021. Back-analysis of Donghekou landslide using improved DDA considering joint roughness degradation. Landslides. https://doi.org/10.1007/s10346-020-01586-1

Wang, J., Zheng, J., Liu, T., Guo, J., Lü, Q., 2020. A comprehensive dissimilarity method of modeling accuracy evaluation for discontinuity disc models based on the sampling window. Computers and Geotechnics 119, 103381. https://doi.org/10.1016/j.compgeo.2019.103381

Wang, M., Ma, G., Wang, F., 2021. Numerically investigation on blast-induced wave propagation in catastrophic large-scale bedding rockslide. Landslides 18, 785–797. https://doi.org/10.1007/s10346-020-01537-w

Wang, P., Cai, M., Ren, F., Li, C., Yang, T., 2017. A Digital Image-Based Discrete Fracture Network Model and Its Numerical Investigation of Direct Shear Tests. Rock Mech Rock Eng 50, 1801–1816. https://doi.org/10.1007/s00603-017-1200-8

Wang, W., Liu, Q., Ma, H., Lu, H., Wang, Z., 2020. Numerical analysis of material modeling rock reinforcement in 2D FDEM and parameter study. Computers and Geotechnics 126, 103767. https://doi.org/10.1016/j.compgeo.2020.103767

Wang, X., Cai, M., 2020. A DFN–DEM Multi-scale Modeling Approach for Simulating Tunnel Excavation Response in Jointed Rock Masses. Rock Mech Rock Eng 53, 1053–1077. https://doi.org/10.1007/s00603-019-01957-8

Wang, Y., Fang, Z., Hong, H., 2019. Comparison of convolutional neural networks for landslide susceptibility mapping in Yanshan County, China. Science of The Total Environment 666, 975–993. https://doi.org/10.1016/j.scitotenv.2019.02.263

Wang, Y., Seijmonsbergen, A.C., Bouten, W., Chen, Q., 2015. Using statistical learning algorithms in regional landslide susceptibility zonation with limited landslide field data. J. Mt. Sci. 12, 268–288. https://doi.org/10.1007/s11629-014-3134-x

Wang, Z.W., Zhang, J.H., Li, D.Y., 2013. Application of Fuzzy Weights of Evidence Method in Landslide Susceptibility Assessment Based on GIS. AMR 864–867, 2756–2759. https://doi.org/10.4028/www.scientific.net/AMR.864-867.2756

Wei, X., Zhang, L., Luo, J., Liu, D., 2021. A hybrid framework integrating physical model and convolutional neural network for regional landslide susceptibility mapping. Nat Hazards 109, 471–497. https://doi.org/10.1007/s11069-021-04844-0

Weidinger, J.T., Korup, O., Munack, H., Altenberger, U., Dunning, S.A., Tippelt, G., Lottermoser, W., 2014. Giant rockslides from the inside. Earth and Planetary Science Letters 389, 62–73. https://doi.org/10.1016/j.epsl.2013.12.017

Wittke, W., 1990. Rock mechanics : theory and applications with case histories. Springer.

Wu, J.H., Wang, W.N., Chang, C.S., Wang, C.L., 2005. Effects of strength properties of discontinuities on the unstable lower slope in the Chiu-fen-erh-shan landslide, Taiwan. Engineering Geology 78, 173–186. https://doi.org/10.1016/j.enggeo.2004.12.005

Xia, M., Chen, G., Yu, P., Peng, X., Zou, J., 2021. Improvement of DDA with a New Unified Tensile Fracture Model for Rock Fragmentation and its Application on Dynamic Seismic Landslides. Rock Mech Rock Eng. https://doi.org/10.1007/s00603-020-02307-9

Xie, J.C., Liu, R., Li, H.W., Lai, Z.L., 2015. Analysis of landslide hazard area in Ludian earthquake based on Random Forests. Int. Arch. Photogramm. Remote Sens. Spatial Inf. Sci. XL-7/W3, 865–869. https://doi.org/10.5194/isprsarchives-XL-7-W3-865-2015

Xu, C., Dai, F., Xu, X., Lee, Y.H., 2012. GIS-based support vector machine modeling of earthquake-triggered landslide susceptibility in the Jianjiang River

watershed, China. Geomorphology 145–146, 70–80. https://doi.org/10.1016/j.geomorph.2011.12.040

Xu, C., Xu, X., Dai, F., Wu, Z., He, H., Shi, F., Wu, X., Xu, S., 2013. Application of an incomplete landslide inventory, logistic regression model and its validation for landslide susceptibility mapping related to the May 12, 2008 Wenchuan earthquake of China. Nat Hazards 68, 883–900. https://doi.org/10.1007/s11069-013-0661-7

Xu, J., Tang, X., Wang, Z., Feng, Y., Bian, K., 2020. Investigating the softening of weak interlayers during landslides using nanoindentation experiments and simulations. Engineering Geology 277, 105801. https://doi.org/10.1016/j.enggeo.2020.105801

Yalcin, A., 2007. The effects of clay on landslides: A case study. Applied Clay Science 38, 77–85. https://doi.org/10.1016/j.clay.2007.01.007

Yang, J., Dai, J., Yao, C., Jiang, S., Zhou, C., Jiang, Q., 2020. Estimation of rock mass properties in excavation damage zones of rock slopes based on the Hoek-Brown criterion and acoustic testing. International Journal of Rock Mechanics and Mining Sciences 126, 104192. https://doi.org/10.1016/j.ijrmms.2019.104192

Yao, W., Sharifzadeh, M., Yang, Z., Xu, G., Fang, Z., 2019. Assessment of fracture characteristics controlling fluid flow performance in discrete fracture networks (DFN). Journal of Petroleum Science and Engineering 178, 1104–1111. https://doi.org/10.1016/j.petrol.2019.04.011

Yao, X., Tham, L.G., Dai, F.C., 2008. Landslide susceptibility mapping based on Support Vector Machine: A case study on natural slopes of Hong Kong, China. Geomorphology 101, 572–582. https://doi.org/10.1016/j.geomorph.2008.02.011

Yi, Y., Zhang, Z., Zhang, W., Jia, H., Zhang, J., 2020. Landslide susceptibility mapping using multiscale sampling strategy and convolutional neural network: A case study in Jiuzhaigou region. CATENA 195, 104851. https://doi.org/10.1016/j.catena.2020.104851

Yilmaz, I., 2010. Comparison of landslide susceptibility mapping methodologies for Koyulhisar, Turkey: conditional probability, logistic regression, artificial neural networks, and support vector machine. Environ Earth Sci 61, 821–836. https://doi.org/10.1007/s12665-009-0394-9

Yilmaz, I., 2009. Landslide susceptibility mapping using frequency ratio, logistic

regression, artificial neural networks and their comparison: A case study from Kat landslides (Tokat—Turkey). Computers & Geosciences 35, 1125–1138. https://doi.org/10.1016/j.cageo.2008.08.007

Yilmaz, I., Marschalko, M., Yildirim, M., Dereli, E., Bednarik, M., 2012. GIS-based kinematic slope instability and slope mass rating (SMR) maps: application to a railway route in Sivas (Turkey). Bull Eng Geol Environ 71, 351–357. https://doi.org/10.1007/s10064-011-0384-5

Yin, T., Chen, Q., 2020. Simulation-based investigation on the accuracy of discrete fracture network (DFN) representation. Computers and Geotechnics 121, 103487. https://doi.org/10.1016/j.compgeo.2020.103487

Ying, C., Zhang, K., Wang, Z.-N., Siddiqua, S., Makeen, G.M.H., Wang, L., 2021. Analysis of the run-out processes of the Xinlu Village landslide using the generalized interpolation material point method. Landslides 18, 1519–1529. https://doi.org/10.1007/s10346-020-01581-6

Yokoyama, O., 2020. Evolution of uphill-facing scarps by flexural toppling of slate with high-angle faults. Geomorphology 352, 106977. https://doi.org/10.1016/j.geomorph.2019.106977

Youssef, A.M., Pourghasemi, H.R., 2021. Landslide susceptibility mapping using machine learning algorithms and comparison of their performance at Abha Basin, Asir Region, Saudi Arabia. Geoscience Frontiers 12, 639–655. https://doi.org/10.1016/j.gsf.2020.05.010

Yu, X., Zhang, K., Song, Y., Jiang, W., Zhou, J., 2021. Study on landslide susceptibility mapping based on rock–soil characteristic factors. Sci Rep 11, 15476. https://doi.org/10.1038/s41598-021-94936-5

Zanbak, C., 1977. Statistical interpretation of discontinuity contour diagrams. International Journal of Rock Mechanics and Mining Sciences & Geomechanics Abstracts 14, 111–120. https://doi.org/10.1016/0148-9062(77)90001-8

Zeeb, C., Gomez-Rivas, E., Bons, P.D., Virgo, S., Blum, P., 2013. Fracture network evaluation program (FraNEP): A software for analyzing 2D fracture trace-line maps. Computers & Geosciences 60, 11–22. https://doi.org/10.1016/j.cageo.2013.04.027

Zhan, J., Xu, P., Chen, J., Zhang, W., Niu, C., Han, X., 2016. A stepwise approach for 3D fracture intersection analysis and application to a hydropower station in Southwest China. International Journal of Rock Mechanics and Mining

Sciences 89, 116–128. https://doi.org/10.1016/j.ijrmms.2016.08.006

Zhang, L., Einstein, H.H., 2000. Estimating the intensity of rock discontinuities. International Journal of Rock Mechanics and Mining Sciences 37, 819–837. https://doi.org/10.1016/S1365-1609(00)00022-8

Zhang, L., Einstein, H.H., 1998. Estimating the Mean Trace Length of Rock Discontinuities. Rock Mechanics and Rock Engineering 31, 217–235. https://doi.org/10.1007/s006030050022

Zhang, M., McSaveney, M., Shao, H., Zhang, C., 2018. The 2009 Jiweishan rock avalanche, Wulong, China: Precursor conditions and factors leading to failure. Engineering Geology 233, 225–230. https://doi.org/10.1016/j.enggeo.2017.12.010

Zhang, Q., Wang, X., He, L., Tian, L., 2021. Estimation of Fracture Orientation Distributions from a Sampling Window Based on Geometric Probabilistic Method. Rock Mech Rock Eng 54, 3051–3075. https://doi.org/10.1007/s00603-021-02431-0

Zhang, W., Lan, Z., Ma, Z., Tan, C., Que, J., Wang, F., Cao, C., 2020. Determination of statistical discontinuity persistence for a rock mass characterized by non-persistent fractures. International Journal of Rock Mechanics and Mining Sciences 126, 104177. https://doi.org/10.1016/j.ijrmms.2019.104177

Zhang, Y., Jiang, Y., Asahina, D., Wang, C., 2020. Experimental and Numerical Investigation on Shear Failure Behavior of Rock-like Samples Containing Multiple Non-Persistent Joints. Rock Mech. Rock Eng. 53, 4717–4744. https://doi.org/10.1007/s00603-020-02186-0

Zhang, Y., Ren, F.Y., Yang, T.H., Wang, S.Y., Zhang, W.F., Yu, M.X., 2018. An Improved Rock Mass Characterization Method Using a Quantified Geological Strength Index and Synthetic Rock Mass Model. Rock Mech Rock Eng 51, 3521–3536. https://doi.org/10.1007/s00603-018-1532-z

Zheng, D., Ju, N., Zhao, H., Li, H., 2015. Study on Formation Mechanism and Evolution of Cracking-Toppling Rockfall Affected by Underground Mining: A Case Study of Shangyang River Rockfall, in: Lollino, G., Giordan, D., Crosta, G.B., Corominas, J., Azzam, R., Wasowski, J., Sciarra, N. (Eds.), Engineering Geology for Society and Territory - Volume 2. Springer International Publishing, Cham, pp. 1969–1973. https://doi.org/10.1007/978-3-319-09057-3_349

Zheng, J., Deng, J., Yang, X., Wei, J., Zheng, H., Cui, Y., 2014. An improved Monte

Carlo simulation method for discontinuity orientations based on Fisher distribution and its program implementation. Computers and Geotechnics 61, 266–276. https://doi.org/10.1016/j.compgeo.2014.06.006

Zheng, J., Kulatilake, P.H.S.W., Deng, J., 2015. Development of a probabilistic block theory analysis procedure and its application to a rock slope at a hydropower station in China. Engineering Geology 188, 110–125. https://doi.org/10.1016/j.enggeo.2015.01.010

Zheng, J., Kulatilake, P.H.S.W., Shu, B., 2017. Improved Probabilistic Kinematic Analysis Procedure Based on Finite Size Discontinuities and Its Application to a Rock Slope at Open Pit Mine in U.S. Int. J. Geomech. 17, 04016052. https://doi.org/10.1061/(ASCE)GM.1943-5622.0000721

Zhou, J., Cui, P., Hao, M., 2016. Comprehensive analyses of the initiation and entrainment processes of the 2000 Yigong catastrophic landslide in Tibet, China. Landslides 13, 39–54. https://doi.org/10.1007/s10346-014-0553-2

Zhou, Z., Sun, J., Lai, Y., Wei, C., Hou, J., Bai, S., Huang, X., Liu, H., Xiong, K., Cheng, S., 2022. Study on size effect of jointed rock mass and influencing factors of the REV size based on the SRM method. Tunnelling and Underground Space Technology 127, 104613. https://doi.org/10.1016/j.tust.2022.104613

Zhu, H., Zuo, Y., Li, X., Deng, J., Zhuang, X., 2014. Estimation of the fracture diameter distributions using the maximum entropy principle. International Journal of Rock Mechanics and Mining Sciences 72, 127–137. https://doi.org/10.1016/j.ijrmms.2014.09.006

Zhu, L., Cui, S., Pei, X., Wang, S., He, S., Shi, X., 2021. Experimental investigation on the seismically induced cumulative damage and progressive deformation of the 2017 Xinmo landslide in China. Landslides 18, 1485–1498. https://doi.org/10.1007/s10346-020-01608-y

Zhu, L., Huang, L., Fan, L., Huang, J., Huang, F., Chen, J., Zhang, Z., Wang, Y., 2020. Landslide Susceptibility Prediction Modeling Based on Remote Sensing and a Novel Deep Learning Algorithm of a Cascade-Parallel Recurrent Neural Network. Sensors 20, 1576. https://doi.org/10.3390/s20061576

Zhuang, Y., Xu, Q., Xing, A., 2019. Numerical investigation of the air blast generated by the Wenjia valley rock avalanche in Mianzhu, Sichuan, China. Landslides 16, 2499–2508. https://doi.org/10.1007/s10346-019-01253-0

Zou, L., Håkansson, U., Cvetkovic, V., 2019. Cement grout propagation in two-dimensional fracture networks: Impact of structure and hydraulic variability. International Journal of Rock Mechanics and Mining Sciences 115, 1–10. https://doi.org/10.1016/j.ijrmms.2019.01.004

Appendix A – Joint roughness coefficient graph

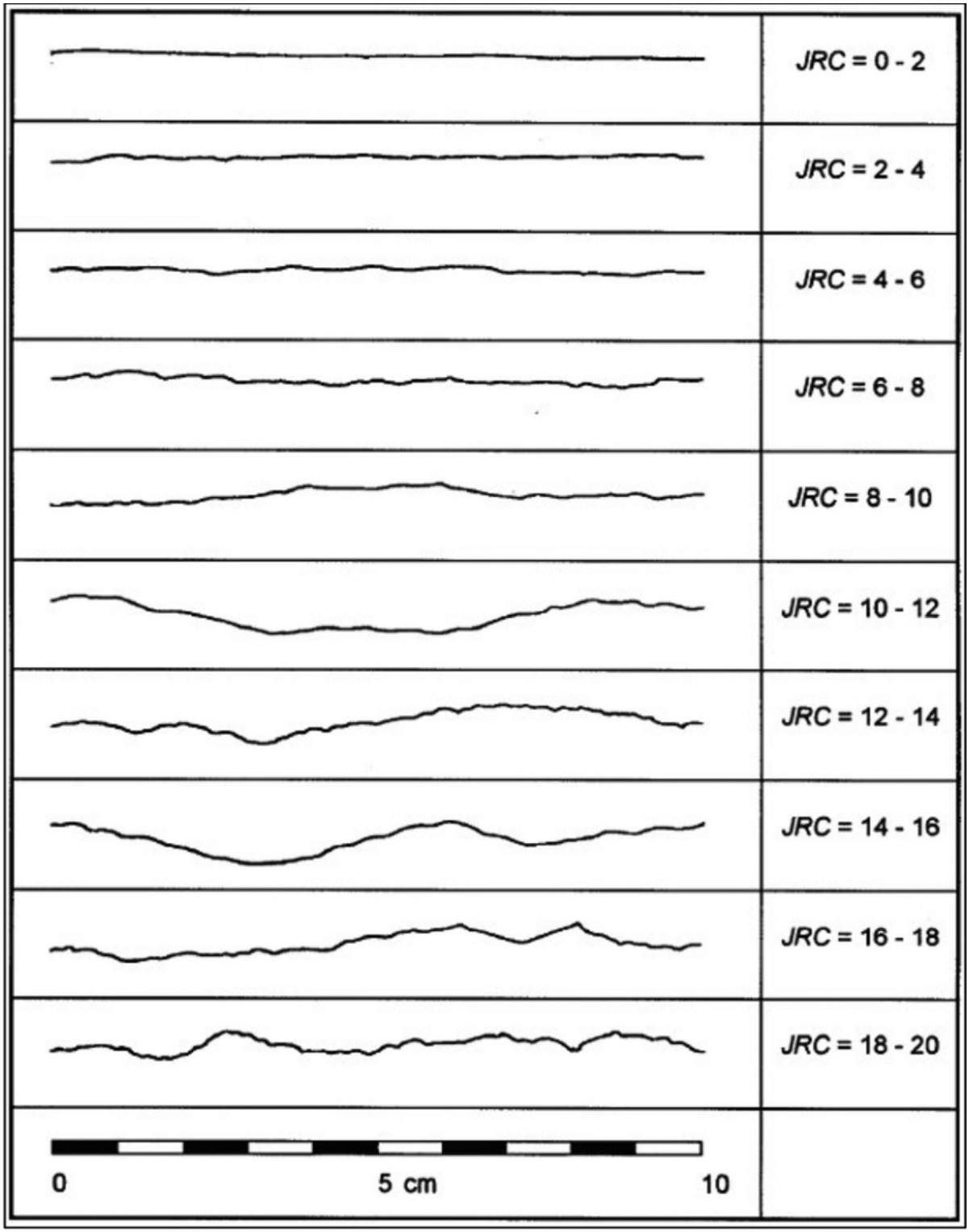

Appendix B – Intact Rock Strength Constant

Rock type	Class	Group	Texture			
			Coarse	Medium	Fine	Very fine
SEDIMENTARY	Clastic		Conglomerates * Breccias *	Sandstones 17 ± 4	Siltstones 7 ± 2 Greywackes (18 ± 3)	Claystones 4 ± 2 Shales (6 ± 2) Marls (7 ± 2)
	Non-Clastic	Carbonates	Crystalline Limestone (12 ± 3)	Sparitic Limestones (10 ± 2)	Micritic Limestones (9 ± 2)	Dolomites (9 ± 3)
		Evaporites		Gypsum 8 ± 2	Anhydrite 12 ± 2	
		Organic				Chalk 7 ± 2
METAMORPHIC	Non Foliated		Marble 9 ± 3	Hornfels (19 ± 4) Metasandstone (19 ± 3)	Quartzites 20 ± 3	
	Slightly foliated		Migmatite (29 ± 3)	Amphibolites 26 ± 6	Gneiss 28 ± 5	
	Foliated**			Schists 12 ± 3	Phyllites (7 ± 3)	Slates 7 ± 4
IGNEOUS	Plutonic	Light	Granite 32 ± 3 Granodiorite (29 ± 3)	Diorite 25 ± 5		
		Dark	Gabbro 27 ± 3 Norite 20 ± 5	Dolerite (16 ± 5)		
	Hypabyssal		Porphyries (20 ± 5)		Diabase (15 ± 5)	Peridotite (25 ± 5)
	Volcanic	Lava		Rhyolite (25 ± 5) Andesite 25 ± 5	Dacite (25 ± 3) Basalt (25 ± 5)	
		Pyroclastic	Agglomerate (19 ± 3)	Breccia (19 ± 5)	Tuff (13 ± 5)	